Quantitative ultrasound in transverse transmission for bone quality assessment and monitoring fracture healing

Dissertation

zur Erlangung des akademischen Grades

doctor rerum naturalium

(Dr. rer. nat)

im Fach Biophysik

eingereicht an der

Mathematisch-Naturwissenschaftlichen Fakultät I

der Humboldt-Universität zu Berlin

von

Dipl. Bioinformatiker, Daniel Rohrbach

Präsident der Humboldt-Universität zu Berlin

Prof. Dr. Jan-Hendrik Olbertz

Dekan der Mathematisch-Naturwissenschaftlichen Fakultät I

Prof. Dr. Stefan Hecht

Gutachter/in: 1. Univ.-Prof. Dr.rer.nat. Kay Raum

2. Prof. Dr. med. Hans-Dieter Volk

3. PD Dr. Detlef Reichert

Tag der mündlichen Prüfung: 27.08.2013

Schlagwörter

Quantitativer Ultraschall, QUS, Osteoporose, non-union, Transverse-Transmission, Knochen, Femurhals, Frakturheilung, Akustische Mikroskopie, SAM, μCT, Synchrotron, Knochenqualität, Knochenporosität, Finite-Differenz-Zeit Simulationen, FDTD, Osteotomie,

Key words

Quantitative ultrasoun, QUS, osteoporis, non-union, transverse transmission, bone, femur neck, fracture healing, scanning acoustic microscopy, synchrotron, μCT, bone quality, bone porosity, finite difference time domain simulations, FDTD, osteotomy,

Zusammenfassung

Osteoporose und gestörte Heilungsverläufe von Knochenbrüchen verursachen immer noch beachtliche klinische Komplikationen. Ein vielversprechender Ansatz für die nichtinvasive und nichtionisierende Abschätzung des Frakturrisikos und der Bildgebung von Frakturheilung ist quantitativer Ultraschall (QUS). Dennoch liegt die derzeitige Akzeptanz für die Knochenqualitätsabschätzung noch weit hinter herkömmlichen röntgenbasierten Anwendungen.

Es wurden akustische Mikroskopie und Synchrotronstrahlen-Mikrotomographie für die Anatomie und altersabhängige Erfassung von strukturellen und elastischen Variationen auf der mikroskopischen Ebene von humanen Femora verwendet. Die gewonnenen Daten dienten als Grundlage für die Erstellung mikromechanischer Modelle von Knochen für numerische Simulationen der Schallausbreitung im humanen Femurhals. Dabei wurde der Aufbau eines US-basierten Femur-Scanners in transversaler Transmission (TT) nachempfunden. Im letzten Abschnitt der Arbeit wurde QUS in TT in *in vitro* Experimenten am Rattenfrakturmodell auf eine Anwendung für die Bildgebung der Frakturheilung getestet.

Die Studien konnten zeigen, dass ein Großteil der adaptiven Fähigkeiten von Knochen auf mikroskopischer Ebene auf eine Kombination von extrazellulärer Matrixelastizität und Gewebeporosität zurückzuführen ist. Die Simulationen des zweiten Teils konnten die Existenz von geführten Wellen im humanen Femurhals bestätigen. Die sensitive Abhängigkeit von US-parametern von frakturrelevanten Knocheneigenschaften zeigt das hohe Potential von QUS für die Frakturrisikoabschätzung. Der zweite Teil der Arbeit konnte erfolgreich die Möglichkeit von QUS in TT zur Diskriminierung von zeitigen Heilungsstadien demonstrieren.

Zusammenfassend bestätigt die Studie das hohe Potential von QUS für die Frakturrisikoabschätzung und die Bildgebung der Frakturheilung.

Abstract

Osteoporosis and impaired bone healing are of high relevance. A promising non-invasive, non-ionizing candidate for fracture risk prediction and monitoring fracture healing is quantitative ultrasound (QUS). However, the acceptance of QUS for bone quality assessment is still not comparable to X-ray based methods.

Scanning acoustic microscopy (SAM) and Synchrotron Radiation micro-computer tomography (SRμCT) has been used to investigate anatomical and age dependent variations of micro elastic, structural and mineralization parameters at the tissue level of human femoral bone. Femoral neck models were created based on these data for numerical sound propagation simulations emulating a transverse transmission (TT) setup of an *in vivo* QUS prototype. In the last part of the project the TT approach has been tested in *ex vivo* experiments in a rat healing model. The power of QUS, to discriminate two early healing stages has been compared to μCT measurements at the same specimens.

It was found that the major contributor to bone adaptation is related to a combination of extracellular matrix elasticity and tissue porosity. It is hypothesized that these parameters are likely to have a considerable impact on the reliability of *in silico* models. The simulations of the second part confirmed the existence of guided wave propagation in the cortical shell and a high dependency of US parameters on fracture relevant bone properties. The results demonstrate the high potential for bone fracture risk prediction at the femoral neck using QUS. Finally, it was successfully demonstrated that early healing stage discrimination of QUS in TT was superior compared to μCT.

In summary these investigations not only show the importance for a precise estimation of micro mechanical properties for numerical modelling but also demonstrate the feasibility and high potential of QUS for bone quality assessment and monitoring of fracture healing.

Table of Content

List of Figures

List of Tables

Abbreviations and Symbols

Abbreviations

aBMD	areal bone mineral density
AFM	atomic force microscopy
ANT	anterior
BMD	bone mineral density
BMDD	bone mineral densitiy distribution
BMP	bone morphogenetic proteins
BMU	basic multi cellular unit
CT	computer tomography
µCT	micro computer tomography
DXA	dual X-ray absorptiometry
FAS	first arriving signal
FDTD	finite difference time domain
FE	finite element
FEM	finite element model
FemUS	prototype of a ultrasound based femur ultrasound scanner
FFT	Fast Fourier Transform
F.head	femoral neck
F.trochanter	femoral trochanter
FN	Femoral neck
HR-pQCT	high resolution peripheral quantitative computer tomography
IGF	important growth factors
INF	inferior
k-NN	k-nearest neighbour
LAT	lateral
LOOCV	leave-one-out cross-validation
MDCT	multi-detector computed tomography
MED	medial
MMA	methylmethacrylate
MRI	magnetic resonance imaging
OT	osteotomy
PCCT	phase-contrast CT
PML	perfectly matched layers
PMMA	Polymethylmethacrylat
POS	posterior
pQCT	peripheral quantitative computer tomography
PS	pseudo-spectral
qBEI	quantitative backscattered electron imaging
QCT	quantitative computer tomography

QUS	quantitative ultrasound
ROC	radius of curvature
ROI	region of interest
RUS	Resonant ultrasound spectroscopy
SAW	surface acoustic waves
SAX	small angle X-ray scattering
SEM	scanning electron microscopy
SR	synchrotron radiation
SRμCT	synchrotron radiation μCT
SSCW	surface skimming compressional waves
SUP	superior
SVM	support vector machine
TGF	transforming growth factors
TOF	time-of-flight
UET MRI	ultrashort echo-time MRI
VOI	volume of interests
WAX	wide angle X-ray scattering
W.H.O.	World Health Organisation

Symbols

A	area [m^2]
α	attenuation coefficient [cm^{-1}]
ar	anisotropic ratio
BMC	bone mineral content [mg HA]
BV	bone volume [mm^3]
BUA	broadband ultrasound attenuation measured in [dB/MHz]
c_{ijkl}	coefficients of elastic tensor in [Pa = kg/m^2]
Ct	cortical, in conjunction with "." e.g. Por ($Ct.Por$) it becomes cortical porosity
Δd	SAM scan increment [µm]
$D_{lateral}$	sound field lateral resolution [m]
DMB	degree of mineralization of bone [g/cm^3]
E	Young's modulus [Pa]
E_{IT}	Young's modulus measured with nanoindentation [Pa]
ε	strain
F	force [N=$kg\,\frac{m}{s^2}$]
F_z	focal depth [m]
f	frequencz [Hz]
G	shear modulus [Pa]
I	intensity [$W \cdot cm^{-2}$]
k	wave number
γ	shear strain
λ	wave length [m]
Δl	displacement [m]
nUA	normalized UA [dB mm^{-1}]
$nBUA$	normalized BUA [dB MHz^{-1} mm^{-1}]
$\phi(f)$	phase spectra
p	pressure [Pa]
Por	porosity (in conjunction with Ct, cortical porosity: $Ct.Por$)
$PorDens$	pore density [$1/mm^2$]
$PorDm$	pore diameter (in conjunction with Ct, cortical pore diameter: $Ct.PorDm$)
$PS(f)$	power spectral density

ρ	density in [g/cm^3]
R	correlation coefficient (R^2 square of correlation coefficient)
$\mathcal{R}$	reflexion coefficient
S	compliance tensor [Pa]
SD	standard deviation
sr	semi partial correlation coefficient (sr^2 square of semipartial correlation coefficient)
sRes	spatial resolution
σ	stress [Pa]
TOF	time of flight [µs].
TV	total volume [mm^3]
t	time vector in [s]
τ	shear stress [Pa]
Th	thickness [m]
SOS	speed of sound [m/s]
U	ultrasound signal amplitude in [V]
UA	ultrasound attenuation *UA* [dB]
v	sound velocity [m/s] (=SOS)
v	particle velocity [m/s]
ϑ	Poisson's ratio
$\vec{x}$	vector representing coordinates in space, $\vec{x} \in \mathbb{R}^3$
Z	acoustic impedance [Mrayl]

1. Introduction and Background

Although, from a mechanical point of view, bone is a very efficient material, injuries and diseases can affect its integrity. The most considerable metabolic disease is Osteoporosis. It has been rated by the World Health Organisation (W.H.O) to be one of the ten most important diseases in the western world. According to the Development Panel on Osteoporosis (1991), osteoporosis is characterised by changes of bone material which leads to a reduced bone strength and consequently to an increased fracture risk. Probably the most dramatic site of osteoporosis related fragility fractures is the proximal femur with mortality rates above 36 % (Abrahamsen et al. 2009; Hu et al. 2012; Kaufman et al. 2013). The associated considerable impairment in quality of life for patients and the strong burden in costs for the health care system emphasize the necessity for early fracture risk prediction systems.

Dual X-ray absorptiometry (DXA) is the current gold standard in osteoporotic fracture risk prediction (Adams 2012; Griffith and Genant 2012; Lewiecki 2012). However, it can only explain for 60 % - 80 % of bone strength (Glüer 1997; Adams 2012) and 50 % of the patients who suffered from a fragility fracture are rated to be non-osteoporotic (Stone et al. 2003; Schuit et al. 2004; Sornay-Rendu et al. 2005).

Impaired bone fracture healing, such as non-union or delayed healing, also causes severe clinical complications. The current standards are still plain radiographs (Pedrotti et al. 2006), though was shown to be doubtful for monitoring fracture healing in many studies (Nicholls et al. 1979; Hammer et al. 1985; Panjabi et al. 1989; Blokhuis et al. 2001). It is limited to mineralized tissue and therefore fails to detect the important early stages of healing where only soft tissue formations are present (Panjabi et al. 1985).

Quantitative ultrasound (QUS) in transverse transmission at the femoral neck, though clinically less accepted and still poorly understood, is expected to be a promising diagnostic alternative for fracture risk prediction and monitoring fracture healing (Laugier and Haïat 2011a). It is a non-invasive and non-ionizing method. Furthermore, ultrasound (US) is a mechanical wave and thus carries information about structure and the elasticity of the interrogated material (Laugier and Haïat 2011a) which cannot be assessed by X-ray (Adams 2012). Finally, US is sensitive to both hard and soft tissues. The latter in particular, is important for fracture healing where soft tissue is prevalent in the early healing phases.

However, currently the only clinical accepted US based fracture risk prediction method is QUS on the calcaneus. Although QUS on the heel was reported to be at least as good as DXA, the calcaneus is located far from fracture relevant sites such as the femoral neck. In fact, the femoral neck exhibits a considerable different structure compared to the heel which is also reflected in the mechanical properties (Holzer et al. 2009). Therefore, a novel prototype - the *FemUS* - has been developed recently by Barkmann et al. (2008a) which enables the measurement of ultrasonic parameters directly at the proximal femur for the first time. Preliminary *in vivo* tests revealed a good discriminatory power for separating patients with a history of a fragility fracture from controls (Barkmann et al. 2010a).

Although QUS in transverse transmission has excellent imaging abilities, almost no study reports its use for monitoring fracture healing (Rohrbach et al. 2012a). The prevalent method is axial transmission (Protopappas et al. 2008) but provides no imaging capabilities.

In order to investigate the complex nature of bone-ultrasound-interaction, numerical simulation methods have been developed within the past decade (Bossy et al. 2004a). First studies showed promising results for relating fracture risk relevant properties, such as moment of inertia or cortical thickness, to ultrasound propagation parameters, such as speed of sound (*SOS*) or broadband ultrasound attenuation (*BUA*) (Barkmann et al. 2000; Grondin et al. 2010). The reliability of the outcome of these approaches crucially depends on the mechanical models of bone. However, the exact anatomical and age dependent variations of the mechanical properties at the micro level (5 µm – 500 µm), such as bone elastic stiffness, mineralization and porosity, and their relation to each other are still poorly understood. Nowadays, the assessment of material properties at these length scales is enabled by novel technologies such as scanning acoustic microscopy (SAM) or synchrotron radiation µCT (SRµCT) for the first time (Raum et al. 2006b; Raum 2008; Granke et al. 2011).

1.1 Aims and hypotheses

The overall aim of this present thesis is the development and investigation of new ultrasound based transverse transmission approaches. The work is divided into two sub projects with study I focusing on the assessment of bone quality in terms of osteoporotic fracture risk prediction in human femoral bone and study II concentrates on monitoring bone fracture healing in a rat osteotomy model.

Aims and Hypotheses Study I

The aim of study I is the establishment of a framework for numerical ultrasound simulations at the human femoral neck based on SAM data. The framework will be used to validate an *in vivo* QUS transverse transmission device by the identification of bone quality relevant parameters that have an impact on ultrasound propagation. The mechanical bone models will be based on realistic micro elastic and structural data. It is hypothesized that the physiological variations of these parameters and not only the degree of mineralization, are crucial for the reliability of numerical bone models. Therefore, SAM and SRμCT will be used in a first step to assess micro structural, mineralization and elastic stiffness variations of the femoral neck with respect to age and anatomical location. It is expected that elasticity changes significantly with age and anatomical locations and that these variations are related to the adaptation of bone to external loading conditions.

Aims and Hypothesis Study II

The aim of Study II is the application and development of a novel transverse transmission approach for the identification of the very early healing stages in a rat osteotomy model and its comparison to a μCT evaluation approach. It is hypothesized that QUS in transverse transmission can be used for detecting early healing stages in a rat osteotomy model and has superior sensitivity to soft tissue variations compared to X-ray based methods. The investigations will encompass *in vitro* QUS experiments at rat femora osteotomies as well as first preliminary numerical ultrasound propagation simulations.

1.2 Thesis outline

The thesis is divided into eight main chapters. The first four chapters provide theoretical backgrounds on the relevant topics which are related to the present work. First, an overview of the structure, function, mechanics and diseases of bone is given. Chapter three reviews the literature on bone quality assessment relevant state-of-the-art modalities and their weaknesses and strengths. Chapter four gives an introduction to the theoretical background of ultrasound, which is required to understand the methods used in the present work.

Chapter five to eight contain the description of the conducted experiments and analyses to achieve the aims. It is divided into material and methods (chapter 5), results (chapter 6), discussion (chapter 7) and conclusions (chapter 8).

2. Human Bone

2.1 Structure and function

From an engineering point of view, bone is an exceptional material. It is remarkably lightweight but at the same time very efficient in terms of resisting fractures under heavy load conditions. Cortical bone, for instance, can be considered as strong as titanium relative to its weight. This property is crucial for the major mechanical function of the long bones of the limbs which is, in combination with muscles, the facilitation of locomotion. The long tube-like bones have to resist bending, torsion or compressional deformations due to weight bearing and muscle forces (Duda et al. 1997; Duda et al. 1998; Heller et al. 2005; Currey 2006; Speirs et al. 2007). However, bone is a living and biological organ and is not only extremely optimized but also exceedingly adaptable to external conditions (Huiskes et al. 2000; Ruimerman et al. 2005; Schulte et al. 2011). The first reference postulating an adaptability of bone dates back to over one century and is known as Wolff's law (Wolff 1892).

Another important feature of bone is its highly hierarchical (Rho et al. 1998; Weiner 1998; Currey 2002; Reisinger et al. 2010) (Figure 2.1).

A scheme of the human femur, the main target of the present work, is shown in Figure 2.2. At the macroscopic level, it basically consists of lamellar bone. In the proximal epiphysis, two tissue types can be considered, i.e. cancellous and compact bone. The "spongy" like trabecular bone with porosities of 50 % - 90 % (Currey 2002) is commonly surrounded by compact or cortical bone with thicknesses ranging from a few millimetres to even centimetres in the mid shaft (Ericksen 1982; Fratzl and Weinkamer 2008).

The next level of organisation of compact bone, commonly considered in literature, is the microstructure (Figure 2.1 b, h). It exhibits tube like structures - the Haversian canals - which are preferably arranged parallel to the long axis of the bone, and are filled with blood vessels, nerves and connective tissue. They are surrounded by concentric arranged lamellar structures which form together with the Haversian canals, the osteons with total diameters of about 220 µm (Pfeiffer et al. 2006; Britz et al. 2009). Additionally to the Haversian canals, the Volkmann canals can be found in human cortical bone. They are filled with blood vessels, too. However, they are arranged transversal to the bone's long axis.

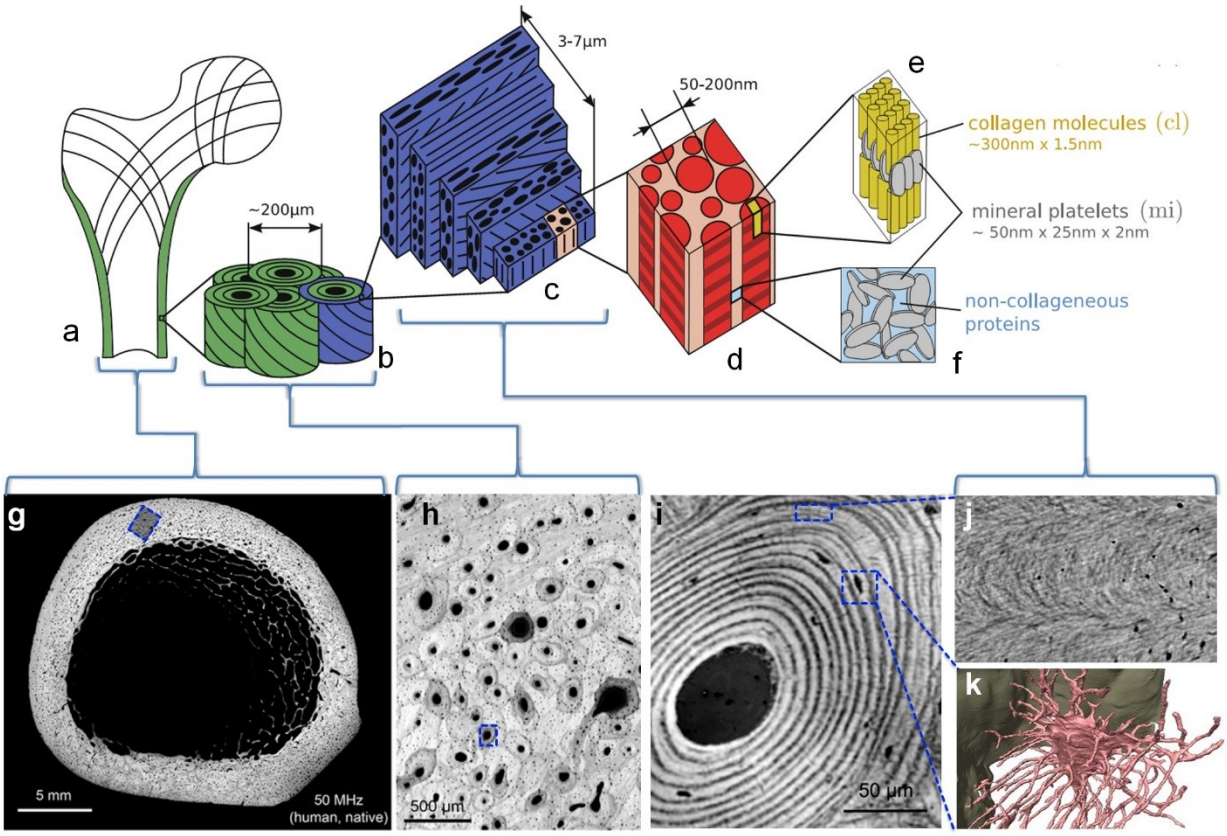

Figure 2.1 (a-f) Schematic illustration of hierarchical levels of cortical bone (reprinted with permission from Reisinger et al. (2010) © Biomechanics and Modeling in Mechanobiology). (a) Macrostructure with compact and cancellous bone; (b) microstructure of compact bone containing osteons; (c) sub-microstructure with the single bone lamellae unit, (d) nanostructure mineralized collagen fibres; (e) mineralized collagen fibril (f) extra-fibrillar matrix (g-i) Acoustic microscopy maps at different resolutions (Reprinted with authorization from Raum (2008) © IEEE), with (g) 50 MHz impedance map of a diaphysis section from a human femora, (h) 200 MHz measurement of the rectangular region in (g). (i) a single osteon measured at 1223 MHz with visible lamellar units and Osteocyte lacunae. (j-k) Reconstructed images from nano X-ray phase tomography (© (Langer et al. 2012)) with (j) visible fibril orientation (small dark spots are canaliculi) and (k) reconstructed 3D volume of Osteocyte lacunae and connected canaliculi.

Investigations in the past decade and the increased usage of numerical simulation models suggest that an introduction of an intermediate scale - the mesoscale - would be appropriate (Parnell and Grimal 2009; Granke et al. 2011; Grimal et al. 2011; Bernard et al. 2012). One unit in this length scale spans about 1 mm^2 to 1.5 mm^2 containing several osteons and is therefore also referred to as the millimetre scale.

Scanning acoustic microscopy (SAM) (Hofmann et al. 2005) and nanoindentation (Franzoso and Zysset 2009) revealed an oscillating pattern of stiffness within single osteons referred to be lamellae. Each lammelar unit, sizes of 7 µm – 10 µm, is composed of a subset of several

sub-layers forming a series of coaxial cylinders (Giraud-Guille 1988; Raum et al. 2011). The variations in stiffness are related to different orientations of the collagen fibres. The exact pattern of orientation has not been completely understood but is expected to be based on a plywood model (Giraud-Guille 1988; Weiner et al. 1997; Wagermaier et al. 2006; Reisinger et al. 2011). Embedded in the osteons are the osteocytes (Figure 2.1 k) with an average volume of 286 to 408 μm^3 (Langer et al. 2012; Carter et al. 2013) leading to a porosity of approximately 1.85 % ± 0.19 (Wang and Ni 2003). These bone cells are well connected via the canaliculi network (Figure 2.1 k). Finally, at the sub-nanostructure, the fibres consist of approximately 0.5 µm thick fibrils which in turn consists of a bundle of 300 mm long collagen molecules reinforced by hydroxyapatite crystals (Rho et al. 1998).

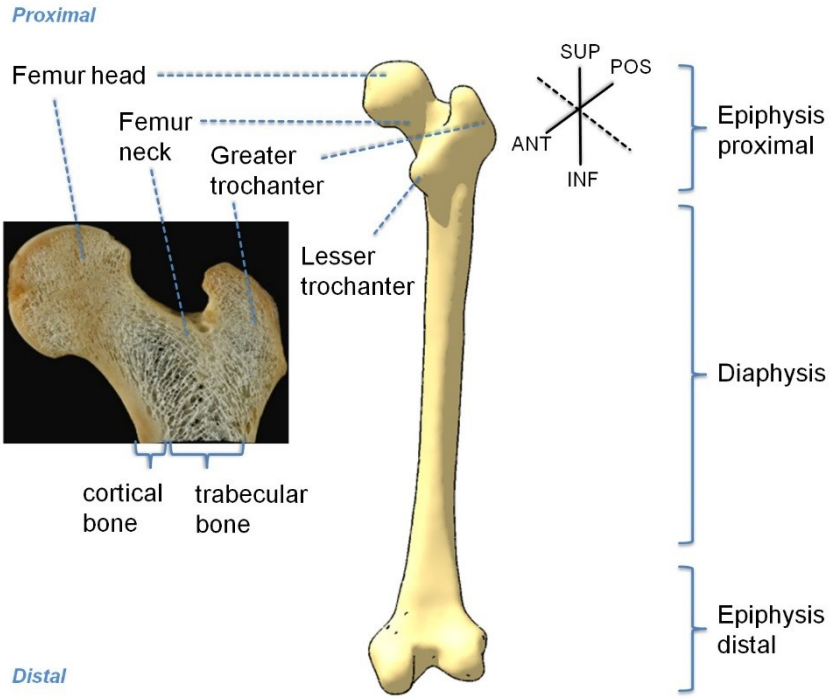

Figure 2.2 Cross-section of a human proximal femur (left image) and scheme of left human femur (right image). Abbreviations in the femoral neck are, superior (SUP), inferior (INF), anterior (ANT) and posterior (POS).

2.2 Bone mechanics

The material properties describing bone integrity are in principle based on the relationship of an applied load and the resulting displacement of the material. This is commonly expressed by a load displacement curve (Turner 2006). These curves can be e.g. derived from three or four point bending tests or single stance phase configurations (Cheng et al. 1997; Nicholson et al. 1997) and are common in studying the mechanical response of bone at the macroscale. In

smaller length scales, e.g. the mesoscale, it is more suitable to measure the intrinsic material properties which are independent of the shape of the investigated subject. This is done by normalizing the load (F) by a given area (A) which yields stress ($\sigma = F/A$, in MPa). Strain (ε) is given by the ratio of displacement (Δl) and the initial length (l_0) of the specimen.

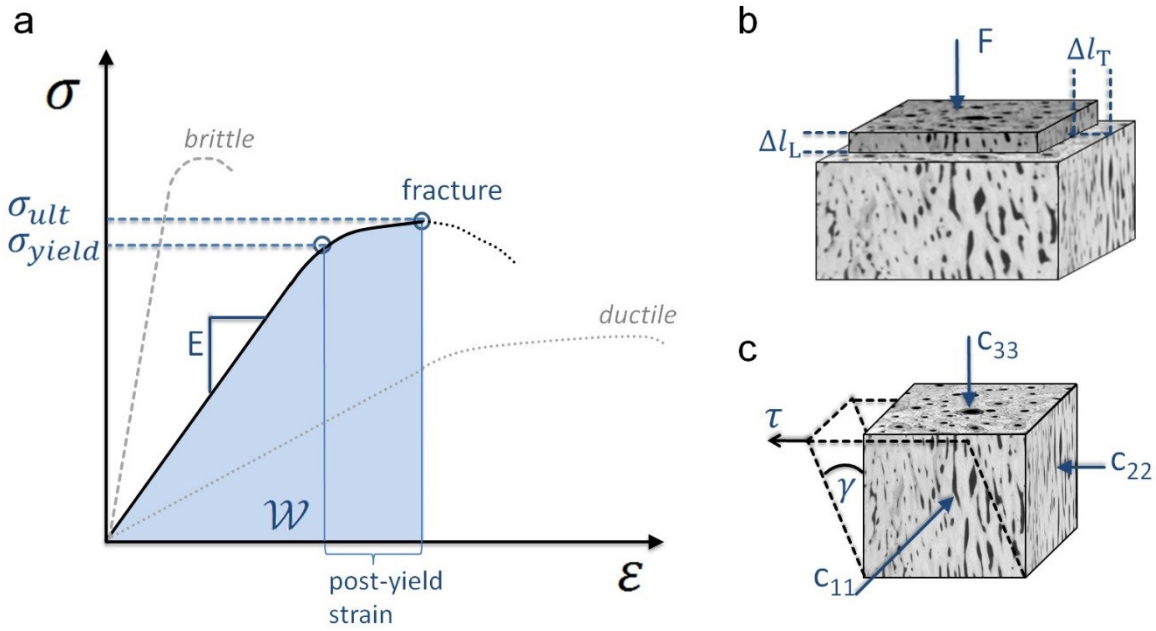

Figure 2.3 (a) Stress strain curve with given stress ($\boldsymbol{\sigma}$), strain ($\boldsymbol{\varepsilon}$), area under the curve ($\boldsymbol{\mathcal{W}}$), Young's modulus ($\boldsymbol{E}$), ultimate stress ($\boldsymbol{\sigma_{ult}}$), and yield stress ($\boldsymbol{\sigma_{yield}}$). (b) displacement of a bone sample by applied force $\boldsymbol{F}$. Deformations are observed in longitudinal (L) and transversal direction (T) which yield $\boldsymbol{\varepsilon_T = \Delta l_T / l_{0_T}}$ and $\boldsymbol{\varepsilon_L = \Delta l_L / l_{0_L}}$ if the parameter $\boldsymbol{l_{0_L}}$ and $\boldsymbol{l_{0_T}}$ give the initial length in longitudinal and transverse direction, respectively. (c) Elastic stiffness constants in orthogonal directions ($\boldsymbol{c_{11}, c_{22}, c_{33}}$) and shear strain $\boldsymbol{\gamma}$ and shear stress $\boldsymbol{\tau}$.

Similar to the load displacement curve, a stress strain curve can be plotted in the same fashion (Figure 2.3 a). In poorly elastic media, the first part of the curve exhibits a linear increase until the yield stress (σ_{yield}). From this point on, the bone undergoes plastic deformations including micro cracks and thus the stress strain curve does not behave in a linear fashion anymore. Bone integrity commonly is determined by three parameters. First, bone strength is defined as the ultimate stress (σ_{ult}) measured when the bone fractures. Second, toughness of bone is related to the whole energy which is absorbed during loading until fracture occurs and

is measured by the area under the curve ($\mathcal{W}$). Finally the intrinsic stiffness expressed by the Young's moduls (E), which is equal to the slope of the linear part of the curve. These quantities can be used to discriminate different material characteristics such as brittle (ceramics) or ductile (metals) (Figure 2.3 a). The problem of the destructive properties, e.g. toughness and ultimate strength, is that their direct *in vivo* assessment is often not feasible. Therefore, the aim of most studies is the assessment of the nondestructive parameters, such as elastic stiffness, mineralization or bone volume to total volume, as a surrogate for bone quality.

The following equations and considerations are based on Mitton et al. (2011) and Kundu (2004). The relation of stress, strain, and the Young's modulus (E) is well-known as Hooke's law and is written as

$$\sigma = E\varepsilon. \tag{2.1}$$

However, bone can be considered as an orthotropic material, i.e. the material prproperties are different for different spatial directions. Hooke's law in this case is usually written using the fourth order stiffness tensor C_{ijkl},

$$\sigma_{ij} = C_{ijkl}\varepsilon_{kl}. \tag{2.2}$$

The assumption of orthotropy reduces the number of independent elastic coefficients to 9 and equation 2.2 can be written in matrix notation by

$$\begin{bmatrix}\sigma_{11}\\ \sigma_{22}\\ \sigma_{33}\\ \sigma_{23}\\ \sigma_{31}\\ \sigma_{12}\end{bmatrix} = \begin{bmatrix}c_{11} & c_{12} & c_{13} & 0 & 0 & 0\\ c_{12} & c_{22} & c_{13} & 0 & 0 & 0\\ c_{13} & c_{13} & c_{33} & 0 & 0 & 0\\ 0 & 0 & 0 & c_{44} & 0 & 0\\ 0 & 0 & 0 & 0 & c_{55} & 0\\ 0 & 0 & 0 & 0 & 0 & c_{66}\end{bmatrix} \cdot \begin{bmatrix}\varepsilon_{11}\\ \varepsilon_{22}\\ \varepsilon_{33}\\ 2\varepsilon_{23}\\ 2\varepsilon_{31}\\ 2\varepsilon_{12}\end{bmatrix}. \tag{2.3}$$

Some bone tissues exhibit one axis of symmetry which is referred to be transverse isotropic. In this case, the elastic coefficient in one orthogonal direction can be considered to be independent and significantly different from the remaining constants. It is common to define the elastic stiffness parallel to the osteons, i.e. parallel to the bone long axis, to be c_{33} (Figure

2.3 c) which leads to $c_{33} > c_{11} = c_{22}$ and the elastic tensor reduces to only 5 independent coefficients. c_{66} is then given by

$$c_{66} = \frac{c_{11} - c_{12}}{2} \tag{2.4}$$

and $c_{55} = c_{44}$. The simplest case that can be considered is isotropy which reduces the independent elastic coefficients to only 2 with $c_{33} = c_{11} = c_{22}, c_{ij} = c_{kl}$ $(i \neq j, k \neq l$ and $i, j, k, < 3)$, $c_{44} = c_{55} = c_{66}$.

The elastic constants can be transformed into the engineering constants Young's modulus (E_i), shear modulus (G_{ij}) and Poisson's ratio (ϑ_{ij}) by using a compliance tensor S_{ij}.

The Poisson's ratio in the one dimensional case defines the ratio of strain in the transversal to the longitudinal strain as defined by (Figure 2.3 b),

$$\vartheta = \frac{\varepsilon_T}{\varepsilon_L}. \tag{2.5}$$

For isotropic elastic media, these considerations lead to a conversion from mechanical to engineering constants, which is for c_{33}

$$E = \frac{c_{33}(1 - 2\vartheta)(1 + \vartheta)}{1 - \vartheta} \tag{2.6}$$

and

$$c_{44} = G = \frac{E}{2(1 + \vartheta)}. \tag{2.7}$$

2.3 Bone Quality

Although nowadays bone quality can be assessed at different length scales (see chapter 3), little is still only known about the mechanical consequences that arise from biological variations of mechanical properties at the next lower length scale. For instance, the relative contributions of cortical versus trabecular bone to femoral neck bone strength have been revisited recently. Holzer et al. (2009) demonstrated that the trabecular bone loss at the femoral neck explains for only 10 % of the loss in bone strength. Moreover, most of the variations of the effective elastic stiffness in elderly women have been recently shown to be accounted for intra-cortical porosity (Granke et al. 2011). This assumption has further been supported by a cross-sectional study by Zebaze et al. (2010) who suggested that cortical porosity is the major determinant of non-vertebral fracture risk (Rohrbach et al. 2012b). Although the data from Granke et al. (2011) suggest that the elastic stiffness at the tissue level explains for only 26 % of the macroscopic elastic stiffness, no systematic survey of the matrix stiffness relating age and porosity exist. However, the precise understanding of the elastic properties, from the μm to the mm range, is crucial for the development of new diagnostic tools (Raum et al. 2005a; Barkmann et al. 2008a; 2008b; Barkmann et al. 2010a; Karjalainen et al. 2012). In fact, the predictive strength is highly dependent on the sensitivity of these parameters. Moreover, the elastic properties are important input parameters for numerical simulations (Bossy et al. 2004a; Austman et al. 2008; Boccaccio et al. 2008; Verhulp et al. 2008; Vetter et al. 2011).

Today, the most common input data for numerical models comes from clinical computed tomography (CT), quantitative CT (QCT) or μCT measurements, as they are easily assessable and provide detailed 3D structural information non-destructively. However, elastic material properties cannot be derived directly from clinical CT, QCT or desktop μCT data. Instead, either homogenous isotropic material properties (Van Rietbergen et al. 2003; Verhulp et al. 2008; Qian et al. 2009) or empirical Hounsfield-to-Young's modulus conversion rules have been applied to assign elastic properties to models of the mineralized tissue matrix (Austman et al. 2008). However, bone matrix at the meso- and microlevel is neither homogeneous nor isotropic (Hofmann et al. 2005; Raum et al. 2005a; Raum et al. 2006a; Lakshmanan et al. 2007). Models relating Hounsfield units and E showed variations of up to 50 % (Austman et al. 2008).

Moreover, bone exhibit fairly low variation of mineral density (Raum et al. 2005a; Roschger et al. 2008; Zebaze et al. 2011). Although certain diseases or treatments directly affect the mineral turnover and thus the total bone mineral density (Roschger et al. 2008), neither age, gender, skeletal sites nor ethnicity has a strong impact on the bone mineral density distribution at tissue level (Raum et al. 2005a; Roschger et al. 2008; Zebaze et al. 2011).

2.4 Bone remodelling

The exceptional ability of bone to adapt to altering load conditions during lifetime and maturation, is achieved by a complex biological process called remodelling. Bone undergoes a permanent but balanced process of bone formation and resorption. Between 5 % and 25 % turnover each year has been reported, depending on the skeleton side and tissue (Parfitt 2002).

Remodelling is the predominant metabolic process regulating bone structure and function and is a complex, tightly regulated process carried out by a cohort of cells termed the basic multi cellular unit (BMU) (Kular et al. 2012). The major members of the BMU that play a prevalent role in bone remodelling are osteoclasts, osteoblasts, osteocytes, bone lining cells, and capillaries for blood supply. The multinuclear giant osteoclasts are the bone resorbing cells originating from the macrophage family. Bone formation is performed by the osteoblasts. They originate from mesenchymal stem cells and can further differentiate into bone lining cells or osteocytes. The whole process can be considered as a complex feedback loop between the cells involving a variety of important growth factors (IGFs) like, bone morphogenetic proteins (BMPs) as well as transforming growth factors (TGFß) (Kular et al. 2012). It has been discovered that osteocytes play a pivotal role in maintaining bone structure and function by acting as mechano-sensing cells (Bonewald 2011).

2.5 Osteoporosis and bone ageing

Osteoporosis has been defined by the Consensus Development Panel on Osteoporosis (1991) to be a skeletal disease characterized by low bone density and microarchitectural deterioration of bone tissue with a consequent increase in bone fragility. This emphasizes the circumstance that an increased fracture risk is not only determined by loss of bone mass but also by numerous structural and compositional factors (Raum et al. 2010) such as trabecular and cortical properties (Figure 2.4), geometry, quality of collagen or presence of micro cracks (Pothuaud et al. 2000).

The relevance of the disease is emphasized by the high mortality rates in the following years of a fragility fracture (>36 % hip) (Abrahamsen et al. 2009; Hu et al. 2012), the high live time risks (>50 % for women) and the considerable burden for the health care system due to high costs (2.5 to 4.5 billion € per year Germany) (Pientka and Friedrich 2000; Oberender and Fritschi 2003). Sustaining a hip fracture is the second most frequent type with 14 % occurring in women and 3 % in men (Kaufman et al. 2013).

The diagnosis of osteoporosis is based on the T-score definitions of the W.H.O. (1994) whereas the T-score is derived from BMD measured with dual energy X-Ray absorptiometry (DXA) (for more details see chapter 3.2.2.1). However, several studies show that DXA is not sufficient enough to determine the osteoporotic fracture risk. Therefore, attempts have been made to develop new diagnostic tools which resulted in the W.H.O. fracture risk assessment tool (FRAX ®, released in 2008) which was shown to improve, in conjunction with BMD, fracture risk prediction (Kanis et al. 2007).

However, it is well accepted that in addition to these extrinsic factors, bone intrinsic quality parameters far beyond BMD are affected by osteoporosis, suggesting the need for alternative diagnostic tools that can further improve fracture risk prediction (Mitton et al. 2011). For the development of such new approaches, the identification of fracture relevant parameters, their variation with age, anatomical sites, gender and their impact on the measurement tools are mandatory.

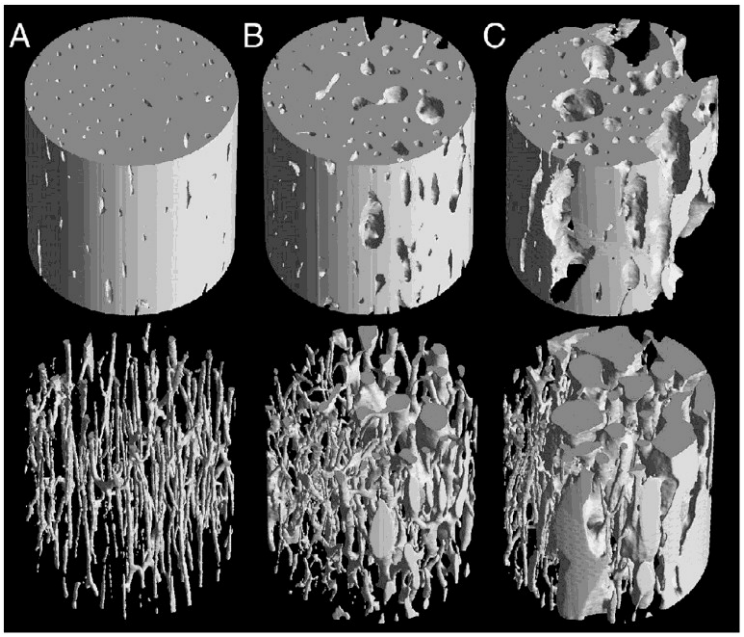

Figure 2.4 µCT 3D reconstruction of cortical samples taken from right anterior femoral midshaft. The diameter of the cylinders is about 8 mm. The top row depicts the solid bone phase, while the lower row depicts the porous (canal) phase. (A) 20-year-old female, (B) 61-year-old female, (C) 87-year-old female. The periosteal surface faces are on the left side for all specimens (reprint from Cooper et al. (2007) with permission from © Bone).

2.6 Bone fracture healing

The orchestrated mechanism of fracture healing has been extensively investigated in animal models during the past decade. Histological analyses of sheep (Hube et al. 2006; Lienau et al. 2009; Manjubala et al. 2009; Preininger et al. 2011) and rat models (Strube et al. 2008a; Strube et al. 2008b; Mehta et al. 2010; Preininger et al. 2012a) have gained new insights in the complex molecular signal cascades and mechanical competence involved in that process.

Two distinct healing processes are differentiated namely primary and secondary healing. Primary or contact bone healing refers to a process when the fractured sides are directly connected under stable conditions. In that case the same processes are involved as during bone remodelling and the fracture usually heals without any complication. Since direct bone contact is not likely for traumas of long bones, the most frequent types of fracture repair are secondary healing which is considered in the following when reffering to fracture healing.

In principle, three major stages of secondary bone healing can be considered which involve the formation of a massive callus. These overlapping phases are the inflammatory phase, the repair stage and finally a period of remodelling (Figure 2.5). During that process the callus

undergoes a continues process of stiffening starting from a very soft hematoma which undergoes granulation and cartilage formation which finally leads to mineralization and the formation of a hard callus (Harwood et al. 2010; Claes et al. 2012). It was shown that the hematoma and the inflammatory response play a pivotal role in the success of bone healing. Recently Preininger et al. (2012a) has demonstrated that an artificial hematoma charged with BMP can induce a successful healing process in an impaired rat osteotomy healing model. The proper and balanced temporal and spatial cascade of factors and cells during the initial phase is important for a successful healing outcome (Mountziaris et al. 2011; Preininger et al. 2012a).

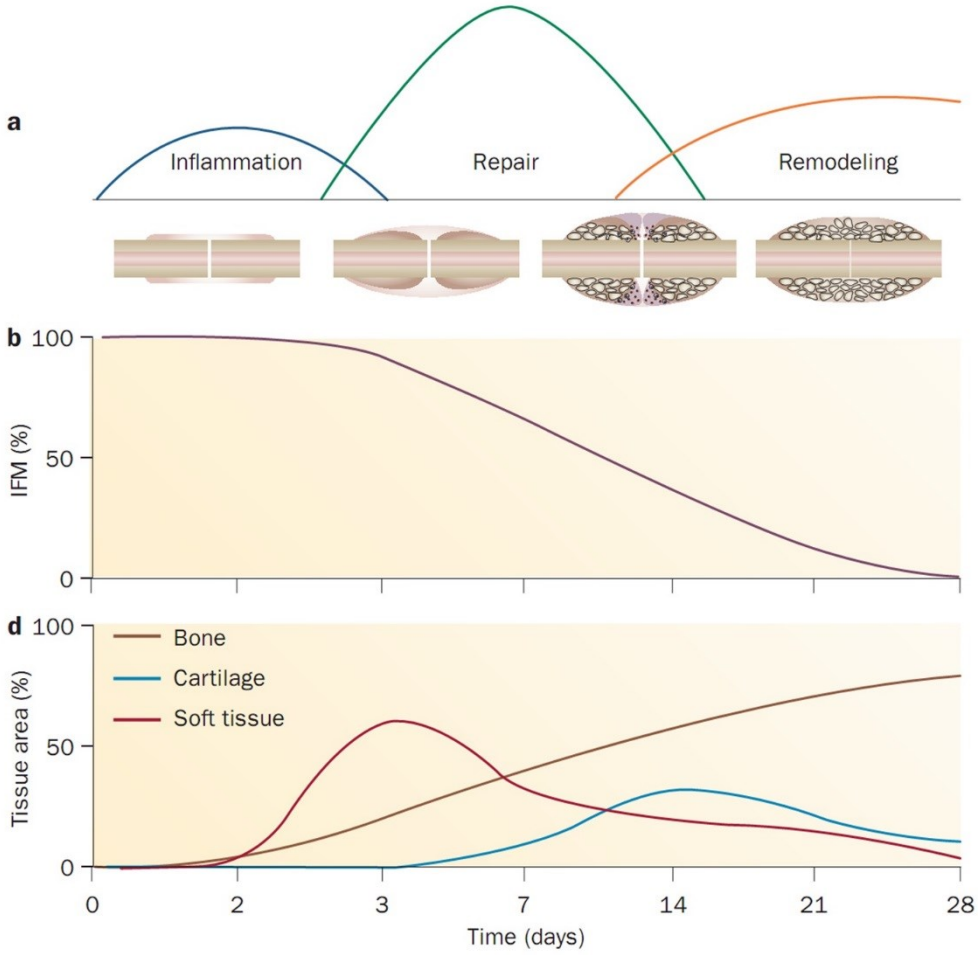

Figure 2.5 (a) Three overlapping healing stages. (b) Constantly decreasing of interfragmentary movement (IFM) starting during the beginning of the repair phase. (c) Tissue composition varies throughout fracture repair. Initially, soft tissue predominates, but gives way to cartilage after around 7–14 days. The cartilage is then replaced by bone. Bone formation increases soon after fracture in regions least affected by the trauma and with low interfragmentary strain, and progresses as IFM decreases (from Claes et al. (2012) © Nature).

2.7 Impaired fracture healing

Although bone fracture healing is a very efficient process, non-union and delayed healing serve considerable clinical complications. Depending on the treatment and fracture type in 1 % to 12 %, a non-union is present and up to 27 % require further operation due to healing complications (Kooistra et al. 2010). The consequences for patients are a significant reduction in quality of life due to limited mobility, prolonged pain and extended hospitalization. For the health care system, the results are immense costs (Sprague and Bhandari 2002; Laurencin et al. 2006).

During bone repair, numerous factors can lead to delayed healing or non-unions, though, a precise understanding of the exact biological mechanisms is still limited (Mehta et al. 2012b). A delayed union is considered at a 3 to 6 month post injury (Gelalis et al. 2012). However, it is well accepted that the determination of an impaired healing can occur at almost every phase of healing, depending on biological factors, age, pathologic history and mechanical conditions (Peters et al. 2010; Mehta et al. 2012b). Since soft and cartilaginous tissue types are the most prevalent at this stage, plane radiography, the standard modality for bone healing assessment, fails at these early stages (Nicholls et al. 1979; Hammer et al. 1985; Panjabi et al. 1989; Blokhuis et al. 2001). Therefore, the development of new diagnostic approaches, capable of assessing the subtle changes of the soft tissue properties, such as prolonged presence of hematoma (Peters et al. 2010), would be beneficial for the diagnostics of impaired fracture healing.

3. Modalities for bone characterization

3.1 *In vitro* methods

3.1.1 Scanning acoustic microscopy (SAM)

Since its introduction by Lemons and Quate (1974), scanning acoustic microscopy (SAM) has become a valuable tool in bone research. Currently, it is the only method which allows fast and non-destructive assessment of bone elastic stiffness at the micro scale with high spatial and lateral resolution (Raum 2008).

3.1.1.1 SAM impedance mapping

The acoustic impedance mapping of the confocal reflection amplitude has become the most straightforward approach for SAM based assessment of bone (Raum 2008). Samples are scanned by conducting a C-scan mode, i.e. signals are acquired at distinct locations in space (x,y) while keeping the z-position constant and aligning the sample with the focal plane of the ultrasonic sound field (Figure 3.1). For each signal the acoustic Impedance is calculated.

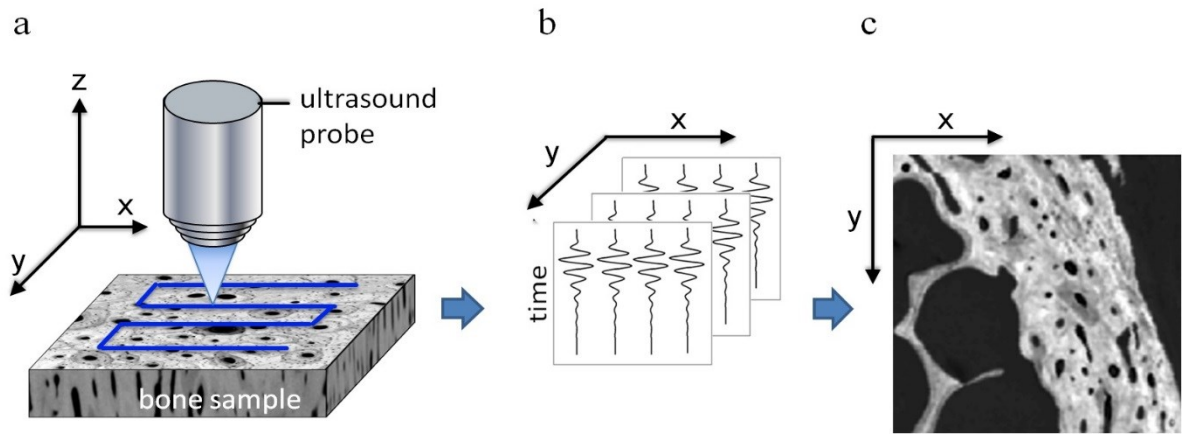

Figure 3.1 By measuring at equidistant positions using a C-scan mode, (b) a set of time resolved signals are obtained. By calculating features for each signal, such as amplitude (c) acoustical images of impedance can be derived (c). The acoustic grey level in (c) corresponds to the amplitudes measured at each location (x,y) using a Hilbert transformation (Raum 2011).

The acoustic impedance relates traction force to particle velocity. It can be shown that Z_{ii}^2 is proportional to the elastic stiffness c_{ii} and mass density ρ if the incidence longitudinal wave is perpendicular to the sample surface and parallel to direction i (Raum 2008). Z can then be written as

$$Z_{ii} = \sqrt{c_{ii} \cdot \rho}. \qquad 3.1$$

In order to derive reliable estimates of the acoustic impedance, crucial preconditions must be ensured. Stable measurement conditions are as mandatory as accurate sample preparation such as smooth and plane surfaces placed perpendicular to the sound beam axis (Raum 2011). Nevertheless, acoustic impedance mapping has a considerable amount of advantages compared with the other SAM approaches. For instance, only one surface needs to be prepared and a high range of frequencies can be used, i.e. from the MHz to GHz range. The

latter enables the assessment of bone properties under different resolutions, i.e. down to 1 µm (Raum et al. 2003; Hofmann et al. 2005), and thus at different length scales and hierarchical levels of bone. Moreover, it was shown that the acoustic impedance Z_{ii}, as opposed to the mass density, is a strong predictor for the elastic stiffness of the mineralized collagen matrix (Raum et al. 2006a; Raum 2008; Rupin et al. 2009). Hence, in addition to the microstructure, it provides information which cannot be assessed by other high resolution modalities such as µCT. Further validation of the approach is achieved by good correlations (R^2>0.6, p<0.001) between the elastic modulus derived from SAM and nanoindentation (Hofmann et al. 2005; Rupin et al. 2009). In the past decade, a considerable amount of animal and human studies have successfully shown the applicability of the method and have revealed new insights in the anisotropic elastic properties and their contribution to bone development and strength (Raum et al. 2005a; Hube et al. 2006; Raum et al. 2006b; Raum 2008; Preininger et al. 2011).

3.1.1.2 SAM approaches: surface acoustic and compressional wave velocity

In principle, two other SAM approaches reported in literature are the measurement of surface acoustic waves (SAW) and the measurement of sound velocity of the compressional wave transmitted through thin samples.

Although it was demonstrated in several studies that the elastic anisotropic properties of bone and human tooth enamel and dentin can be assessed by measuring SAW (Peck and Briggs 1986; Peck et al. 1989; Jorgensen and Kundu 2002; Raum et al. 2007b), the approach has some drawbacks. For instance, due to the necessary defocusing, the interrogated area is increased and thus the spatial resolution is lost (Raum 2008).

The measurement of speed of sound in thin samples has been successfully used to study cortical and trabecular bone elastic properties in human (Turner et al. 1999; Bensamoun et al. 2004a; Bensamoun et al. 2004b) and animal models (Turner et al. 1995; Pidaparti et al. 1996). Due to the high attenuation of bone, only frequencies up to 50 MHz have been applied and the resolution degrades if front and back side echoes cannot be placed within the depth of focus (Raum 2008). Moreover, two parallel and flat surfaces needs to be prepared for the very thin samples (100 µm -2 mm) and additional methods are required for the measurement of density and sample thickness (Raum 2008).

3.1.2 Micro computer tomography (µCT)

Desktop micro computer tomography (µCT) is a well-established and versatile tool that is often used for qualitative and quantitative 3D analysis of mineralized tissue formations (Schulte et al. 2011), their pathologies (Zupan et al. 2012) and regeneration (Mehta et al. 2012a; Preininger et al. 2012a). Since the radiation dosage of µCT is too high and the flux too low, *in vivo* measurements are only conducted in animal studies. However, new developments, such as HR-pQCT or XtremeCT (see chapter 3.2.2.2), allow a local assessment of structural information even in clinical trials.

A strong limitation of most desktop µCT systems is the use of low intensity polychromatic sources which in contrast to SRµCT limits the resolution (10 µm – 50 µm) and quantitative assessment of mineralization due to effects such as beam-hardening. New developments such as beam monochromatization, beam-hardening correction or new technical approaches, however already show auspicious enhancements but are still not surrogates for SRµCT (Zou et al. 2011).

As opposed to histological analysis, X-ray based analysis can be done *in vivo*. The advantages of µCT in mineralized tissue research are excellent, that is, the strong contrast between soft and mineralized tissues provides 3D distribution and structural properties of mineralized tissue non-destructively with a high spatial resolution (about 10 µm, new systems even 1 µm). Recently, it has been shown that the contrast for tissues with low mineralization and soft tissues can be greatly enhanced by using phase-contrast CT (PCCT) imaging (Momose 2005; Zhou and Brahme 2008; Langer et al. 2010). However, this technology has not been implemented in clinical CT or experimental micro-CT systems. Donath et al. (2010) expected that both preclinical and clinical phase-contrast scanners will be developed within the next decade.

3.1.3 Synchrotron radiation µCT (SRµCT)

By using a monochromatic synchrotron radiation (SR) beam, it becomes possible to image the micro architecture (Salome et al. 1999; Cooper et al. 2011) and the degree of mineralization of bone (*DMB*) with a very high resolution of 1 µm (Nuzzo et al. 2002a) to even submicron scale (Langer et al. 2012). A SR source offers a continuous energy spectrum combined with a high photon flux which in conjunction with a monochromator, prevent beam hardening effects and geometrical blurring as opposed to conventional desktop µCT systems (Salome et al.

1999). These features are crucial for the estimation of *DMB*. While the sample is being rotated in the SR beam, attenuation projection images are acquired for several angles and the 3D volume can then be reconstructed using an efficient standard filtered backprojection algorithm (Salome et al. 1999). As absorption depends on the amount of mineral in bone, a suitable calibration is able to relate the reconstructed grey levels in SRμCT images to the local *DMB* expressed in g cm^{-3} (Nuzzo et al. 2002a; Nuzzo et al. 2002b).

Novel developments, such as phase contrast imaging, even enable the imaging of the osteocyte and canaliculi network (Cooper et al. 2011; Langer et al. 2012; Pacureanu et al. 2012) (Figure 2.1 j-k).

3.1.4 Histological staining

Histological staining and subsequent light microscopy is the gold standard procedure for investigating bone healing and diseases in animal models. By selecting an appropriate staining procedure, high contrasts between different tissue types and even single cell types can be achieved. This allows the unique evaluation of tissue compositions. In bone research, staining commonly requires an embedding procedure. The most frequent are either paraffin or Polymethylmethacrylat (PMMA).

For calcified tissue visualization, the most considerable staining are Movat Pentachrome with PMMA embedding (Kratzel et al. 2008; Mehta et al. 2010; Preininger et al. 2012a) (Figure 5.22), Toluidinblue, Safranin-Orange (Kratzel et al. 2008; Manjubala et al. 2009), Alizarin Red, von Kossa. Some of the staining can be combined and thus are commonly referred to as Safranin-Orange/von Kossa or Von Kossa/ Toluidinblue staining.

Although histological staining is widely used in bone research, there are some limitations. These include relatively long and elaborate preparation steps including embedding and thin sectioning (6 μm) of the specimen. Moreover, quantitative analysis is limited due to high variations in colour saturations and the sections only represent 2D segments and conclusion about 3D properties must be made with caution.

3.1.5 Other modalities

Nanoindentation is a common tool for the assessment of the elastic (Zysset 2009) and visco elastic (Isaksson et al. 2010a; 2010b) properties of bone at the μm-scale (resolution 10 μm down to 1 μm). In order to derive the elastic modulus, almost all studies dealing with bone

have adopted the approach developed by Oliver and Pharr (1992; 2004). This method consists of measuring the load-displacement curve while pushing a tip of defined geometry into the sample. Common measurements are hardness (Amprino 1958; Hodgskinson et al. 1989; Evans et al. 1990) and indentation modulus (E_{ind}) (Zysset 2009).

Although nanoindentation enables the direct assessment of the elastic modulus and the measurement of additional properties relating viscoelasticity and hardness, it has some crucial drawbacks compared with other modalities such as SAM. It is not only a technique of destructive nature but has also a limited lateral resolution in terms of measurement points per area. The latter results from the relatively long time required for each indentation tip (up to 100 s for a holding-period at maximum indentation depth). Thus, nanoindentation has restricted capabilities to assess the smooth transitions and large scale distributions of elastic properties along different tissue types and anatomical locations.

Other SRμCT based methods which have been used to study bone micro-architecture are small and wide angle X-ray scattering (SAXS, WAXS). Instead of measuring the attenuation of the straight beam, the spectrum of the scattering in certain angles is captured. The spectrum pattern, thereby is related to molecular structures and orientations. It has been successfully used to investigate the orientation and size of apatitic crystals in human cortical and trabecular bone (Camacho et al. 1999) or fibril orientation in murine disease models (Karunaratne et al. 2013). Wagermaier et al. (2006) investigated the fibril orientation in single osteon lamella. They deduced a 3D spiral (helicoidal) appearance of the fibrils, which was wound around the blood vessel within coaxial cylinders. This led to anisotropic properties of the whole osteon and was further supported by later finite element studies of Reisinger et al. (2011).

The qBEI method allows the direct 2D measurement of the calcium concentration using a scanning electron microscope (SEM) (Roschger et al. 1995; Roschger et al. 1998; Misof et al. 2011). Resolutions in the order of 1-4 μm have been reported (Misof et al. 2011). However, the samples require electrical coating (carbon or gold) and very plane surfaces which, in contrast to other modalities such as SAM and nanoindentation, makes embedding necessary (Misof et al. 2011). In conjunction with qBEI of bone, commonly the bone mineral density distribution (BMDD) and its features are assessed. It can be considered as a mineralization fingerprint of bone, reflecting bone turnover, mineralization kinetics and average tissue age (Roschger et al. 2008).

3.2 Modalities for *in vivo* applications

3.2.1 Quantitative low frequency ultrasound

Although first clinical trials ranges back to the late 1950s with the work of Anast et al. (1958), quantitative ultrasound is a fairly young approach (Laugier and Haïat 2011a) in terms of bone quality assessment. Anast et al. (1958) applied QUS for the monitoring of fracture healing. For the first time, it was shown that the sound velocity is affected by a tibia fracture and may reflect maturity and union of callus. Nowadays, QUS has been evolved to become a promising modality and diagnostic tool for bone, due to its numerous advantages compared to current gold standard approaches such as X-rays. QUS can be considered as a non-invasive and in contrast to X-rays as a non-ionizing technique. Moreover, ultrasound is a mechanical wave and therefore carries information on the mechanical competence of the interrogated material, such as elastic stiffness, microstructure or the structural anisotropy (Yamamoto et al. 2012). Several physical phenomena of ultrasound, such as guided waves, multiple path ways, scattering or dispersion, allows the distinct investigation and assessment of different properties of bone.

However, the clinical application of QUS is still at a premature stage (Barkmann and Glüer 2011). Although several devices have been developed and used in clinics, QUS is still less accurate than X-ray and other modalities. Several reasons have been reported explaining this circumstance. These are, for example. unresolved quality assurance issues, the diversity of the approaches (Barkmann and Glüer 2011), the missing of standards and still the limited understanding of the complex bone structure and its impact on sound propagation (Laugier and Haïat 2011a). However, recent investigations using novel approaches such as numerical computer simulations (Bossy et al. 2004a; Bossy and Grimal 2011), new innovative signal analysis methods (Dencks et al. 2008; Foiret et al. 2012) or the development of new scanning devices for the proximal femur (Barkmann et al. 2008a) eliminate the restriction to peripheral bone sites and emphasize the potential of ultrasound which extends far beyond the currently available techniques (Laugier and Haïat 2011a).

3.2.1.1 QUS based fracture risk prediction in transverse transmission

The transverse or through transmission approach consists of placing a pair of ultrasound transducers at opposite sides of the bone. Thus, in long bones as opposed to axial

transmission, the ultrasound beam axis is aligned perpendicular to the bone axis. Standard parameters, e.g. *SOS* and ultrasound attenuation are commonly measured.

The first and until now the only clinical accepted and validated skeletal site for fracture risk prediction using QUS is the calcaneus. Langton et al. (1984) introduced the measurement of the broadband ultrasound attenuation (*BUA*, see chapter 4.1.3). For the first time, it was shown that osteoporotic patients could be discriminated from a healthy group using *BUA*. The International Society for Clinical Densitometry (Krieg et al. 2008) rated in a position statement paper that QUS measurements at the heel is the only validated skeletal site for clinical use and is able to predict fragility fractures.

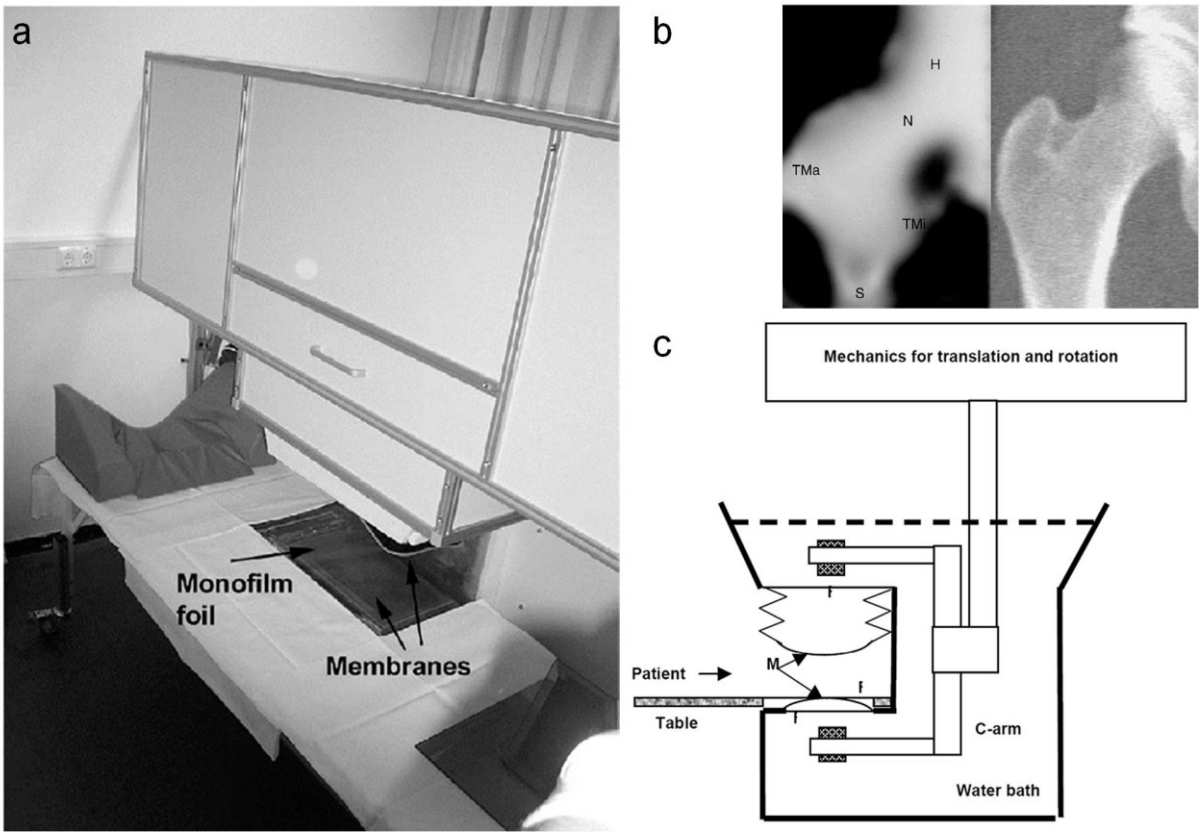

Figure 3.2 (a) FemUs device for the assessment of ultrasonic parameters at the human proximal femur. (b) Comparison of BUA (left) measured with FemUS and X-ray projection measured with DXA (right). (c) scheme of principle setup of FemUS device. Reprint from Barkmann et al. (2008a) (with permission © IEEE).

Nowadays, not only studies on the calcaneus (Chaffai et al. 2000; Wear 2001) have been conducted but also other skeletal sites such as forearm (Mano et al. 2006; Le Floch et al. 2008; Breban et al. 2010) or finger phalanges (Barkmann et al. 2000) have been assessed.

However, these sites are far from the most affected fracture sites such as the hip. Therefore, novel developments have been shifted to the assessment of the proximal femur. One example is the FemUs prototype developed by Barkmann and co-workers (Figure 3.2). First *ex vivo* and *in vivo* experiments showed very good results in predicting *BMD*. *SOS* was correlated *in vitro* with R^2=0.81-0.93 (Barkmann et al. 2007) and significantly *in vivo* with R^2=0.66 (Barkmann et al. 2008a; Barkmann et al. 2008b). A recent clinical trial has demonstrated the power of the approach for predicting osteoporotic fracture risk superior to DXA (Barkmann et al. 2010a). However, there is still a lack of precise understanding of wave propagation in the femoral neck. Although recent studies give evidence for the existence of different wave paths such as guided waves (Grondin et al. 2010), the impact of structural and mechanical parameters on the wave propagation remains unclear.

3.2.1.2 QUS based monitoring of fracture healing and axial transmission

Since the first clinical study by Anast et al. (1958) a considerable amount of animal (Abendsch.Wf and Hyatt 1972; Saha et al. 1981; Gill et al. 1989; Maylia and Nokes 1999; Protopappas et al. 2005; Malizos et al. 2006; Barbieri et al. 2011a), phantom (Njeh et al. 1998; Gheduzzi et al. 2009) but also clinical studies (Gerlanc et al. 1975; Cunningham et al. 1990; Saulgozis et al. 1996) have already demonstrated the feasibility and potential of QUS for monitoring fracture healing. It was shown that (i) different healing outcomes, such as non-unions and partially-healed fractures, can be differentiated (Gerlanc et al. 1975), (ii) measured velocities correlate with material properties, such as Young's Modulus or load at failure (Abendsch.Wf and Hyatt 1972; Gill et al. 1989; Protopappas et al. 2005), and (iii) the process of healing can be traced (Gerlanc et al. 1975; Saha et al. 1981). Recently, Barbieri et al. (2011b) reported that the sound velocity measured by axial transmission was at least as precise as conventional CT for the grading of the healing stage (Barbieri et al. 2011b).

The prevalent method for monitoring fracture healing is axial transmission which consists of placing a pair or array of ultrasonic transducers on the skin axially aligned with a peripheral long bone such as the tibia or radius (Figure 3.3 a). A single receiver or a receiver array measures the ultrasonic signals propagating through the skin and cortical bone (Figure 3.3 b). However, axial transmission limits imaging capabilities providing only restricted access to the fracture zone and is only applicable for fractures of long bones. Currently no study exists which aims on *in vivo* monitoring fracture healing using transverse transmission.

Recently developed finite difference time domain (FDTD) algorithms (Bossy et al. 2001; Bossy et al. 2005) allowed new insights into the complex ultrasound tissue interactions and confirmed previous experimental studies. Machado et al. (2010a), for example, found that besides the expected effect of decreasing time of flight (*TOF*) with increasing healing time, TOF is sensitive to variations on the concentration of fibrous tissue. Protopappas et al. (2006) related guided wave modes to mechanical and structural changes during the healing process. These findings were supported further by relations found between micro structural bone parameters, such as cortical width, porosity and matrix elasticity, and QUS velocities in axial transmission (Raum et al. 2005b) and by the sensitivity of US attenuation and *SOS* to cartilage (Nieminen et al. 2004; Gelse et al. 2010).

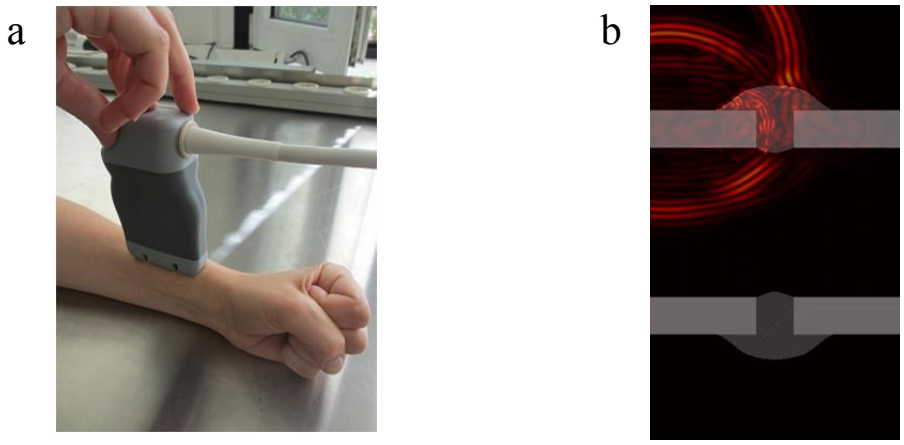

Figure 3.3 (a) Axial transmission measurement at the radius. (b) SimSonic simulation snapshot of a ultrasonic wave axial transmitted in a bone healing model with callus. Cortical bone is drawn in light gray and callus tissue in darker gray.

3.2.2 Other modalities

3.2.2.1 Dual Energy X-ray Absorptiometry and Radiographs

Dual energy X-ray absorptiometry (DXA) is currently the most prevalent method for predicting osteoporotic fracture risk (Adams 2012; Griffith and Genant 2012; Lewiecki 2012) and is the basis for the diagnostic definition of osteoporosis (W.H.O. 1994) by measuring bone mineral density (BMD g/cm^2) and deriving the T-Score. Figure 3.4 depicts a conventional DXA device (a) and a typical DXA scan of the proximal femur (b).

For the determination of BMD, DXA utilizes two X-ray beams of different energy in order to compensate for soft tissue attenuation The T-score is derived by standardizing the individual

BMD by the *BMD* of a young healthy population (Binkley and Adler 2010). The World Health Organisation (W.H.O. 1994) introduced a scoring system for the definition of osteoporosis in postmenopausal woman. The state of disease is considered to be normal if T > -1, osteopenia if -1 > T > -2.5 and osteoporosis if T < -2.5 (Raum et al. 2010). Although this system has advanced the fields of osteoporosis diagnostics, it has several drawbacks (Binkley and Adler 2010). For instance, it was shown that it is not suitable for children (< 20 years) who have not reached their bone peak mass yet, and also men younger than 50 years (Blake and Fogelman 2010; Adams 2012; Lewiecki 2012).

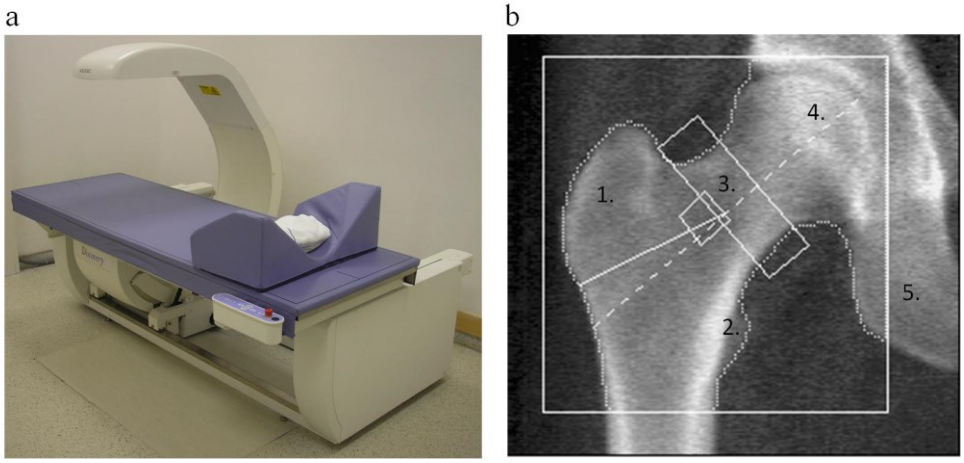

Figure 3.4 (a) A typical DXA device (HOLOGIC, Discoverz.). (b) A DXA scan of the proximal femur taking with device (a) including ROIs for BMD evaluation (white lines and rectangles). The numbers in the figures represent anatomical positions with being 1. greater trochanter, 2. lesser trochanter, 3. femoral neck with ROI, 4. fenoral neck and Acetabulum and 5. Ichium. (b) Image courtesy Reinhard Barkmann.

Moreover, it has been demonstrated in several studies that DXA only describes 60 % - 80 % of bone strength (Glüer 1997; Adams 2012) which is a major determinant for fracture risk. The weaknesses are even more emphasised by the fact that in 50 % of the cases, which sustained fractures, had a T-score greater than -2.5 and thus were not categorised to be osteoporotic (Stone et al. 2003; Schuit et al. 2004; Sornay-Rendu et al. 2005). In terms of treatment, it was demonstrated that a decrease of fracture incidence of 50 % - 60 % is only reflected by 5 % - 8 % improvement of BMD (Delmas et al. 2004; Chen et al. 2007).

3.2.2.2 X-ray based Methods

Recent developments, such as high resolution peripheral quantitative CT (HR-pQCT) scanners, enable the measurements of skeletal sites such as the tibia and radius with a resolution of about 80 µm isotropic voxel size (Krug et al. 2010; Griffith and Genant 2012).

Challenges are movement artefacts due to long scanning times. However, the high resolution of the systems enables a promising new approach for estimating bone strength, for instance in combination with finite element (FE) modelling (Varga et al. 2010; 2011; Nishiyama et al. 2012). Nevertheless, the approach is limited to the peripheral bones of the limbs and cannot be applied to the most frequent osteoporotic fracture sites, the spine and the hip. For the more central sites, new x-ray developments such as multi-detector computed tomography (MDCT, resolution of about 500 μm) or more general quantitative CT (QCT) seems to provide additional information to predict fracture risk or to predict bone strength important parameter (Krug et al. 2010; Griffith and Genant 2012).

Although there is rapid progress in this field with promising developments, still DXA remains the only accepted clinical modality for diagnosing osteoporosis and predicting fracture risk. The reasons are likely attributed to missing standards, expert knowledge for working with 3D data and the higher radiation dosage which is a considerable issue that all 3D X-ray techniques share. The latter increases the risk to induce cancer (Pearce et al. 2012).

3.2.2.3 Magnetic Resonance Imaging (MRI)

Conventional MRI intrinsically is not able to directly assess bone. It appears as black regions in the MRI images (Krug et al. 2010). However, at skeletal sites with relatively high fat content, such as cancellous bone, the microstructure geometry can be extracted indirectly using post image processing techniques (Griffith and Genant 2012). It was demonstrated in several studies that apparent microstructural parameters can be estimated (Krug et al. 2008) and correlate with bone strength (Majumdar et al. 1996; Hwang et al. 1997). Indeed, MRI without any ionizing radiation exposure and its sensitivity to soft tissue has a very attractive advantage compared to X-ray based high resolution 3D modalities such as QCT or HR-pQCT.

However, drawbacks of MRI are very long scanning times, relatively high costs, availability and technical challenges (Guo et al. 2010; Krug et al. 2010; Griffith and Genant 2012). The assessment of non-peripheral sites such as the proximal femur, is limited due to high signal to noise ratios (Krug et al. 2005). Furthermore, MRI has only limited potential for practical application in monitoring fracture healing due to the vicinity of metallic fixation devices that are often necessary for the stabilization of the defect (Harwood et al. 2010).

4. Acoustic Theory

4.1 Wave Propagation in Biological Tissues

An ultrasonic wave in homogenous isotropic elastic media can be described as a periodic change in the pressure distribution over time and thus can be expressed by the second order wave equation

$$\frac{\nabla^2 p(x,t)}{\partial t} = \frac{1}{v^2} \cdot \frac{\partial^2 p(x,t)}{\partial x^2}. \quad 4.1$$

In equation 4.1 the change in the pressure field (p) over time is dependent on the spatial change of pressure and the properties of the interrogated material which in that case is given by the sound velocity (v) of the medium. The wave propagation, in particular the sound velocity (v_l), is dependent on the elastic properties in the propagation direction (i) and the density of the material and relates

$$v_l = \sqrt{\frac{c_{ii}}{\rho}}. \quad 4.2$$

The derivation of equation 4.1 is based on the first order equations expressing the momentum conservation, mass conservation and pressure-density relation and is widely described in standard textbooks such as Royer (2000).

For biological tissues, different waveforms need to be considered. Ideal fluids only support pure bulk compressional waves (Figure 4.1 a) in which tension and compression occur in the propagation direction of the wave (Laugier and Haïat 2011b). Shear waves can be generated in soft tissue (Bercoff et al. 2004) and play an important role in elastic solids. Another type of wave which plays a role in ultrasound imaging of bone are surface waves such as Rayleigh waves (Figure 4.1 c).

One of the most fundamental relations is given by the wave length (λ, in m) and frequency (f, in Hz) and the fact that an acoustic wave travels a distance of λ during one period:

$$v = \lambda \cdot f. \tag{4.3}$$

Another important quantity when dealing with biological tissue is attenuation, which is the loss of ultrasound intensity (I, in $[\mathrm{W} \cdot \mathrm{cm}^{-2}]$) over the travelling distance of an ultrasonic wave. The major mechanisms which contribute to attenuation are absorption and scattering (Laugier and Haïat 2011b). Attenuation can be characterized by the exponential decrease of the pressure amplitude (p) and I with the travelling distance z:

$$p = p_0 e^{-\alpha z} \; and \; I = I_0 e^{-2\alpha z}, \tag{4.4}$$

where I_0 and p_0 are the intensity and pressure at $z = 0$ (Laugier and Haïat 2011b). In water, the attenuation coefficient α (in cm^{-1}) is proportional to the square of the frequency (Briggs 2010). It immediately follows that the maximum resolution of acoustic systems is limited by the maximum frequency providing a suitable low attenuation.

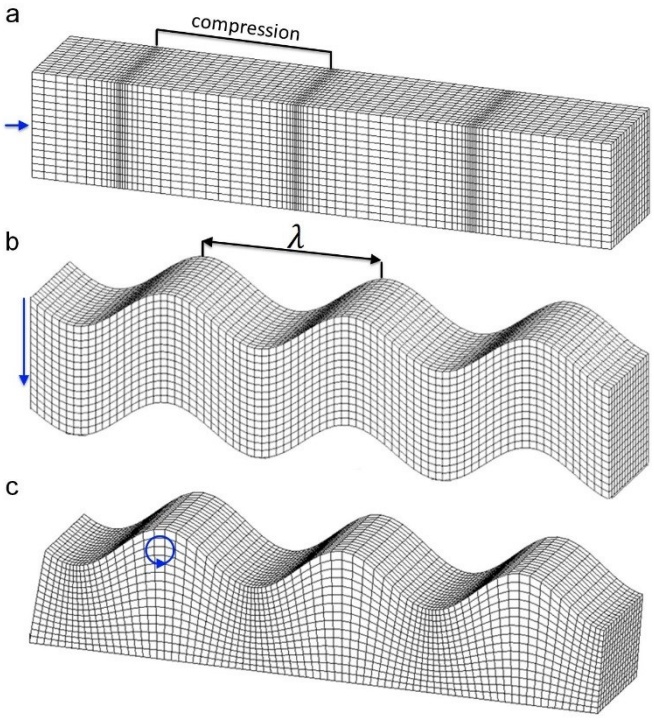

Figure 4.1 Schematic view of three different wave types that can occur. The blue arrows give the principle direction of the particle displacement. (a) longitudinal bulk compressional wave. (b) transversal or shear wave. (c) Rayleigh surface wave.

Scattering can be observed at inhomogeneities that are smaller than or are in the same order as the wavelength. Important structures in bone that causes scattering in the frequency ranges of diagnostic ultrasound are the trabecular rods or the Haversian channels of cortical bone.

Overall attenuation in biological tissue often involves a complex system of factors. In addition to absorption and scattering, effects such as refraction, diffraction, reflection and mode conversions from longitudinal to shear waves are further contributors to the total loss of signal amplitude (Laugier and Haïat 2011b).

4.1.1 Sound field

The lens aperture and the ultrasonic wavelength define the sound beam diameter and minimum pulse length and thus the spatial resolution of the system. If a spherical focused transducer is considered, a field similar to that shown in Figure 4.2 will be emitted. The sound field characteristics, such as focal depth (F_z) and beam diameter ($D_{lateral}$), can be estimated for the -3 dB range using

$$F_z = 7.08 \cdot \lambda \cdot \left(\frac{ROC}{d}\right)^2, \tag{4.5}$$

and

$$D_{lateral} = 1.028 \cdot \lambda \cdot \left(\frac{ROC}{d}\right), \tag{4.6}$$

where ROC is the radius of curvature and d the diameter of the acoustic lens (Kino 1987; Foster et al. 2000). The soundfield can be measured, for instance, using the thin wire technique (Raum and OBrien 1997).

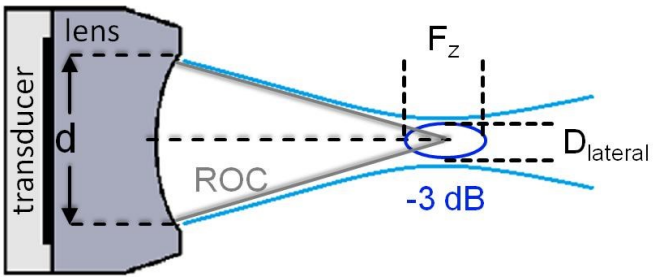

Figure 4.2 Scheme of an emitted sound field of a spherical focused transducer and its characteristic parameters.

4.1.2 Impedance

The acoustic impedance is defined as the ratio of sound pressure (p) and particle velocity ($\mathbf{v}$) and is related to density (ρ) and speed of sound (v):

$$Z = \frac{p}{v} = \rho v, \tag{4.7}$$

where Z is expressed in Mrayl ($1\,\text{rayl} = 1\,kg * m^{-2}s^{-1}$). For an ultrasound plane wave incident at the interface of two different materials, the acoustic impedances can be used to describe how much of the energy of the wave is reflected and how much is transmitted into the second material. This is commonly expressed by the amplitude reflexion coefficient ($\mathcal{R}$)

giving the ratio of reflected to the incident acoustic pressure amplitude. For normal sound beam incidence and by using Snells's law, $\mathcal{R}$ becomes

$$\mathcal{R} = \frac{Z_l - Z_{fluid}}{Z_l + Z_{fluid}}. \tag{4.8}$$

4.1.3 Speed of Sound and Attenuation measurement

Sound velocity (equation 4.2) and attenuation are the most prevalent parameters and can be assessed in the time and frequency domain. Attenuation can measured by the loss of the signal envelope amplitude in dB relative to a reference signal amplitude. The power spectral density or power spectrum ($PS(f)$, in dB) of the frequency domain is obtained by using a Fast Fourier Transform (FFT) algorithm:

$$PS(f) = 10\, log_{10}(FFT\{sig, f\} \cdot conj(FFT\{sig, f\})). \tag{4.9}$$

The FFT implements efficiently the Fourier Transform of the signal $sig(t)$ with

$$FFT\{sig, f\} = \int_{t=-\infty}^{t=+\infty} sig(t) \cdot e^{-2\pi i t f}\, dt\,, \tag{4.10}$$

where sig represents the signal in the time domain and $conj$ gives the function of complex conjugate. To measure the attenuation in the frequency domain, the difference spectrum ($\Delta PS(f)$) of $PS(f)$ and a reference spectrum $PS_{ref}(f)$ are commonly used

$$\Delta PS(f) = PS_{ref}(f) - PS(f). \tag{4.11}$$

A common measurement is the frequency dependent attenuation which can be expressed by the slope of $\Delta PS(f)$ in a certain frequency band. This parameter is often referred as the broad

band ultrasound attenuation (*BUA*) and was first introduced by Langton et al. (1984) for ultrasound based bone assessment.

In transverse transmission it is common to measure the average *SOS* over the whole propagation path within the subject since the precise tissue composition, including soft tissue or bone marrow for instance, are not easy accessible at the same time during ultrasound measurement. The *SOS* (v) can then be derived from the ratio of propagation path length (l) and time of flight (TOF),

$$v = \frac{l}{TOF_{sample}}. \tag{4.12}$$

Equation 4.12 holds for direct contact measurements. However, most applications implement a coupling fluid in which the wave needs to travel a certain distance before it hits the subject. In the case of fixed transducer separations the *SOS* can be calculated using (Laugier 2008),

$$v = \frac{l}{\frac{1}{v_{ref}} + \frac{\Delta TOF'}{l}} \tag{4.13}$$

where v_{ref} gives the sound velocity of the coupling fluid and ΔTOF the difference in TOF with (TOF_{sample}) and without the sample (TOF_{ref}). Several approaches have been suggested to determine the time of signal arrival which is not straightforward. The transmitted signals only have a limited frequency band-width and thus the signal pulse width cannot be infinitesimally narrow. The pulse width is commonly defined to be the width in time at 20 dB signal amplitude (sig) loss:

$$20\,log_{10}\left(\frac{hilbert(sig(t))}{\max_t\left(hilbert(sig(t))\right)}\right) + 20dB = 0. \tag{4.14}$$

If equation 4.14 has two solutions, t_1 and t_2, the pulse width is given by $|t_1 - t_2|$. Another reason is the complex behaviour of ultrasound while interrogating with heterogeneous biological tissue which could lead to several effects, such as multiple wave paths, frequency dependent attenuation or dispersion, and can affect and distort the signals shape (Nicholson et al. 1996; Wear 2000; Haiat et al. 2006). The most common approaches are the capturing of first peaks of the signal by using amplitude thresholds (Grondin et al. 2010), the first zero crossing (Nicholson et al. 1996; Wear 2000) and the time point of the maximum of the Hilbert transformed of the signal (Dencks et al. 2008). It was shown by several authors (Nicholson et al. 1996; Wear 2000; Haiat et al. 2006) that the SOS measurement by these time domain based approaches is highly dependent on the selected method.

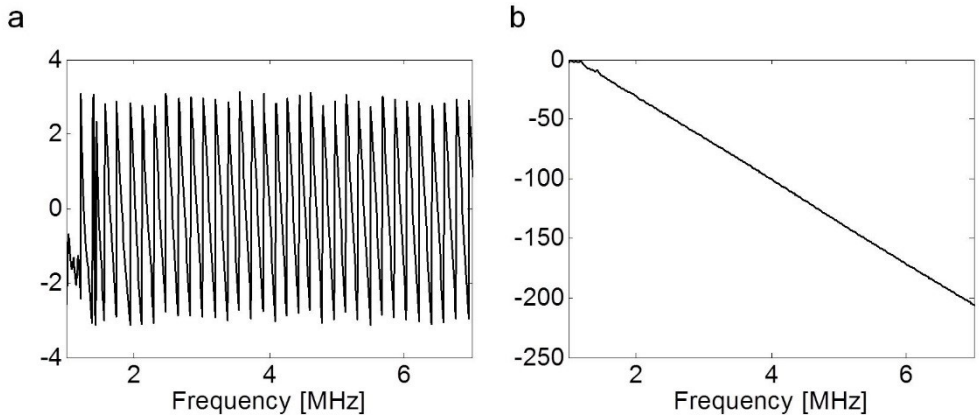

Figure 4.3 (a) Phase spectra and (b) unwrapped phase.

To compensate for dispersive effects, methods have been suggested to derive the *TOF* from the phase spectrum ($\phi(f)$). The phase spectrum can be obtained from the complex ratio of the power spectra by using a Fast Fourier Transform (FFT) algorithm and relating the *TOF* of a reference (TOF_{ref}) and the *TOF* in the sample (TOF_{sample}) by (Laugier 2008)

$$\phi(f) = atan\left(\frac{PS(f)}{PS_{ref}}\right) = \omega \cdot (TOF_{ref} - TOF_{sample}) \qquad 4.15$$

The term ω is the angular spectrum and is given by $\omega = 2\pi f$. In equation 4.15 the arctangent ($atan$) function leads to valid phase values in intervals of $-\pi$ to π depicted in Figure 4.3 (a).

This can be corrected by using an unwrap algorithm yielding a linear slope for a certain frequency band as shown in Figure 4.3 (b). By using the unwrapped phase spectra ($\phi_u(f)$) as an estimate for $\phi(f)$ the TOF_{sample} can be derived from equation 4.15 by using the linear slope of $\phi_u(f)$ (Kim and Grill 1998; Raum et al. 2006b)

$$TOF_{sample} = TOF_{ref} - \frac{\partial \phi_u(f)}{2\pi \partial f}, \tag{4.16}$$

4.1.4 Comparison to µCT

Although both methods, QUS in transverse transmission and µCT can be considered as projection approaches, they have remarkably different properties. For µCT, the major parameter measured is the intensity $\hat{I}$ and its attenuation when passing through matter (Blake and Fogelman 1997). $\hat{I}$ is directly related to the atomic number and thus to the areal mass density (M) by

$$\hat{I} = \hat{I}_0 e^{-\mu M}, \tag{4.17}$$

where $\hat{I}_0$ is the incident photon energy and µ the mass attenuation coefficient. In contrast to ultrasound, almost no refraction or reflection (at normal incidence) occurs at material boundaries. Moreover, effects similar to guided waves or scattering by structures in the size of Haversian canals cannot be observed. DXA and desktop µCT systems often use polychromatic X-ray tubes which could lead to beam hardening effects due to the different attenuation of the different energies ($\hat{I}_0$). However, DXA uses two energies in order to separate bone from soft tissue.

4.2 Numerical solutions for wave propagation

4.2.1 The Finite Difference Time Domain (FDTD) Method

The FDTD approach is the most frequently used method for modelling the ultrasound propagation in bone (Bossy and Grimal 2011). The applications range from axial (Bossy et al. 2002; Nicholson et al. 2002; Bossy et al. 2004a) and transverse transmission (Barkmann et al. 2000; Kaufman et al. 2008; Grondin et al. 2010; Rohrbach et al. 2010) at cortical bone sites but also investigations in trabecular bone models (Luo et al. 1999; Bossy et al. 2005; Padilla et al. 2006; Bossy et al. 2007; Haiat et al. 2008; Nagatani et al. 2008; Hosokawa 2011).

The most frequent simulated QUS setting is axial transmission for monitoring fracture healing or for the assessment of bone quality (Moilanen et al. 2007a; Moilanen et al. 2007b). By using different healing models and phantoms it was consistently demonstrated in various studies (Protopappas et al. 2006; Dodd et al. 2007; Machado et al. 2010b) that SOS is significantly increased during the healing process.

Only few FDTD simulations were conducted in transverse transmission (Barkmann et al. 2000; Grondin et al. 2010; Rohrbach et al. 2010). The focus was on the investigation of the impact of bone quality relating properties such as the cross sectional area, moment of inertia, bone matrix elastic stiffness or porosity on ultrasonic parameters (*SOS*, *UA*, *BUA*). Transverse transmission for fracture healing has not been applied *in silico* so far.

If attenuation is neglected, ultrasound wave propagation in elastic media can be fully described by two equations (Bossy et al. 2004a). The first describes the change of particle velocity ($\mathbf{v}_i$) over time, with

$$\frac{\partial v_i}{\partial t} = \frac{1}{\rho} \cdot \frac{\partial \sigma_{ij}}{\partial x_j}, \tag{4.18}$$

and the second describes the change of stress (σ_{ij}) over time, with

$$\frac{\partial \sigma_{ij}}{\partial t} = C_{ijkl} \frac{1}{2} \left(\frac{\partial v_k}{\partial x_l} + \frac{\partial v_l}{\partial x_k} \right). \tag{4.19}$$

The subscripts, i, j, k and l, indicate the spatial direction varying all from 1 to 3. The formulas are written using Einstein's convention for implicit summation (Bossy et al. 2004a).

The first equiation 4.18 is derived based on the definition of stress

$$\nabla F_i = A \cdot \frac{\partial \sigma_{ij}}{\partial x_j} \tag{4.20}$$

and Newtons second law

$$\nabla F_i = \rho A \cdot \frac{\partial^2 u_i}{\partial t^2} \tag{4.21}$$

where F_i denotes the force in direction i, A gives the area and u_i the particle displacement. By using Hook's law of linear elasticity, 4.19 can be derived based on equation 2.2. The discretization of 4.18 and 4.19, and therefore the computer based implementation, is done by using finite differences. A detailed description of the procedure and application to modelling ultrasound propagation can be found in Bossy and Grimal (2011). Briefly, the approximation of the gradients is based on the Taylor expansion of differentiable functions. The gradients are computed by fitting a line between two adjacent discrete points of the function. Equiation of 4.18, for example, can be written in the form

$$\frac{\partial v_i}{\partial t} = \frac{1}{\Delta t}(v_i^{t+1} - v_i^t) \tag{4.22}$$

Substituting 4.22 in 4.18 gives

$$v_i^{t+1} = v_i^t + \frac{\partial \sigma_{ij}}{\partial x_j} \tag{4.23}$$

The same procedure can be applied for all derivates and thus leads to 9 equations in total for 2 dimensions ($v_1, v_2, \sigma_{11}, \sigma_{12}, \sigma_{22}$). The problem with these formulas is that all are defined at the same point in space and time. Common solutions for this problem are staggered grids. SimSonic is based on the scheme proposed by Virieux (1986) for 2D and Graves (1996) for 3D.

4.2.2 Other simulation software and algorithms

The usage of the impulse response to calculate ultrasonic pressure fields for a given transducer geometry has been implemented in the freely available software Field II[1] and is based on the studies by J.A Jensen (1991; 1992; 1993; 1996b; 1996a; 1999). The advantage of the approach is the direct and efficient calculation of the acoustic pressure for a given point in space and time. Therefore the program is perfect for predicting ultrasound fields and is thereby perfectly suitable to optimize geometry, phasing and apodization of an ultrasound transducer (Jensen et al. 1993). The simulation of time varying sound propagation in complex hard tisues is difficult or not feasible.

Another interesting approach is the k-space PS method, recently developed and available as a MATLAB toolbox called k-wave[2] (Treeby and Cox 2010a). It allows the simulation of a time varying wave propagating through a heterogeneous medium as opposed to the impulse response approach (Treeby and Cox 2010b; Treeby et al. 2010). A weakness of the code is that it neglects shear waves. Although models for solids implementing shear compressional waves exist, as recently published (Firouzi et al. 2011), they are currently not implemented. However, models describing the anisotropic nature of bone have already been developed.

The only numerical methods which have been applied to bone QUS so far are finite element (FE) and finite difference time domain (FDTD) models (Bossy and Grimal 2011). For the last decade a commercial software package (WAVE2000-WAVE3500) from CyberLogic®, Inc[3] exists which solves the linear visco-elastic wave propagation using a FDTD approach. Although the software provides a graphical user interface, it acts in most cases as a black box and customization or the adaption to particular cases, as it is often needed in natural science, is very complicated or not feasible.

As opposed to FDTD methods, FE approaches are more flexible. However, the counterpart is a higher complexity for implementation. Although it is not as common as FDTD, it has been successfully applied for studying guided wave propagation in a bone healing model (Protopappas et al. 2007).

---

[1] Field II is available at: http://field-ii.dk//

[2] k-wave is available at http://www.k-wave.org/index.php

[3] Homepage of CyberLogic®,inc and WAVE2000-3000: http://www.cyberlogic.org/software.html

5. Material and Methods

5.1 Complementary methods

5.1.1 PMMA embedding and polishing

For long term tissue fixation the bone samples were embedded in polymethylmethacrylate (PMMA). The procedure followed a standard protocol described by Lakshmanan et al. (2007) and Raum (2008). Briefly, the samples were dehydrated in a graded series of ethanol (70 %, 96 % and 100 %) and immersed in each solution for 24 h. Degreasing was accomplished by a Histoclear (National Diagnostics, Atlanta, GA) solution for 12 h prior to the ethanol series. Finally, the unpolymerized embedding material methylmethacrylate (MMA) was infiltrated by immersing the samples in a solution mixture of 94 % MMA, 5 % dibuthylphtalate (softener), and 1 % benzoylperoxide (activator) for 24 h at 4 °C. In order to initiate the polymerization, a solution with a higher activator concentration was used (93 % MMA, 4 % dibuthylphtalate, and 3 % benzoylperoxide). The polymerization of MMA is an exothermic reaction. To prevent considerable heating, which would cause alterations of the tissue and inclusions of air bubbles, the moulds were packed in a temperature controlled water tank. This procedure is intended to replace almost all water content of the bone tissue (Raum 2008).

For SAM measurements planar and smooth sample surfaces are an essential requirement. Therefore the specimens were grinded and polished within the studies of this work (Rohrbach et al. 2010; Rohrbach et al. 2012b; Grimal et al. 2013b; Malo et al. 2013). For the studies of Rohrbach et. al (2010; 2012b) and Grimal et al. (2013b) the procedure consisted of grinding using successively decreasing grain sizes (SiC paper 2400 and 4000; Struers GmbH, Willich, Germany) and a final polishing step (Logitech WG2, Struers GmbH, Willich, Germany) with a hard synthetic cloth (Microtex 500, Struers GmbH, Willich, Germany), ethyleneglycol suspension and 3 mm diamond particles as abrasive. For the study of Malo et al. (2013) the measurement protocol slightly changed due to the movement of laboratories and new equipment. Grinding was done using a plane grinder (EXAKT 400 CS, Exakt Apparatebau, Norderstedt, Germany) with successively decreasing grain size (ISO/FEPA grit: P500, P800, P1000, P1200 and P4000, Hermes Abrasives Ltd., Virginia 15 Beach, VA and Struers A/S, Ballerup, Denmark). Finally, the samples were polished using cloths, containing 6 μm and 1

µm diamond particle suspensions in ethylene glycol (Phoenix 400, Buehler Ltd., Lake Bluff, IL.).

After polishing and directly before SAM measurements, the samples were purified using an ultrasound bath and a soft paint brush in order to remove debris of the specimens and the diamond suspensions.

The embedding of the specimens of Rohrbach et al. (2012b) was conducted in a previous study by Lakshmanan et al. (2007). The femoral neck samples of Malo et al. (2013) were embedded by our colleagues in Finland and polishing, as well as grinding, was done with assistance in our laboratory. However, the embedding procedure followed the same procedure mentioned at the beginning of this chapter.

5.1.2 Scanning Acoustic Microscopy

SAM has been utilized to measure tissue structural and elastic properties of cortical bone at the micron level. The results served as a basis for the numerical modelling of cortical bone for sound propagation simulations.

All measurements were based on a standard approach extensively described in literature (Lakshmanan et al. 2007; Raum 2008; Raum 2011). The custom built quantitative scanning acoustic microscope consists of a three-axis high precision scanning stage, 400 MS/s 12-bit A/D-board (CompuScope 12400, GaGe, Lockport, IL) and a 200 MHz pulser-receiver (Panametrics 5900PR, Panametrics-NDT, Waltham, MA). The hardware is controlled by custom written C++ software (SAM200Ex, Q-BAM, Halle, Germany). The system was equipped with a 50 MHz spherical focused transducer (V605/60°, -6 dB bandwidth 26 - 64 MHz, Valpey Fisher, Hopkinton, USA) with a focal length of 5.2 mm which leads to beam diameter of 23 µm at focus. The embedded samples were immersed in a temperature controlled water tank at 25 °C. Distilled and degassed water was used as coupling fluid. The principle setup is depicted in Figure 5.1

The movement of the transducer for the three spatial directions (x,y,z) was controlled via high precision scanning stages and the motor controller. While moving the transducer, a position trigger signal is generated at fixed positions by the scanning stages. These triggers induce the AD-card to prepare for acquisition and to inform the pulser to generate an excitation signal. The sample surface reflected and recorded signal is then pre-processed by the receiver (e.g. band pass filtered) and passed to the AD-card for digitalisation.

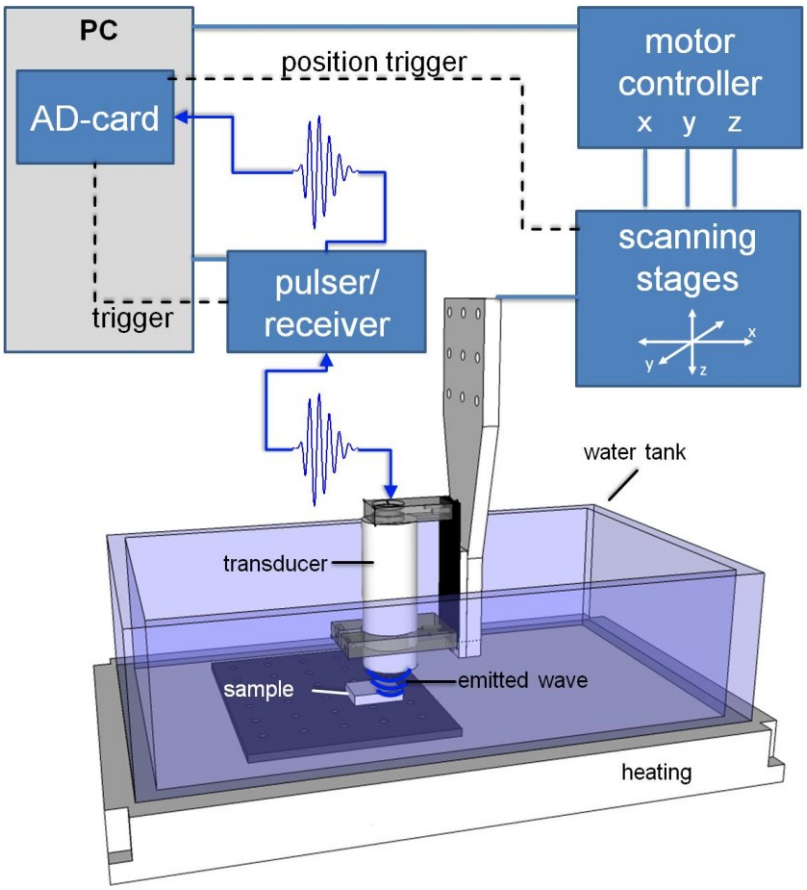

Figure 5.1 Schematic setup of a conventional scanning acoustic microscope as used in the present studies

5.1.2.1 Signal acquisition and impedance estimation

The radio frequency ultrasound signals were digitized at each point in x and y (C-mode, Figure 3.1) using a scan increment (Δd) of 16 µm in each direction and a sampling rate of 400 MHz. For noise reduction purposes, each signal was band pass filtered using a zero-phase type II Chebyshev filter with cutoff frequencies of 5 and 90 MHz. The voltage, defined as the amplitude of the signal, was calculated by extracting the maximum of the signal's envelope using a Hilbert transform (Figure 5.2). The principle steps involved in the signal processing procedure are depicted in a flow chart in Figure 5.5.

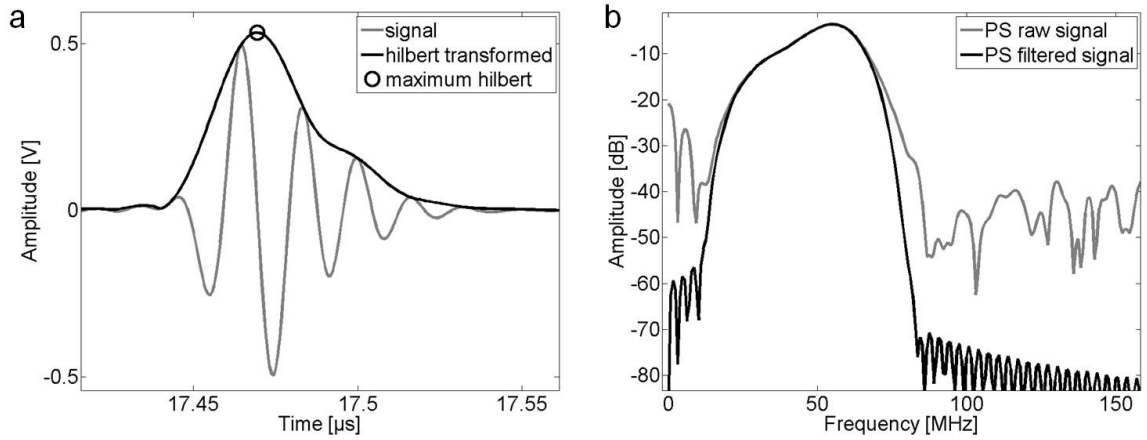

Figure 5.2 (a) A time resolved signal and the maximum of its Hilbert transformed. (b) Power spectra (PS) of the filtered and unfiltered signal.

The voltage values are further corrected for small misalignments of the focus using a defocus correction (Figure 5.4 d), and for temperature variations using a temperature calibration curve. The temperature calibration curve (Figure 5.3 a) was measured prior to the measurements at 25 °C water temperature. Both corrections are obtained from a Bz-scan conducted post to each C-scan (Figure 5.4).

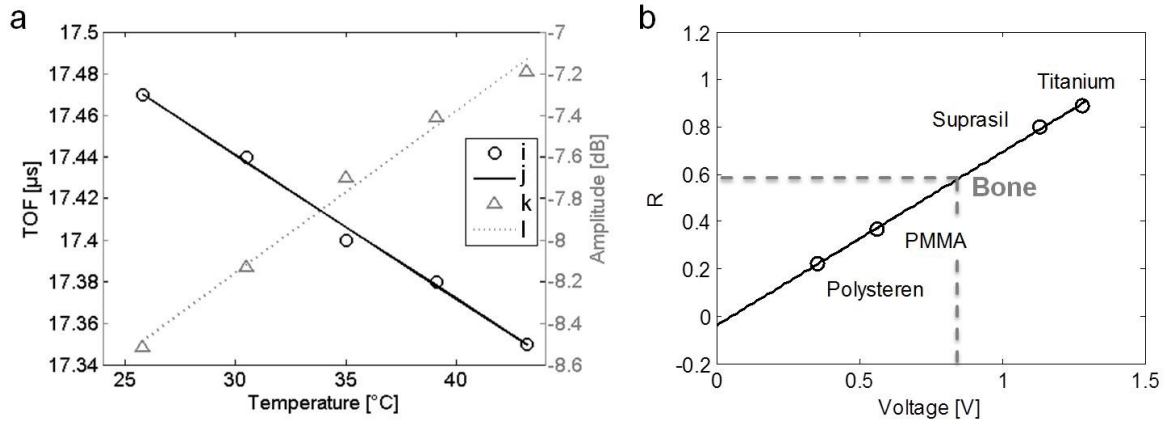

Figure 5.3 (a) Relationship of temperature with TOF (left axes) and amplitude (right axis) of the 50 MHz transducer. Both measurements – (i) *TOF* and (k) Amplitude - show a linear relationship. The amplitude can be corrected by the appropriate amount of dB by calculating the temperature which is based on the linear fit of *TOF* (j). The linear fit of (l) is then used to calculate the amplitude correction. (b) Example of a calibration curve relating voltage and reflection coefficient (R).

Acoustic impedance (Z, unit rayl=$1\frac{\mathrm{kg}}{\mathrm{sm}^2}$) values were derived from the reflexion coefficient ($\mathcal{R}$) relating

$$Z = -\frac{Z_{coupling}(1+\mathcal{R})}{1-\mathcal{R}} \qquad 5.1$$

where $Z_{coupling}$ (409.4 rayl at 25 °C) is defined as the acoustic impedance of the coupling fluid (water). The value for $\mathcal{R}$ of unknown voltage values, such as bone, was obtained from a calibration curve correlating voltage and $\mathcal{R}$ (Figure 5.3 b). In order to plot the linear dependency of $\mathcal{R}$ and V, homogeneous elastic materials with known *Z* (Titanium, Suprasil® [Heraeus Quarzglas GmbH & Co., KG, Hanau, Germany], PMMA, polystyrene and polymethylpentene [TPX®]) were measured and used as a reference.

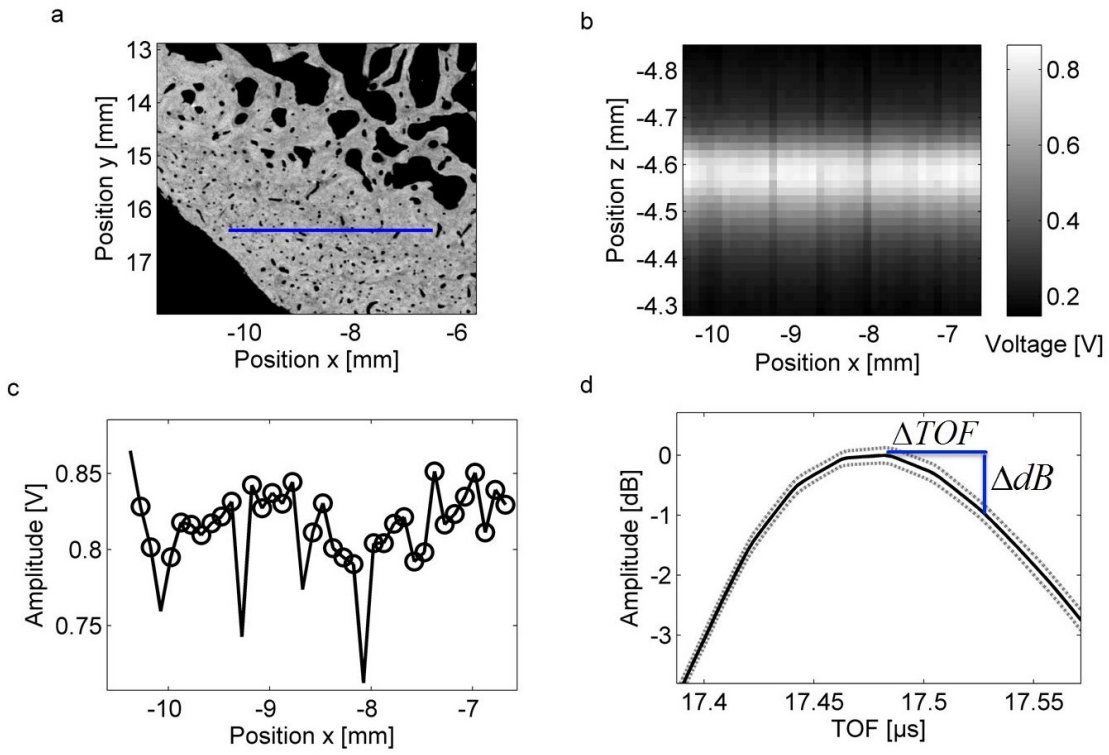

Figure 5.4 (a) 50 MHz SAM measurement map of the femoral neck. The gray values correspond to the maximum of the signal amplitudes. The blue line corresponds to the Bz scan location used for the V(z) correction curve. (b) Bz scan at location of the blue line in (a). For each z and x position the maximum of the Hilbert transformed signals is plotted (in V). (c) Selected positions for the calculation of the correction curve in (d). Points with amplitudes larger than the standard deviation of all amplitudes were excluded. (d) The correction in dB. The correction curve is calculated as an average over x at positions identified in (c). *TOF* is calculated from the z Position by assuming a *SOS* of 1497 m/s (*SOS* of H2O at 25 °C). For a given *TOF* shift ($\Delta\, TOF$) the correction in dB (ΔdB) can be calculated.

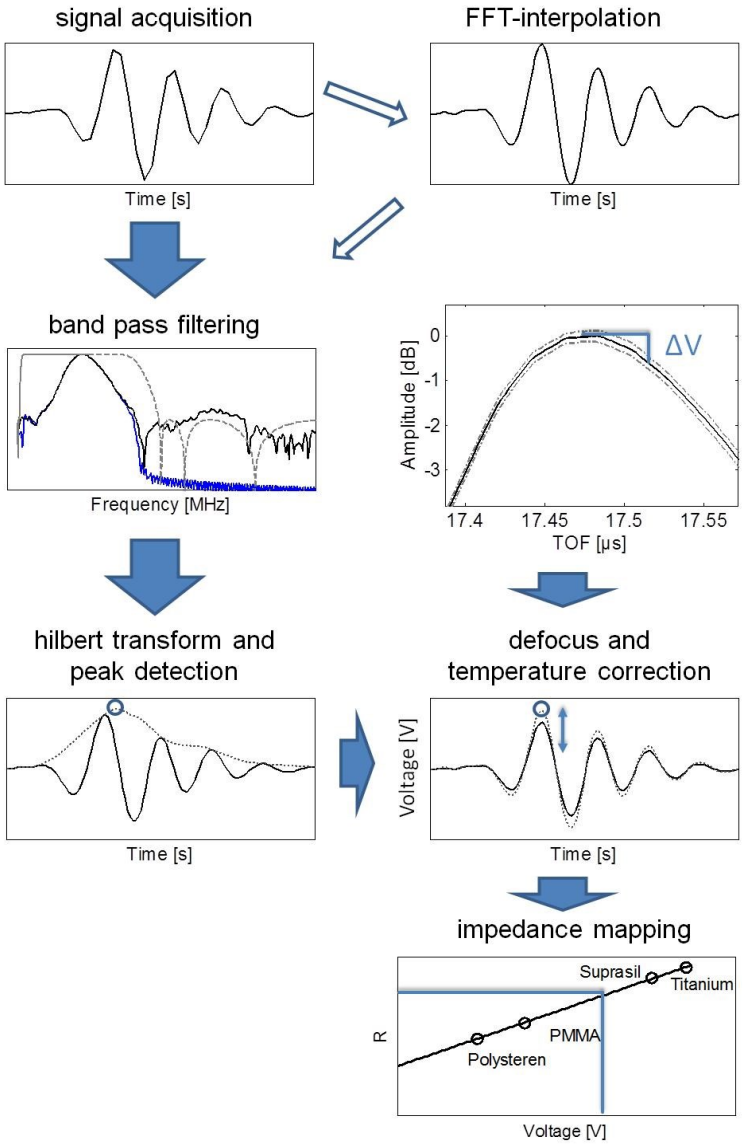

Figure 5.5 Flow chart of required signal processing steps for acoustic impedance mapping.

5.1.2.2 SAM image processing and parameter extraction

After signal processing, several image processing steps were necessary to extract pore parameters and matrix stiffness. First an adaptive threshold procedure was implemented as described by Lakshmanan et al. (2007). The threshold was iteratively calculated according to Figure 5.6 (a) and a binary mask was derived separating background (pores, voids) from bone matrix (Figure 5.6 b). Cortical porosity (*Ct.Por*) was defined to be

$$Ct.Por = \left(1 - \frac{A_{cortical\ bone} - A_{pore}}{A_{cortical\ bone}}\right) \quad 5.2$$

with A specifying area of pores (A_{pore}) and cortical bone ($A_{cortical\ bone} = A_{pore} + A_{matrix}$), respectively. Single pores were identified in the binary maps by using a 2D connected component labelling algorithm. Cortical pore diameter (*Ct.PorDm*) was extracted from the labelled binary maps by fitting an ellipse to each single pore. Following Bell et al. (1999a) the minor axis of each ellipse were defined to be equal to the *Ct.PorDm*. Two estimates were calculated for each ROI which were average (mean) *Ct.PorDm* and the median of *Ct.PorDm*. Finally cortical pore density (*Ct.PorDens*) was defined as the mean pore number per mm^2.

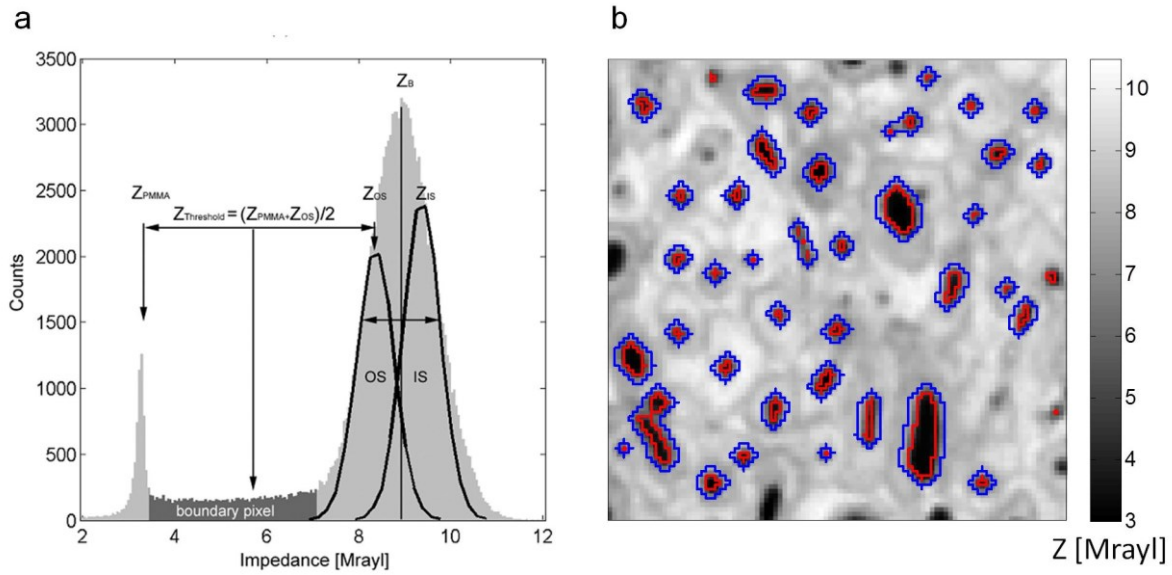

Figure 5.6 (a) Threshold procedure as introduced by Lakshmanan et al. (2007) (reprinted from Lakshmanan et al. (2007) with permissions © IEEE).(b) Magnified impedance map from Figure 5.12 b showing thresholding (redlines) and effects of erosion (blue lines). Pores at the border where excluded from evaluation in that image.

In order to estimate reliable measurements of the averaged matrix impedance and thus elasticity, the acoustic maps needed compensation for partially filled pixels (partial volume effect, Figure 5.7 a). Pixels at the borders between bone matrix and background (viod, pores) suffer from these effects due to the limited spatial resolution (*sRes*) and scan increment (Δd) and thus would lead to underestimates of the acoustic impedance (Figure 5.7 b). The effect is illustrated in Figure 5.7. The maximum number of pixels (ER) that can be affected by the partial volume effect relates $sRes$ and Δd can be estimated by

$$ER = \left\lceil \frac{sRes}{\Delta d}\, pixel \right\rceil \qquad 5.3$$

where $\lceil x \rceil$ means round towards infinity. An efficient way to remove these pixels is to use a morphological erosion operator with a disk shaped kernel of diameter ER. For the 50 MHz measurements of the present study this leads to a spatial resolution of $sRes = 23\ \mu m$ and a scan increment of $\Delta d = 16\ \mu m$ and thus to $ER = 2$ pixel.

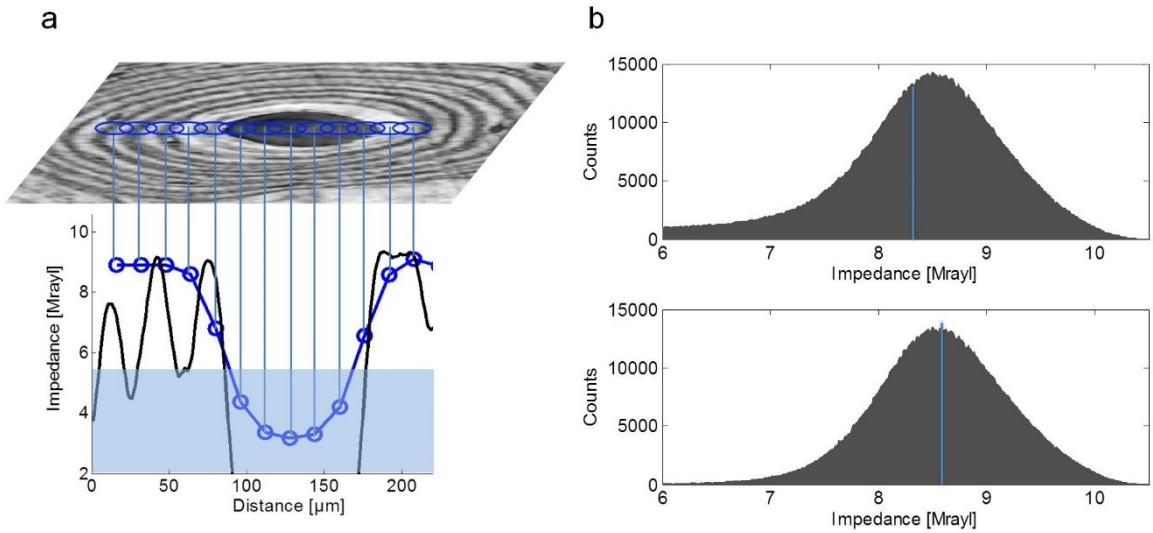

Figure 5.7 (a) Effect of scan increment and resolution. The upper grey scale image is an osteon scanned using a 1.2 GHz transducer. The lower plot gives the Z values measured using a 50 MHz transducer (20 µm spatial resolution, Δd =16 µm, blue dots and line) and 1.2 GHz (black line). The light blue area gives the values which were excluded while thresholding the 50 MHz impedance map (threshold = 5.3 Mrayl). The Haversian canal closest values above the threshold (at 80 µm and 176 µm) are affected by the partial volume effect but determine the size of the pore. To estimate the average impedance these values need to be excluded. (b) histograms of impedance at cortical area in sample of Figure 5.12 b. The effect shows the mean impedance of histograms without erosion (mean=8.3 Mrayl, upper) and with erosion (mean=8.6 Mrayl, lower)

5.1.3 Estimation of Material Constants from Acoustic Impedance

It was shown that the acoustic impedance is highly correlated with the elastic stiffness (c) in the probing direction (Raum et al. 2006a; Preininger et al. 2011). The relation used in the

present studies was obtained from Preininger et al. (2011) who correlated elastic stiffness for cortical bone from different species, anatomical sites, measurement directions and sample preparation and is given by

$$c = 0.61 \cdot Z^{1.92} \qquad 5.4$$

The data were collected from Raum et al. (2006a; 2007a). However, for study I another empirical relationship reported earlier was used (Raum et al. 2006a)

$$c = 1.31 + 0.075 \cdot Z + 0.5 \cdot Z^2 \qquad 5.5$$

5.1.4 Finite difference time domain (FDTD) based ultrasound propagation simulations

5.1.4.1 Simulation Software

A FDTD code (SimSonic, LIP, Paris, France) as described in chapter 4.2.1 was used to solve the wave propagation problem (Auld 1990; Bossy and Grimal 2011). The simulation box was surrounded by perfectly matched layers (PML) to avoid any spurious reflections (PML Thickness = 40 grid points, Attenuation 80 dB). Details of the algorithm can be found in Collino and Tsogka (2001). PML are often referred to as the most convenient way to model unbounded domains (Cohen 2002) while maintaining a reasonable computational cost.

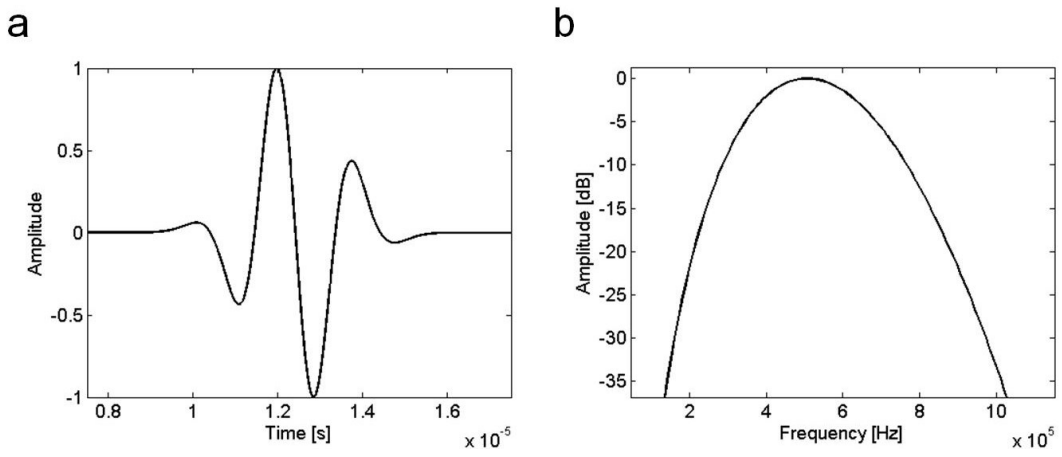

Figure 5.8 (a) Excitation signals and (b) spectra.

The algorithm was designed in a way that SAM maps could be imported directly into the simulation software. The FDTD code uses a structured mesh of an identical grid step in directions x and y. Thus the grid step is identical to the pixel size (16 µm^2), which is small

enough to ensure the stability of the numerical solution (Bossy and Grimal 2011) for 5 MHz and 0.5 MHz.

A Gaussian derivative with a center frequency of 500 kHz was used as an excitation signal (Figure 5.8 a b)

5.1.4.2 Signal processing

Signal processing was mainly focused on the assessment of the first arriving signal (FAS) since this wave part was expected to be associated with the wave propagating circumferentially along the cortical shell of bone. Since the numerical simulated signals can be considered noise free, as opposed to *in vitro* or *in vivo* setups consisting of electronics, no digital filtering of the signals was required.

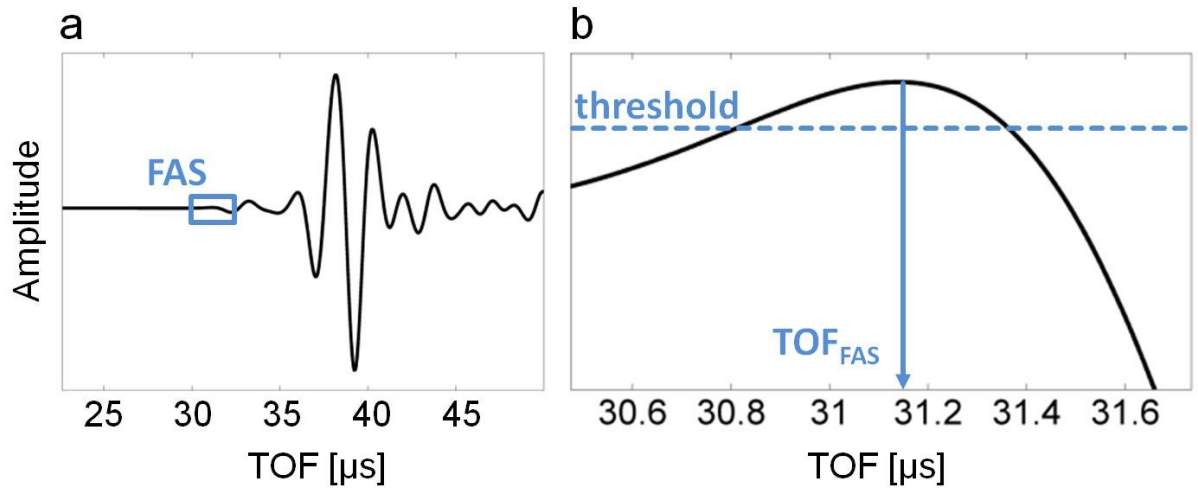

Figure 5.9 Assessment of the TOF_{FAS}. (a) received signal with selected FAS (blue box). (b) Threshold based determination of the FAS (magnification of box in a). TOF_{FAS} is defined as the *TOF* at the maximum of the first amplitude larger than a selected threshold.

A threshold based approach was implemented in order to automatically derive the *TOF* of the FAS (TOF_{FAS}). The procedure is depicted in Figure 5.9 and has been described by Grondin et al. (2010). In that study TOF_{FAS} was defined as the time point of the FAS maximum. The FAS was determined by using (1) an amplitude threshold to detect the FAS, and (2) time oversampling followed by interpolation and detection of signal extremum to obtain a precise estimation of *TOF* (Grondin et al. 2010).

5.1.5 Statistics

Statistical analyses were conducted with custom-made MATLAB software R2010a (The Mathworks Inc., Natick, MA, USA) utilizing the Statistics Toolbox and with SPSS software version 19 (SPSS® Inc., Chicago, IL, USA). All statistical results were considered significant for p values less than 0.05.

5.2 Study I

5.2.1 Specimens

An overview of the samples used to assess micro elastic and structural properties is given in Table 5.1.

Table 5.1 Overview of human specimens and their features.

data set	num. sample	num. indv.	age mean±std (range)	anatomical location	study	comments
Fd_1	56	1	72	femur shaft	(Rohrbach et al. 2012b)	cylindrical shaped samples ($\emptyset = 4.4$ mm), embedded
Fd_2	21	21	47.1 ± 17.8, (17-82)	femur neck,	(Malo et al. 2013)	embedded cross sections of femur neck relating properties with age
Fd_3	9	7	64.4 ± 8.8	femur neck	(Rohrbach et al. 2010; Grimal et al. 2013b)	embedded femoral neck cross sections used for simulation study

5.2.1.1 Human femur cylinder samples (Fd_1)

Cylindrical shaped and embedded bone samples ($\emptyset = 4.4$ mm, N=56, Fd_1 Table 5.1) of one human femur were obtained from a previous study (Lakshmanan et al. 2007). Details of the sample preparation can be found in that study and in the study of Rohrbach et al. (2012b). Briefly, the shaft of a human female femur (age 72) was divided into 14 cross sections from proximal to distal (see Figure 5.10). The thickness of each section was 22 mm. The cross sections were embedded in PMMA and polished following the protocol described in chapter 5.1.1. After the cross-sectional scan using SAM, the discs were further divided into posterior (POS), medial (MED), anterior (ANT) and lateral (LAT) sections. For each quadrant, one

transverse surface was prepared and scanned with SAM. Finally, from each quadrant (N=56), one cylindrically shaped sample with a diameter of 4.4 mm, where the orientation of the long axis was parallel to the radial axis of the femur shaft was obtained (Figure 5.10). The samples were drilled using a high precision lathe equipped with a diamond milling knife. Finally, the smoothness of the cylinder surfaces was obtained by grinding with successively decreasing grain size (SiC paper 2400 and 4000). SAM measurements of the cross-, transverse-sections and the cylinders were conducted within the study of Lakshmanan et al. (2007).

Ethical approval for the collection of the samples was granted by the Ethics Committee of the Medical Faculty of Martin Luther University (Halle, Germany). The legal guardian of the tissue donor provided informed written consent to provide their tissues for investigation (Rohrbach et al. 2012b).

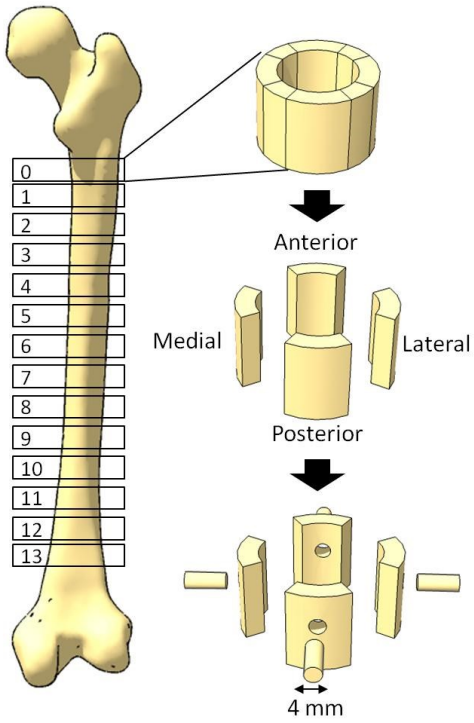

Figure 5.10 Preparation of human femur of the study of Lakshmanan et al. (2007). (a) cutting of a human femur shaft into 14 cross sections. (b) cutting into 4 parts regarding their anatomical location (Anterior, Lateral, Posterior, Medial) (c) drilling of cylinders.

5.2.1.2 Femoral neck cross sections (Fd_2,Fd_3)

Two sets of proximal femur samples were prepared for the SAM investigations.

The first set (Fd_2 Table 5.1) consists of a set of twenty-one human proximal femurs of male cadavers (n = 21, aged 47.1 ± 17.8 years, range 17-82 years). The sample set was used within

the collaboration with Malo et al. (2013) and details of sample preparation can be found in that publication. Sample preparation, except the final grinding and polishing, was conducted in collaboration with Kuopio University Hospital (Finland) who provided the specimens. The final grinding and polishing step was conducted in Berlin as part of the present project following the protocol described in chapter 5.1.1. Ethical approval for the collection of the samples was granted by the National Authority for Medicolegal Affairs (permission number: 5783/04/044/07). The cadavers had no pre-existing conditions that might have affected bone metabolism (Table 5.2). After soft tissue removal, the proximal femurs were stored in a freezer (-20°C) until preparation for measurements. It has been reported that freezing and thawing do not affect significantly the elastic properties of bone tissue (Sedlin and Hirsch 1966; Linde and Sorensen 1993; van Haaren et al. 2008). Transversal cross-sections were cut perpendicular to the long axis of the femoral neck (n = 21, Figure 5.11) using a band saw (KT-210, Koneteollisuus Oy, Helsinki, Finland). In order to ease orientation of the samples, the cross sections were slightly cut on the medial bone surface. Finally, the cross-sections were embedded in PMMA following the protocol in chapter 5.1.1.

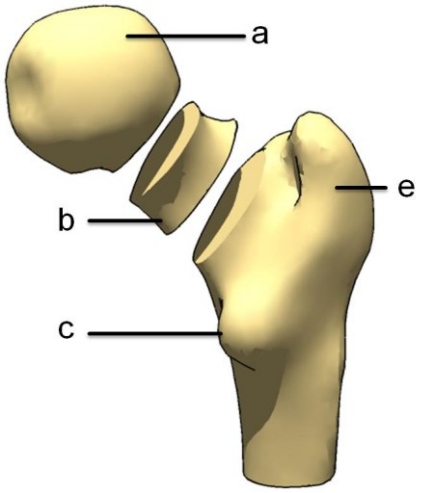

Figure 5.11 A schematic illustration of the sample preparation of a human femur with (a) femoral head, (b) femoral neck. (c) lesser trochanter

The second set of femoral neck samples (Fd_3 Table 5.1)) consisted of nine femoral neck cross-sectional slabs with a thickness of about 10 mm (Rohrbach et al. 2010; Grimal et al. 2013b). The specimens were obtained from 7 human donors (age: 64.4 ± 8.8 years) who received a hip implant. One donor provided a complete proximal femur and therefore enabled the measurement at three sites of the central part of the femoral neck. One site close to the femoral trochanter (F.trochanter) and one close to the femoral head (F.head) were prepared for measurements although F.head was excluded from the statistics regarding simulations of

different bone models (chapter 5.2.4.3) since its location was considered too close to the head. However, for assessing variations of the TOF_{FAS} with respect to the long axis of the femoral neck, the F.head was included (chapter 5.2.5). Two further cross sections were measured at two opposite sites which were extracted from a cut in the central part of the femoral neck (F.centre1, F.centre2).

The experimental protocol was approved by the Ethic Commission of the Martin Luther University (Halle Saale, Germany) and informed consent for the study was obtained from all subjects. Preparation of the samples was conducted within the present project and is published as part of the studies by Rohrbach et al. (2010) and Grimal et al. (2013b). The cross-sections were cut approximately perpendicular to the femoral axis between the femoral head and the central region of the femoral neck (Figure 5.11 b). Final embedding and polishing was done following the protocols described in chapter 5.1.1.

Table 5.2 Basic anthropometric data of the cadavers.

Age [years]	Age group	Height [cm]	Weight [kg]	BMI [kg·m^{-2}]
17	1	178	74	23.4
22	1	186	106	30.6
26	1	175	60	19.6
30	1	184	105	31.0
32	1	171	69	23.6
34	1	187	102	29.2
37	1	177	74	23.6
39	1	185	84	24.5
43	2	171	98	33.5
44	2	179	96	30.0
46	2	185	85	24.8
49	2	178	85	26.8
51	2	185	108	31.6
52	2	180	136	42.0
54	2	176	73	23.6
58	2	169	96	33.6
59	2	175	73	23.8
63	3	170	68	23.5
74	3	166	64	23.2
78	3	177	72	23.0
82	3	165	53	19.5

47.1 ± 17.8	-	177.1 ± 6.7	84.8 ± 20.0	26.9 ± 5.5

5.2.2 Material properties based on SAM

The embedded cylinder samples of Rohrbach et al. (2012b) (Fd_1 Table 5.1) were scanned by Lakshmanan et al. (2007) using SAM as described in chapter 5.1.2. The impedance maps of the cylinders were unwrapped and an ROI between endosteal and periosteal region was selected. Angular dependent evaluation of impedance was conducted by Lakshmanan et al. (2007) and details can be found in that paper. Registration of impedance and SRμCT data and evaluation of cross and transverse sections was done in the present study.

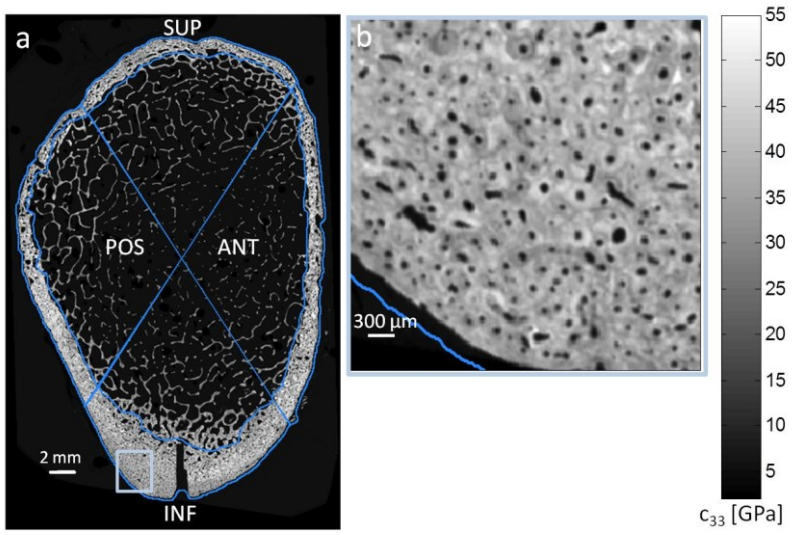

Figure 5.12 (a) SAM elasticity map and anatomical quadrants of a femoral neck and (b) magnified map of light blue box in a..

The femoral neck cross-sections of Malo et al. (2013) (Fd_2 Table 5.1) were scanned in collaboration using SAM (chapter 5.1.2). The data from studies of Rohrbach et al. (2010) and Grimal et al. (2013b) (Fd_3 Table 5.1) were acquired from the present project.

In order to evaluate anatomical dependent variations, the cross sections of Fd_2 and Fd_3 were automatically divided into quadrants by region of interests (ROIs). The procedure is described in those studies (Rohrbach et al. 2012b; Malo et al. 2013). The four ROIs for the neck were superior (SUP), inferior (INF), anterior (ANT), posterior (POS) (Figure 5.12). Within each ROI, the endocortical boundary between cortical and trabecular bone was determined by an experienced histomorphometrist. In most cases, cortical bone could easily be distinguished. In cases with marked cortical trabecularisation, the pore size and density demarcation were used to define the line between the cortical and trabecular bone (Malo et al. 2013).

For each quadrant, elastic and structural parameters were automatically and separately derived using the procedures already mentioned (chapter 5.1.2.2). Furthermore, cortical thickness was estimated based on a custom made algorithm. Briefly, first the cross section maps were binarized, thresholded, dilated, filled and finally eroded. The kernel size was the same for dilation and erosion. However, an individual kernel size was manually selected for each sample in order to ensure perfect filling. Centre of mass was calculated for each filled cross section (the crossing of the quadrants in Figure 5.12). The local cortical thickness is then defined as the distance of two intersections point with a line that has its origin in the centre of mass Figure 5.13.

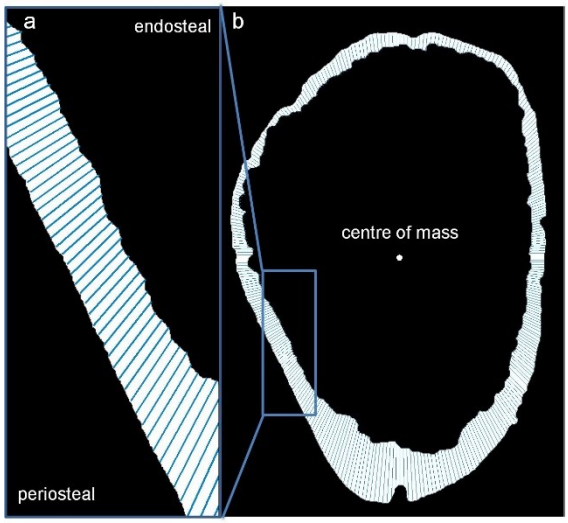

Figure 5.13 Estimation of cortical thickness. (a) magnified pore filled cortex at position indicated by the box in (b). (b) cross section of the same sample of Figure 5.12

5.2.3 Synchrotron µCT

5.2.3.1 Measurement setup

SRµCT measurements were conducted during the study of Rohrbach et al. (2012b) in order to derive the degree of mineralization (*DMB*) of bone. The samples were imaged on beamline ID19 at the ESRF (European Synchrotron Radiation Facility, Grenoble, France). The principle setup is depicted in Figure 5.14. An isotropic voxel size of 10.1 µm and a field of view of 6.06×6.06 mm^2 was selected. The energy was set to 26 keV with a bandwidth of $\Delta E/E$ of 10^{-4} using a double Si-crystal monochromator set to reflect in the vertical plane. The samples were mounted on a goniometer for high precision translation and rotation inside the

monochromatic white beam. For 1600 angles (Figure 5.16 a) of view, radiographic images were recorded.

Calibrated 3D images of the tissue degree of mineralization (*DMB*) were then obtained by applying an exact tomographic reconstruction algorithm (Salome et al. 1999), and by converting the local grey levels of the voxels of the 3-D volume ($600 \times 600 \times 650$ pixel) to volumetric tissue mineralization expressed as gcm^{-3} of hydroxyapatite crystals (Figure 5.16 b), as detailed in (Nuzzo et al. 2002b).

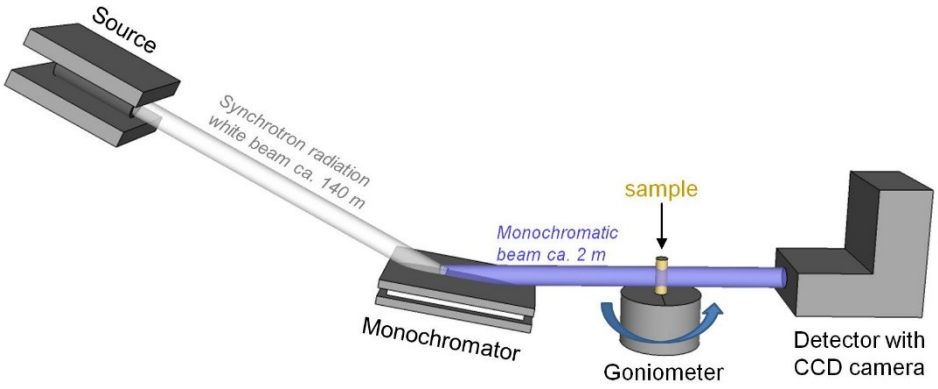

Figure 5.14 Synchrotron setup at the ESRF. Multimonochromator selects a single energy from the synchrotron radiation white beam. Sample is mounted on a Goniometer for rotations. At 1600 angles the projections are recorded using a detector system with a CCD camera. Adapted from Salome et al. (1999) and Pacureanu et al. (2012).

5.2.3.2 SRμCT image and data processing

In order to site-match the SAM and SRμCT data, several post processing steps were necessary. In the first step, the central axis of the cylinders were determined automatically by fitting a line to the centre of mass of each binarized and pore filled z-slide (Figure 5.16). Filling the pores of each z-slide consisted of a stepwise procedure using morphological operations. Each slide was dilated, first to close peripheral pores, second, Matlabs (MATLAB® 7.1, The MathWorks Inc., Natick, MA, 2000) image processing toolbox was used to fill these pores. Finally, the images were eroded. The kernel size was the same for dilation and erosion. However, for each sample an individual kernel size was manually selected in order to ensure perfect filling. Binarization was done by implementing an adaptive threshold as described by Lakshmanan et al. (2007) (Figure 5.15). The cylinders were then rotated and translated to align the central cylinder long axis with the coordinate z-axis.

Finally, the surface of the *DMB* volumes was derived. Binary masks for both the volumetric and surface data were created by using the adaptive threshold procedure. These maps were used to calculate cortical porosity (*Ct.Por*) by

$$Ct.Por = \frac{B - B_{por}}{B} \qquad 5.6$$

In equation 5.6, B stands for bone volume including pores and B_{por} for the volume of the voids. To estimate the average *DMB* and to reduce effects of partial filled volumes (pixel), the binary maps were further eroded (1 pixel kernel size). In the 3D case, a 3D morphological operator using a ball shaped kernel of radius 1 voxel was implemented.

All image processing steps were implemented using Matlab in conjunction with image processing toolbox (MATLAB® 7.1, The MathWorks Inc., Natick, MA, 2000).

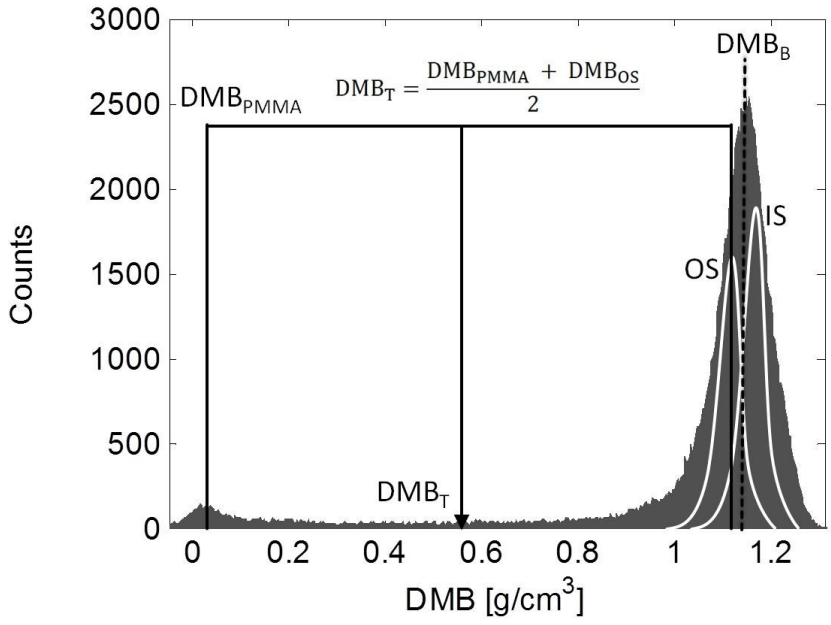

Figure 5.15 Adaptive threshold procedure. The threshold for the *DMB* distribution (DMB_T) was calculated as the mean between the *DMB* of PMMA (DMB_{PMMA}) and *DBM* of the osteonal tissue (DMB_{OS}). DMB_{OS} was estimated by $DMB_{OS} = DMB_B$ -std(DMB_B).

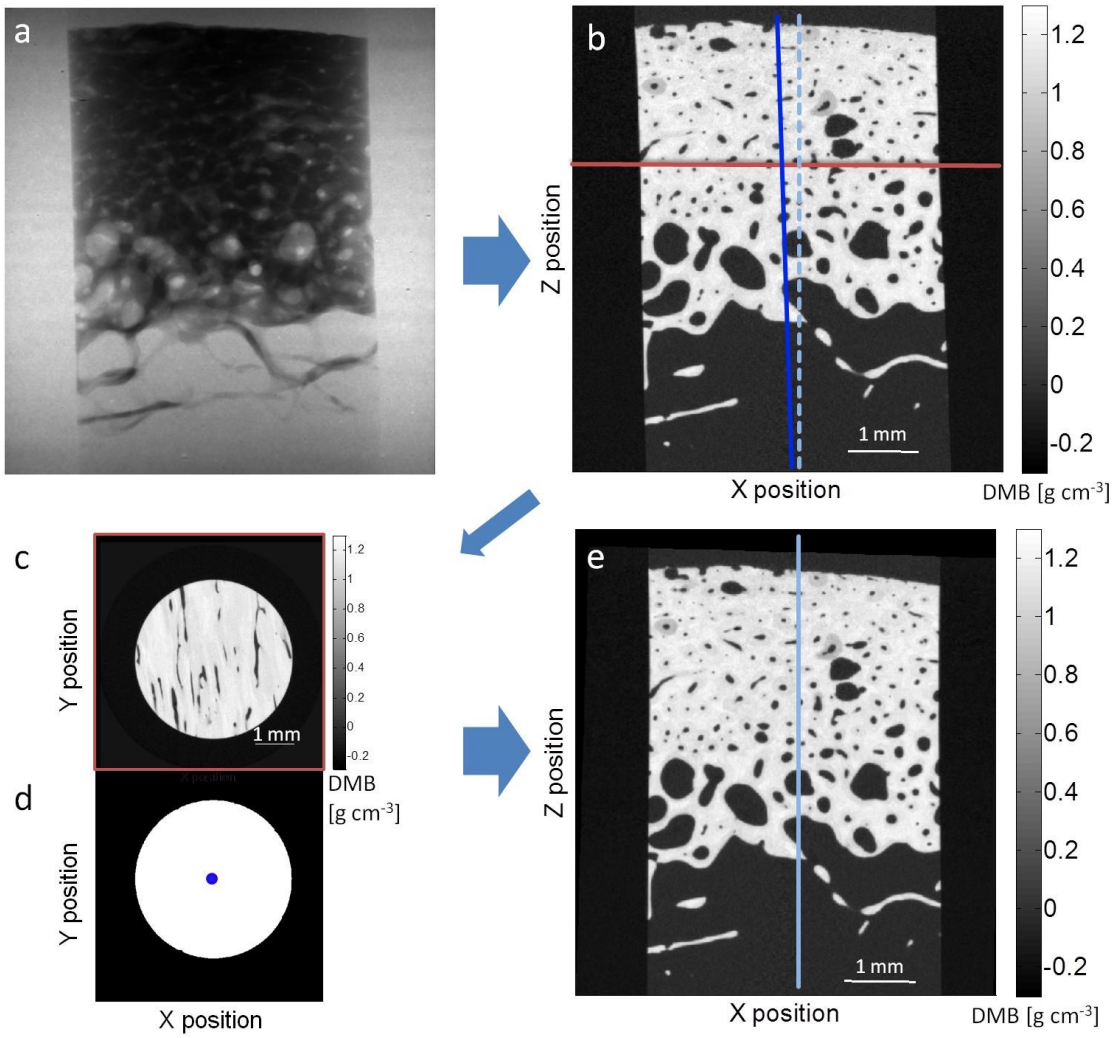

Figure 5.16 Steps for 3D reconstruction and post processing of volumetric data. (a) Single projection (N=1600) were 3D reconstructed using a filtered backprojection algorithm. (b) However, some of the resulting cylinders were oblique. This was corrected for by using a 3D transformation algorithm by fitting a line (dark blue line in b) through the centre of mass (dark blue dot in d) of each z-slice (c). Finally a calibrated and with the coordinate system aligned volumetric data of *DMB* was generated (e).

5.2.4 FDTD Simulations

5.2.4.1 Simulation Setup

In the studies of Rohrbach et al. (2010) and Grimal et al. (2013b) a quantitative ultrasound transverse transmission technique at the hip (Barkmann et al. 2010b) was simulated following Grondin et al. (2010) in the framework of linear elasticity and assuming a lossless propagation

medium. A FDTD code as described in chapter 5.1.4.1 was used. The description of the settings can be found in the publications of Rohrbach et al. (2010) and Grimal et al. (2013b).

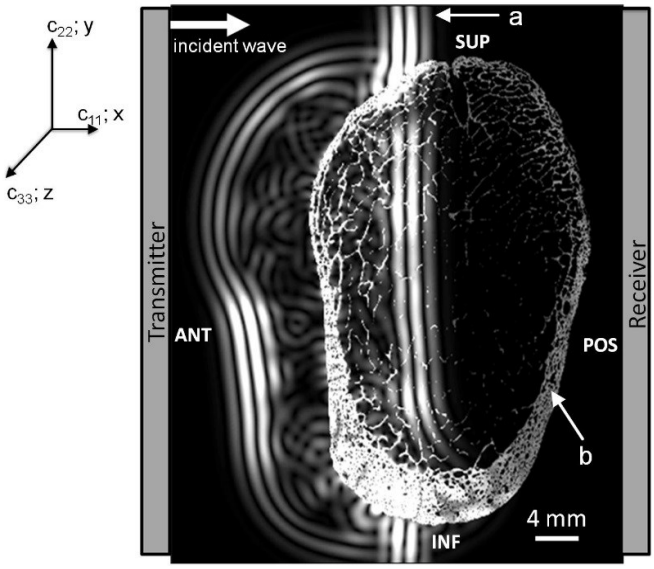

Figure 5.17 Simulation setup. A plane wave is emitted by a transmitter and send through a femoral neck cross section measured with SAM and is detected by a receiver. (a) wave send thorough water, (b) cortical bone model.

A two-dimensional numerical experiment (Figure 5.17) was considered where a plane wave emitted by a virtual single-element transducer is incident on a bone model. The direction of propagation, which is approximately the anterior-posterior direction (parallel to x direction Figure 5.17) of the femoral neck, was chosen consistent with easy *in vivo* accessibility of the neck with ultrasound as demonstrated by Barkmann et al. (2010b). At the opposite (posterior) side of the bone model, a single element receiver of 48 mm in height was placed. The diameter was selected to be larger than the largest diameter of the bone models.

5.2.4.2 SAM based mechanical modelling of bone

The elastic coefficients in c_{33} direction were estimated from the cross sectional scans (Fd_3 Table 5.1) as described in section 5.1.3.

For the simulation studies, an elastic tensor and the density are required to precisely model the tissue. Cortical bone was assumed to be transversely isotropic with the longitudinal direction as the axis of symmetry. Thus, the material properties are fully described by five independent stiffness coefficients of the stiffness tensor c_{ij} and its density. Note however that the simulations were 2D with the wave polarization in the isotropy plane (y-x, Figure 5.17).

Under this condition, only two independent coefficients (i.e. c_{11} and c_{44}) are required for the simulation.

The bone models included a complete description of the elastic behavior and mass density of the bone. The fluids and soft tissues filling the pores (porosity mask) and the medullar cavity were allocated elastic properties and density close to those of water (Kubo et al. 2011), i.e., the bulk modulus, shear modulus and density are respectively 2.25 GPa, zero, and 1000 $kg.m^{-3}$ (Grimal et al. 2013b).

SimSonic permits the definition of only 255 different material properties. Therefore the estimated C_{ij} and ρ_{tissue} for each coordinate point in the models were mapped into the range of 0 to 255 and the actual values of C_{ij} and ρ_{tissue} were stored in a lookup table.

The elastic coefficients in the bone long axis (c_{33}) were derived following the steps described in chapter 5.1.2.2 and 5.1.3 using equation 5.5. The remaining coefficients were derived using a micro-mechanical model proposed by Hellmich et al. (2004), which estimates the stiffness tensor C_{ij} as a function of the volume fractions of the three elementary constituents water (vf_{H2O}), collagen (vf_{col}) and hydroxyapatite (vf_{HA}). The sum of the volume fractions is necessarily one. Raum et al. (2006a) (eq. 10 of that paper) found that the ratio vf_{col}/vf_{H2O} is highly correlated with the variation of vf_{HA} ($R^2 > 0.99$). With this assumption, the Hellmich model is fully predicted by vf_{HA}

$$C_{ij} = f_H(vf_{HA}) \tag{5.7}$$

where f_H denotes the Hellmich model. Finally, the mass density of the bone matrix was obtained using the well-known relation

$$\rho = \frac{Z^2}{c_{33}} \tag{5.8}$$

5.2.4.3 Artificial bone models of decreasing complexity

The model of each femoral neck cross-section, which was directly derived from SAM measurements without modifications, is referred to as the S_0-type model. It accounts for the sample overall shape, microstructure, cortical porosity and heterogeneous matrix elasticity and density. The numerical simulations of wave propagation based on S_0-type models are as realistic as possible, being based on state-of-the-art quantitative imaging techniques of bone properties. In order to determine which bone characteristics have a significant impact on the transmitted ultrasonic signal, four other model-types were obtained by progressive simplification of the initial S_0-type model (Figure 5.18 and Table 5.3). Model-type S_1 was derived from S_0 in order to assess specifically the impact of the trabecular compartment. S_1 was obtained by removing the trabecular bone and replacing it by water (Figure 5.18 b), all cortical characteristics remaining identical for S_0 and S_1.

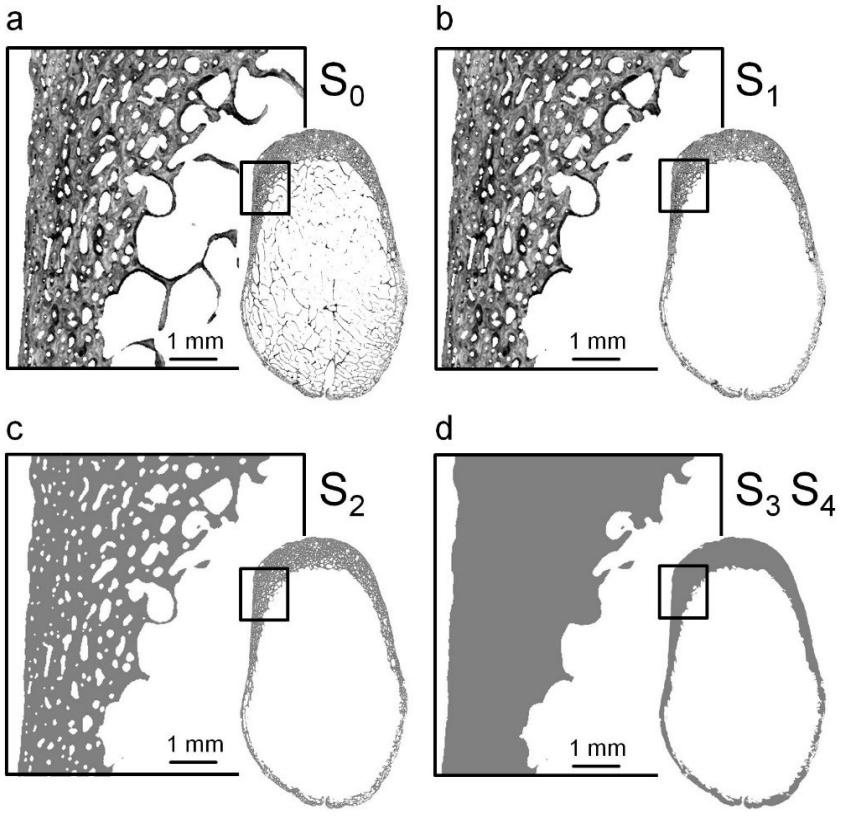

Figure 5.18 Illustration, for one of the nine femoral neck cross-sections, of the five bone model-types constructed based SAM data. See the description of the models in Table 5.3. The gray levels in S_0 and S_1 represent impedance values which were converted to stiffness values as described in the text; light and dark grays correspond to large and low impedance values; respectively.

The aim with model-type S_2 was to assess the effect of the heterogeneous spatial distribution of the tissue matrix elasticity. S_2 was identical to S_1 except that the matrix elasticity was no

longer heterogeneous: The average elasticity of each sample replaced the point dependent elasticity (Figure 5.18 c).

The effect of porosity on *TOF* was investigated with model-types S_3 and S_4 in which the pores were not modelled explicitly (Figure 5.18 d). In S_3, the cortical shell was considered as being a non-porous homogeneous material with properties identical to those of the cortical tissue defined in S_2, that is, all the points of the cortical shell (inside and outside the porosity mask) had the same stiffness and density. In contrast, the cortical shell in S_4 was made out of a homogeneous material whose properties were "effective" properties defined to account for the presence of pores. Cortical bone was regarded as a two-phase composite material made of a mineralized matrix (transversely isotropic as described above) pervaded by infinitely long cylindrical pores. The effective elasticity tensor was obtained by using the Mori-Tanaka homogenization method (Mori and Tanaka 1973). Effective elasticity was calculated for each bone using the corresponding porosity and elasticity derived from the SAM measurement. The effective density in model-type S_4 was calculated as the arithmetic average of matrix and water densities.

The procedure is described in the publication of Rohrbach et al. (2010) and Grimal et al. (2013b).

Table 5.3 Description of model-types which serve as a basis for the simulation of ultrasound propagation in individualized femoral neck models. Nine individualized models of bone samples pertaining to each model-type were constructed from acoustic microscopy data. See illustrations Figure 5.18.

Model-type	Description
S_0	Reference model: detailed description of microstructure and elastic heterogeneity with resolution 23 µm constructed after the SAM image. This model describes: cortical and trabecular bone; microstructure in the cortical shell (vascular porosity); stiffness heterogeneity of the mineralized matrix
S_1	Identical to S_0-type with the trabecular tissue removed
S_2	Identical to S_1-type with the mineralised matrix properties homogenized (averaged)
S_3	Identical to S2-type but the pores are also allocated the averaged matrix properties
S_4	Mechanical properties are homogeneous in the cortical shell. These properties are obtained through homogenization of pores and matrix properties with the Mori-Tanaka method.

5.2.4.4 Assessment of the sensitivity to variation of material properties

Another set of FDTD simulations was conducted for three cross-sections (S_2-type models) in order to assess the sensitivity of *TOF* to physiological variations of porosity (*Ct.Por*) and

mineralized matrix elasticity ($Ct.c_{33}$) (Bousson et al. 2004; Fratzl-Zelman et al. 2009), independently of variations of cross-sectional sample shapes (Rohrbach et al. 2010; Grimal et al. 2013b). Only independent variations of *Ct.Por* ("porosity" data set) and $Ct.c_{33}$ ("elasticity" data set) were considered. To obtain the "porosity" data set, *Ct.Por* was increased and decreased stepwise by dilation and erosion of pixels starting from the measured porosity mask, while $Ct.c_{33}$ was set to its measured value at each point of the cross-sections (Figure 5.19 e-h). To obtain the "elasticity" data set, $Ct.c_{33}$ was increased and decreased in steps starting from the measured value, while the porosity mask remained unchanged (Figure 5.19 a-d). Numerical simulations were performed for each cross-section of the "porosity" and "elasticity" data sets and arrival time (*TOF*) was calculated. For each cross-section, the variations of time-of-flight (ΔTOF), with respect to the non-modified model, associated with variations of porosity ($\Delta Ct.Por$) and matrix stiffness ($\Delta Ct.c_{33}$) was assessed. The influence of porosity variations (respectively, matrix stiffness) on the acoustic response was quantified with linear regressions of ΔTOF versus $\Delta Ct.Por$ (respectively, $\Delta Ct.c_{33}$) using the "porosity" dataset (respectively, the "elasticity" data set).

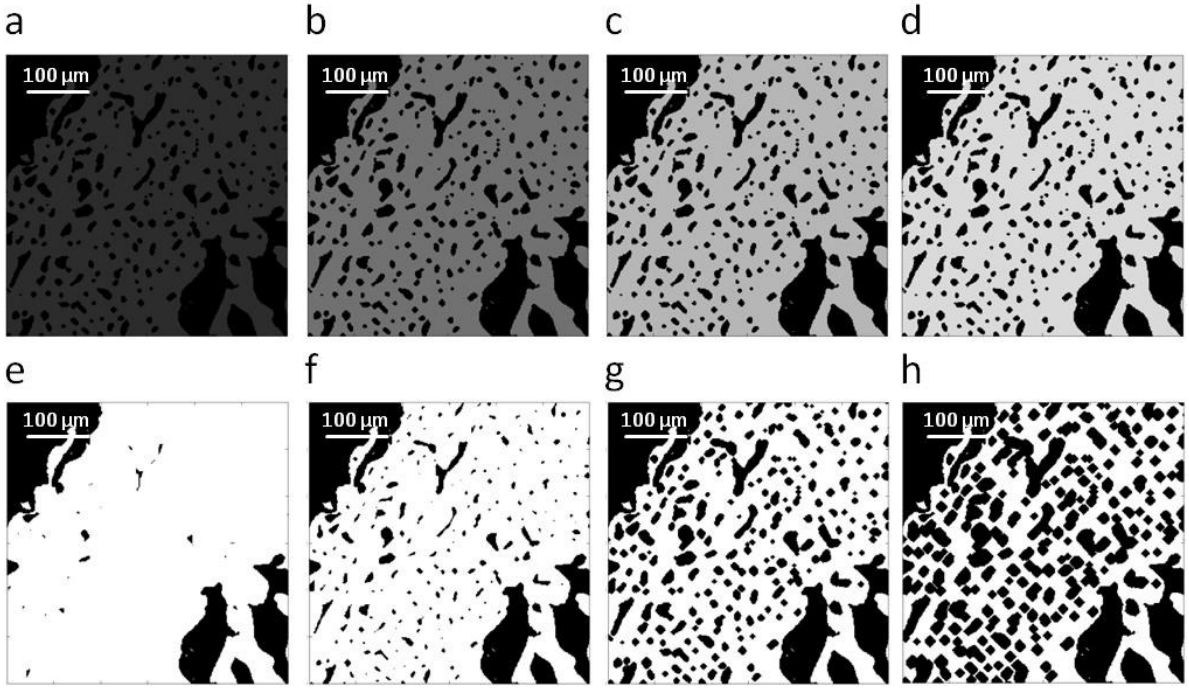

Figure 5.19 An example of one specimen used for the assessment of the sensitivity to variations of material properties. *Ct.c*$_{33}$ (a-d) and *Ct.Por* (e-h) have been stepwise modified independently, i.e. (a-d) had constant porosity (*Ct.Por* = 18.7 %) and (e-f) had constant elasticity (c_{33} = 37.7 GPa). Only the minimum and maximum variations of the data are shown with (a) c_{33} = 16.7 GPa, (b) c_{33} = 29.7 GPa, (c) c_{33} = 46.7 GPa, (d) c_{33} = 67.7 GPa, (e) por = 4 %, (f) por = 10 %, (g) por = 25 % and (h) por = 40 %.

5.2.5 TOF_{FAS} with respect to the long axis of the femoral neck

From one donor of data set Fd_3, three sections were measured along different locations at the femoral neck (chapter 5.2.1.2, Table 5.1) which allowed the relation of the femoral neck long axis location with TOF_{FAS}. In total, four regions were assessed which were close to the trochanter (F.trochanter, Figure 6.10 d), two sites of the femoral neck center (F.centre1, Figure 6.10 e, F.centre2, Figure 6.10 f) and finally the site closest to the femoral head (F.head). In order to simulate variations of the positioning of the samples as it would occur in *in vivo* measurements, the major axis of the models were slightly rotated in four steps by 5, 10 and 15 degrees in both directions (Figure 5.20). This setup resulted in seven simulations for each location. The simulation setup including transducer geometry and spacing was kept the same as in the simulations described in chapter 5.2.4.1. The distance between each measurement site in the femoral neck was not equally spaced. F.trochanter and F.head were approximately 1 cm away from the inner parts (F.centre2 and F.centre1) whereas the distance between the two inner parts was only a few millimeters caused by the central cut of the femoral neck and subsequent grinding and polishing (see chapter 5.2.1.2).

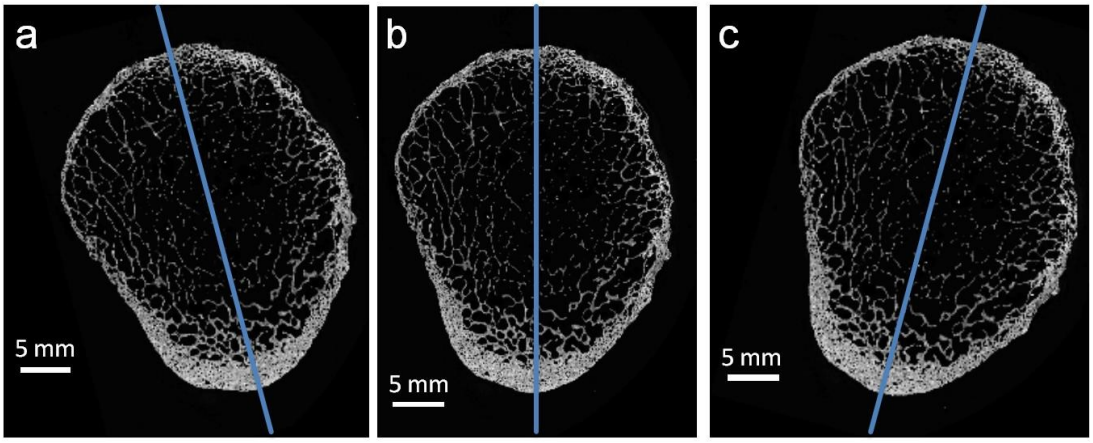

Figure 5.20 Rotation of the central part of the sample which provides three locations along the long axis. To simulate measurement variations due to positioning of the subjects the samples were slightly rotated in three steps in each direction (maximum of 15 °). The figure shows (a) rotation in -15 °, (b) origin and (c) rotation in 15 °.

5.2.6 Statistics study I

5.2.6.1 Evalutation of micro elastic parameters derived from SAM and SRμCT

Linear, non-linear and multivariate regression analyses and ANOVA followed by post-hoc multi-comparison Tukey-Kramer tests, were used to evaluate anatomical influences on the derived tissue properties.

Differences between the tissue types (trabecular and cortex), and skeletal sites were evaluated by one-way analysis of variance (ANOVA) followed by post hoc multiple comparison Tukey–Kramer tests. The significances of difference in cortical porosity and elastic coefficient between the quadrants of the femur neck cross-sections were evaluated using the one-way ANOVA with post hoc Tukey Kramer multiple comparison tests. The association between the impedance values and porosity was assessed by linear regression analysis.

5.2.6.2 US simulations of bone models relating complexity

Post-processing of simulations output yields nine time-of-flights (cross-sections $i = 1 \cdots 9$) $TOF_k\ (i)$ for each model-type ($k = 0 \cdots 4$). Several quantities were calculated to gain insight into the relationships between the model characteristics and the acoustic response $TOF_k(i)$:

- For each cross-section, the difference between the reference time-of-flight TOF_0 obtained for the S0-type model, and TOF_k obtained for another model-type,8 was calculated using:

$$\delta TOF_k(i) = TOF_k(i) - TOF_0(i), i = 1 \cdots 9;\ k = 1 \cdots 4;. \quad 5.9$$

- Student t-tests were performed to test whether the mean of each of δTOF_k $(k = 1 \cdots 4)$ is significantly different from zero;
- The statistical relationships between $TOF_0(i)$ and the output of one of the simplified models are summarized in the equations:

$$\delta TOF_k = \delta Mk \pm ICk;\ k = 1 \cdots 4;. \quad 5.10$$

  where $\delta Mk = \frac{1}{9}\sum_{i=1}^{9} \delta TOF_k(i)$ is group-averaged a bias and ICk is the 95 % confidence interval which represents a random fluctuation due to differences in geometry and material properties distribution in the cross-sections (inter-sample variability);

- Linear regressions between TOF_0 and TOF_k $(k = 1 \cdots 4)$ were calculated.

5.3 Study II

5.3.1 Specimens:

5.3.1.1 Rat osteotomy model

In the studies of Preininger et al. (2012b) and Rohrbach et al. (2013) a rat osteotomy model was used for investigations of monitoring fracture healing. The sample set and preparation were published in these studies (reprinted in the present work with permission © Journal of computer assisted tomography). From a larger cohort study 15 representative Sprague-Dawley rats at the age of 12 months, had been selected. The animals received a double osteotomy in the femoral mid-shaft (2-mm gap) that was stabilized with an external fixator Figure 5.21.

Without further treatment, the 2-mm osteotomy (OT) leads to a delayed healing. A broad range of different healing stages after 6 weeks of consolidation was achieved by different treatments, i.e. implantation of progenitor cells, BMP2 or blood clots into the OT gap. The animal experiments were carried out following the protocol described in Preininger et al. (2012a). µCT scans were conducted after 6 weeks of consolidation. Afterwards, the rats were sacrificed and the OT femora were harvested for histological analysis. All animal experiments were carried out according to the policies and principles established by the Animal Welfare Act. The design of the animal surgeries was critically reviewed and approved by the local legal representative (Landesamt für Arbeitsschutz, Gesundheitsschutz und technische Sicherheit, Berlin: G 0428/08).

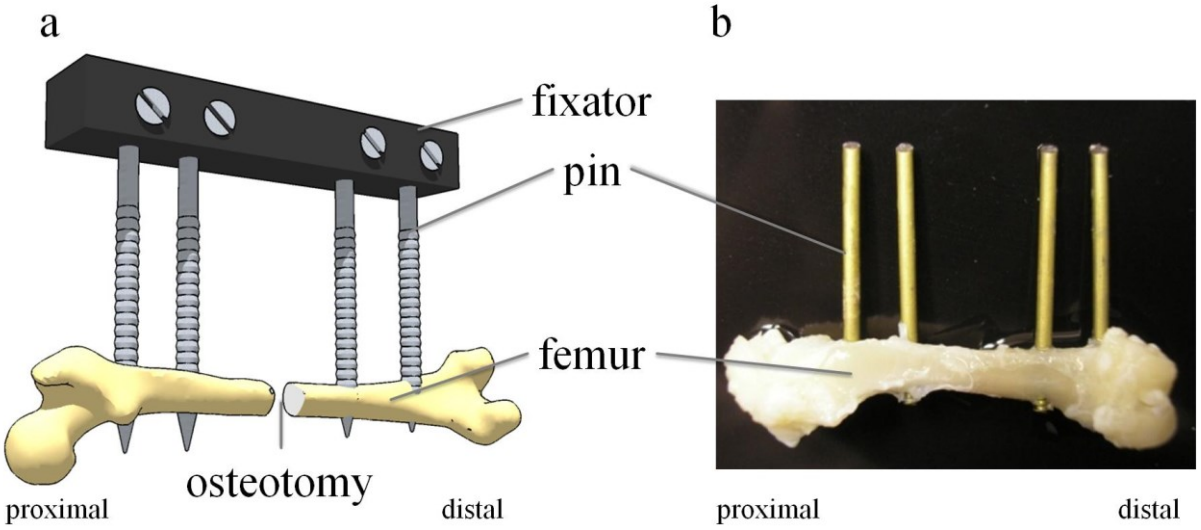

Figure 5.21 (a) Schematic illustration of rat osteotomy fixation. (b) an intact femur without osteotomy. Fixator and soft tissue was removed.

Specimen treatment and preparations including surgeries, animal supervision, animal sacrifice was conducted by a medical surgery and are described in detail in the work of Preininger et al. (2012a)

5.3.1.2 Staining of rat osteotomy models

Embedding, histological staining and analysis of the rat femora were conducted within a larger cohort study (Preininger et al. 2012a). In contrast to the human samples of the other studies, some of the rat specimens were decalcified and embedded in paraffin. The procedure consists of fixation in normal buffered formaldehyde decalcification in EDTA (42 days at 37 °C), dehydration in ethanol and xylol, and embedding in paraffin (Preininger et al. 2012a).

BMP group animals were embedded in PMMA (Technovit1 9100, Heraeus Kulzer) using the procedure described in chapter 5.1.1. Afterwards, 4 µm sections were cut in the plane of the K-wire ducts of all femora using a microtome. All sections were stained with Movat Pentachrome according to the protocol of Table 5.4. The staining allows differentiation between fibrous tissue (light green-blue), cartilage (deep green), and bone (yellow) (Preininger et al. 2012b).

Table 5.4 Protocol Movat Pentachrome staining

	step and involved solution	**time duration**
1	Methylmethacrylate (MEA)	3x30 min
2	decreasing ethanol series (100 %, 96 %, 80 %, 70 %)	2 min each
3	aqua dest.	2 min
4	1 % alcian blue	10 min
5	washing in water	5 min
6	alkaline alcohol	60 min
7	washing under running tap water	10 min
8	aqua dest.	immerse
9	Hematoxylin solution	10 min
10	washing under running tap water	15 min
11	washing in aqua dest.	shortly
12	Acid Fuchsin	5 min
13	acetic acid (0.5 %)	shortly washing
14	phosphotungstic acid (5 %)	20 min
15	acetic acid (0.5 %)	2 min
16	3 times in 100 % ethyl alcohol	
17	100 % ethyl alcohol	2 min
18	xylol	2 x 5 min
19	Vitro-Clud ®	

5.3.1.3 Rat osteotomy healing stages

The different treatment of the rat models led to different healing outcomes and thus enabled the separation of the animals into three different groups (N=5 animals / group). The selection was based on the histology staining. Depending on the type of tissue predominantly found within the OT gap, the specimens were assigned to one of the following healing phases: A – fibrous connective tissue; B - hyaline cartilage and fibrous connective tissue; C - woven bone.

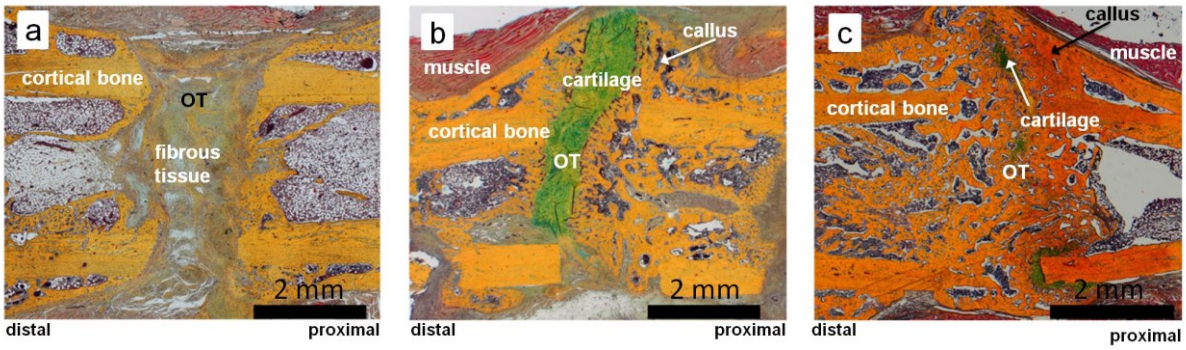

Figure 5.22 Representative Movat's Pentachrome stained tissue sections of the three healing stages. (a) In the early healing stage (group A) the tissue in the OT gap consists mainly of fibrous connective tissue. (b) In group B hyaline cartilage synthesis is present. (c) In the late healing stage (group C) the entire callus has been mineralized. (reprinted with permission from Preininger et al. (2012b) © Journal of computer assisted tomography)

Within the study of Preininger et al. (2012), all three groups were compared using two different µCT methods, a novel moment based approach and a standard procedure (chapter 5.3.2). Whereas in the study of Rohrbach et al. (2013) only group A and B were compared because the more advanced stage of group C did not allow an ultrasonic characterisation due to high attenuations.

Classification of the samples into the three healing groups was done by an experienced histomorphometrist in collaboration with Preininger et al. (2012a).

5.3.2 Micro-Computed Tomography

The rat samples were scanned *in vivo* prior to sacrifice using µCT imaging. Scanning was conducted within a larger cohort study by Preininger et al. (2012a). However, the following µCT data evaluation was conducted in collaboration as part of the present work. It was published by Preininger et al. (2012b) and has been reprinted in the present work with permission (© Journal of computer assisted tomography).

5.3.2.1 µCT setup

The osteotomized femora were imaged using a vivaCT 40 (Scanco Medical AG, Switzerland) at a voltage of 55 kVp and a current of 145 µA. The exposure time for each projection was set to 150 ms. An isotropic voxel size of 35 µm was selected for acquisition and reconstruction. Linear attenuation data were scaled by multiplying by 4096 and stored as 16-bit signed integer values, which corresponds to the native units of the CT manufacturer. Hereinafter, these integer values will be referred to as gray scale or integer values.

5.3.2.2 Conventional Threshold Based Evaluation

A cylindrical Volume of Interest (VOI) of 4 mm total length was defined, covering the 2-mm gap region and 1 mm in both proximal and distal directions of the original osteotomy gap. Callus formed around the fixator pins was excluded from the analysis. A fixed global threshold value that segmented mineralized callus and cortical tissue from soft tissue was defined as 50 % of the mean integer value found in intact cortical bone tissue. The proper segmentation was verified by visual inspection of ten randomly selected 2D-slices from each sample. Afterwards, the callus tissue was segmented from the adjacent cortical tissue by manual polygon contouring of the interface in transverse 2D sections. From the segmented 3D callus data within the VOI, the following parameters were calculated, as described by Mehta et al. (2010): bone volume (BV in mm^3), total volume (TV in mm^3), bone volume fraction (BV/TV in %), bone mineral content in the segmented callus tissue (BMC_{BV} in mg HA), and BMC in the total callus volume (BMC_{TV} in mg HA).

The procedure was conducted during the study of Preininger et al. (2012a).

5.3.2.3 Moment Based Evaluation

In each 3D reconstructed µCT VOI the pin axes were detected and the VOI was transformed by translation and rotation operations in order to align pin axes with the *xz* plane. Figure 5.23 shows representative *xy* grayscale slices and corresponding histograms. Each histogram exhibits a peak at a value of about 5000 corresponding to background and soft tissue pixels (Figure 5.23 C). A broader distribution between 5000 and 25000 corresponds to pixels filled with mineralized tissues.

A Gaussian function was fitted to the background peak and the fitted curve was subtracted from the histogram. The remaining bimodal distribution was composed of mineralized

cortical and callus tissues, as illustrated in Figure 5.23 D, where two Gaussian distributions were fitted to these distributions. However, since callus and cortical tissues cannot be assumed to be normally distributed, the j^{th} order central moments M_j of the entire background-subtracted distributions were evaluated, whereas $j \epsilon \{0,1,2,3,4\}$. A description of the features of these moments is summarized in Table 5.5.

Table 5.5 Description of the moments *Mi* derived from the grayscale histograms.

Image moment	Name	Histogram property
M_0	Area	Number of pixels in the histogram: corresponds to the amount of the mineralized tissue
M_1	Mean	Mean gray value: qualitative measure of the mean degree of mineralization
M_2	Variance	Variance of the gray value distribution: corresponds to the variance of the degree of mineralization
M_3	Skewness	Asymmetry of the gray value distribution: depends on the amount and mineralization of callus and cortical tissues
M_4	Kurtosis	A measure that describes the shape of the gray value distribution, e.g. peaked or flat: depends on the relative amounts and overlap of the distributions of callus and cortical tissues

Subsequently, the variation of M_j was analyzed with respect to the long axis position z. The left and right boundaries of the OT gap were defined as z_l and z_r, respectively. The area under the curve IM_j between z_l and z_r characterizes the OT gap region:

$$IM_j = \sum_{z=z_l}^{z_r} M_j(z) \cdot \Delta z, \qquad 5.11$$

whereas Δz is the slice thickness. The values of the image moments at the locations z_l and z_r approximate the cortical tissue directly adjacent to the OT gap. It should be noted that $M_j(z_l)$ and $M_j(z_r)$ can be influenced by periosteal and endosteal callus formations. The area under a linear function that connects $M_j(z_l)$ and $M_j(z_r)$ is an approximation of a very advanced healing case:

$$A_j = \frac{\left(M_j(z_l) + M_j(z_r)\right)}{2} \cdot (z_l - z_r). \qquad 5.12$$

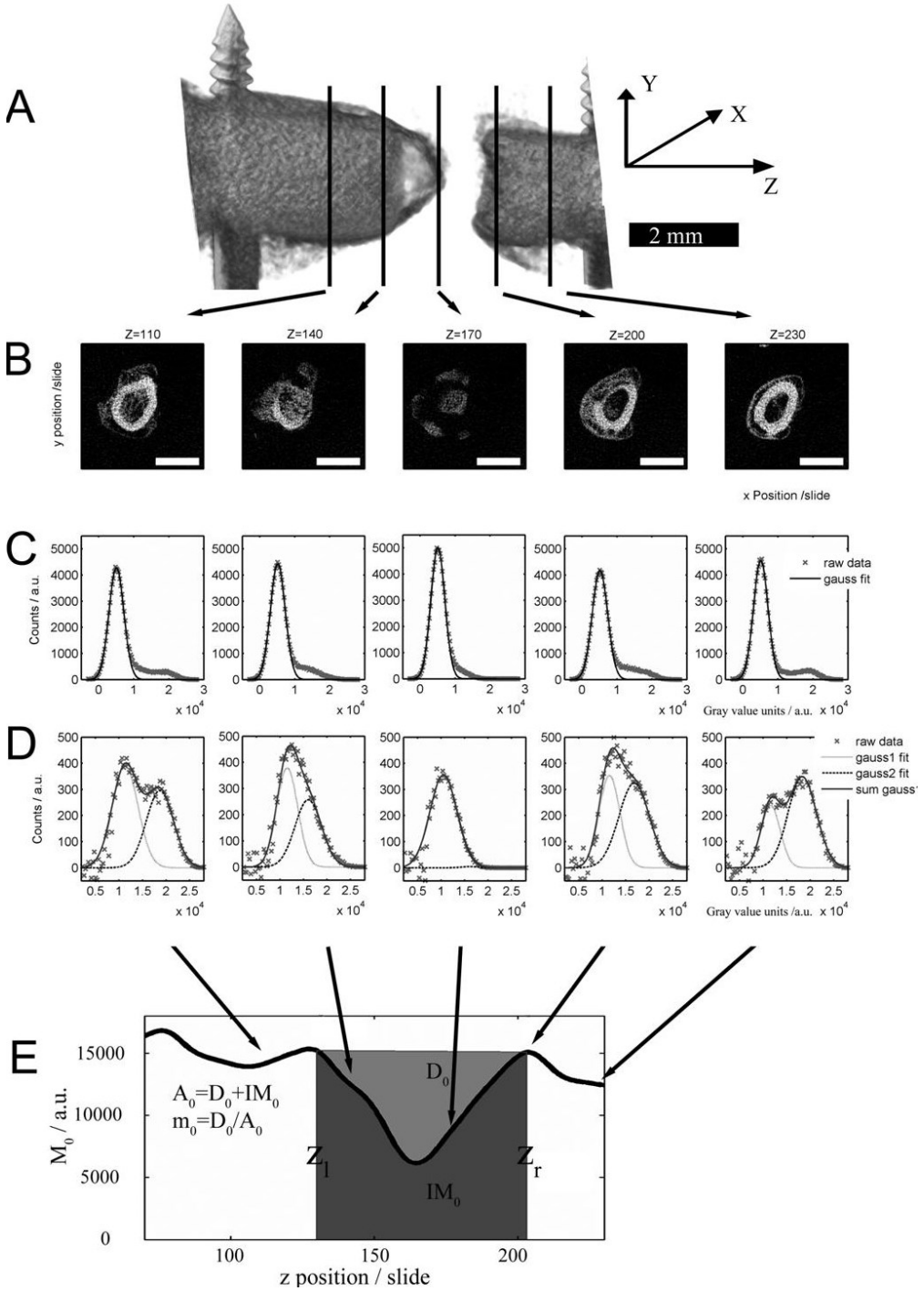

Figure 5.23 Summary of the moment based evaluation method. A volume rendered image shows the pins, cortical and callus tissues and the OT gap (A). Transverse sections, separated by 30 *z*-slices, are shown in (B). The corresponding histograms (C) exhibit a sharp background peak and a broader distribution of mineralized callus and cortical tissues. The background was approximated by a Gaussian profile. The background-subtracted histograms (D) reveal bimodal distributions with low and high gray values corresponding to callus and cortical tissues, respectively (the two Gaussian profiles are fitted to the data for illustration purposes only). The parameters derived from variation of the histogram moments M_j with respect to the long axis *z* are illustrated for j=0 in (E).

The difference of the two areas, $D_j=A_j-IM_j$ characterizes the difference of the actual magnitude of M_j compared to the approximated fully healed osteotomy (Figure 5.23 E). Moreover, to minimize the potential impacts of bone geometry and grey scale calibration, D_j were normalized to the respective A_j and expressed as a percentage:

$$m_j = \frac{D_j}{A_j} \cdot 100. \qquad 5.13$$

The resulting fractions m_j were used for classification of the samples (Figure 5.23 E). Representative profiles of M_0, M_1, and M_2 are shown in Figure 6.18.

Note that an important feature of the parameters m_j is their invariance to linear scaling of the gray value units of the µCT images.

In this study, the osteotomy (OT) boundaries along the z axis were determined manually from sagittal X-ray projections reconstructed from the volume data (not shown). In order to assess the sensitivity of the measured parameters with respect to the selection of the boundary position, the parameter estimations were repeated, while z_l and z_r were varied ± 5 slides from their manually selected positions.

The development of the moment based procedure and its implementation was done in collaboration with Bernhard Hesse and is published in Preininger et al. (2012b) (reprinted in the present work with permission © Journal of computer assisted tomography).

5.3.2.4 Classification

Two different types of classifiers were used in this study, a support vector machine (SVM) and a *k*-nearest neighbour (*k*-NN) classifier.

The SVM method (Cortes and Vapnik 1995) is suitable for two class problems. To extend SVM to multi-class problems, the most common solutions are the strategies "one-against-all" and "one-against-one" (Chih-Wei and Chih-Jen 2002). For this study a simple approach was used consisting of a mixture of both techniques. For each test the outcome of the decision function was counted for each class and the decision was made for the class with the highest count. A linear kernel was used for training.

In order to confirm the results obtained using SVM, a k-NN classifier (Cover and Hart 1967) was utilized, which belongs to the family of non-parametric or instance based classifiers

(Mitchell 1997). The parameter *k* in this approach specifies the amount of neighbours taken into account when classifying an unknown sample. Euclidean distance metric was used in this study and the accuracy of *k*-NN was tested for different $k \in \{1,2,3\}$.

The accuracy of the two classifiers was assessed using an *n*-fold cross-validation. It has been shown that stratified *n*-fold cross-validation with $n = 10$ is better than other methods, e.g. bootstrapping (Kohavi 1995). Due to the low sample number in this study, we decided to use *n* = sample number, which is equal to a leave-one-out cross-validation (LOOCV) (Kohavi 1995).

Accuracy, precision and sensitivity were derived by applying a 3 by 3 confusion matrix (Fieldsend and Everson 2005; Fawcett 2006). Accuracy was defined as the ratio of correctly classified samples and the total amount of samples involved in the classification, whereas sensitivity gives the rate of the worst classified class (Fernandez Caballero et al. 2010).

5.3.3 QUS Transverse transmission fracture healing assessment *in vitro*

5.3.3.1 QUS Setup

QUS measurements at the rat osteotomy models were conducted using the scanning acoustic microscope (SAM200Ex, Q-Bam, Halle, Germany) described in chapter 5.1.2. The system was equipped with two spherically focused 5-MHz transducers (diameter: 15 mm; STT, Richter, Mühlanger, Germany). The -6 dB sound field characteristics (transmit-receive) of the transducers were measured using the wire technique (Raum and O'Brien 1997). The axial and lateral resolutions were found to be 3.77 mm and 0.48 mm, respectively with a focal length of 16.5 mm. The transducers were aligned in a confocal configuration (Figure 5.24). The external bone fixator was mounted to the scanning stage of the microscope such that the callus region was positioned in the focal plane of the transducers. 2D scans of the entire repair zone including the two inner fixation pins were conducted by lateral and axial displacements of the entire bone with a scan increment of 0.1 mm in both directions (Figure 5.24). Two consecutive scans were performed to acquire the transmitted and reflected signals. Each signal was digitized at 100 MS/sec using a 12-bit A/D-card (Gage Compuscope CS12400, Gage Applied Technologies, Inc., Lachine, Canada). Distilled and degassed water at 25 °C was used

as coupling fluid. Preprocessing of the radio frequency signals was done by band-pass filtering using a Chebyshev Type II filter with cutoff frequencies of 0.1 and 10 MHz.

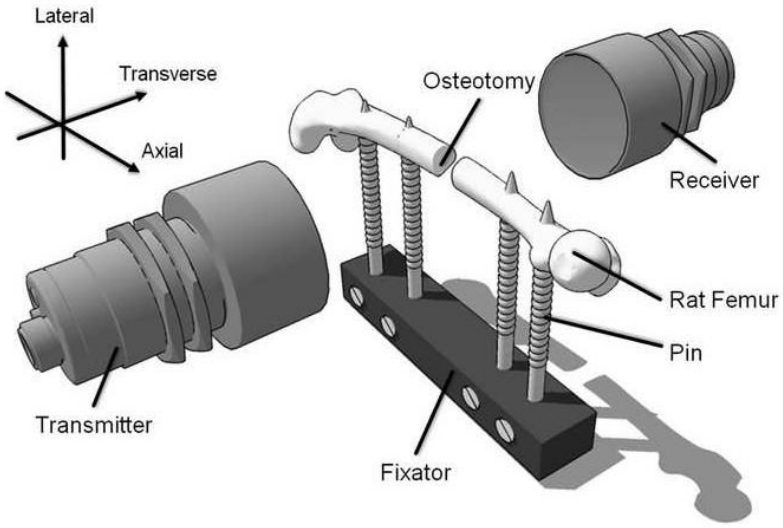

Figure 5.24 Schematic setup of the QUS system. Two spherically focused 5-MHz transducers are confocally aligned. The rat femur with the OT gap is placed in the focal plane. The fixator is attached to the scanning unit of the microscope.

5.3.3.2 Estimation of sample thickness

The propagation path length through the sample (soft tissue and bone) was estimated from the pulse echo measurements. For each cross-sectional scan (transverse-lateral plane, see Figure 5.24) the locations of the surface were detected using a simple threshold method (Figure 5.25. a). An ellipsoidal function was then fitted to the detected surface positions to estimate the boundary on the opposite side (Figure 5.25 b). Position and length of the ellipsoidal axes (l_a and t_a of Figure 5.25 b) were limited in order to have a reasonable tradeoff between variability and smoothness of the 3D data for all specimens. The lateral axis length of the ellipsoid (l_a) was calculated from binarized through-transmission maps. For the binarization a threshold of 90 % of the amplitude of the signals propagated through water was used. An example of a 3D reconstruction is shown in Figure 5.25 (c).

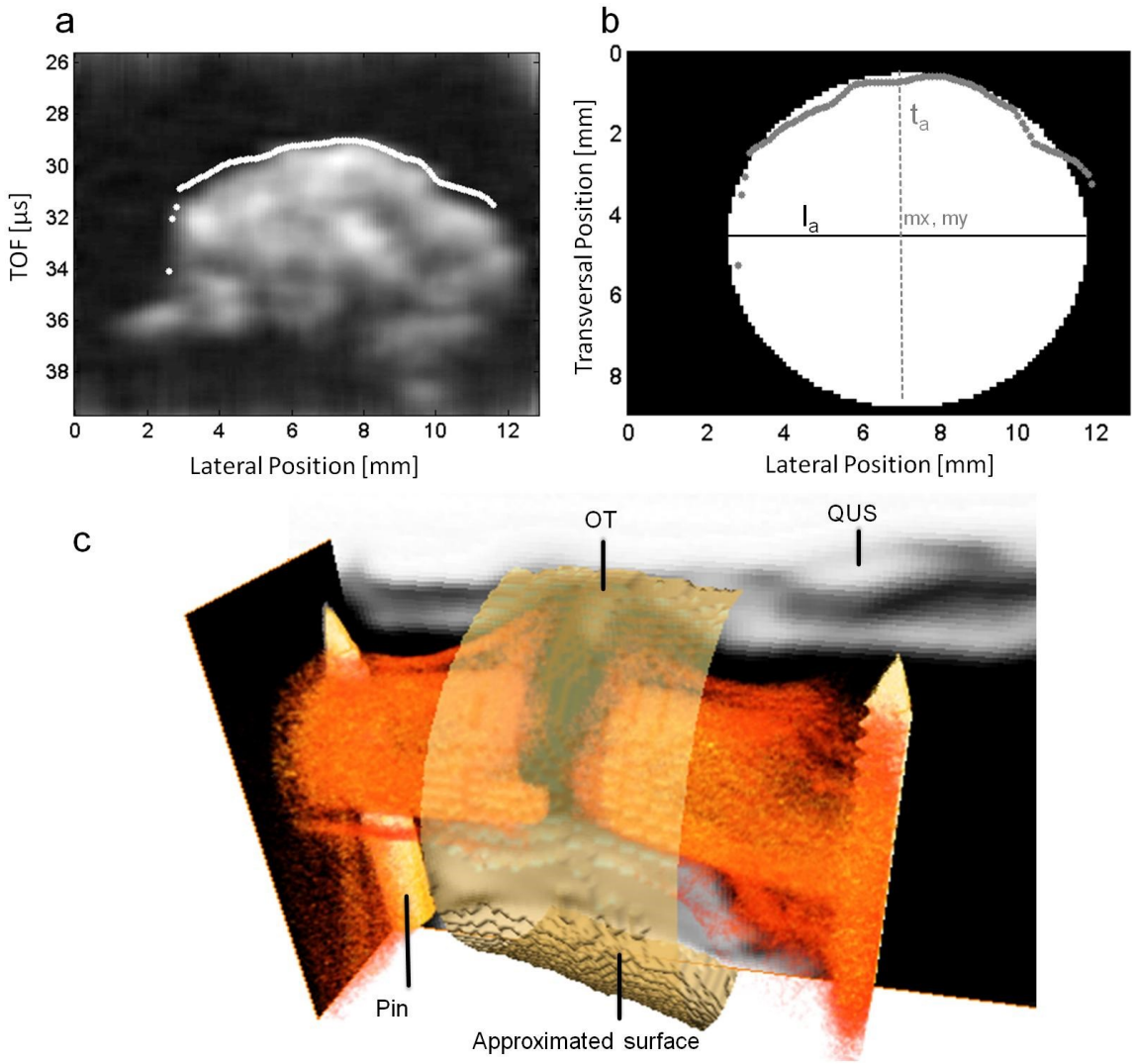

Figure 5.25 (a) Filtered B-mode image (at one axial position). The white dots indicate the detected surface. (b) An ellipse fitted to the surface points (grey dots) approximates the outer soft-tissue boundary of the cross-section. l_a specifies the length of the lateral axis of the sample, t_a the transversal axis and m_x, m_y the centroid of the ellipse. (c) 3D QUS reconstruction (yellow surface) of the outer soft tissue boundary with the superimposed 3D µCT reconstruction of the mineralized tissue (orange). In the background a QUS through-transmission attenuation map is plotted.

5.3.3.3 Parameter extraction and Image processing

Six ultrasonic parameters, i.e. amplitude *U* of the Hilbert-transformed envelope signal (in V), absolute ultrasound attenuation *UA* (in dB), broadband ultrasound attenuation *BUA* (in dB MHz^{-1}), normalized *BUA* (*nBUA* in dB MHz^{-1} mm^{-1}), time of flight *TOF* (in µs) and speed of sound *SOS* (in m/s) were extracted from the transmitted signals in a predefined region of interest (ROI) within the repair zone. A semi-automated procedure was implemented to select

the ROI which determines the OT healing zone. First, a Sobel operator was used to detect edges in the logarithmic amplitude images. The edges were used as a guidance to manually select the boundaries of the OT-gap and the bony edges in the lateral direction. The width of the ROI was set as 1.5 times the initial gap size.

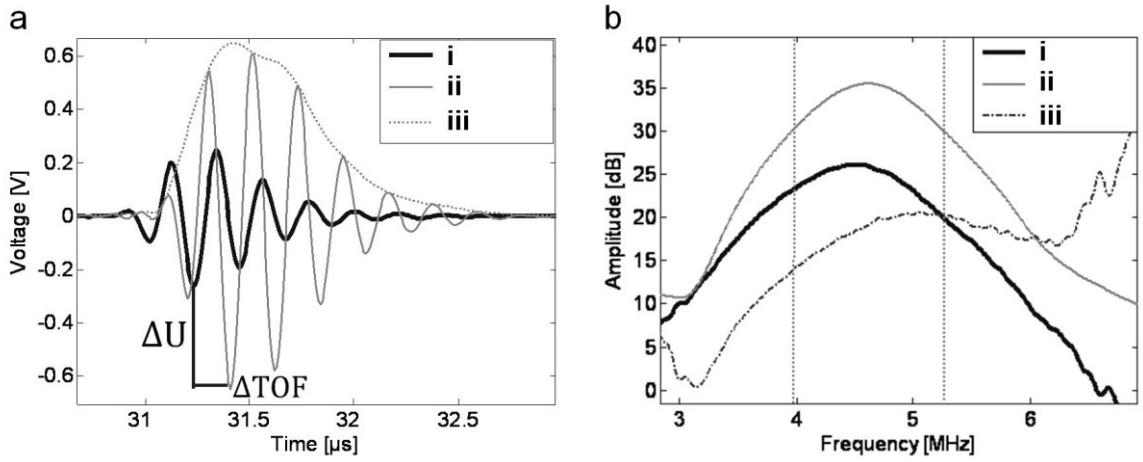

Figure 5.26 (a) Signals transmitted through (i) cartilage and (ii) water. The amplitude *U* and time of flight $TOF_{Hilbert}$ were derived from the amplitude and position of the maximum of the Hilbert-transformed envelope signal (iii), respectively. (b) The power spectral density *A(f)* of the cartilage signal (i) and the reference signal (ii). From the spectral difference (iii) within the -6 dB range (dotted vertical lines) UA and BUA were calculated.

Within the ROIs, maps of all US parameters were computed. The amplitude *U* was derived from the maximum of the Hilbert-transformed envelope signal (Lakshmanan et al. 2007) (Figure 5.26). *UA* and *BUA* were computed from the difference of the power spectra of a reference signal $PS_{ref}(f)$ and the signal *PS(f)*. The reference signal was obtained from scan regions where the sound propagated through water. *UA* was defined as the average difference between *PS(f)* and $PS_{ref}(f)$ within the -6dB range, normalized to the transversal thickness (*l*) of the sample (for *PS* calculation see chapter 4.1.3). *BUA* and *nBUA* were defined as the slope of the difference spectrum without and with normalization to the thickness, respectively. *TOF* was measured using two approaches, i.e. $TOF_{Hilbert}$ corresponds to the time at the maximum of the Hilbert-transformed signal, and TOF_{phase} was determined from the slope of the unwrapped phase spectrum within the bandwidth of the transducer according to formula 4.16 (Raum et al. 2006). *SOS* was then calculated using equation 4.13.

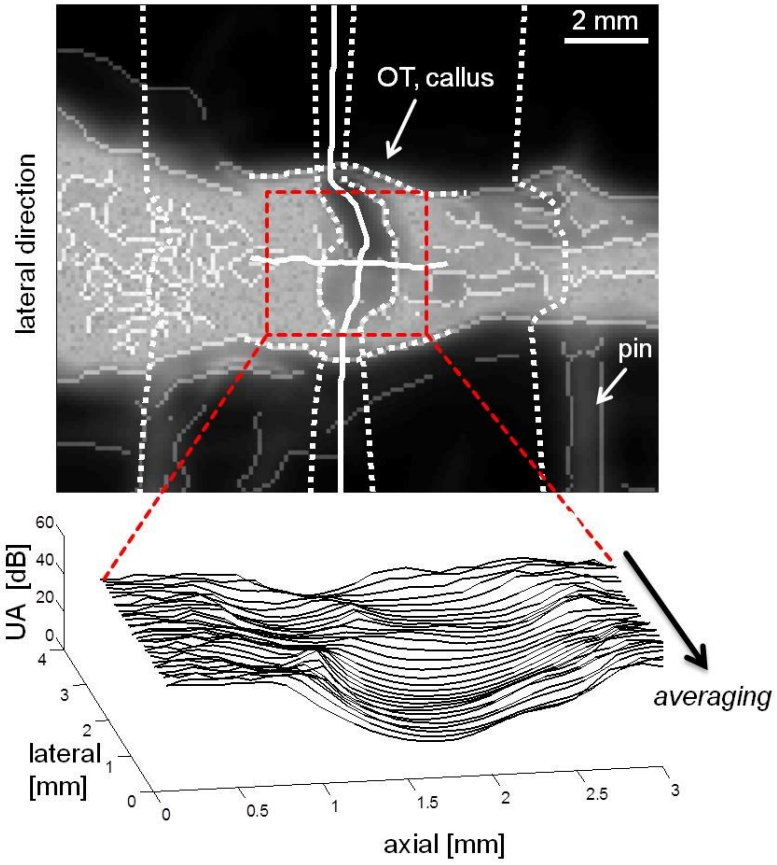

Figure 5.27 ROI selection in a QUS attenuation image. The dotted white lines indicate the manually selected boundaries. The selection was guided by the edges detected using the Sobel operator (grey lines). The white line in the centre of the OT gap indicates the centre between the manually selected ROI's. The sample was taken from group B, thus callus formation is visible. The dotted red square determines the final ROI. The height (lateral direction) of the ROI was calculated by taking 90 % of the distance between the horizontal (axial) bony edges. The lower part of the image illustrates the calculation of the profile. At each lateral position a profile was taken and averaged along that direction.

In addition to the characteristic distribution parameters within the selected ROIs, the changes of properties along the axial direction were assessed by a profile analysis similar to that of the µCT moment based approach (chapter 5.3.2.3). The procedure is illustrated in Figure 5.27 for the *UA* parameter. Briefly, the values within the ROI were averaged in the lateral direction, which results in an axial profile $\overline{UA}_y(z)$ with a characteristic minimum in central region of the OT gap and maxima slightly adjacent to the initial gap boundaries (Figure 5.28). Subsequently, the variation of the profile was analyzed with respect to the long axis position *z*.

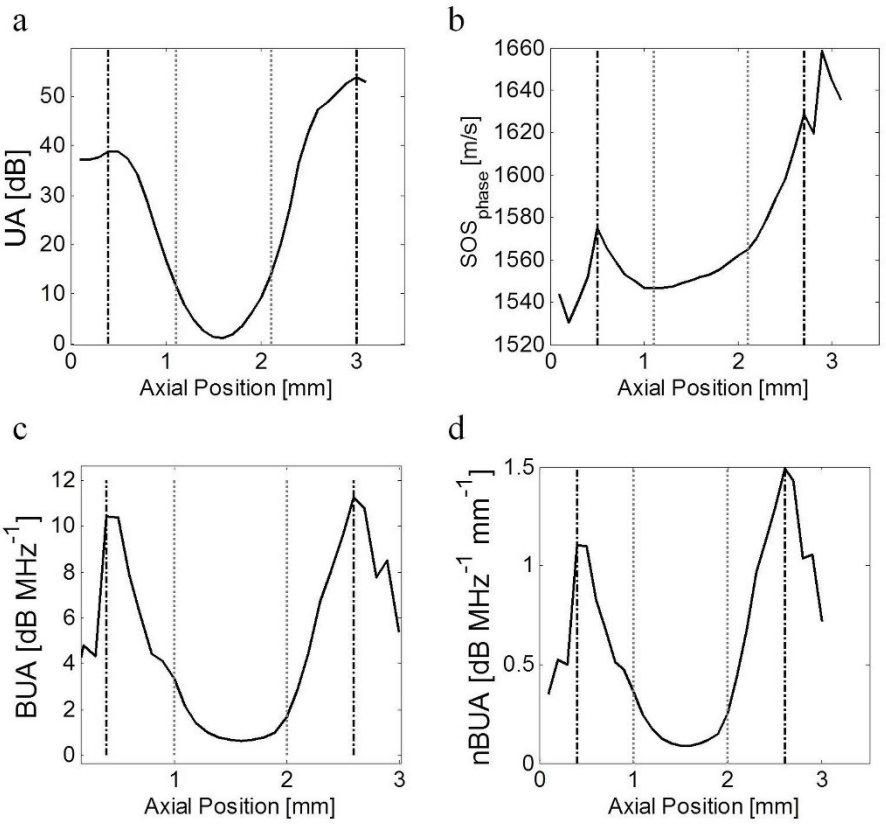

Figure 5.28 (a) Profile plots *UA*, (b) *SOS*$_{Phase}$,(c) *BUA* and (d) *nBUA* of a sample from group A. Regions between the dotted grey lines specify the range used for calculating the median parameters. Dashed-dotted black lines indicate the range used for the profile parameter calculations

The left and right boundaries of the OT gap were defined as z_l and z_r, respectively. The area under the profile curve A_{UA} between z_l and z_r characterizes the OT gap region:

$$A_{UA} = \sum_{z=z_l}^{z_r} \overline{UA}_y(z) \cdot \Delta z,. \qquad 5.14$$

where Δz is the scan increment the axial direction. The area under a linear function that connects $\overline{UA}_y(z_l)$ and $\overline{UA}_y(z_r)$ is an approximation of a very advanced healing case:

$$A_{UA_0} = \frac{\overline{UA}_y(z_l) + \overline{UA}_y(z_r)}{2} \cdot (z_l - z_r),. \qquad 5.15$$

Relative profile changes UA^{PR} were compared between the healing groups.

$$UA^{PR} = \frac{A_{UA_0} - A_{UA}}{A_{UA_0}} \cdot 100,. \qquad 5.16$$

It should be noted that $\overline{UA}_y(z_l)$ and $\overline{UA}_y(z_r)$ can be influenced by periosteal and endosteal callus formations. The positions z_l and z_r (dashed lines in Figure 5.28) were determined by an iterative algorithm that starts at the centre of the OT gap and searches for the first maxima in both directions.

5.3.4 FDTD simulations

Preliminary FDTD ultrasound propagation simulations were conducted in order to validate *in silico* the transverse transmission approach and to build a framework for future *in silico* investigations.

In order to model the bone geometry, cross-sections (lateral-transversal plane, Figure 5.24) of one sample embedded in PMMA of group B were measured using SAM at two different axial positions. The procedure follows the steps and settings described in chapter 5.1.2. Binarized maps were extracted using the adaptive threshold procedure described in 5.1.2.2. The first region was located in the central gap region with mineralized tissue only related to callus tissue (Figure 5.29 a). In the second region callus and cortical tissue were prevalent (Figure 5.29 b).

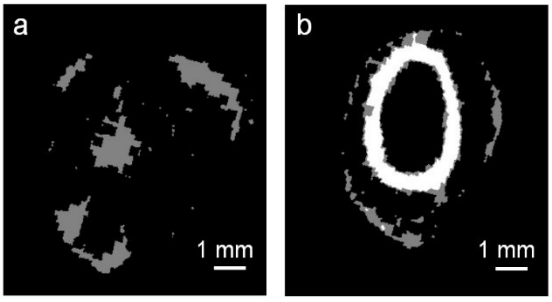

Figure 5.29 Binary maps of cross sections of (a) central gap region only callus tissue, (b) more distal region exhibiting cortical and callus tissue. regions in light grey are callus tissue and white regions correspond to cortical tissue.

In order to derive realistic estimates of the elastic stiffness for callus and cortical bone, rat femoral osteotomy (gap size 1.5 mm) transverse sections (axial-lateral plane, Figure 5.24) were obtained from a larger cohort study of Mehta et al. (2010). Embedded samples of sixteen female Sprague Dawley-Rats of different age (12 weeks N=5, 52 weeks N=9) were derived

from that study and measured with SAM using the protocol of chapter 5.1.2. Embedding was done within the study of Mehta et al. (2010) but using the protocol described in chapter 5.1.1. Grinding, polishing and SAM measurements were conducted in the present study. The measured impedance maps were analysed using a semi automated ROI based Matlab program (Figure 5.30). Briefly, the gap region was manually selected by two horizontal lines in a first step. In a second step ROIs identifying cortical tissue were manually selected (Figure 5.30 green area). Finally, callus tissue was automatically calculated (Figure 5.30 blue area). The background was separated from the bone using a simple threshold procedure. Average elastic stiffness was calculated using the procedures described in 5.1.2.2 and 5.1.3 using equation 5.4.

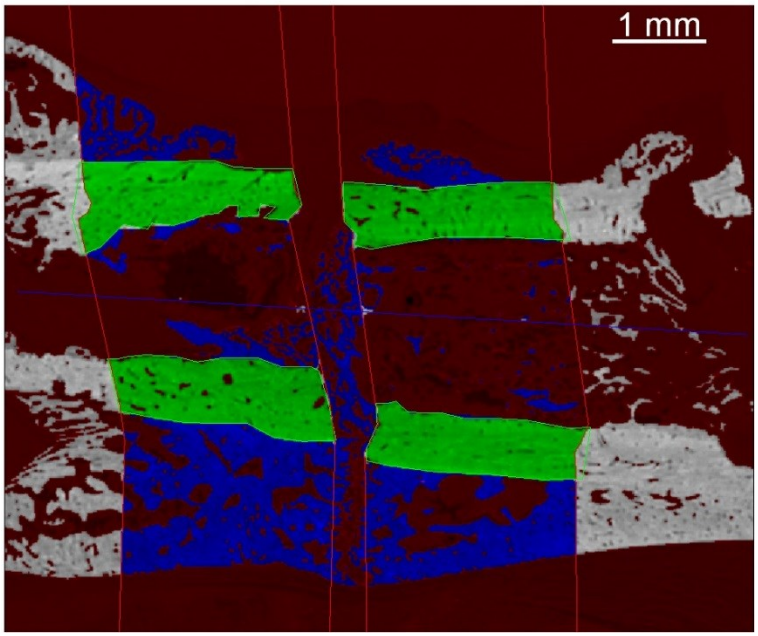

Figure 5.30 Semiautomatic ROI based analysis of rat osteotomy transverse section impedance map. Horizontal red lines identify gap region and 1.5 times towards distal and proximal. Green ROI specifies cortical tissue and blue specifies callus tissue. Red areas are related to background (PMMA) and grey areas are bone areas not included in the evaluation.

In total, six 2D models were created based on the binary masks. Four models were based on the map in Figure 5.29 a where according to Table 5.6, the values of soft tissue ($RM_{soft\ tissue}$), cartilage ($RM_{cartilage}$), soft callus ($RM_{soft\ callus}$) and hard callus ($RM_{hard\ callus}$) were assigned to the callus region. The second set of two samples was based on map b in Figure 5.29 with soft callus ($RM_{cortical\ soft}$) and hard callus ($RM_{cortical\ hard}$) as the callus region and the values of cortical bone according to Table 5.6 for the cortical region in map b of Figure 5.29. The values for c_{11} of cortical bone and hard callus were directly derived from the average values of

the SAM measurements; c_{12} of hard and soft callus and cortical bone was calculated using the relations obtained during the studies of Rohrbach et al. (2012b) (Table 6.2); c_{44} was derived using equation 2.4. The matrix density of the mineralized tissues was estimated based on a study by Raum et al. (2006b). A correlation between c_{33} and degree of mineralization of bone (*DMB*) is given by

$$c_{33} = 26.67\ DMB^{2.72} \tag{5.17}$$

and tissue density (ρ_{tissue}) by

$$\rho_{tissue} = 1.12 + 0.73\ DMB - 0.03\ DMB^2 \tag{5.18}$$

The values for soft tissue and cartilage are based on literature data (Segal et al. 1986; Isaksson et al. 2006; Leicht and Raum 2008).

Table 5.6 Elastic coefficients and density used for the simulations

Model	c_{11}	c_{12}	c_{44}	ρ
Soft tissue	2.5	2.5	0	1.06
Cartilage	3.4	3.4	0.00065	1.35
Soft callus	10	6.7	1.65	1.40
Hard callus	19.32	8.83	5.5	1.63
Cortical bone	33.05	11.91	10.57	1.86

A FDTD simulation was conducted for each model according to the protocol described in chapter 5.1.4. A pair of 5 MHz focused transducer, with a focal length of 25 mm, was placed on the two opposite transverse sites (Figure 5.24). The distance between the two transducers was 50 mm and the rat cross section models were placed in the centre, i.e. at the focus position. The setup aimed on mimicking the *in vitro* setup of chapter 5.3.3. The transducers, of a diameter of 16 mm, were modelled as arrays (high of each element was 16 µm) and focusing was realized using phase shift excitations using the excitation signal of Figure 5.8.

Analysis of the synthetic measured signals comprised the TOF_{FAS} analysis as described in chapter 5.1.4.2.

5.3.5 Statistics study II

5.3.5.1 µCT evaluation rat osteotomy

Associations between the parameters determined with the threshold and moment based methods were evaluated using regression analysis.

In order to determine healing stage-specific differences of the parameters, analysis of variance (ANOVA) followed by *post-hoc* Tukey-Kramer multiple comparison tests were used.

The distributions of the parameters were tested for normality and variance homogeneity using Lilliefors (1967) and Bartlett's (Kolios and Foster) test, respectively.

To explore the sensitivity of different parameters on the three healing groups, multivariate ANOVA (MANOVA) (Krzanowski 2000; Tabachnick 2007) was performed with a *post-hoc* Bonferroni adjustment (Tabachnick 2007). Based on MANOVA, a canonical analysis was conducted in order to find the linear combination of the features which best separated the three groups (Tabachnick 2007). Hereinafter, C_k is defined as the k^{th} canonical component.

5.3.5.2 QUS evaluation and µCT comparison of rat osteotomies

The normality of the distributions was tested using the Lilliefors test. Associations between the parameters derived from QUS and µCT evaluated by linear regression analysis. In order to determine healing stage-specific differences of the parameters, analysis of variance (ANOVA) followed by post-hoc Tukey-Kramer multiple comparison tests were used. All statistical results were considered significant for p values smaller than 0.05. The F-value, i.e. the ratio of the between-group variability and the within-group variability provides a quantitative measurement of the strength of analyzed effects, was used to compare the evaluated parameters with respect to their ability to differentiate between the two healing groups. All statistical tests were performed using the Statistics Toolbox of MATLAB R2010a (The Mathworks Inc., Natick, MA, USA).

6. Results

6.1 Study I

6.1.1 Material Properties

6.1.1.1 Site matched bone axial distribution of DMB and elasticity (Fd_1)

The following results were reprinted and adapted from the publication of Rohrbach et al. (2012b) with permission (© JBM).

The spatial fusion of SRμCT and SAM data of one sample is shown in Figure 6.1. It can be seen that at the chosen spatial resolution of both methods resolve the Haversian canal network, but not the osteocyte lacunae. Differences between osteonal and interstitial tissues are visible both in *DMB* and SAM maps. As expected, a characteristic dependence on the orientation θ is evident in the surface maps of $Z(x_1,\theta)$, but not in those of $DMB(x_1,\theta)$ (Figure 6.1).

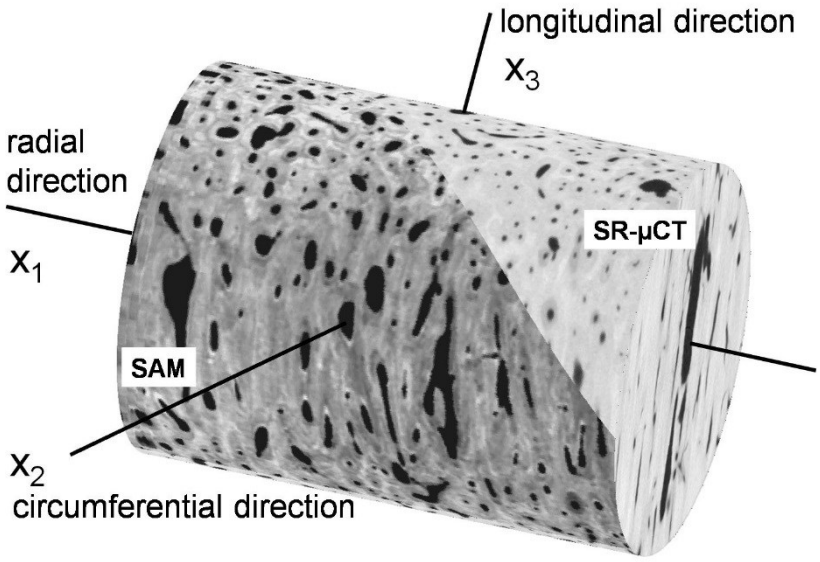

Figure 6.1 Example of site-matched SAM and synchrotron μCT data. The grey levels correspond to *DMB* in the volumetric SRμCT data and to Z(θ) in the SAM data. Both methods allow a reliable segmentation of the Haversian canal network. Moreover, a directional dependence is evident for Z(θ), but not for *DMB*. Reprinted with permission from Rohrbach et al. (2012b) (© Journal of Biomechanics).

The average values and ranges of *DMB*, elastic coefficients and technical constants of all samples are listed in Table 6.1. The anisotropy ratio $ar=c_{33}/c_{11}$ was predominantly determined

by a variation of c_{33} (R^2=0.25), but not by that of c_{11} (R^2=0.09). Moreover, we observed a minor increase of ar with an increasing degree of mineralization (R^2= 0.29). The three experimentally derived elastic parameters were highly correlated ($0.37 \leq R^2 \leq 0.55$). Therefore, a reasonable approximation of the elastic tensor (except for c_{44}) was possible based on the stiffness values measured in only one direction, e.g. from transverse (c_{11}) or from cross (c_{33}) sections (Table 6.2).

Table 6.1 Summary of microscale properties. For comparison with literature data, also the technical constants E_1 and E_3 and the Poisson ratios ϑ_{ij} were derived from the elastic coefficients *cij*. For significant variations between the circumferential regions the ANOVA F-statistic, p-value, and the result of the Tukey test are provided. The last column indicates directional changes in the axial direction, as revealed by linear or non-linear regression analysis.

Parameter	mean ±std	Circumferential position	Tukey test	Axial position
DMB [g/cm^3]	1.11±0.02	F=3.64, p=0.018	POS<MED,LAT	Central>Prox, Dist., R^2=0.83
r [g/cm^3]	1.93±0.01	F=3.64, p=0.018	POS<MED,LAT	Central>Prox, Dist., R^2=0.83
Ct.Por [%]	10.1±4.8	F=5.98, p=0.001	POS>ANT,LAT	Prox>Dist, R^2=0.71
Z_3 [Mrayl]	7.97±0.37	n.s.	n.a.	Prox<Dist, R^2=0.48
Z_1 [Mrayl]	6.75±0.28	n.s.	n.a.	Prox<Dist, R^2=0.39
c_{33} [GPa]	33.0±3.0	n.s.	n.a.	Prox<Dist, R^2=0.43
c_{11} [GPa]	23.7±1.94	n.s.	n.a.	Prox<Dist, R^2=0.38
c_{12} [GPa]	9.5±1.2	n.s.	n.a.	Prox<Dist, R^2=0.48
c_{13} [GPa]	10.0±1.3	n.s.	n.a.	Prox<Dist, R^2=0.48
c_{44}=G_{13} [GPa]	6.6±3.0	n.s.	n.a.	Prox<Dist, R^2=0.36
E_3 [GPa]	26.1±2.5	n.s.	n.a.	Prox<Dist, R^2=0.50
E_1 [GPa]	18.5±1.8	n.s.	n.a.	Prox<Dist, R^2=0.34
ϑ_{12}	0.31±0.02	F=6.12, p=0.001	POS>ANT,MED,LAT	n.s.
ϑ_{13}	0.22±0.01	F=6.97, p=0.00051	POS<ANT,MED,LAT	n.s.
ϑ_{31}	0.32±0.01	F=3.97, p=0.001	POS>MED	n.s.
ar=c_{33}/c_{11}	1.4±0.1	F=7.38, p=0.0003	POS<ANT,MED,LAT	Central>Prox, Dist., R^2=0.51

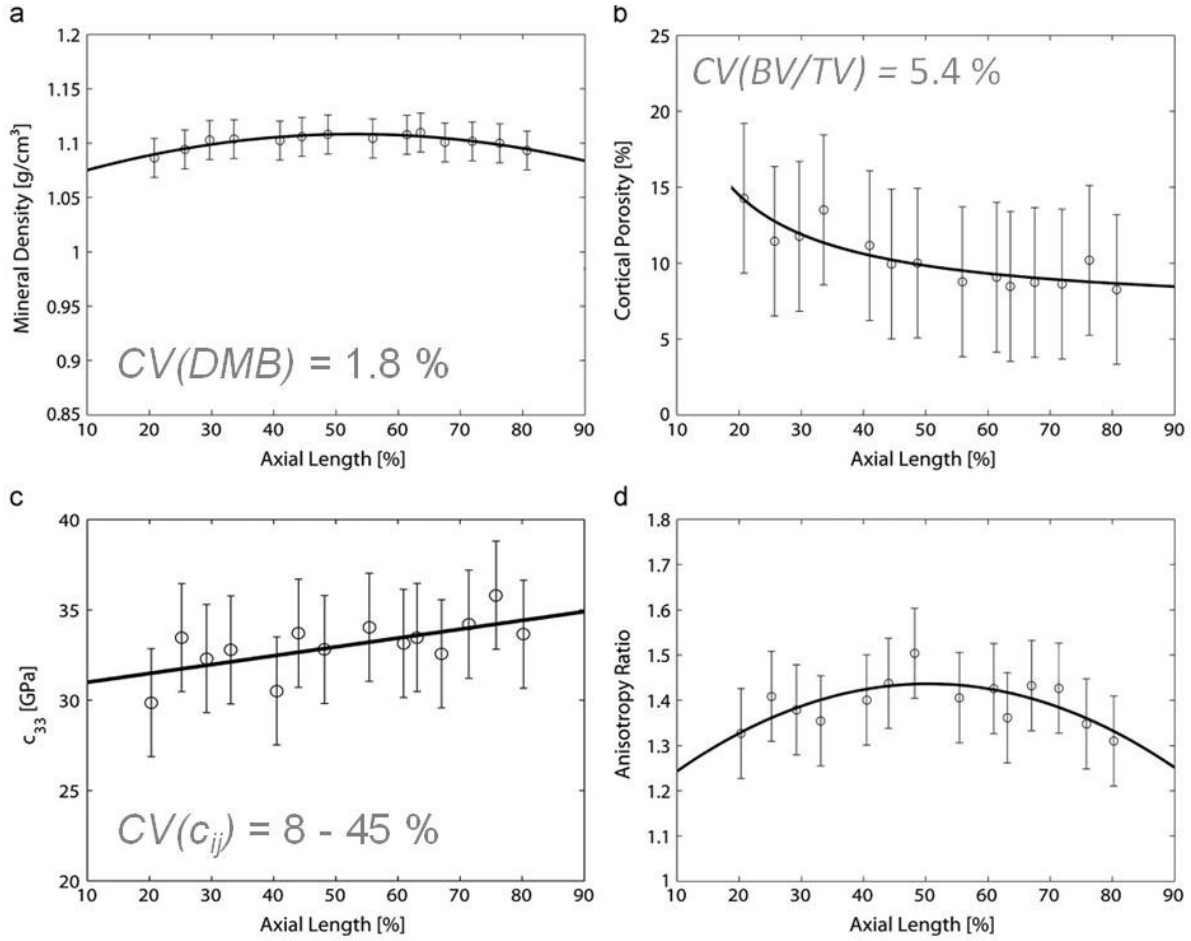

Figure 6.2 Significant and different variation of micro parameter (a) *DMB*, (b) porosity, (c) c_{33} and (d) *ar* with respect to the bone long axis. Lowest coefficient of variation for *DMB*. Reprinted with permission from Rohrbach et al. (2012b) (© Journal of Biomechanics).

Table 6.2 Prediction of the elastic tensor based on elastic parameters measured in the cross (c33) and transverse (c11) sections.

c_{33}	R^2	RMSE	c_{11}	R^2	RMSE
c_{11}=0.43 c_{33}+9.36 GPa	0.44	1.46 GPa	c_{33}=1.02 c_{11}+8.73 GPa	0.44	2.24 GPa
c_{12}=0.22 c_{33}+2.58 GPa	0.99	0.03 GPa	c_{12}=0.22 c_{11}+4.62 GPa	0.43	0.50 GPa
c_{13}=0.22 c_{33}+3.44 GPa	0.99	0.03 GPa	c_{13}=0.22 c_{11}+5.49 GPa	0.43	0.51 GPa
c_{44}=0.18 c_{33}+1.25 GPa	0.18	1.14 GPa	c_{44}=0.43 c_{11}-3.00 GPa	0.45	0.94 GPa

Tissue mineralization, density and *ar* were lower in the posterior region than in the medial and lateral regions. In contrast to this, the highest *Ct.Por* was found in the posterior region. Other significant variations between the circumferential regions are summarized in Table 6.1. Different variations were also observed along the axial direction. *DMB* and ρ increased from the proximal region towards the mid-diaphysis, and only marginally decreased towards the distal end (Figure 6.2 a). A reverse trend was observed for *Ct.Por* (Figure 6.2 b). However, all

elastic coefficients increased from the proximal to the distal regions (Figure 6.2 c). The highest anisotropy ratio *ar* was found in the mid-diaphyseal region of the femoral shaft and decreased towards the proximal and distal sides (Figure 6.2 d). The regression coefficients for all parameters are summarized in Table 6.2.

6.1.1.2 Material properties of femoral neck cross section (Fd_2)

The following results were reprinted and adapted from the publication of Malo et al. (2013) with permission (© Bone).

An overview of average and standard deviations of structural and elastic parameters is given in Table 6.3. *Ct.Th* and *Ct.PorDm* varied significantly with respect to the anatomical quadrant (Figure 6.3). For the femoral neck, the cortex was significantly thicker in the inferior part compared to the rest (Tukey Kramer, F=10.3).

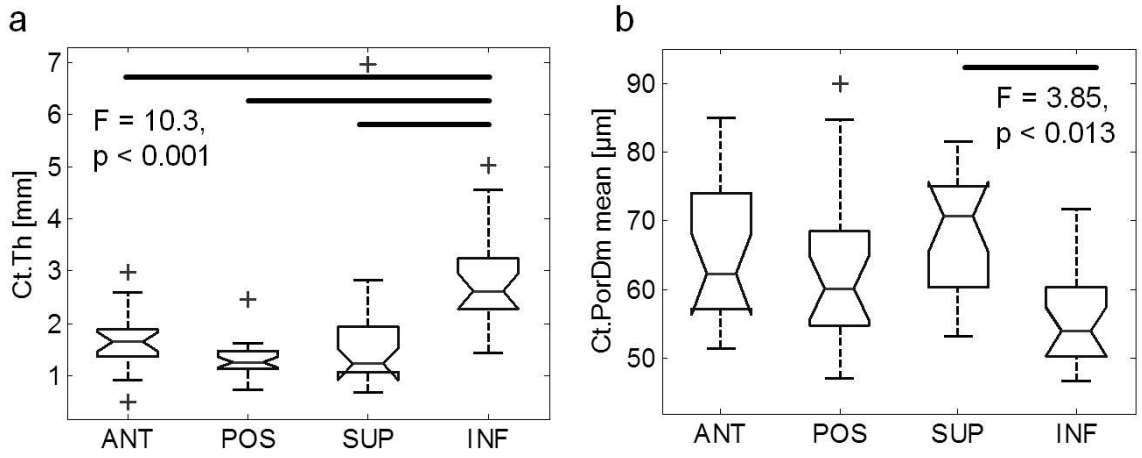

Figure 6.3 Box plots for (a) *Ct.Th* and (b) *Ct.PorDm* show significant variations with respect to the anatomical quadrant in the femoral neck.

Table 6.3 Microstructural and elastic parameters (mean ± standard error) for all evaluated regions(n=21).

	Ct.Th **[mm]**	***Ct.Por*** **[%]**	***Ct.PorDens*** **[1/mm²]**	***Tr.c₃₃*** **[GPa]**	***Ct.c₃₃*** **[GPa]**	***Ct.PorDm*** **[µm]**
ANT	1.6 ± 0.1	12.0 ± 0.9	11.2 ± 0.5	31.3 ± 0.4	34.7 ± 0.5	66.5±15.3
POS	1.3 ± 0.1	9.1 ± 0.8	10.4 ± 0.4	31.5 ± 0.3	35.8 ± 0.5	63.6±11.8
SUP	1.7 ± 0.3	13.8 ± 1.2	11.0 ± 0.5	30.6 ± 0.5	33.7 ± 0.6	73.2±26.6
INF	2.8 ± 0.2	7.0 ± 0.6	11.6 ± 0.6	31.8 ± 0.4	35.9 ± 0.5	55.8±6.9

The smallest pores in the femoral neck were found in the inferior part where the average size was significantly lower compared to superior quadrant.

The distribution of *Ct.PorDm* of the whole data set including all quadrants is plotted in the histogram of Figure 6.4. The largest pores which can be found are about 350 µm, although most of the pores have sizes approximately between 28 µm and 136 µm.

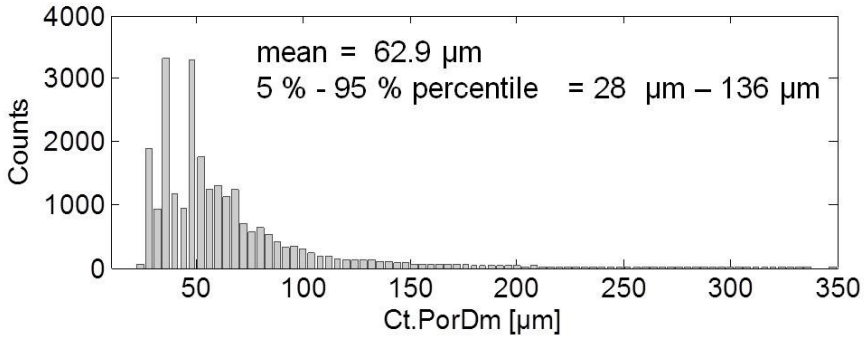

Figure 6.4 Distribution of *Ct.PorDm* for the femoral neck. Bar width is 4 µm. Most of the pores lie between 30 µm and 50 µm, largest pores are about 350 µm.

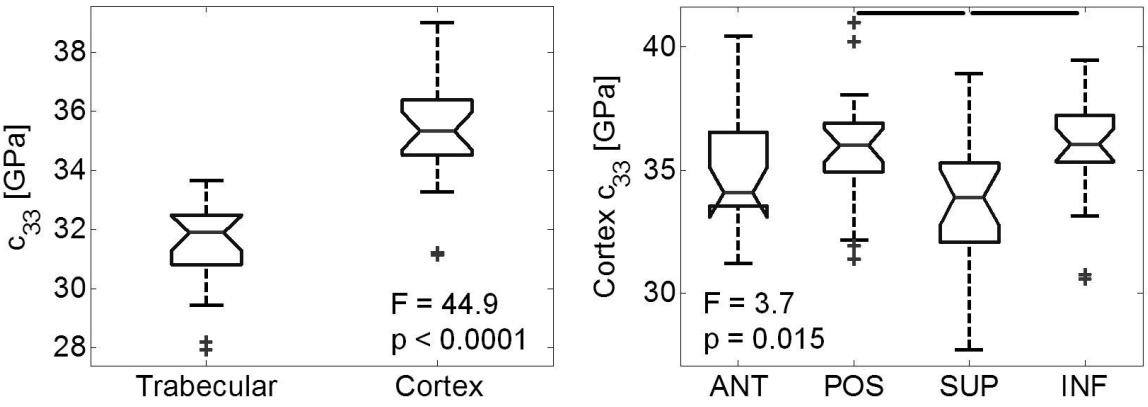

Figure 6.5 (a) Elastic coefficients of cortical and trabecular bone showed significant ($p < 0.05$) variation between the skeletal locations. (b) Elastic coefficient of cortex varied significantly ($p < 0.05$) between quadrants. Each group contains values from all cadavers ($n = 21$). The bars on top of the figure indicate significant ($p < 0.05$) differences between the groups. The central line in the boxes indicates the median, the edges are the 25th and 75th percentiles, the whiskers represent the extreme values, and the crosses denote outliers. Reprinted with permission Malo et al. (2013) (© Bone)

The elastic coefficients for cortex in the posterior and inferior quadrants were significantly (F=3.7, p = 0.015, Figure 6.5 b) higher than those in the superior quadrant. The values of elastic coefficients in trabecular tissue were lowest in the superior quadrant (Table 6.3).

The elastic coefficients of cortical and trabecular bone were significantly correlated in the femoral neck ($R^2 = 0.56$, $p < 0.01$) (Figure 6.6).

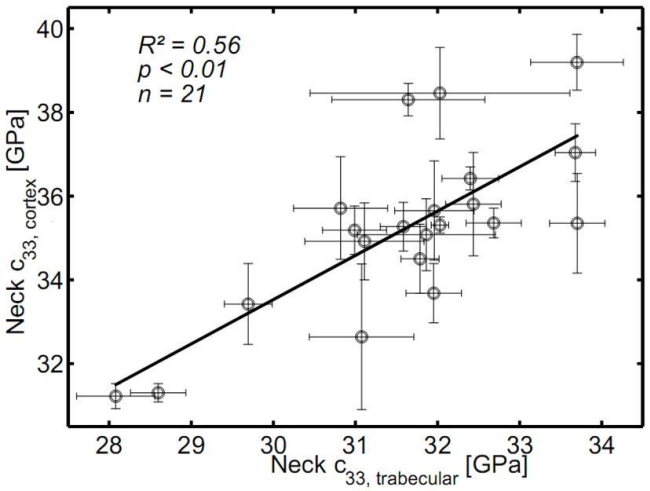

Figure 6.6 Elastic coefficients (c_{33}) of cortical and trabecular bone were significantly correlated. The dots and error bars represent the weighted means and standard errors, respectively, of the mean values measured within the four quadrants of each cross-section. Reprinted with permission Malo et al. (2013) (© Bone)

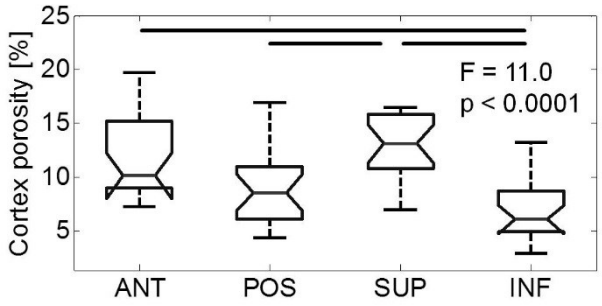

Figure 6.7 Cortex porosity varied significantly between quadrants. Each group contains values from all cadavers (n = 21). The bars on top of the figure indicate significant ($p < 0.05$) differences between the groups. The central line in the boxes indicates the median, the edges are the 25th and 75th percentiles, the whiskers represent the extreme values, and the crosses denote outliers. Reprinted with permission Malo et al. (2013) (© Bone)

The cortical porosity in the superior quadrant of the femoral neck was significantly ($p < 0.05$) higher than that detected in the posterior and inferior quadrants. Moreover, cortical porosity in the anterior quadrant was significantly ($p < 0.05$) higher than the porosity in the inferior quadrant (Figure 6.7). In the femoral neck, cortical porosity and pore density were lowest and highest, respectively, in the inferior quartile (Table 6.3).

Cortical porosity correlated negatively with the elastic coefficient in the femoral neck (R^2 = 0.27, $p < 0.05$). Furthermore, cortical porosity correlated positively (R^2 = 0.20, $p < 0.05$) with the thickness of the cortex (Table 6.4).

Table 6.4 Pearson correlation coefficients between cadaver characteristics, microstructure, and elastic coefficients of human femoral neck (n = 42).

	Femoral neck cortical bone	
	Ct.Th	c_{33}
Ct.Por	0.20*	0.27*
Ct.PorDens	0.20*	0.41**
c_{33}	0.26*	1
Age	0.27*	0.38**
BMI	*ns.*	*ns.*

* $p < 0.05$, ** $p < 0.01$, and *ns.*: not significant. *Ct.Th* = cortical thickness, c_{33} = elastic coefficient, *Ct.Por* = cortical porosity, *Ct.PorDens* = cortical pore density, and *BMI* = body mass index.

Subject age was positively associated with the elastic coefficient of trabecular and cortical bone in the femoral neck ($R^2_{trabecular}$ = 0.46, R^2_{cortex} = 0.38, $p < 0.01$), (Figure 6.8, Table 6.4). No correlation was found between the age and cortical thickness (Table 6.4).

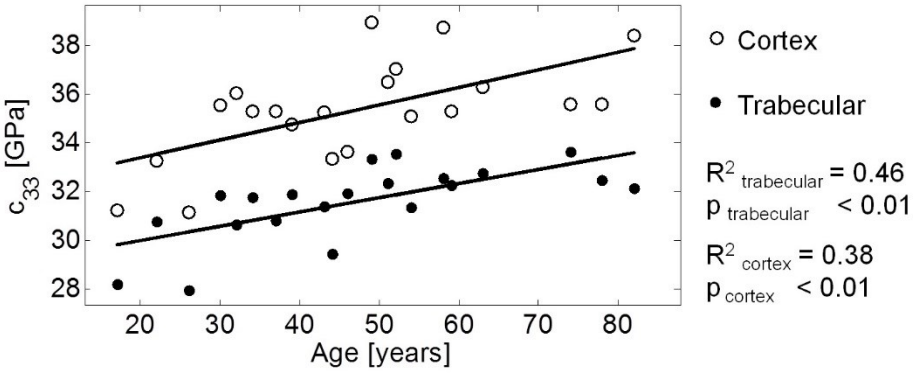

Figure 6.8 Age accounted for a significant part of the variation in the values of elastic coefficient at different anatomical sites (n = 21 for each group). Reprinted with permission Malo et al. (2013) (© Bone)

6.1.1.3 SAM cross sections for simulation (Fd_3)

Bone characteristics assessed with SAM demonstrated a noticeable variability indicating the diversity of the selected femoral neck cross-sections (Table 6.5).

Table 6.5 Geometrical parameters and tissue mechanical properties of the femoral cross-sections derived from SAM measurements (N = 9)

Experimentally derived bone properties	
Mineralized matrix elasticity (cortical bone): $Ct.c_{33}$	38.6 ± 3.2 GPa
Mineralized matrix elasticity (trabecular bone): $Tb.c_{33}$	32.9 ± 2.1 GPa
Cortical porosity: *Ct.Por*	18.1 ± 3.5 %
Cortical thickness: *Ct.Th*	2.5 ± 0.7 mm
Ct.ar /*Tb.ar*	58.7 ± 21.6 %

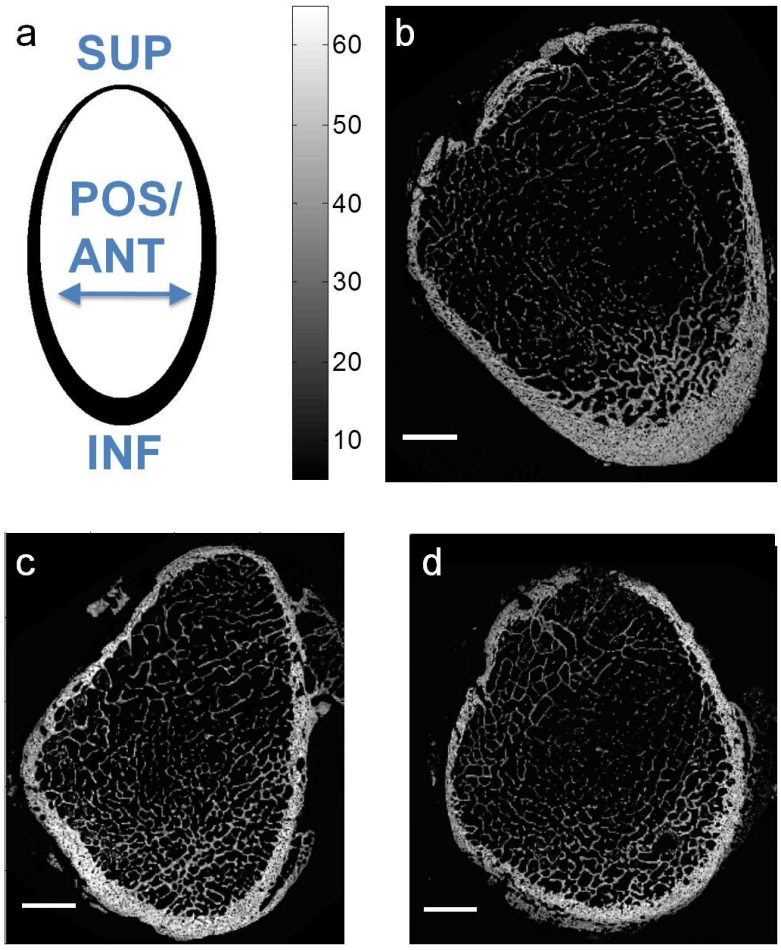

Figure 6.9 (b-d) Three cross sections used in the simulations showing heterogeneity in elasticity (grey value in GPa) and geometry. The white bar indicates 5 mm. (a) orientation of femoral neck samples.

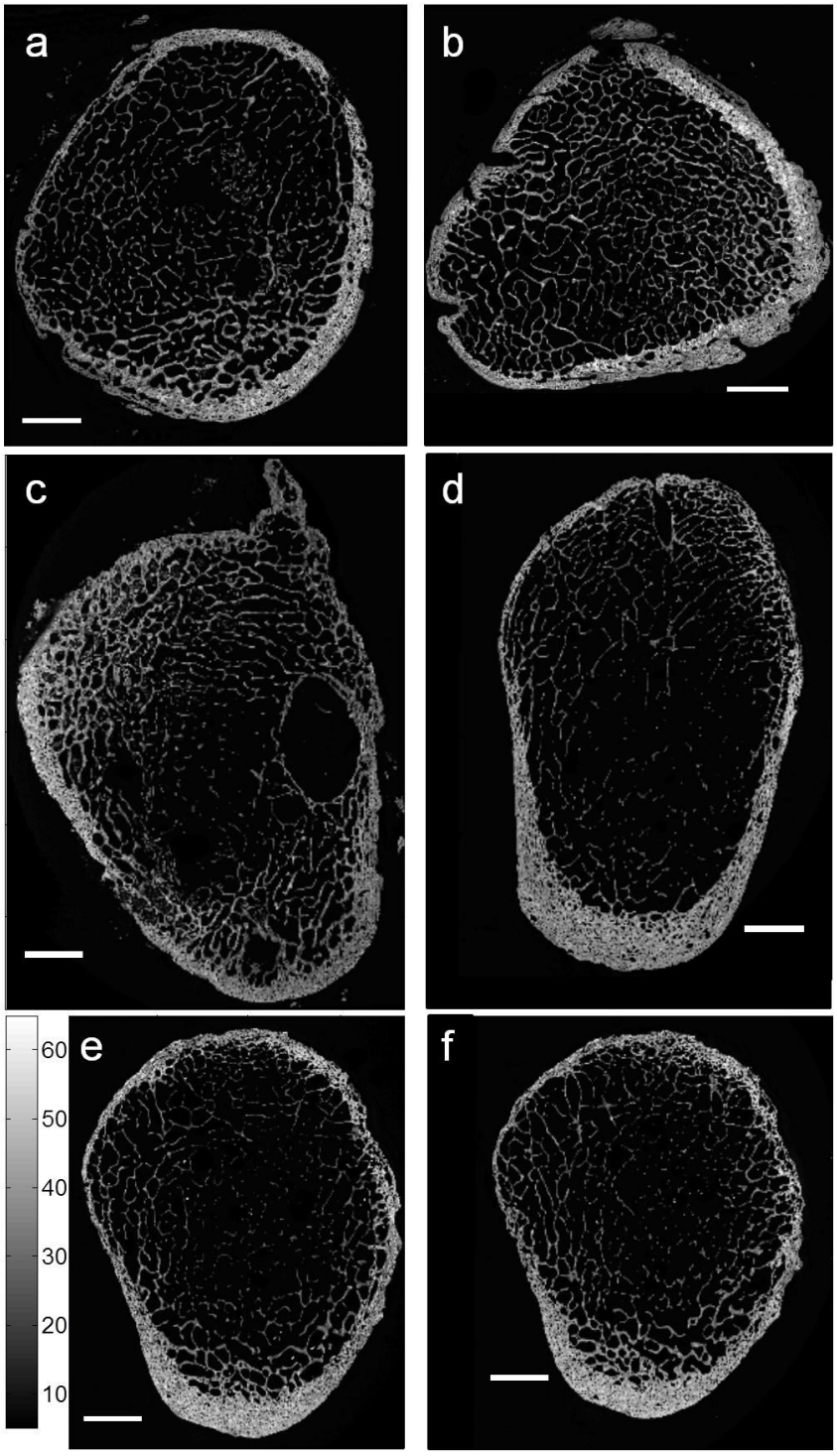

Figure 6.10 (a-f) Six cross sections used in the simulations showing heterogeneity in elasticity (grey value in GPa) and geometry. The white bar indicates 5 mm. Sample d – f are from the same donor, with d being the closest to the trochanter , f the closest to the neck and e in between.

The SAM cross sections used in the simulations are depicted in Figure 6.9 and Figure 6.10.

The cross sections used for the simulation were analysed for anatomical variations in the same way as described in chapter 5.1.2.2 (Malo et al. 2013). However, a discrimination of ANT and

POS site was not possible after a cross section extraction. Therefore, the analysis was reduced to the comparison of SUP and INF and $Ct.c_{33}$ and $Trab.c_{33}$. The results of the ANOVA are depicted in Figure 6.11. Significant differences between SUP and INF were found for $Ct.c_{33}$ (F=7.35, SUP<INF), *Ct.Th* (F=63.7, SUP<<INF) and the ratio of trabecular to cortical volume (*Tb.V/Ct.V*, F=14.1, SUP > INF).

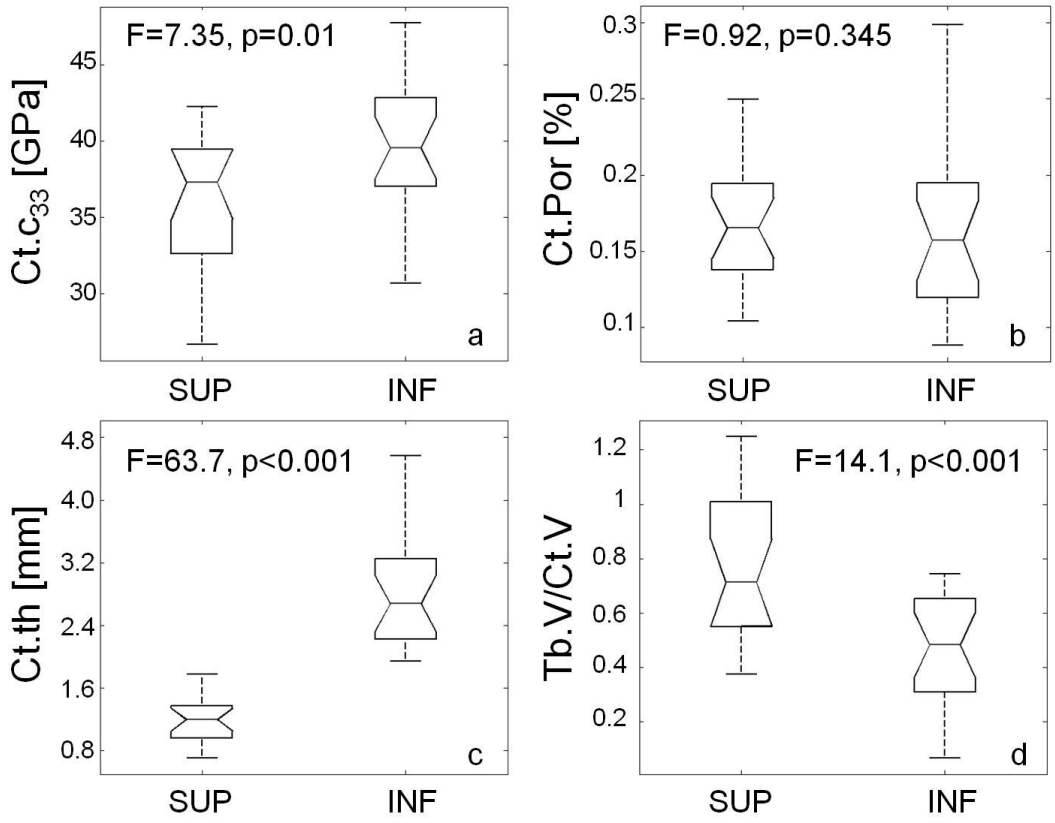

Figure 6.11 ANOVA revealed significant differences for (a) *Ct.c33*, (c) *Ct.Th*, and (d) *Tb.V/Ct.V* between superior (SUP) and inferior (INF) part of the neck.

Moreover, the data set exhibited a large variation of $Ct.c_{33}$ as evidenced by significant inter individual variations (ANOVA, F=7.7, Figure 6.12 a). Separate analysis of cortical and trabecular tissue revealed significant lower c_{33} values for trabecular tissue compared to cortical tissue (ANOVA, F=161, Figure 6.12 b).

Except for *Ct.Por* these findings are in line with the study of Malo et al. (2013) (compare Figure 6.5 and Figure 6.7).

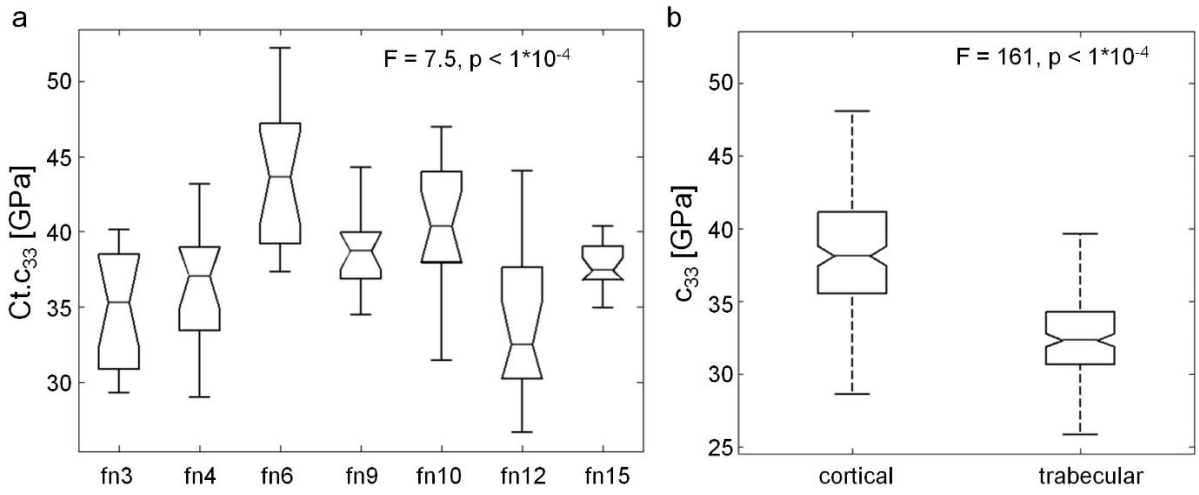

Figure 6.12 (a) Significant inter individual variations of c_{33}. (b) Trabecular tissue is significantly smaller than cortical tissue.

For one sample, *Ct.c33* was assessed with respect to the long axis (chapter 5.2.1.2) of the femoral neck. The results are depicted in Figure 6.13. ANOVA ($F=9.88$, $p<0.001$) revealed significant higher *Ct.c33* values at the central part of the femoral neck.

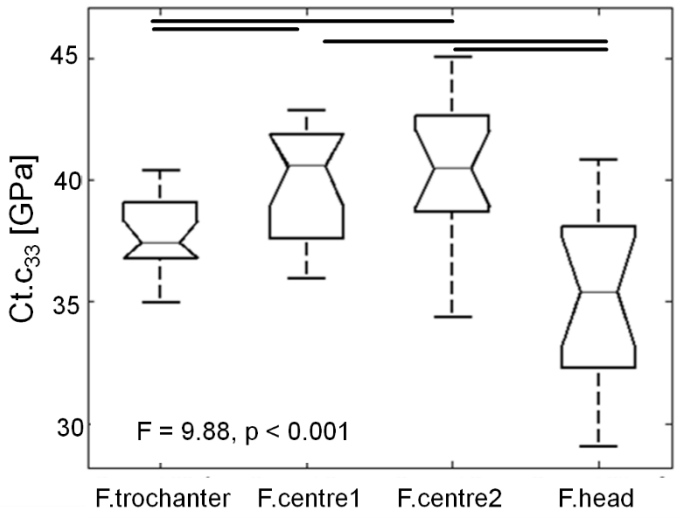

Figure 6.13 Significant variations of *c33* with respect to the long axis. The central parts of the femoral neck are significantly different to the outer parts closer to the trochanter and head. The bars indicate significant variations.

6.1.2 Artifical bone models

The differences in the acoustic propagation in the different model-types are illustrated in Figure 6.14. The received signals for the different model-types had similar profiles although the amplitude of the "direct wave" (which travels along a straight line through the trabecular compartment) was smaller for S_0 due to the scattering by the trabeculae. In particular, the wave fronts and received signals for S_4 were very similar to those for S_1, although porosity is not modelled explicitly.

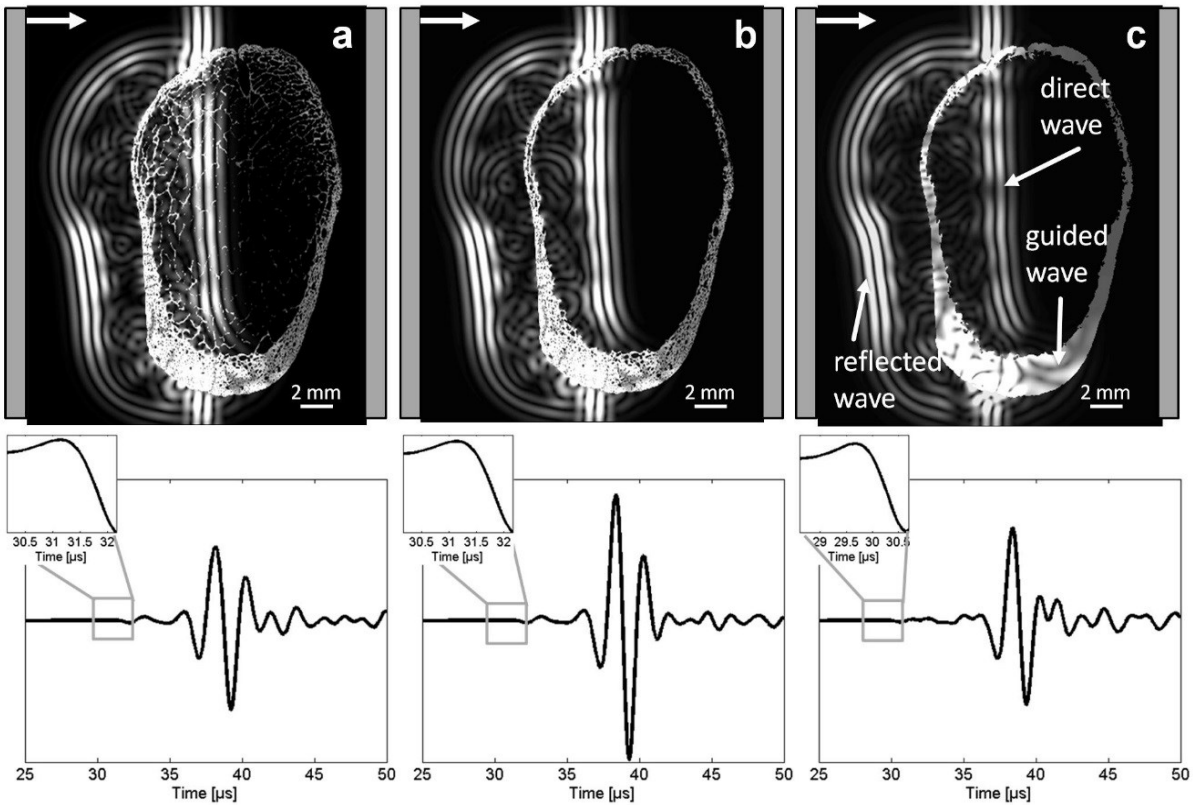

Figure 6.14 Snapshots of the acoustic displacement field in one of the femoral neck cross-sections for three model-types: (a) S_0; (b) S1; (c) S4. The circumferential wave propagating in the cortical shell is visible in advance of the direct wave (in the medullar cavity), in particular in the inferior part of the femoral neck. The acoustic signal integrated on the whole surface of the receiver is shown together with a magnification of the early arriving signal where TOF is retrieved.

Inspection of the snapshots of the simulated acoustic fields indicated that the FAS time-of-flight *TOF* was always associated with the wave guided by the cortical shell. The direct wave does not contribute to the FAS. This is consistent with previous simulations and experimental results (Grondin et al. 2010; Grimal et al. 2013a).

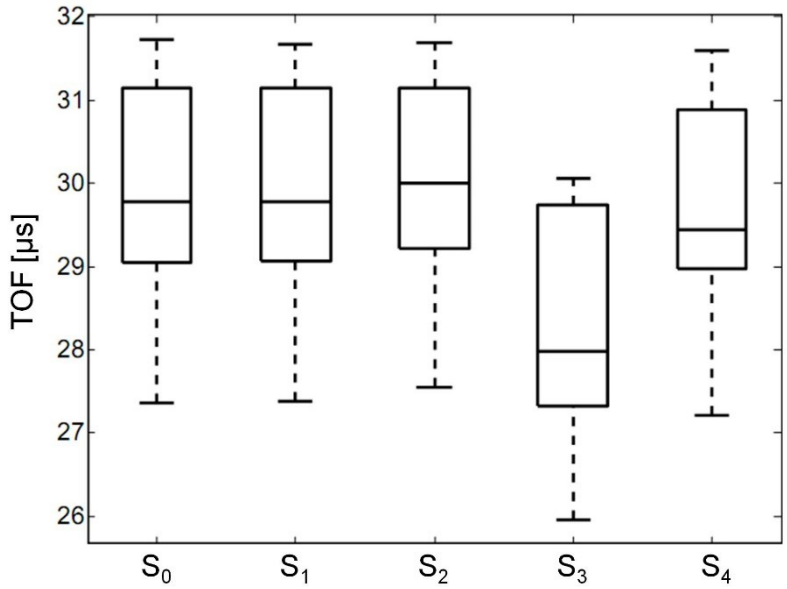

Figure 6.15 Cortical porosity (S_3) has a significant impact on TOF_{FAS} as opposed to trabecular tissue (S_1) and matrix heterogeneity (S_2). Effective model (S_4) is comparable to S_0. The box plot of *TOF* for the model-types $S_0 - S_4$ are pooled data of nine cross-sections. The 25th and 75th percentiles are given by the lower and upper bounds of the box, median value is indicated by the line inside of the box and extreme values are indicated by the ends of the vertical dashed bar.

Lilliefors test indicated that none of the sets of δTOF_k followed a non-normal distribution. Model-types S_1 and S_2 were not significantly different from S_0 as evidenced by the outcome of the t-test and the small confidence intervals (Figure 6.15, Table 6.6). TOF_3 as expected, times-of-flight for S_3 - which are stiffer models because they do not account for the porosity - were significantly less than for S_0 (negative bias δM).

Table 6.6 TOF_{FAS} obtained with each model-type compared to that obtained with the reference model (S_0). The fourth column gives the result of the Student t-test testing whether a model gives in average different *TOF* values: $p < 0.05$ means statistically different results between model S_0 and tested model

Model type	Bias δM (µs)	confidence interval (µs)	p (t-test)	regression quation (R^2)
S_1	$-1.2 \cdot 10^{-3}$	$4.4 \cdot 10^{-2}$	0.88	TOF_1=0.99TOF_0+0.32 (>0.99)
S_2	$6.1 \cdot 10^{-2}$	0.28	0.22	TOF_2=0.96TOF_0+1.14 (0.99)
S_3	−1.6	0.90	$5 \cdot 10^{-6}$	TOF_3=1.06TOF_0-3.53 (0.92)
S_4	−0.24	0.57	$3.5 \cdot 10^{-2}$	TOF_4=TOF_0-0.31 (0.96)

The effective model S4 was found to be statistically different from the reference case S_0 but with a moderate bias. Times-of-flight obtained with S_0 and S_4 were highly correlated (R^2 = 0.96) and the slope of the linear regression was equal to one.

6.1.3 TOF_{FAS} variations with respect to the long axis of the femoral neck

No significant variation of TOF_{FAS} was observed for the two central regions of one femoral neck (see chapter 5.2.1.2 and 5.2.5). However, towards the trochanter and head, a small increase of TOF_{FAS} is evidenced by ANOVA and Tukey Kramer (F=4.89, Figure 6.16).

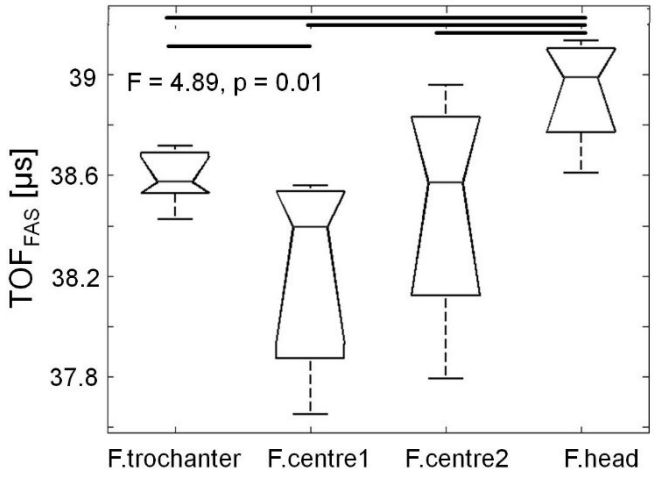

Figure 6.16 No significant variation between the two central parts of the femoral neck. Significant but small increase of TOF_{FAS} towards trochanter and head.

6.1.4 sensitivity to variation of material properties

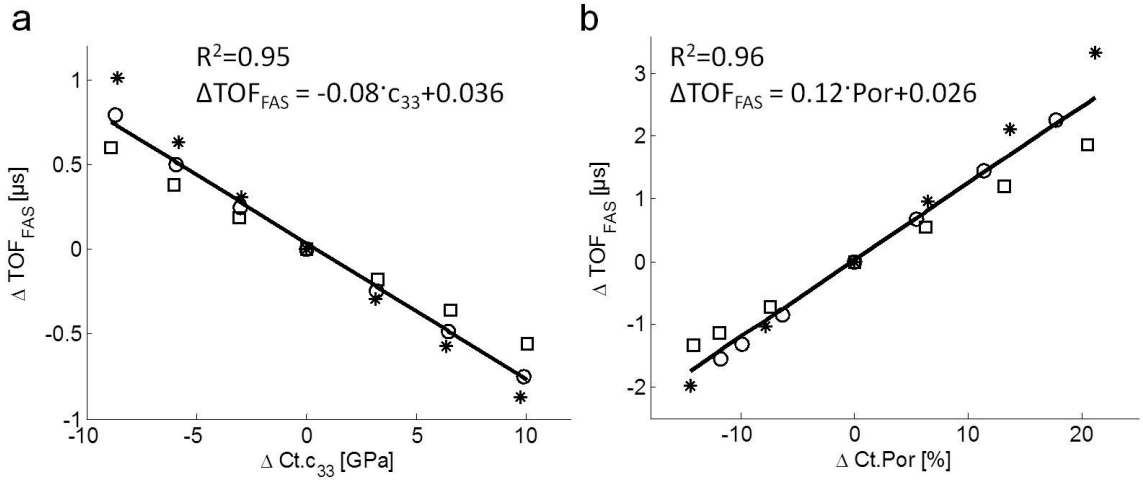

Figure 6.17 (a) Change of c33 is linearly correlated with the change in TOF_{FAS} (decreasing). (b) Change in *Ct.Por* increases significantly linear with change in TOF_{FAS}. Each marker represents a sample (total of 3).

Regarding the sensitivity of *TOF* to variations of porosity and matrix elasticity, a linear relationship between Δ*TOF* (µs) and Δ*TOF* (µs) and Δ*Ct.C33* (GPa) was found ($\Delta TOF = -0.08\Delta Ct.C33 + 0.04$; $R^2 = 0.95$, $p < 5.10{-}3$, Figure 6.17 a) and between Δ*Ct.Por* (%) ($\Delta TOF = 0.12\Delta Ct.Por + 0.03$; $R^2 = 0.94$, $p < 5.10{-}3$, Figure 6.17 b).

6.2 Study II

6.2.1 Improved µCT evaluation

6.2.1.1 Comparison of µCT healing outcome

The following results were reprinted from publication of Preininger et al. (2012b) (© Journal of computer assisted tomography).

Representative sagittal µCT images for each healing group are shown in Figure 6.18 a and b. In group A, no intra-membranous callus formation could be observed. In group B, mineralized callus was partially found in the gap region. However, cartilage formation, as revealed by histology, was not visible in the µCT images. In group C, massive mineralized callus formation with partial to full bridging of both ends could be seen. The moment profiles $M_j(z)$ exhibited a minimum in the central region of the gap. Note that local maxima did not necessarily occur at the OT boundaries, but rather further away from the gap, which was caused by the periosteal callus formations proximal and distal to the OT boundaries.

Table 6.7 µCT parameter *TV* and *BV* best separate healing group A & C. no discrimination between A&B and B&C. The table shows threshold based parameters (means and standard deviations) for each healing group. The ANOVA result (F-value) is given in the last row. Superscript letters (a, b) indicate significant differences between the healing groups.

	TV **(mm³)**	***BV*** **(mm³)**	***BV / TV***	***BMC*$_{TV}$** **(mg)**	***BMC*$_{BC}$** **(mg)**
A	22.7 ± 6.0[a]	14.9 ± 5.5[a]	0.64 ± 0.11	7.9 ± 3.5[a]	11.0 ± 4.4[a]
B	61.5 ± 25.8	47.4 ± 19.5	0.77 ± 0.04	28.8 ± 12.0	36.2 ± 14.7
C	122.8 ± 56.4[b]	91.9 ± 43.0[b]	0.75 ± 0.08	51.9 ± 26.7[b]	67.3 ± 32.3[b]
F	9.8	9.9	n.s.	8.3	9.3

The values of the derived relative moments were slightly influenced by the selection of the boundary positions. However, these variations were much smaller compared to the variations observed between the healing groups (Figure 6.18 c).

The threshold based evaluation took approximately 1.5 hours per sample while the analyses using the moment based evaluation was done within minutes per sample on a standard PC

(Intel Core Duo, 3 GHz, 1.9 GB RAM). The average parameters determined by both methods in each healing group are summarized in Table 6.7 and Table 6.8.

For the threshold based method, the segmented callus tissue volumes *TV* (F = 9.8) and *BV* (F = 9.9) as well as both *BMC* ($8.3 \leq F \leq 9.3$) parameters were significantly higher in healing group C than in group A. In contrast, the moments m_0, m_1, and m_2 were different between all healing groups ($14.3 \leq F \leq 62.9$; Table 6.8).

Table 6.8 Moment based parameters (means and standard deviations) allows the distinction between each group A,B,C. Highest F-value is given for m_0. The ANOVA result (F-value) is given in the last row. Superscript letters (a,b,c) indicate significant differences between the healing groups.

	m_0 (%)	m_1 (%)	m_2 (%)	m_3 (%)	m_4 (%)
A	60 ± 8^a	21 ± 5^a	49 ± 6^a	183 ± 106^a	63 ± 6^a
B	34 ± 10^b	14 ± 3^b	39 ± 5^a	15 ± 94^b	57 ± 7^a
C	4 ± 5^c	6 ± 2^c	29 ± 7^b	40 ± 12^b	45 ± 6^b
F	62.9	23.0	14.3	6.1	9.2

All threshold based parameters were highly correlated ($R^2 \geq 0.96$). Therefore, the canonical combination of threshold based parameters did not result in remarkable improvement of the differentiability between the healing groups (Table 6.9).

The correlations between threshold and moment based parameters were moderate or not significant (Table 6.10). Moreover, the correlations between the individual m_i were much weaker than those between the threshold based parameters and in some cases not significant. Therefore, the canonical combination of moment based parameters led to a further improvement of the differentiability between the healing groups (Table 6.10).

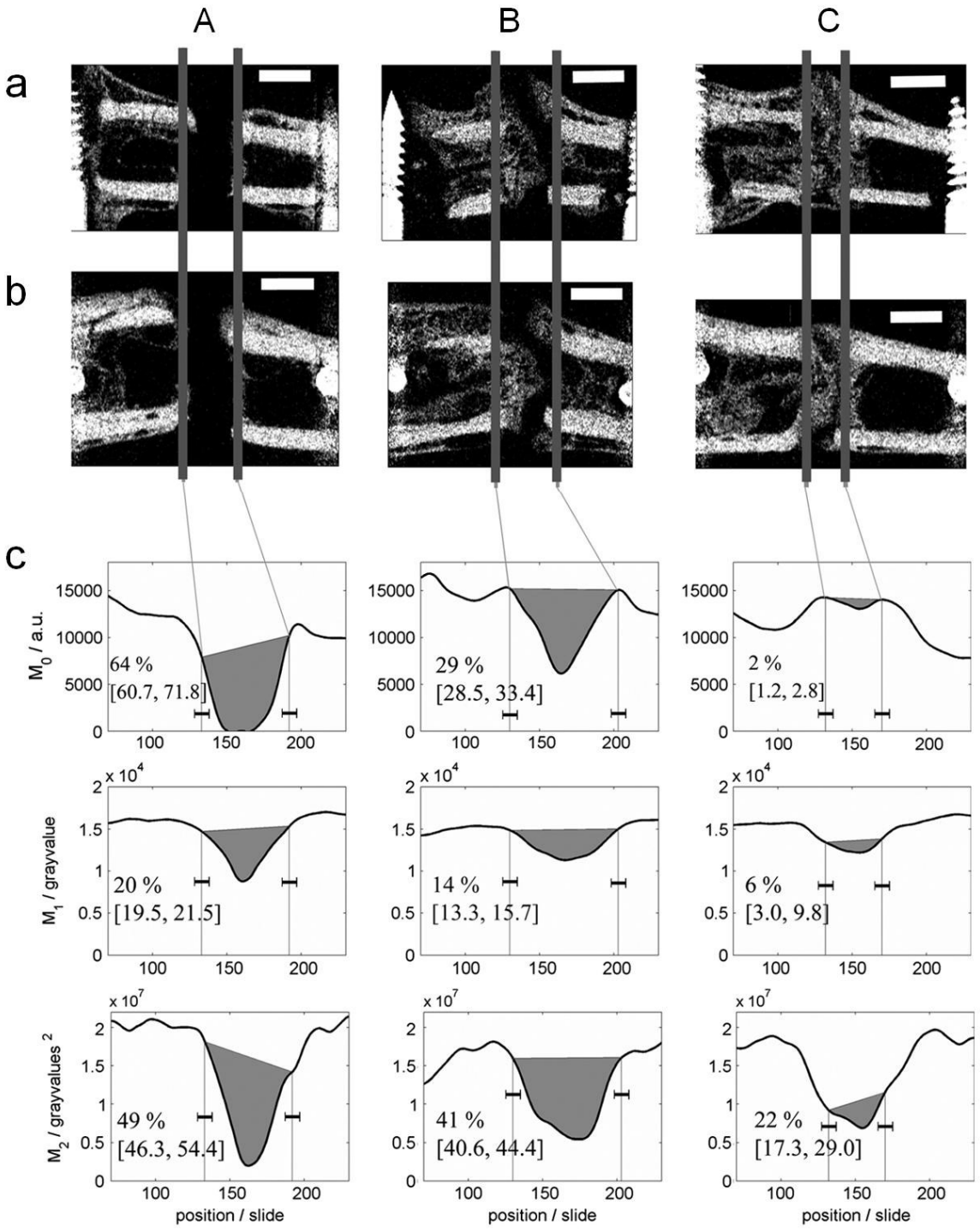

Figure 6.18 Different healing outcomes (A,B,C) are reflected in different profile parameters as shown by an example. (a) Representative sagittal µCT slices parallel and (b) perpendicular to the fixator pins for the three healing groups (white scale bar: 2 mm). The gray vertical lines indicate the manually defined OT boundaries. (c) The corresponding moment profiles $M_0(z)$, $M_1(z)$, and $M_2(z)$ are shown in. The shaded areas indicate the difference D_j relative to the approximated advanced healing stage. The normalized m_j values and their variations due to variations of the boundary positions (±5 slides) are plotted in the graphs.

Table 6.9. Variance analyses of the canonical variables derived from the moment and threshold based approaches (F-value and post-hoc multiple comparison test (MC)).

	F	MC
Threshold based C_1	16.4	(B,C) < A
Threshold based C_2	6.8	C < B
Moment based C_1	84.8	A<B<C
Moment based C_2	5.1	B < C

Table 6.10 Correlation coefficients (R^2) for each pair of features. Non-significant relations are denoted by "--" and R2 values larger than 0.7 are marked in light gray.

	m_1	m_2	m_3	m_4	*TV*	*BV*	*BV/TV*	BMC_{TV}	BMC_{BV}
m_0	0.89	0.67	0.29	0.51	0.59	0.61	n.s.	0.60	0.61
m_1		0.7	n.s.	0.51	0.53	0.58	0.33	0.58	0.57
m_2			n.s.	0.83	0.3	0.34	n.s.	0.36	0.34
m_3				n.s.	n.s.	n.s.	n.s.	n.s.	n.s.
m_4					0.24	0.24	n.s.	n.s.	n.s.
TV						0.97	n.s.	0.90	0.96
BV							n.s.	0.98	>0.99
BV/TV								n.s.	n.s.
TMD									0.99

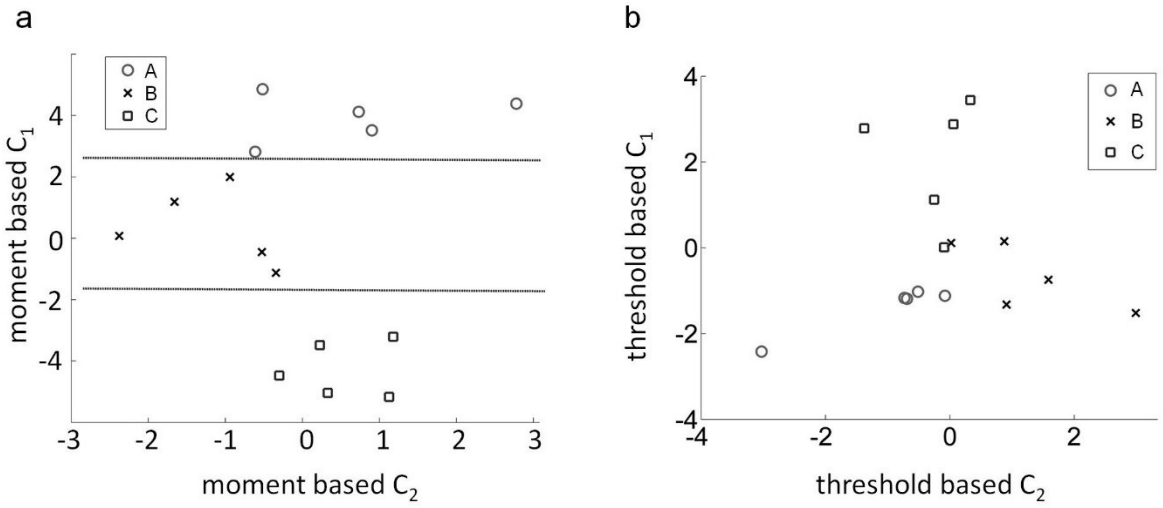

Figure 6.19. Scatter plots show clear distinction of moment based canonical components (first two) between groups A,B,C but not for threshold based.

The scatter plots in Figure 6.19 show the first two canonical components derived from the approaches. It can be seen that the moment based C_1 allowed a clear separation of the three

groups. A separation of the healing groups without overlap was not possible using either C_1 or C_2 of the threshold based method.

6.2.1.2 Classification

For k-NN classifier, several models with varying $k \in \{1,2,3\}$ were tested. In most cases the highest accuracy was found for $k = 3$. Therefore, in the following the results are limited to this case. First, each single parameter was used to train both classification models (k-NN, SVM). The results are summarized in Table 6.11. The highest accuracy in terms of prediction of the group membership was reached for m_0 using the SVM (87 %). For the threshold based approach the best accuracy was found for BV using the SVM (73 %). Finally, the classifiers were trained using the combination of variables C_1 and C_2 obtained from the canonical analysis. For the moment based technique, a higher accuracy for both, k-NN and SVM could be achieved as for any single parameter of the threshold based method. Contrarily, for the threshold based approach, the accuracy could not be increased for the canonical components compared to that obtained with the single parameters.

Table 6.11 Classification accuracy for k-NN and SVM classifiers trained by single parameter.

	k-NN	SVM
m_0	0.87	0.87
m_1	0.80	0.80
m_2	0.47	0.67
m_3	0.53	0.53
m_4	0.67	0.47
Moment based C_1	0.93	0.93
Moment based C_2	0.20	0.20
TV	0.67	0.67
BV	0.67	0.73
BV/TV	0.40	0.13
BMC(TMD)	0.13	0.13
BMC(BMD)	0.60	0.67
Threshold based C_1	0.60	0.67
Threshold based C_2	0.60	0.47

6.2.2 QUS evaluation

Figure 6.20 (c) and (d) show representative attenuation maps for the two healing stages. In all attenuation images, the gap region was clearly visible and matched the shape observed by histology and μCT. In contrast to the μCT projections, soft tissue surrounding the bone and inside the OT gap can be clearly distinguished from regions, where the sound propagated through water or mineralized bone. In intact bone regions two distinct signals arising from direct and guided waves could be observed (data not shown). However, in regions where the cortical tissue was surrounded by periosteal mineralized callus tissue, the attenuation was too strong to observe any signal with the chosen system settings.

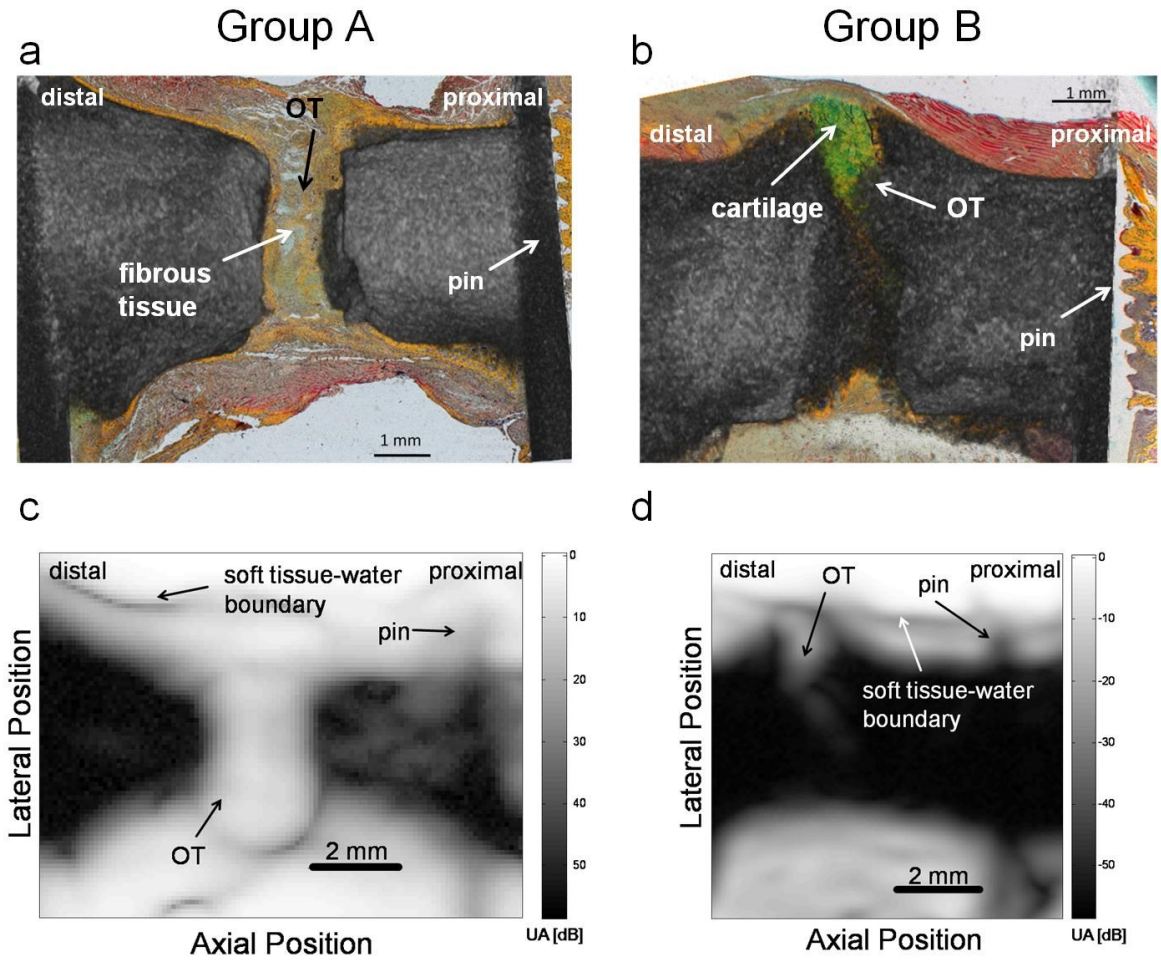

Figure 6.20 (a-b) Representative Movat's Pentachrome histology sections of Figure 5.22 with superimposed µCT projections and (c-d) QUS attenuation maps of the two healing groups. In the early healing stage (group A) the tissue in the OT gap consists mainly of fibrous connective tissue (a). In group B cartilage formation (green) is present in the gap region (b). Site-matched histology slides and µCT projections (a-b) confirm the absence of mineralized tissue in the OT region in group A and partial bridging in group B. In the µCT projections, mineralized tissue is visualized in shades of grey. The corresponding QUS attenuation maps (c-d) exhibit high attenuation values in regions with mineralized tissue (dark grey), and lower values (light grey) in soft tissues. The reference signals through water path were set 0 dB.

6.2.2.1 US propagation properties in soft tissues and partially mineralized callus

For the two samples in Figure 6.20, regions of distinct tissue compositions were manually selected within the ultrasonic parameter maps (Figure 6.21 a-b). The selections were based on the site-matched histology images and µCT projections and were identified to contain muscle, fibrous tissue, cartilage, or partially mineralized callus.

In the sample of group A, only fibrous tissue was found in the gap region. These regions exhibited slightly increased velocity and attenuation values (SOS_{phase}: $F = 58$, $p < 0.001$; *nBUA*: $F = 197$, $p < 0.001$) compared to those measured in an adjacent muscle tissue region (Figure 6.21 e and Figure 6.22 c). In contrast, most of the parameters measured in the cartilage region of the sample from group B were distinctly different compared to those measured in the muscle and mineralized callus regions. The amplitudes (*U:* $F = 3.9$, $p = 0.02$) and travel times (TOF_{phase}*:* $F = 73.6$, $p < 0.001$; data not shown) measured in the cartilage region were smaller than in the muscle region, but higher than in the mineralized tissue region (Figure 6.21 d). The normalized attenuation parameter (Figure 6.22 b), broadband attenuation (*BUA*; $F=109$, $p<0.001$; data not shown), and *nBUA* (Figure 6.22 d), in cartilage were higher than in muscle and lower than in mineralized tissue. For SOS_{phase} higher values were found in cartilage compared to those measured in muscle tissue (Figure 6.21 f). The differences in $TOF_{Hilbert}$, $SOS_{Hilbert}$, and SOS_{Phase} between the cartilage and mineralized callus regions were not significant.

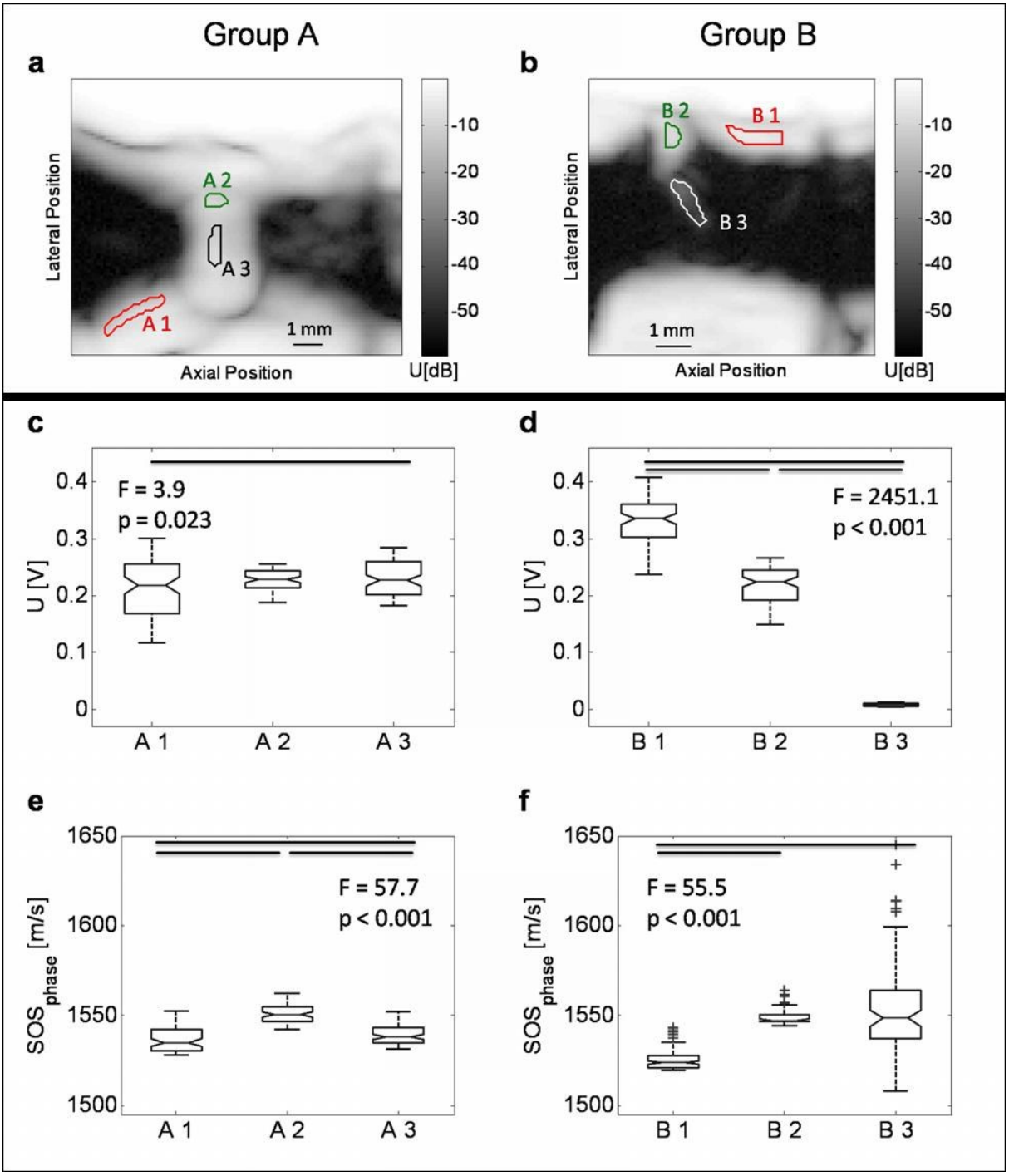

Figure 6.21 Significant discrimination by ultrasound parameter (SOS, U) of regions exhibiting different tissue compositions. The figures shows QUS attenuation maps with the regions used for a local parameter estimation in samples from (a) group A and (b) group B. The individual regions correspond to: muscle tissue (A1 and B1); fibrous tissue (A2 and A3); cartilage tissue (B2); partially mineralized callus (B3). The tissue types were confirmed by site-matched histology sections and µCT projections (Figure 6.20 a-b). ANOVA shows the differences in the transmitted amplitude *U* and sound velocity SOS_{Phase} between the selected regions ROIs in (c-d) and (e-f), respectively. Horizontal lines indicate significant differences between the ROIs.

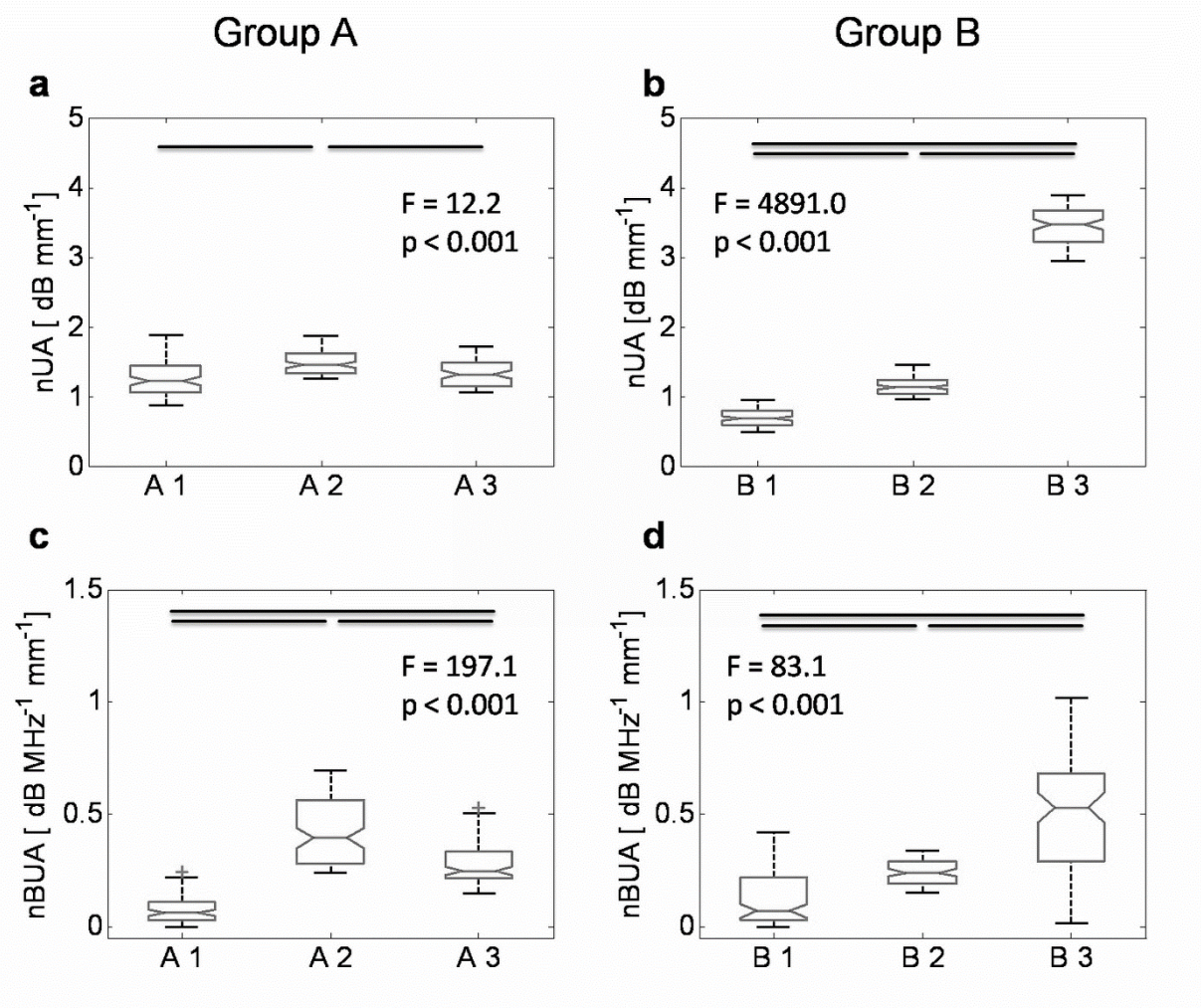

Figure 6.22 ANOVA of (a-b) the normalized *UA* and (c-d) normalized broadband attenuation values between the selected tissue regions in Figure 6.21 shows significant discrimination of regions exhibiting different tissue compositions. Horizontal lines indicate significant differences between the ROIs

6.2.2.2 Variation of US parameters between the healing groups

The ROI based evaluation revealed significant differences between the two healing groups for all amplitude related parameters (*U*, *UA*, *nBUA*, *BUA*) and for the sound velocities (Table 6.12) except of $SOS_{Hilbert}$. Both *TOF* values were not different between the healing groups (data not shown). The profile based differences between the healing groups were more pronounced (higher F-values) for U^{PR}, UA^{PR}, and nUA^{PR}, while for the other parameters the F-values were either lower or did not reach the significance level (Table 6.13). Despite the different types of evaluation, the amplitude differences *U*, *UA* and *nUA* ($25 < F < 35$, $p < 0.01$) appeared to be much stronger than the differences found for travel times (n.s.), sound velocities ($F < 15$, $p < 0.01$), and µCT based parameters ($F < 22$, $p<0.01$).

Table 6.12. QUS properties derived from the ROI analysis (mean ± SD) and F-values of the ANOVA test. For comparison the most sensitive threshold based parameter from the µCT analysis (BV) is also shown.

	U	***UA***	***nUA***	***BUA***	***nBUA***	SOS_{phase}	$SOS_{Hilbert}$	***BV***
	(V)	(dB)	**(dB mm^{-1})**	**(dB MHz^{-1})**	**(dB MHz^{-1} mm^{-1})**	**(ms^{-1})**	**(µs)**	**(mm³)**
A	0.2 ±0.1	9.2 ± 4.5	1.3 ± 0.8	2.1 ± 0.8	0.3 ± 0.2	1533 ± 10	1568 ± 16	14.9 ±5.5
B	0.0 ±0.1	36.4 ±11.6	4.1 ± 1.0	6.1 ± 1.7	0.7 ± 0.2	1583 ± 27	1604 ± 30	47.4 ±19.5
F	29.7	25.2	26.6	20.7	16.7	14.3	n.s.	12.9
p	< 0.001	0.001	< 0.001	0.002	0.003	0.005	0.060	0.007

n.s.: not significant

Table 6.13. QUS properties derived from the profile analysis (mean ± SD in percent) and F-Values of the ANOVA test. For comparison the most sensitive µCT based profile parameter m_0 is also shown.

	U^{PR}	UA^{PR}	nUA^{PR}	BUA^{PR}	$nBUA^{PR}$	SOS^{PR}_{phase}	$SOS^{PR}_{hilbert}$	**m0**
A	38 ± 8	42 ± 8	41 ± 8	21 ± 30	16 ± 21	1 ± 3	1 ± 2	60 ± 8
B	10 ± 7	12 ± 8	13 ± 7	-1 ± 20	8 ± 17	1 ± 2	4 ± 5	34 ± 10
F	34.9	34.5	33.3	n.s.	n.s.	n.s.	n.s.	21.5
p	< 0.001	< 0.001	< 0.001	0.16	0.52	0.87	0.20	0.002

n.s.: not significant

6.2.2.3 Correlation between QUS and µCT parameters

The first moment m_0 was highly correlated with the profile based amplitude parameters U^{PR}, UA^{PR} and nUA^{PR} ($R^2 \geq 0.9$). The correlations between broadband ultrasound attenuation and sound velocity with either µCT based parameter were moderate or not significant (Table 6.13, Table 6.14). Moreover, it was highly dependent on the type of analysis, whether a correlation was found or not.

Table 6.14. Correlation coefficients R2 between QUS and µCT based parameter for the ROI based estimations and in parentheses, for the profile based estimations.

	U (V)	UA (dB)	nUA (dB mm^{-1})	BUA (dB MHz^{-1})	nBUA (dB MHz^{-1} mm^{-1})	SOS_{phase} (ms^{-1})	$SOS_{hilbert}$ (µs)
m_0	0.79 (0.92)	0.75 (0.90)	0.73 (0.94)	0.64 (0.34)	0.53 (n.s.)	0.84 (n.s.)	0.64 (n.s.)
BV	0.71 (0.73)	0.68 (0.68)	0.65 (0.76)	0.65 (n.s.)	0.56 (n.s.)	0.89 (n.s.)	0.76 (n.s.)

6.2.3 FDTD simulation

Three snapshots of the simulations through one cross section model ($RM_{cortical\ soft}$ chapter 5.3.4) is shown in Figure 6.23. Reflected, direct and guided wave was observed in the two models containing cortical tissue ($RM_{cortical\ soft}$, $RM_{cortical\ hard}$).

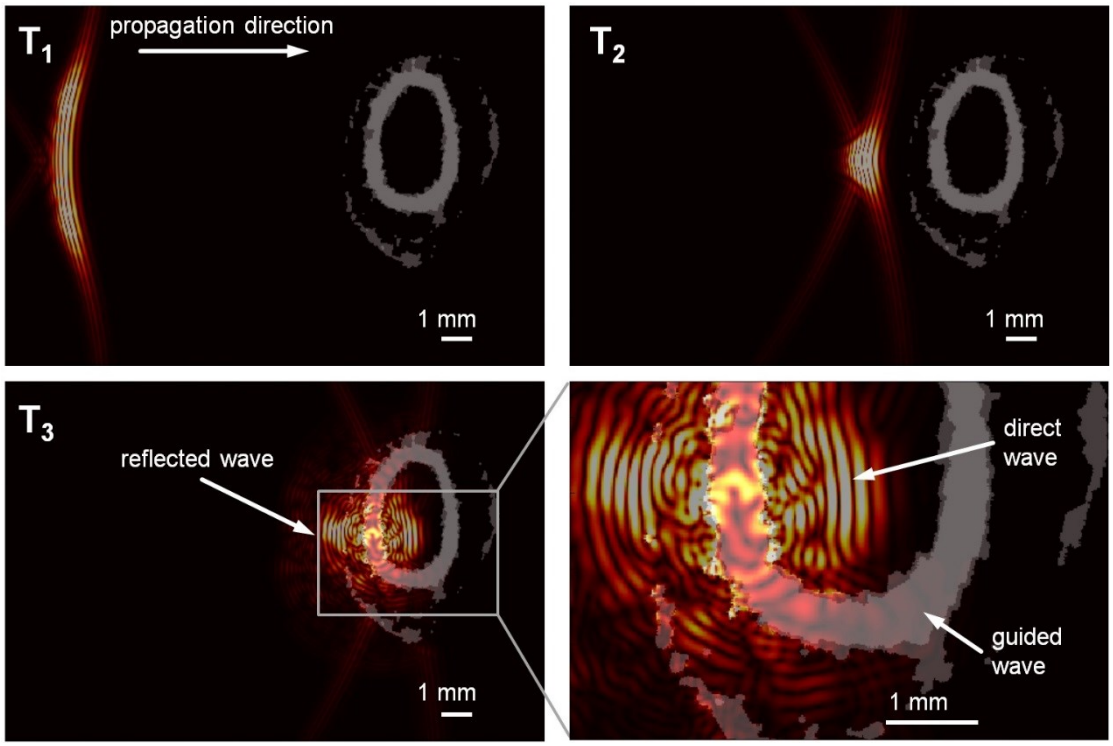

Figure 6.23 Simulations of focused wave travelling through bone model $RM_{cortical\ soft}$ (chapter 5.3.4). T_1 = 12 µs, T_2 =18 µs, T_3 =19 µs. Magnification of T_3 shows direct and guided wave propagation.

The TOF_{FAS} analysis of the detected synthetic signals revealed a successive decreasing of the TOF with callus maturation Figure 6.24.

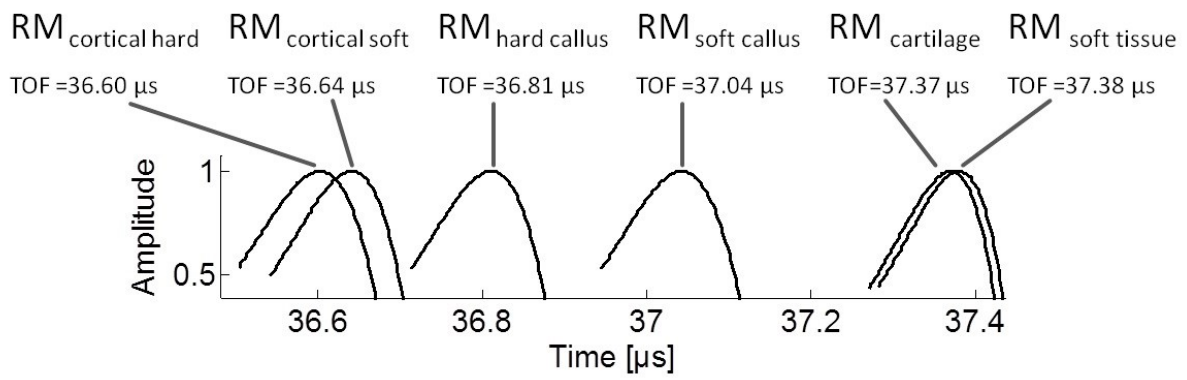

Figure 6.24 TOF_{FAS} decreases with callus maturation. TOF_{FAS} were calculated for each synthetic signal of the models described in chapter 5.3.4.

7. Discussion

7.1 General findings and achievements

The results of the present work support the hypothesis that QUS in transverse transmission is a valuable tool for both osteoporotic fracture risk prediction and monitoring of fracture healing. This was confirmed by two major studies which successfully investigated the potential of QUS including *in vitro* experiments on a rat osteotomy healing model and numerical ultrasound propagation simulations. The reliability of the bone models, used for the *in silico* experiments, was based on the investigations of the micro structural and elastic parameters.

In the first part of study I, large scale anatomical and age dependent variations of elastic stiffness and its relation to mineralization and porosity were assessed for the first time. The data suggest an adaptation of bone micro structural and elastic properties to external loading conditions. For example, at the inferior femoral neck, the smallest pores (Figure 6.7) and the highest matrix stiffest (Figure 6.5) were found and were significantly different to the superior region. Moreover, the cortex was found to be considerably thicker in the inferior region (Figure 6.3). These variations are likely attributed to high compressional stress in these regions (Van Rietbergen et al. 2003; Qian et al. 2009). Figure 7.1 (a) shows a finite element simulation of the principle strain of a sheep femur whilst walking[4]. Bone stiffness was modelled isotropic and homogeneous which led to a high compressional strain at the inferior part of the femur. Similar effects are expected for the human femur seen in evidence in other FE studies at the proximal femur (Van Rietbergen et al. 2003; Verhulp et al. 2008; Qian et al. 2009). The higher stiffness and smaller porosity would lead to higher mesoscale (a few mm) stiffness (Figure 7.1 b, not investigated in the present study), where the mesoscale has often been the length scale (one voxel) of such numerical models. Obviously, bone properties at the micro and mesoscale countervail the theoretically high compressional stresses at the inferior part of the femoral neck. Therefore, it is hypothesized that the micro elastic and structural parameters are likely to have a considerable impact on the reliability of *in silico* models and were therefore fundamental for the numerical ultrasound simulations. *DMB* or other mineralization related parameters alone are not adequate surrogates for estimating bone elastic

[4] With courtesy of PhD Peter Varga

properties which is further supported by the very low and distinct variations of *DMB* compared to the elastic stiffness. Moreover, in the present work, a moderate but significant variation of $Ct.c_{33}$ with age was found (chapter 6.1.1.2). However, other studies using qBEI could not confirm such a dependency for BMDD (Roschger et al. 2003).

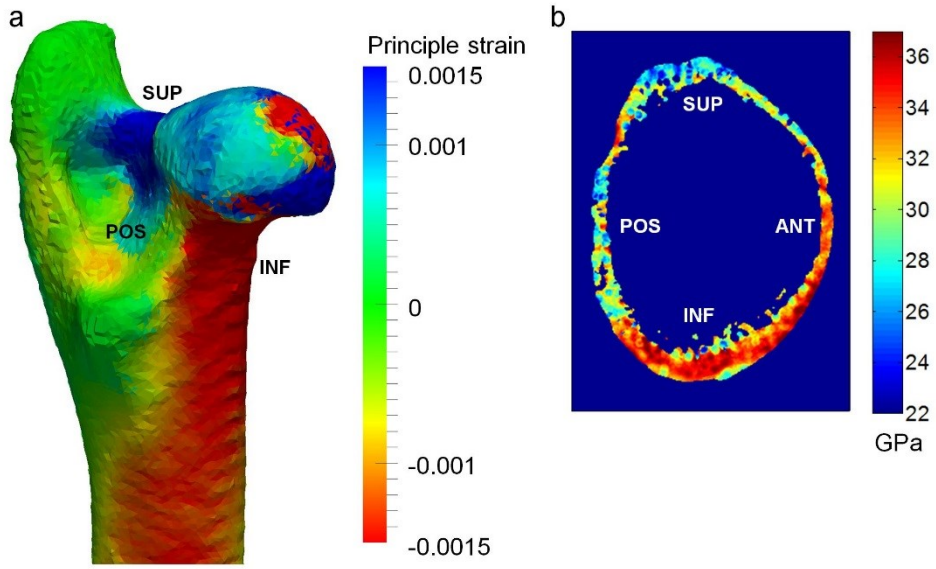

Figure 7.1 (a) High compressional local strain distribution at the inferior femoral neck. Finite element simulation of principle strain distribution during the walking of a sheep is shown. Bone was modelled as an isotropic homogeneous media. Courtesy of Dr. Peter Varga. (b) Mori-Tanaka homogenization revealed high mesoscale elastic (C_{ij}) stiffness at the inferior part. For mesoscale stiffness $C_{ij} = f(c_{ij}, Ct.Por)$

These results confirm the necessity of micro mechanical models based on elastic stiffness values rather than the degree of mineralization of bone.

The present work can be considered as the first study using SAM data for the modelling of bone suitable for numerical simulations. A unique framework, comprising all steps from measuring, signal and image processing, up to a simulation setup, has been developed. It is expected to provide not only a basis for numerical ultrasound propagation simulation but also for further *in silico* experiments such as finite element modelling. The developed tools were used to demonstrate and confirm the existence of fast ultrasound guided wave propagation in the cortical shell of the human femoral neck (Figure 6.14) and a rat femur (Figure 6.23) by numerical ultrasound simulations. By extracting parameter from the FAS, cortex properties of the femoral neck were directly related to guided wave propagation. As expected, the ultrasound parameter were highly correlated with important bone quality properties at the micro scale such as *Ct.Por* (R2=0.96) and $Ct.c_{33}$ (R2=0.95) (Figure 6.17). However, matrix heterogeneity and trabecular bone showed no impact on TOF_{FAS} (chapter 6.1.2) which arises

the hypothesis that different tissue types can be assessed using QUS by evaluating different ultrasonic wave paths. The investigations demonstrate the high potential for bone quality assessment and fracture risk prediction. Although further validations are required, for instance by using the already developed FemUS prototype (Barkmann et al. 2008a), the findings of this study are expected to have a high potential for *in vivo* applications. These results are not only important for fracture risk prediction but also for future applications in monitoring fracture healing. A recent study suggests that not only the callus tissue undergoes gradual changes in stiffness during the healing process but also the fracture gap adjacent cortical tissue decreases in its stiffness (Preininger et al. 2011). As demonstrated by the simulations of the present study, these changes are expected to be detectable by transverse transmission QUS approaches. This is supported by the preliminary simulations on rat osteotomy cross sections which also showed guided and direct wave propagation (chapter 6.2.3).

The data of the present work serves as a basis for further numerical ultrasound propagation analysis. Current *in silico* investigations by Rohde et al. (2012) uses the micro elastic and structural parameters including *Ct.Por, Ct.Th, Ct.PorDm* (chapter 6.1.1.2). First results show a very high predictive power for these parameters using multivariate models relating more elaborated wave characteristics to the structural parameters. The relation of predicted *Ct.Por* and original *Ct.Por* of one of these models is shown in Figure 7.2.

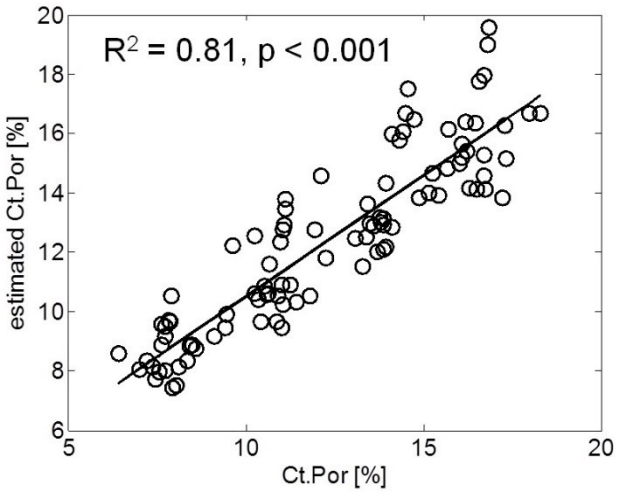

Figure 7.2 High predictive power of model relating ultrasound parameter to cortical porosity. The correlation shows the cortical porosity values estimated by the model in relation to the real cortical porosity values. Data from Rohde et al. (2012).

The principle feasibility of a transverse transmission setup for monitoring fracture healing in small animals has been demonstrated in study II of the present work. For the first time, a focused transverse transmission scanning approach was used to assess the early stages of fracture healing in a small animal model, which can be used as a basis for further developments. It was found that ultrasound can distinguish between soft tissue formations (muscle, cartilage, partial mineralized tissue Figure 6.21and Figure 6.22) which are important for determining the healing outcome. These formations cannot be assessed using standard µCT methods which is likely to be the reason why µCT has been found to be of less power for separating the two early healing stages in that study (Table 6.12 and Table 6.13). Furthermore, these findings supports the hypothesis that not only parameters related to mineralization are biomarkers for the evaluation of the healing progression, but also other parameters such as stiffness.

In order to strengthen these statements, a novel evaluation µCT algorithm for small animal osteotomies was developed. Although that procedure tremendously improved the healing state characterisation (chapter 6.2.1 and 7.3.1), its discriminatory power was not superior to that of the QUS approach (chapter 6.2.2).

In summary, these investigations not only show the importance of a precise estimation of micro mechanical properties for numerical modelling but also demonstrates the feasibility and high potential of QUS for bone quality assessment and monitoring of fracture healing.

7.2 Discussion Study I

7.2.1 Site matched bone axial distribution of DMB and elasticity

The first part of study I presents the first systematic survey of microstructure, tissue mineralization and anisotropic elastic properties of the cortical tissue matrix within the same human femoral shaft (Rohrbach et al. 2012b). The estimated anatomical variations of material properties and tissue porosity are consistent with previously reported data. For example, Ashman et al. (1984) observed that density was greater in the central part than in the proximal region. Similar to all previous investigations, the proximal posterior region exhibits the lowest density, highest porosity and the lowest stiffness values (Ashman et al. 1984; Weiss et al. 1998; Bensamoun et al. 2004b; Espinoza Orias et al. 2009). Other variations, e.g. the course of the anisotropy ratio ar with respect to the long axis position, were different compared to

those measured by low-frequency ultrasound (Rudy et al. 2011). A potential explanation for the different course of tissue level and macroscopic anisotropy ratio may be the different anatomical variations of tissue mineralization, elastic properties, and porosity observed in this study. It should also be noted that in the study by Rohrbach et al. (2012b) the major orientation of the Haversian canals was always defined as the x_3 – direction (Figure 7.3). Particularly in the proximal and distal epiphyses, the orientations of the Haversian canals are considerably tilted relative to the long axis of the femur. For a direct comparison, homogenization models that take into account the matrix properties, porosity and pore structure are necessary (Grimal et al. 2011).

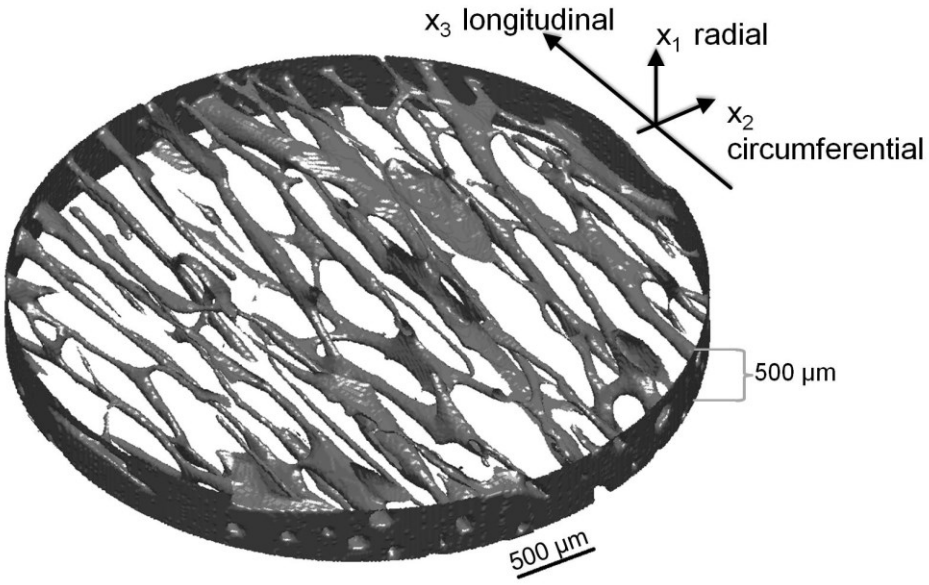

Figure 7.3 3D cross section (high 500 µm) of SRµCT cylinders showing the preferred orientation of the Haversian canals with the longitudinal direction of human femur cortical bone.

Interestingly, tissue mineralization does not always vary in a similar way as the elastic coefficients between the anatomical regions. The variation of *ar* along the axial direction can be explained by a change of the ultra-structural arrangement of the mineralized fibrils relative to the bone long axis, whereas the highest values correspond to a higher degree of fibril alignment with the bone axis. This is reasonable since the central region requires the highest ultimate tensile strength and compressional stiffness due to tensile muscle forces and weight bearing under physiological loading conditions (Duda et al. 1998), while the proximal and distal regions are more exposed to bending and torsion.

The lowest variance was observed for *DMB*. This finding is consistent with previous investigations at the human radius (Raum et al. 2005a) and the human trochanter (Zebaze et

al. 2011). Bone mineral density distributions (BMDD*)* have been extensively investigated by quantitative backscattered electron microscopy (qBEI). Reference data exist for trabecular BMDD from iliac crest samples of adults for healthy, diseased and various treatment conditions (Roschger et al., 2008). In healthy subjects, the coefficient of variation CV is small (2.1 % for 52 individuals). Lower distribution values have been observed in osteoporotic subjects and mild primary hyperparathyroidism, while a shift towards higher mineralization was found in osteogenesis imperfecta. A slight shift towards lower values (-5.6 %) was also observed in iliac crest biopsies of children, adolescent and young adults (Fratzl-Zelman et al. 2009). Within the femoral shaft investigated by Rohrbach et al. (2012b) in the present project, it was found that variations with respect to the anatomical position were different for *DMB* and elastic coefficients. This supports the hypothesis that no global relation between tissue mineralization and tissue elastic properties exists. Instead, it appears that despite a fairly constant mineralization at the microscale, elastic adaptation of about 7 % is achieved by variations of the matrix *ar*. Moreover, significant correlations that have been observed, even between the independently assessed parameters (c_{11}, c_{33}) suggesting that the assessment of one or two coefficients, e.g. in the transverse and cross-sectional planes, may be sufficient for a reasonable approximation of the transverse isotropic stiffness tensor for particular tissue types and anatomical locations. In combination with analytical (Parnell and Grimal 2009; Grimal et al. 2011) or numerical (Grimal et al. 2008) homogenization techniques, a rapid evaluation of the complex interplay between structural, compositional and elastic adaptation is possible. Moreover, it was shown that variations of cortical porosity and microscale elastic properties of the tissue matrix are much stronger than variations of tissue mineralization.

Some parts of the discussion has been reprinted and adapted from the publication of Rohrbach et al. (2012b) with permission (© JBM).

7.2.2 Parameter variation of the femoral neck

The increase in cortical porosity, the thinning of cortex and the resorption of trabeculae cause a reduction in bone mass, which increases the fracture risk while an individual is ageing. In addition, an age related increase in the bone tissue elastic coefficient may be linked to increased tissue brittleness, induced by either an increased tissue mineralization, changes in the collagen-cross linking composition, or a combination thereof (Raum et al. 2006a). Indeed, it has been shown that the mesoscale cortical bone strength (*i.e.* a few millimetres in size) in the longitudinal direction are correlated with the longitudinal Young's modulus ($R \sim 0.5$)

(Grimal et al. 2009). The mesoscale elastic properties are determined by the microstructure (*i.e.* the porous network) and the elastic properties of the tissue (Grimal et al. 2008). Therefore, variations of these microscale properties may contribute to the macroscopic mechanical properties and risk of fracture. It was hypothesized that two parameters, *i.e.*, elastic coefficient and cortical porosity would display significant variation with aging and tissue types (cortical vs. trabecular). In order to evaluate these hypotheses, scanning acoustic microscopy (50 MHz) measurements were made on cross-sectional samples from the femoral neck of male cadavers of different ages without pre-existing conditions that might have affected bone metabolism. Femoral neck samples were obtained from typical transcervical fracture sites.

It was found that the trabecular bone stiffness at the human femoral neck was lower than the stiffness of the cortex (Figure 6.5 a). This contradicts the findings of Turner *et al.* (Turner et al. 1999) who claimed that the elasticity of trabecular tissue was similar to that of cortical tissue. In their study, the value of Young's modulus (E) for trabecular bone tissue was intermediate between the values of the transverse Young's moduli (E_T) and average E composed of E_T and the longitudinal Young's moduli (E_L) measured from cortical bone tissue. However, if one compares the E_L and E values for the trabecular tissue, their results become consistent with the present findings. Moreover, their study was limited by a smaller sample number (cross-sections from one human donor) and the low spatial resolution of the applied ultrasound transducer (60 μm). Despite the significant difference identified in the elastic coefficients between the tissue types, the elastic coefficients of trabecular and cortical bone tissue were positively correlated. This suggests that the general loading of the femur can have a similar effect on the stiffness of both cortical and trabecular bone matrix at the neck, via changes in the bone turnover and mineralization.

In the assessment of the spatial variations of elastic coefficient and microstructural properties, the samples were divided into four quadrants in which the cortical and trabecular bone were individually analysed. The elastic coefficients were highest in the posterior and inferior quadrants which are the areas bearing most of the loading whilst standing and walking (Figure 6.5 b) (Bergmann et al. 2001). This indicates that the elastic coefficient of the bone tissue adapts to the existing loading conditions.

Cortical and trabecular bone elastic coefficients were found to increase with age (Figure 6.8). This may be related to the age dependent changes in bone tissue mineral (*i.e.* crystallinity and mineral content) and organic phases (*i.e.* collagen cross-links and re-orientation) (Zioupos

2001; Nyman et al. 2005). The importance of the organic phase is supported by the results of Wall et al. (1979), who reported that bone tensile strength decreased by 27 % accompanied by a simultaneous decrease in density by only 3 %, with increasing age.

The results of the present study are in line with previous publications (Bell et al. 1999a; Bell et al. 1999b; Yeni and Norman 2000; Bell et al. 2001; Chen et al. 2010; Chappard et al. 2012). The same regional variations of *Ct.Th* and *Ct.PorDm* of the femoral neck were found in the work by Bell et al. (1999a; 1999b). The lower pore diameters and larger cortices at the inferior part suggest an adaptation to the high loading under compression acting at these sites (Lotz et al. 1995). However, *Ct.PorDm* could not solely account for the variations observed for cortical porosity indicating an impact of few but larger pores as already found by Bell et al. (1999a). This is supported by the different variation of averaged *Ct.PorDm* (Figure 6.3) compared to no significant variations of the medians of *Ct.PorDm*. The medians are in contrast to the mean expected to be less effected by the few larger pores. Although cortical porosity is an important determinant of cortical bone strength and toughness (Yeni and Norman 2000), its relation with matrix elastic stiffness, as a function of age, has not been addressed so far. Femoral neck porosity was positively correlated with cortical thickness and negatively correlated with elastic coefficient. This gives evidence that the thick cortex of the femoral neck is porous and trabecularizes with aging, contributing to decreased cortical thickness while the dense core in the periosteum remains structurally unchanged with its high elastic coefficient.

As there has been increasing interest in conducting diagnostic ultrasound measurements directly in the most severe fracture sites, *e.g.*, the femoral neck, it is essential to understand the natural variation of tissue elastic properties and porosity with aging and between different skeletal sites (Barkmann et al. 2008a; Barkmann et al. 2008b; Barkmann et al. 2009; Karjalainen et al. 2012). The elastic properties and porosity affect the speed of sound in bone; this is vital information when evaluating the cortical thickness with ultrasound. Thus, if one neglected these factors and used a fixed speed of sound for bone, this would lead to inaccuracies in the measurement of cortical thickness (Raum et al. 2005a; Karjalainen et al. 2008; Cowin and Cardoso 2011). The data obtained in the present study could be transferred into computational models, *e.g.*, for evaluating the acoustic wave propagation through the femoral neck with realistic geometry, elastic coefficient, and porosity. Moreover, the present data may be suplemented with micro-computed tomography (μCT) data *e.g.* it can be used as

an input for numerical simulations of mechanical properties of proximal femur (Hakulinen et al. 2006; Grimal et al. 2008; Aula et al. 2009; Grassi et al. 2012).

In conclusion, there was age-dependent variation in the elastic coefficient of calcified tissue in the human femoral neck. Moreover, values of elastic coefficient and porosity were found to vary within cross-sections of the femoral neck. Furthermore, the properties of trabecular and cortical bone were interrelated in the femoral neck. The age related increase in elastic coefficient of bone tissue may contribute to increased fragility of elderly bone and this should be taken into account when using ultrasound in the diagnostics of fracture susceptibility.

Some parts of the discussion has been reprinted and adapted from the publication of Malo et al. (2013) with permission (© Bone).

7.2.3 FDTD simulations at the femoral neck

Different models of femoral neck cross-sections with sample specific geometry and mechanical properties were tested to assess the impact of modeling assumptions for the simulation of through-transmission ultrasound measurements in the MHz-range. SAM, with a resolution of 23 µm, not only gave access to the overall shape of the cross-sections but also allowed the mapping of the vascular porosity, the trabecular microstructure, and the elastic properties of the matrix after conversion of impedance to elasticity. Reliability of the model data, including micro elastic and structural parameter, was confirmed by the second data set of femoral neck samples (Fd_2) of Malo et al. (2013). The variations of the parameters were in well accordance with the properties found in the simulation data set (Fd_3, compare 6.1.1.2 and 6.1.1.3).

The focus of the simulation studies was on TOF_{FAS} of the wave transmitted through the femoral neck, a parameter which can be measured with a clinical prototype (Barkmann et al. 2010a). Furthermore TOF_{FAS} was found to be highly correlated to femur strength in an *ex vivo* study (Grimal et al. 2013a).

The most comprehensive model-type (S_0) appeared to be unnecessarily complex for the purpose of modeling the propagation of the waves guided by the cortical shell and of determining *TOF*. Firstly, *TOF* was not changed when trabecular bone was removed and replaced by water. This is a consequence of the weak coupling of the guided waves in the cortical shell to the low-density trabecular bone. This strongly suggests that it is not necessary to model the trabecular compartment to simulate FAS measurements. Secondly, the

heterogeneity of the mineralized matrix did not have an effect on *TOF* which remained unchanged in models of type S_2 compared to type S_0. The latter heterogeneity is due to local variations of the degree of mineralization and elasticity of osteons and interstitial tissue (Currey 2002). Thirdly, it seems that it is not necessary to know the detailed structure of the cortical porosity. The results obtained with S_4-type models are close to those obtained with the reference cases S_0 as evidenced by linear regressions (Figure 7.4), although a small but significant difference of the mean values exists (T-test). This means that the representation of the pore structure in the cross-section may be replaced by a homogeneous material with effective properties estimated solely from the overall cross-section porosity and the mean value of the matrix elasticity. The Mori-Tanaka method was chosen to derive effective properties because it is known to model the decrease of effective bone stiffness correctly for increasing porosity. More precisely, cortical bone effective stiffness coefficients calculated with the Mori-Tanaka method and the method of asymptotic homogenization[5] (Parnell and Abrahams 2006; Parnell and Grimal 2009) are virtually identical (Parnell et al. 2012), and the latter was validated by comparison with experiments (Granke et al. 2011).

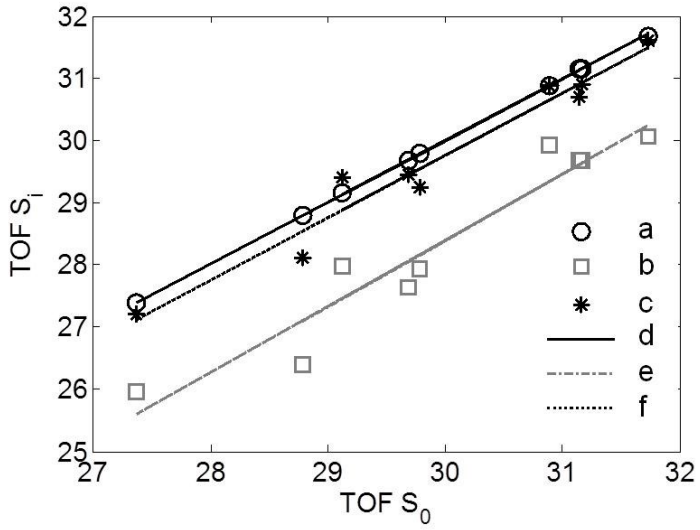

Figure 7.4 Significant correlations of *TOF* of different models with S_0. It reveals that S_4 (c and f) is highly correlated with S_0 (R^2= 0.98) but shows a small offset. In contrast S_3 (b and e) has a larger offset and is worse correlated (R^2=0.93). S_1 and S_0 are almost identical (a and d, R^2=0.99).

Possible explanations for the small bias between *TOF* values obtained for the S_4 and S_0 model-types are: (1) the homogenization method may not give a sufficiently accurate

[5] Asymptotic homogenization code at http://www.labos.upmc.fr/lip/spip.php?rubrique133

estimation of the apparent elasticity sensed by the propagating wave. Parnell et al. (2012) found that the Mori-Tanaka solution is close to the upper Hashin-Rosen bound. Therefore the Mori-Tanaka method may overestimate the apparent elastic properties sensed by the wave and (2) the wave propagation paths may be slightly modified in the homogenized cross-sections compared to the S_0 case, due to a heterogeneous distribution of pores and matrix properties in the cross-section. The measured value of *TOF* is related to a certain wave path, likely through the inferior part of the cortex. Compared to the case of the full model S_0, in the simplified model S_4, the material properties of the cross-section are identical at all points. In particular, if a difference exists between properties in the upper and lower part of the femoral neck, this difference is lost in S_4 for which the material properties will lie between the inferior and superior properties of model S_0. It might prove useful to incorporate in future modeling, possible differences in effective material properties as observed in the present study (chapter 6.1.1.2 and 6.1.1.3). In this study, for instance, significant differences in porosity and elasticity between the inferior and superior part of the femoral neck were found which indicate that the effective material properties at the inferior part are much stiffer compared to the superior part (Malo et al. 2013). The FDTD simulations with these incorporated heterogeneities can be done without additional numerical costs.

The absence of noticeable effects of the bone matrix heterogeneity and the possibility to replace the pore structure by effective properties is related to the fact that the wavelength ($\sim$ 8 mm at the central frequency) was much larger than the characteristic dimension of inhomogeneities.

The possibility to replace the pore structure by effective properties is an important finding because it allows a considerable simplification of sample-specific models for the simulation of the FAS and also more general femur QUS measurements. The actual porosity and matrix elasticity of one sample can be accounted for without the need to model the pores explicitly. Rather, they can be taken into account in an implicit manner by homogenization. Therefore, the FDTD spatial grid step can selected for numerical simulations larger than it would be to model explicitly the microstructure, leading to important reduction of computational costs. In additional computations it was found that the computation time is reduced by a factor of three by changing the FDTD grid step from 16 μm to 80 μm, without compromising the stability of the numerical solution. The size and complexity of the simulation input data is also reduced by resorting to homogenization. An example of such a simulation is shown in Figure 7.5.

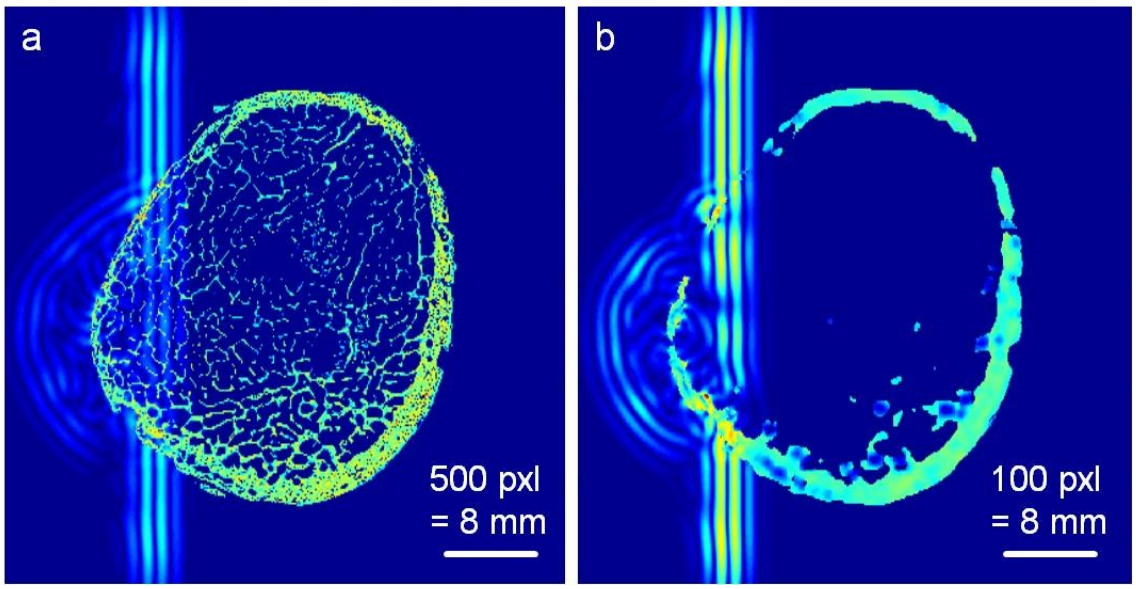

Figure 7.5 (b) Homogenized models of decreased complexity (missing trabecular tissue) and resolution (80 µm) show similar wave propagation but have significantly less computational costs (factor 3) compared to (a) more complex SAM model.

The models presented in study I (chapter 5.2.4.3) enabled a systematic investigation of the influence of the variations of bone properties, such as porosity and elasticity, which have a possible impact on strength. Bone pathologies and therapeutic agents for osteoporosis have been reported to alter the porosity and the mineral content or elasticity of the cortical bone matrix (Boivin and Meunier 2002; Brennan et al. 2009; Borah et al. 2010). Simply disregarding the pores (model S_3) leads to a large decrease of *TOF* meaning that, although the porosity is in average less than 20 %, it contributes to a large part of variations of *TOF*. Also, the sensitivity of QUS to variations of cortical porosity has been reported in experimental studies (Bossy et al. 2004b; Raum et al. 2005a; Grondin et al. 2012; Grimal et al. 2013a). The simulations both indicate that variations of porosity and elasticity of the mineralized matrix, within a physiological range have an impact on *TOF* (Figure 6.17). The latter is likely to be measurable in an experiment given that precision of the estimation of *TOF* is typically well below 1 µs (Grimal et al. 2013a). The rate of variation of *TOF* with varying porosity and c_{33} slightly depends on the sample (Figure 6.17), that is, of the shape of each cross-section. Therefore it seems important, in future studies, to perform multivariate analyses on large collections of samples in order to investigate separately the effects of matrix material properties, porosity, thickness and shape of the sample.

In the model, the effective elasticity of cortical bone was derived from estimations of porosity and elastic properties (c_{33}) of the mineralized matrix obtained with acoustic microscopy. The

latter was estimated from acoustic impedance following the method explained in chapter 5.2.4.2. The effective stiffness in the direction of the femoral neck axis, which is strongly related to the macroscopic Young's modulus in this direction, is an important determinant of the behavior of the femoral neck in axial loading (traction-compression) as well as in bending. The purpose of using QUS is to obtain non-invasively a proxy of strength. Therefore the question of the relationship between the latter and the elasticity of the mineralized matrix, or the cortical porosity, warrants consideration. The porosity is a well-established determinant of strength (Zioupos 2001; Wachter et al. 2002; Zebaze et al. 2010) but the relationship between strength and c_{33} has not been investigated, to the best of knowledge. It should be noted, however, that some authors have found a positive correlation between matrix Young modulus assessed with nanoindentation and strength (Zioupos 2001).

The TOF_{FAS} was found to be influenced by the stiffness of the mineralized matrix and by the porosity. In a previous work, Grondin et al. (2010) found that the TOF_{FAS} is also sensitive to the geometrical parameters of the femoral neck, such as its moments of inertia and cross-sectional area. Since *TOF* is sensitive to several bone properties of the femur neck – material and geometrical properties – it will not be possible in clinical configurations to interpret variations of *TOF* in terms of one or the other properties. Instead, several QUS parameters should be measured. The emerging new generation of QUS methods aims at recovering different bone characteristics (e.g., porosity, stiffness, geometrical parameters)–some of which are not measurable with X-ray approaches–to enhance fracture risk prediction. Elaborated ultrasound measurement and signal processing techniques are under development to derive several independent variables from an experiment (Minonzio et al. 2010; Nauleau et al. 2012). The measured variables can then be used to solve an inverse problem to determine elementary bone characteristics. The inverse problem will be based on a physical model such as those investigated in the present work.

7.2.4 Limitations

7.2.4.1 Limitation Samples

Although the investigation of only one healthy elderly subject (Fd_1 chapter 5.2.1) does not allow drawing of a conclusion on the role of cortical porosity on fracture risk, it does support the findings of a cross-sectional study by Zebaze et al. (2010), who suggested that cortical

porosity may be an important indicator for the identification of individuals at high and low risk of fracture.

The sample set Fd_2 (chapter 5.2.1) includes only bone samples from men, since access to sufficient bone material from female cadavers was limited. Cortical and trabecular tissue areas were identified using the SAM impedance maps, instead of the gold standard method, *i.e.*, histomorphometry. Thus, the present method used for identification of tissue type may include some uncertainty.

7.2.4.2 Limitation SAM

The beam width was 23 µm in the focal plane. This limits the resolution of the SAM images and therefore pores with diameters less than 23 µm *i.e.* canaliculi, Volkmann canals and osteocyte lacunae could not be resolved. However, they make only a minor contribution to the total porosity of the cortical bone (Saied et al. 2008).

For the dataset Fd_2 (chapter 5.2.1), only one elastic coefficient (c_{33}) could be measured to describe elastic behaviour of the bone tissue. In order to obtain other elastic coefficients, samples should be cut into pieces and also measured along transverse directions. However, this was not possible for Fd_2. As evidenced by the present work, it is expected that the anisotropic ratio of the bone matrix also plays an important role during bone aging and for determining bone quality since it is directly connected to ultrastructural arrangement of the mineralized fibrils.

7.2.4.3 Limitation Embedding

The embedding of bone tissue limits the SAM studies, since the replacement of water by the embedding material may increase both the elastic properties and the mass density of the tissue. However, it is a standard procedure for micro-elastic investigations of bone tissue and has been frequently reported in related studies (Gupta et al. 2005; Raum 2008; Manjubala et al. 2009; Isaksson et al. 2010a; Isaksson et al. 2010b)

The effect of embedding was reviewed in Rohrbach et al. (2012b). Embedding was selected for the investigations since it provides long-term tissue fixation. The durability of the samples was essential, since they enabled different measurements using SAM and SRµCT at the same specimens. Moreover, smooth surfaces of the samples are an essential requirement for SAM

measurements which was possible due to easy sample preparation using standard metallographic techniques.

Zimmerman et al. (1994) found an increase of 8 % for apparent stiffness values of embedded bovine samples. The monomer infiltrates the extracellular tissue matrix, cell lacunae and the canalicular network. The replacement of water by the embedding material in the intra- and interfibrillar spaces and in the micro-porous network (osteocyte lacunae and canaliculi) alters the elastic properties of the tissue. For example, tissue having a high degree of mineralization contains less water than tissue with a low degree of mineralization. The samples investigated with data set Fd_1 exhibited a very low variation of *DMB* (coefficient of variation CV = 1.8 %). As evidenced by the present work (Rohrbach et al. 2012b) and previous studies (see chapter 7.2.1), in general the variation of *DMB*, with an average of approximately 1.1 g cm^{-3} (Raum et al. 2006b; Rohrbach et al. 2013) (Table 6.1), or BMDD can be considered to be fairly low (see chapter before). The corresponding volume fractions (*vf*) of mineral (*HA*), collagen (*coll*), and water (H_2O) are vf_{HA} = 0.37, vf_{coll} = 0.36 and vf_{H2O} = 0.27, respectively (Raum et al. 2006a). Wang and Ni investigated the variability of osteocyte lacunar (*OL*) porosity in human cortical tissue (Wang and Ni 2003). They observed a slight age-dependent decrease in osteocyte lacunar porosity (mean ± standard deviation: 1.85 % ± 0.19 %, with a 0.0074 % decrease per year). The variation of matrix stiffness induced by the embedding can be estimated by the rule of mixtures:

$$C_{eff\_native} = \left(1 - vf_{H_2O}\right) C_{native} + vf_{H_2O}\, C_{H_2O} \qquad 7.1$$

and

$$C_{eff\_emb} = \left(1 - vf_{PMMA}\right) C_{native} + vf_{PMMA}\, C_{PMMA} \qquad 7.2$$

With an average measured matrix stiffness of the embedded tissue (C = 35 GPa) and stiffness values for water bound in the lacunae (C_{H2O} = 2.2 GPa (Grimal et al. 2011)) and PMMA (C_{PMMA} = 5.8 GPa (Preininger et al. 2011)), the effective stiffness values and relative difference with embedding compared to native tissue are shown in the Figure 7.6 (a).

This estimation suggests that in addition to a constant increase of approximately 2.8 % at a tissue water volume fraction of 0.27 (*i.e.* for a normal tissue mineralization Figure 7.6 b), potential effects of variations of tissue mineralization (~2 %) and osteocyte lacunar porosity

within the investigated age range (~0.5 %) on the effective stiffness can be considered to be in the order of ~0.3 % and ~0.07 %, respectively. Therefore, it can be assumed that the embedding has an effect on the measured elastic values, but do not considerably contribute to the observed variations with respect to age and anatomical location.

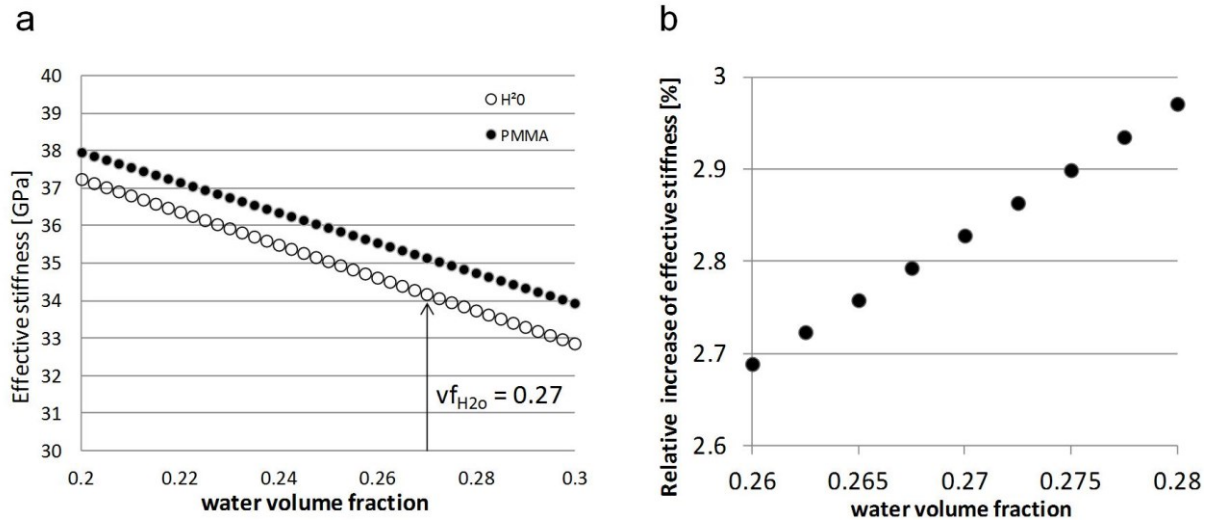

Figure 7.6 (a) Estimated stiffness of native (black circles) and PMMA embedded (black dots) tissue with respect to the water volume fraction. For a normal volume fraction of water (vf_{H2O}=0.27) the replacement of water by the PMMA results in an increase of approximately 2.8 % in the effective stiffness. (b) Relative increase in effective stiffness due to the PMMA embedding as a function of water volume fraction.

7.2.4.4 Limitation FDTM

The simulations have several limitations. Only 2D simulations in a non-dissipative propagation medium were considered. In practice, 3D effects due to the complex femoral neck shape and attenuation expected to play a role needs to be assessed with more complex simulations. Nevertheless, the negligible effect of trabecular bone on the FAS and the possibility to replace, to some extent, the detailed cortical bone microstructure by homogenized properties for simulation are likely to be true also in 3D configurations and when the intrinsic absorption of the tissue is accounted for. In reality (3D), the wave measured via the FAS may not be strictly confined in the plane considered in the simulation due to the slight asymmetry of the femoral neck. A technique to measure the femur neck with a pair of cylindrical transducers (center frequency 0.5 MHz), which probe a cross-sectional slab of the femur neck approximately 6 mm thick, was proposed by Grimal et al. (2013a). Since the effective material properties of the femur neck are not expected to vary significantly within the thickness of the slab, the simulation based on a single cross-section can be considered as a

reasonable model of the physical problem. This is further supported by the investigations of 4 and 5 which could not reveal a significant change in *TOF* of two adjacent sites which are a few mm apart from each other (see chapter 6.1.3, Figure 6.16). Moreover, the effect of bone intrinsic absorption is to diminish the signal amplitude; however it is known that the low-amplitude signal of the circumferential wave can actually be measured (Grimal et al. 2013a).

Moreover, the used simulation code does not implement attenuation effects caused by the viscoelasticity of bone. Future simulation studies should take this into account in order to validate the results and to determine the impact of absorption. However, *in silico* studies at trabecular rich sites have shown that scattering at the trabecular structures mostly account for observed *in vivo* attenuation effects (Bossy et al. 2007)

As samples were embedded in PMMA, the mineralized matrix stiffness probed by SAM is slightly overestimated compared to native stiffness as described in chapter 7.2.4.3. The conclusions of the study should nevertheless be the same for native bones since here relative differences between different models have been investigated and the change in stiffness is only a small offset. The conclusion of the present simulation studies should be confirmed by experiments, that is, in future studies, data simulated with the different models should be compared to measurements.

It is evidenced in previous studies that other bone parameter variations, such as geometry and orientation (Grondin et al. 2010), have a considerable impact on the wave form characteristics such as *TOF*. In future *in silico* experiments considering more complex models, other QUS parameters can be used to obtain additional information on bone quality. For instance the signals could be analyzed in the frequency domain by well-known parameters such as the BUA (Laugier 2008). The scattering behavior of the pores can be used to assess their distribution or size. Recently, Nauleau et al. (2012) have demonstrated the feasibility of measuring different guided wave modes in cortical bone mimicking phantoms. Future studies should identify the combination of easy assessable ultrasound signal characteristics best predicting fracture relevant parameters.

The influence of different center frequencies and/or bandwidths of the excitation signal as well as a further evaluation of adjacent array elements could yield additional information that might be useful to adjust for the impact of geometry and rotation and might deliver additional information for the improvement of the estimation of fracture relevant bone properties.

7.3 Discussion Study II

7.3.1 Using µCT

The evaluation of the bone healing status by X-ray based techniques is highly dependent on the sensitivity of the method to tissues without, or low mineralization. Different image segmentation approaches using thresholds have been reported, for example, the classic global (Muller and Ruegsegger 1997; Muller et al. 1998), adaptive (Burghardt et al. 2007), dual (Buie et al. 2007), and multiple thresholds (Freeman et al. 2009), among others (Duvall et al. 2004; Morgan et al. 2009). The most common approach, however, is to use a fixed global threshold. For this, the proper selection is a delicate step and is user dependent. Moreover, the use of a fixed global threshold implies the assumption of a consistent linear attenuation criterion to the entire reconstructed grayscale image. In addition to the threshold-based segmentation, a manual contouring of the low mineralized callus regions is necessary, which is a very time-consuming and user-dependent procedure.

Within the present work, a novel approach has been developed in collobaration with Bernhard Hesse (Preininger et al. 2012b) to analyze µCT data in terms of sensitivity to small differences in the mineral content of tissues formed within an osteotomy gap after 6 weeks in a small animal model. The proposed method is based on the analysis of gray scale histogram distributions within and adjacent to the tissue repair region. In contrast to conventional segmentation based approaches, the new method does not require manual contouring, which is a very time-consuming and a user-dependent method. Moreover, the novel approach does not use a threshold to segment the mineralized from non-mineralized tissues, which was hypothesized to improve the sensitivity to tissues with very low degrees of mineralization and to reduce the impacts of beam hardening and inter-specimen variability.

A fixed global threshold method, as reported in previous bone healing studies, was used to compare the ability of the new method to differentiate between different healing stages (Mehta et al. 2010). In contrast to the threshold based evaluation, which requires the definition of a global threshold value and the manual contouring of the newly formed callus tissue, the moment based approach proposed in this study only requires the manual selection of the OT gap boundaries along the bone long axis. In terms of processing speed, the conventional method, including defining the VOI, contouring within the VOI, determining the

threshold, rendering, and finally processing the outcome measurements required up to 1.5 hours for each sample. The new method was much more efficient and provided results within a few minutes.

The new method is independent of linear scaling of the gray values and therefore does not require calibration of the µCT images. Therefore, data acquired using different µCT devices, but comparable settings, are anticipated to result in comparable results as long as the correlation of gray values to the linear attenuation coefficients follows a linear relation. If this is not the case, the images must be calibrated before calculation of m_j.

For both the moment and threshold based approaches, correlations between the output parameters were investigated. For the threshold based approach all correlation coefficients were found to be larger than 0.9, which indicated that all parameters describe highly redundant information. Since m_0 and m_1 are calculated based on the amount of mineralized volume obtained from histograms, the observed correlations between BV and m_0 as well as m_1 were not unexpected. However, results of statistical analysis revealed a higher predictive power of the features of the moment based approach. As both parameters are related to the number of voxels that contain mineralized tissue, the moderate correlation between m_0 and BV and the superior predictive value of m_0 support that the histogram based evaluation is more sensitive to tissues with low mineralization than the segmentation based approach. Another reason may be that m_0 describes a relative loss of bone volume in OT region, whereas BV the absolute number of mineralized voxels in the VOI regardless of their location.

Despite the fact that literature offers a rich variety on classifiers, SVM was selected because of its top level rank in performance compared to other popular classifiers (Meyer 2003; Theodoridis 2006) and its wide application (Theodoridis 2006) even in medical imaging (El-Naqa et al. 2002; Zhang et al. 2006). Furthermore, SVM was reported to be robust also with small sample sizes (Hua 2004). In order to minimize the effects of small sample sizes on the outcome, a linear kernel function was used in this study during training. The nearest neighbour algorithm is a very intuitive approach and one of the most and best studied classifiers in literature (Patrick and Fischeriii 1970; Mitchell 1997; Duda 2001; Theodoridis 2006).

Parts of the discussion have been reprinted with permission from the collaboration work with Preininger et al. (2012b) (© Journal of computer assisted tomography).

7.3.2 Using QUS and comparison to µCT

A scanning through-transmission system has been developed and applied to assess the healing status in a small-animal osteotomy model *in vitro*. In contrast to more common approaches that use axial transmission to assess healing in long bones (Barbieri et al. 2011; Barbieri et al. 2012; Protopappas et al. 2008), the scanning approach provides parametric images of the repair region. Until now, similar designs have been used for the assessment of bone fracture risk at the calcaneus (Glüer 1997; Langton and Langton 2000; Laugier 2008) and the proximal femur (Barkmann et al. 2008; Barkmann et al. 2010). Major advantages of a focusing scanning device for the investigation of osteotomies are that i) the OT gap and the surrounding hard and soft tissues can be visualized and ii) quantitative properties can be derived locally from distinct regions within the healing bone. It was demonstrated here that regions filled predominantly with different repair tissues have distinct ultrasound propagation properties. Particularly, the onset of cartilage formation as an indicator of successful healing progression (chapter 2.6) could be seen in the acoustic images, but not in the corresponding µCT projections. The values obtained for the muscle and cartilage regions were consistent with data reported in literature. Nieminen et al. (2004) compared degenerated and normal articular cartilage of bovine specimens using US probes with a center frequency of 10 MHz and found an averaged *BUA* of 0.4 ± 0.14 dB MHz^{-1} mm^{-1} and *SOS* ranging between 1532 m/s and 1633 n/s. Topp and O'Brien, (2000) analyzed semimembranosus and soleus rat muscle tissue at 37 °C in water with focused 6-MHz and 10-MHz transducers. They found *SOS* and *UA* values in the ranges from 1560 to 1590 m/s and 0.2 to 2 dB mm^{-1}, respectively. However, the values measured in the present project may have been altered both, by a mixture of different tissue types along the sound propagation path and the uncertainty in the estimation of the propagation path length.

The focal spot of 0.48 mm of the focused transducer pair allowed the visualization of the OT gap. This enabled the assessment of US transmission properties in the early (non-mineralized) phase, which were not affected by the surrounding mineralized bone tissue. As confirmed by site-matched histology slides, the different attenuation and velocity values were associated with different soft tissues that had been formed in the gap region in the course of healing. While the very early (inflammatory phase, chapter 2.6) phase exhibited predominantly fibrous connective tissue with acoustic properties close to that of muscle tissue, the formation of cartilage results in an appreciable increase of attenuation and a slight increase of the sound velocity. Moreover, it can be seen that the mineralization of the callus results in a dramatic

increase in both, sound velocity (Figure 6.21 f) and attenuation (Figure 6.22 b). The distinction of this healing phase from the two earlier (non-mineralized) phases was therefore not in the focus of the study. However, the data suggest that monitoring in transverse transmission is particularly beneficial for the diagnosis of the early healing process.

While the present work was focused on the analysis on the soft tissue properties, the same setup can also be used to analyze properties of the mineralized tissues. Recent investigations on a sheep tibia OT model have shown that not only the mechanical properties of the mineralized callus change with respect to the healing time but also the cortical tissue undergoes a gradual softening leading to an "elastic handshake" at the cortical-callus tissue interface (Preininger et al. 2011). The measurement of direct and guided waves, as it is done in osteoporosis diagnostics (Laugier 2008), could therefore provide complementary information about the biomechanical competence of the repair zone in the later healing stages. This is further supported by first preliminary numerical simulations showing direct and guided wave propagation and a variation of TOF_{FAS} with the course of healing (chapter 6.2.3). The simulations serve as a first basis for further *in silico* experiments.

The results suggest that attenuation related properties are stronger predictors for different early healing stages than *SOS*. Moreover, *U* and *UA* were found to be the most robust discriminators, since they were almost equally sensitive compared with their propagation-depth normalized counterpart *nUA*.

F-values of most attenuation based parameters were much higher than those obtained from the µCT analyses. Correlations between the µCT and QUS parameters were highly dependent on the analysis type. Good correlations between QUS and µCT based parameters are consistent with previous investigations (Barbieri et al. 2012). Interestingly, the correlation coefficients R^2 were quite high between m_0 and the profile based attenuation parameters U^{PR}, UA^{PR} and nUA^{PR} ($R^2 \geq 0.9$). This suggests that the profile analysis that evaluates changes in the entire OT gap region relative to the adjacent tissue is superior compared to a rather rigid ROI based analysis.

In summary the pilot study is the first step for developing a non-invasive monitoring system for fracture healing in small animals. I expect that the current approach can be refined for *in vivo* measurements in rats. However, further modifications are required to solve practical issues, e.g. fixation and anesthetization of the animal during the experiment, and coupling of the scanning ultrasound transducers to the leg through membranes, additional attenuation

losses caused by the additional soft tissues and interfaces. The latter could require a downshift of the ultrasound frequency, which would decrease the spatial resolution of the system.

7.3.3 Limitations

Study II has several limitations. The most prominent limitation of the studies is the low amount of sample data which could cause a low power of the statistical hypothesis tests (Royall 1986; Dowdy 2004; Tabachnick 2007) and degraded performance of the used classifiers (Raudys and Jain 1991). The relationship between the optimal training size for non-parametric classifiers like k-NN and the dimensionality of the features was reported to be exponential (Raudys and Jain 1991). Since both classifiers used in this study are known to be sensitive to data size and feature dimension, sophisticated statistical testing was utilized to address this limitation. Different statistical analyses (MANOVA, classifier, regression) were performed to verify the results. Canonical analyses were conducted for the μCT evaluation in order to reduce the number of features. The latter was especially important since it was shown that the optimal feature size decreases strongly when the features are highly correlated (Hua 2004), which was the case for the threshold based approach.

Since the number of samples for the QUS investigations was even further reduced, due to the consideration of only two healing stages, sophisticated statistical analysis such as MANOVA or classifiers were inappropriate and have therefore not been conducted. Only group A and B were measured and analysed because the specimens of group C occasionally exhibited strong attenuation which permitted the evaluation of the gap region. The effect was caused by the large callus where the trabecular like woven bone structures act as strong scatters. For the assessment of group C, the QUS system needs refinements, for example by reducing the centre frequency which, however, would result in a decrease in resolution.

In general, the small sample size used in the present study does not allow for generalization of the findings to a larger data set. However, our results indicate that the sensitivity and precision of the classifiers derived from the moment based method are superior than those derived from the threshold based method. Moreover, the higher F-values of ANOVA for some ultrasound parameters such as U^{PR} compared to the even improved moment based μCT evaluation suggest that QUS for the early healing stages (A,B) is a better discriminator. Therefore the results of the present work need to be validated in further and larger case studies.

In addition to the small sample number of this pilot study, a major weakness was the assignment of the specimens into different healing groups based on 2D histology slides (see chapter 5.3.1.3). Bone regeneration is a complex process and healing may occur in an irregular pattern. 2D histology slides may therefore not be representative for the volumetric healing zones measured by US. However, histology is still the "gold standard" method for evaluating soft tissue formation in experimental OT models (Manjubala et al. 2009; Wildemann et al. 2011), and by combining the histology sections with site-matched µCT projections, we have verified that acoustic properties analyzed in the soft tissue regions were non compromised by mineralized callus tissue along the sound propagation path. To further improve the reliability, an experienced observer used well established features that provide clear distinction between the healing stages. It should be noted however that histological analysis is limited to 2-dimensional sections and therefore may not represent the real healing stage of the entire investigated samples.

The QUS experimental setup was restricted to the analysis of 2D time-resolved transmission and reflection projections. The local sample thickness was approximated from the reflected data in one direction only. This approximation can be overcome by an additional pulse-echo scan from the opposite side. However, the approximation proposed in this study demonstrates that the normalization of the thickness was indeed necessary to obtain significant differences between the healing groups, at least for the *SOS* values. In contrast, µCT provides 3D access to the repair region but showed lower discriminatory power for the earlier healing stages which is likely due to the failure in assessing variations of soft tissue formations at these stages.

The moment based and the equivalent QUS profile analysis relies on the evaluation of parameters with respect to the position along the long axis of the bone. A limitation of this method is therefore the assumption that the OT is perpendicular to the z axis. A potential anatomical misalignment of the proximal and distal OT sides may alter the parameters used for the statistical analysis. Hence, only specimens fulfilling this geometric requirement should be evaluated using the described approaches.

8. Conclusion

The present work has successfully demonstrated the high potential of transverse transmission QUS approaches for fracture risk prediction and monitoring fracture healing in small animals. Multimodal and multiscale technologies, such as SAM, SRμCT, μCT or FDTDM simulations were utilized or have been improved. However, most of the conducted studies are considered as pilot studies and their results need to be validated and extended in subsequent investigations. Nevertheless, the developed tools and procedure are expected to be a useful basis.

Several aims should be addressed in further studies. First, numerous case studies with larger sample sets are required to build a database comprising the variations of micro structural and elastic data of human bone. Such a database needs to be established to enable reliable *in silico* experiments. Simulation studies such as FE or FDTDM have been processing rapidly since the past decade but the required profound information about elastic stiffness distributions are still limited and cannot solely be predicted by the mineralization of bone. Second, the proposed methods for modelling bone micro elasticity and structure needs to be extended to build 3D models. Although 2D models were suitable for the applications in the present work, most other investigations rely on more complex 3D models. However, the development of such models involves further challenges since SAM is only a 2D modality. At the moment new models of sheep femora are under development. Third, the application of QUS for fracture risk prediction and monitoring of fracture healing needs further extensive *in silico*, *in vitro*, but also *in vivo* investigations in order to verify the presented results. The development of models which allows a reliable estimation of bone quality related parameters based on ultrasonic signals should be the goal in future studies. I expect that more information can be obtained by using more advanced experimental setups, by assessing different wave paths and ultrasound scattering, and by improving signal processing methods to analyse, for example, guided wave modes. The next steps for monitoring fracture healing on the animal model should be the development of an *in vivo* device and the additional conformation of the presented results by *in silico* experiments.

Nevertheless, the results and developed procedures of the present work provide an important basis for ongoing and future studies to develop QUS approaches for bone quality assessment.

9. Acknowledgment

The present work was carried out during my time as a PhD student at the Berlin-Brandenburg School for Regenerative Therapies and the Julius Wolff Institut of the Charité Berlin.

First of all I would like to give my special thanks to Prof. Kay Raum who provided me with an exceptional level of supervision and guided my research work for more than three years. His remarkable experience and devotion to science and his encouragements, patience and long term support was not only an inspiring example for my own research perspectives but also let me contribute to some open questions in ultrasound based investigations of bone at a very highly international level. With his help, I was able to actively participate and establish some very fruitful collaborations within the successful European QUIMUS and ULAB networks.

With regard to my collaborations, I would like to thank the group of Pascal Laugier, Head of the Laboratoire d'Imagerie Paramétrique, Paris France, and also Quentin Grimal. Their professional comments, critics and productive discussions contributed significantly to the success of the present work. I am very grateful that I had the opportunity of a two month research stay in their group which resulted in a publication of major concern of the present work (Study I).

I also would like to thank the group of Prof. Jukka Jurvelin, Biophysiks of Bone and Cartilage, Kuopio Finland, who provided us with femoral neck cross sections which were the basis for some of the SAM investigations of Study I. I thank Markus Malo for his collaborations in conducting the SAM measurements and his encouragements in publishing that work.

In addition, I would like to thank partners of other collaborations for their discussions, comments and contributions to the present work being Prof. Dr. Claus-C. Glüer, Head of the Biomedical Imaging Group of the Universitätsklinikum Schleswig Holstein, Kiel Germany and Dr. Reinhard Barkmann and Kerstin Rohde of that group. My acknowledgement also goes to the ESRF beamline ID19, Grenoble France in particular to PhD Françoise Peyrin and PhD Max Langer.

I thank my second supervisor Prof. Carsten Perka and my mentor Dr. med. Bernd Preininger for their time, comments, collaborations and their provision of the animal models for study II.

Also thanks go to, Dr. Peter Varga, Bernhard Hesse, Martin Schöne, Nils Männicke, Anke Kadow-Romacker and Nahid Hakiy for being such pleasant colleagues, your comments,

support, discussions and reviews of my work. I thank my students Anne Slawig, Marcus Klüsener and Johannes Schneider for trusting in my mentoring skills. I also thank Gwen Spengler for her professional proofreading and professional comments.

The present work was financially supported by the Deutsche Forschungsgemeinschaft (SPP 1420, grants Ra1380/7; Ge1894/3; BSRT GSC 203, SFB 760 project G-2.2 grant Ra1380/8-1), and the ESFR Long Term Proposal MD239. The project was conducted within the international networks of "Ultrasound Assessment of Bone" (ULAB), Quantitative Imaging of Functional Competence of the Musculoskeletal System (QUIMUS).

Finally I would like to thank my whole family for all their caring and ambitious efforts with regards to all non-scientific but non the less important aspects of my life. In particular, my parents Holger Rohrbach and Cornelia Rohrbach deserve the greatest respect for building a warm and a solid basis for all aspects in my daily life. My special thanks go to my loving girlfriend Saskia Wolff. During the sometimes exhausting time of my PhD with all its deprivations, she always stood by my side and I could always rely on her sympathy and moral support.

10. List of publications

The present thesis is based on the current review of the author's work which has been published in several professional journals of biomedical physics. The following list gives an overview of the author's publications and will be referred in the text by their Roman numerals (Study I**:2,**3; 4-6**;** Study 2: 7,8):

1 Raum K, **Rohrbach D**, Laugier P, Glüer CC, Barkmann R. Bone quality beyond bone mineral density – new diagnostic perspectives by quantitative ultrasound. Osteologie 2010;19:217-24.

2 **Rohrbach D**, Lakshmanan S, Peyrin F, Langer M, Gerisch A, Grimal Q, Laugier P, Raum K. Spatial distribution of tissue level properties in a human femoral cortical bone. Journal of biomechanics 2012;45:2264-70.

3 Malo MKH, **Rohrbach D**, Isaksson H, Töyräs J, Jurvelin JS, Tamminen IS, Kröger H, Raum K. Longitudinal elastic properties and porosity of cortical bone tissue vary with age in human proximal femur. Bone 2013;53:451-8.

4 **Rohrbach D**, Grondin J, Grimal Q, Laugier P, Barkmann R, Raum K. Evidence based numerical ultrasound simulations at the human femoral neck. Biomedizinische Technik, Rostock, conference proceeding 2010

5 Grimal Q, **Rohrbach D**[6], Grondin J, Barkmann R, Glüer C, Raum K, Laugier P. Modeling of femoral neck cortical bone for the numerical simulation of ultrasound propagation. Biomech Model Mechanobiol 2012;submitted, under revision

6 Rohde K, **Rohrbach D**, Glüer C, Laugier P, Grimal Q, Raum K, Barkmann R. Influence of porosity, pore size and cortical thickness on the propagation of ultrasonic waves guided through the femoral neck cortex: a simulation study. Transactions on Ultrasonics, Ferroelectrics, and Frequency Control 2012;submitted paper.

7 Preininger B, Hesse B, **Rohrbach D**, Varga P, Gerigk H, Langer M, Peyrin F, Perka C, Raum K. Histogram feature-based classification improves differentiability of early bone healing stages from micro-computed tomographic data. Journal of computer assisted tomography 2012;36:469-76.

8 **Rohrbach D**, Preininger B, Hesse B, Gerigk H, Perka C, Raum K. The early phases of bone healing can be differentiated in a rat osteotomy model by focused transverse-transmission ultrasound. Ultrasound in medicine & biology 2013;submitted and accepted

[6] shared first authorship

Daniel Rohrbach Berlin, 06.05.2013

11. Selbstständigkeitserklärung

Ich erkläre hiermit, dass ich die vorliegende Arbeit selbstständig und nur unter Verwendung der angegebenen Hilfen und Hilfsmittel angefertigt habe. Alle Stellen, die wörtlich oder sinngemäß aus Quellen entnommen wurden, sind als solche gekennzeichnet. Abbildungen, die anderen Quellen unverändert entnommen oder diesen entlehnt wurden, sind mit der Quellenangabe versehen.

Ich versichere, dass ich mich nicht anderweitig um einen Doktorgrad beworben habe oder einen entsprechenden Doktortitel besitze. Die Promotionsordnung der Mathematisch-Naturwissenschaftlichen Fakultät I der Humboldt-Universität zu Berlin habe ich gelesen und akzeptiert.

Daniel Rohrbach Berlin, 06.05.2013

12. References

Consensus development conference: Diagnosis, prophylaxis and treatment of osteoporosis. American Journal of Medicine 1991;90:107-10.

Abendsch.Wf, Hyatt GW. Ultrasonics and Physical Properties of Healing Bone. J Traum 1972;12:297-&.

Abrahamsen B, van Staa T, Ariely R, Olson M, Cooper C. Excess mortality following hip fracture: a systematic epidemiological review. Osteoporosis international : a journal established as result of cooperation between the European Foundation for Osteoporosis and the National Osteoporosis Foundation of the USA 2009;20:1633-50.

Adams JE. Advances in bone imaging for osteoporosis. Nature reviews Endocrinology 2012;9:28-42.

Amprino R. Investigations on some physical properties of bone tissue. Acta anatomica 1958;34:161-86.

Anast GT, Fields T, Siegel IM. Ultrasonic technique for the evaluation of bone fractures. American journal of physical medicine 1958;37:157-9.

Ashman RB, Cowin SC, Van Buskirk WC, Rice JC. A continuous wave technique for the measurement of the elastic properties of cortical bone. Journal of biomechanics 1984;17:349-61.

Aula AS, Toyras J, Hakulinen MA, Jurvelin JS. Effect of bone marrow on acoustic properties of trabecular bone--3D finite difference modeling study. Ultrasound in medicine & biology 2009;35:308-18.

Auld BA. Acoustic Fields and Waves in Solids. Florida: Krieger Publishing Company, 1990.

Austman RL, Milner JS, Holdsworth DW, Dunning CE. The effect of the density-modulus relationship selected to apply material properties in a finite element model of long bone. Journal of biomechanics 2008;41:3171-6.

Barbieri G, Barbieri CH, Mazzer N, Pela CA. Ultrasound propagation velocity and broadband attenuation can help evaluate the healing process of an experimental fracture. Journal of orthopaedic research : official publication of the Orthopaedic Research Society 2011a;29:444-51.

Barbieri G, Mazzer N, Ribeiro EA, Nogueira-Barbosa MH, Barbieri CH. A comparative analysis between Ultrasonometry and computer-aided tomography to evaluate bone healing. Journal of orthopaedic research : official publication of the Orthopaedic Research Society 2011b;

Barkmann R, Dencks S, Laugier P, Padilla F, Brixen K, Ryg J, Seekamp A, Mahlke L, Bremer A, Heller M, Gluer CC. Femur ultrasound (FemUS)--first clinical results on hip fracture discrimination and estimation of femoral BMD. Osteoporosis international : a journal established as result of cooperation between the European Foundation for Osteoporosis and the National Osteoporosis Foundation of the USA 2009;21:969-76.

Barkmann R, Dencks S, Laugier P, Padilla F, Brixen K, Ryg J, Seekamp A, Mahlke L, Bremer A, Heller M, Gluer CC. Femur ultrasound (FemUS)--first clinical results on hip fracture discrimination and estimation of femoral BMD. Osteoporosis international : a journal established as result of cooperation between the European Foundation for Osteoporosis and the National Osteoporosis Foundation of the USA 2010a;21:969-76.

Barkmann R, Dencks S, Laugier P, Padilla F, Brixen K, Ryg J, Seekamp A, Mahlke L, Bremer A, Heller M, Glüer CC. Femur ultrasound (FemUS)—first clinical results on hip fracture discrimination and estimation of femoral BMD. Osteoporosis international : a journal established as result of cooperation between the European Foundation for Osteoporosis and the National Osteoporosis Foundation of the USA 2010b;21:969-76.

Barkmann R, Glüer C-C. Clinical Applications, Bone Quantitative Ultrasound. In: Laugier P, Haïat G, ed. Springer Netherlands, 2011. pp. 73-81.

Barkmann R, Laugier P, Moser U, Dencks S, Klausner M, Padilla F, Haiat G, Gluer CC. A device for in vivo measurements of quantitative ultrasound variables at the human proximal femur. IEEE Trans Ultrason Ferroelectr Freq Control 2008a;55:1197-204.

Barkmann R, Laugier P, Moser U, Dencks S, Klausner M, Padilla F, Haiat G, Heller M, Gluer CC. In vivo measurements of ultrasound transmission through the human proximal femur. Ultrasound in medicine & biology 2008b;34:1186-90.

Barkmann R, Laugier P, Moser U, Dencks S, Padilla F, Haiat G, Heller M, Gluer CC. A method for the estimation of femoral bone mineral density from variables of ultrasound transmission through the human femur. Bone 2007;40:37-44.

Barkmann R, Lusse S, Stampa B, Sakata S, Heller M, Gluer CC. Assessment of the geometry of human finger phalanges using quantitative ultrasound in vivo. Osteoporosis international : a journal established as result of cooperation between the European Foundation for Osteoporosis and the National Osteoporosis Foundation of the USA 2000;11:745-55.

Bell KL, Loveridge N, Power J, Garrahan N, Meggitt BF, Reeve J. Regional differences in cortical porosity in the fractured femoral neck. Bone 1999a;24:57-64.

Bell KL, Loveridge N, Power J, Garrahan N, Stanton M, Lunt M, Meggitt BF, Reeve J. Structure of the femoral neck in hip fracture: cortical bone loss in the inferoanterior to superoposterior axis. Journal of bone and mineral research : the official journal of the American Society for Bone and Mineral Research 1999b;14:111-9.

Bell KL, Loveridge N, Reeve J, Thomas CD, Feik SA, Clement JG. Super-osteons (remodeling clusters) in the cortex of the femoral shaft: influence of age and gender. Anat Rec 2001;264:378-86.

Bensamoun S, Gherbezza JM, de Belleval JF, Ho Ba Tho MC. Transmission scanning acoustic imaging of human cortical bone and relation with the microstructure. Clin Biomech (Bristol, Avon) 2004a;19:639-47.

Bensamoun S, Ho Ba Tho MC, Luu S, Gherbezza JM, de Belleval JF. Spatial distribution of acoustic and elastic properties of human femoral cortical bone. Journal of biomechanics 2004b;37:503-10.

Bercoff J, Tanter M, Fink M. Supersonic shear imaging: a new technique for soft tissue elasticity mapping. IEEE Trans Ultrason Ferroelectr Freq Control 2004;51:396-409.

Bergmann G, Deuretzbacher G, Heller M, Graichen F, Rohlmann A, Strauss J, Duda GN. Hip contact forces and gait patterns from routine activities. Journal of biomechanics 2001;34:859-71.

Bernard S, Grimal Q, Laugier P. Accurate measurement of cortical bone elasticity tensor with resonant ultrasound spectroscopy. Journal of the mechanical behavior of biomedical materials 2012;

Binkley N, Adler RA. Chapter 43 - Dual-Energy X-ray Absorptiometry (DXA) in Men. In: Eric SO, John PB, Dirk VanderschuerenA2 - Eric S. Orwoll JPB, Dirk V, ed. Osteoporosis in Men (Second Edition). San Diego: Academic Press, 2010. pp. 525-40.

Blake GM, Fogelman I. Technical principles of dual energy x-ray absorptiometry. Seminars in nuclear medicine 1997;27:210-28.

Blake GM, Fogelman I. An update on dual-energy x-ray absorptiometry. Seminars in nuclear medicine 2010;40:62-73.

Blokhuis TJ, de Bruine JH, Bramer JA, den Boer FC, Bakker FC, Patka P, Haarman HJ, Manoliu RA. The reliability of plain radiography in experimental fracture healing. Skeletal radiology 2001;30:151-6.

Boccaccio A, Vena P, Gastaldi D, Franzoso G, Pietrabissa R, Pappalettere C. Finite element analysis of cancellous bone failure in the vertebral body of healthy and osteoporotic subjects. Proceedings of the Institution of Mechanical Engineers Part H, Journal of engineering in medicine 2008;222:1023-36.

Boivin G, Meunier PJ. The degree of mineralization of bone tissue measured by computerized quantitative contact microradiography. CalcifTissue Int 2002;70:503-11.

Bonewald LF. The amazing osteocyte. Journal of bone and mineral research : the official journal of the American Society for Bone and Mineral Research 2011;26:229-38.

Borah B, Dufresne T, Nurre J, Phipps R, Chmielewski P, Wagner L, Lundy M, Bouxsein M, Zebaze R, Seeman E. Risedronate reduces intracortical porosity in women with osteoporosis. Journal of bone and mineral research : the official journal of the American Society for Bone and Mineral Research 2010;25:41-7.

Bossy E, Grimal Q. Numerical Methods for Ultrasonic Bone Characterization, Bone Quantitative Ultrasound. In: Laugier P, Haïat G, ed. Springer Netherlands, 2011. pp. 181-228.

Bossy E, Laugier P, Peyrin F, Padilla F. Attenuation in trabecular bone: A comparison between numerical simulation and experimental results in human femur. J Acoust Soc Am 2007;122:2469-75.

Bossy E, Padilla F, Peyrin F, Laugier P. Three-dimensional simulation of ultrasound propagation through trabecular bone structures measured by synchrotron microtomography. PhysMedBiol 2005;50:5545-56.

Bossy E, Talmant M, Laugier P. Effect of bone cortical thickness on velocity measurements using ultrasonic axial transmission: a 2D simulation study. J Acoust Soc Am 2002;112:297-307.

Bossy E, Talmant M, Laugier P. Three-dimensional simulations of ultrasonic axial transmission velocity measurement on cortical bone models. JAcoustSocAm 2004a;115:2314-24.

Bossy E, Talmant M, Peyrin F, Akrout L, Cloetens P, Laugier P. An in vitro study of the ultrasonic axial transmission technique at the radius: 1-MHz velocity measurements are sensitive to both mineralization and intracortical porosity. JBone MinerRes 2004b;19:1548-56.

Bousson V, Peyrin F, Bergot C, Hausard M, Sautet A, Laredo JD. Cortical bone in the human femoral neck: three-dimensional appearance and porosity using synchrotron radiation. Journal of bone and mineral research : the official journal of the American Society for Bone and Mineral Research 2004;19:794-801.

Breban S, Padilla F, Fujisawa Y, Mano I, Matsukawa M, Benhamou CL, Otani T, Laugier P, Chappard C. Trabecular and cortical bone separately assessed at radius with a new ultrasound device, in a young adult population with various physical activities. Bone 2010;46:1620-5.

Brennan TC, Rizzoli R, Ammann P. Selective modification of bone quality by PTH, pamidronate, or raloxifene. Journal of bone and mineral research : the official journal of the American Society for Bone and Mineral Research 2009;24:800-8.

Briggs A. Acoustic microscopy. Oxford ; New York: Oxford University Press, 2010.

Britz HM, Thomas CD, Clement JG, Cooper DM. The relation of femoral osteon geometry to age, sex, height and weight. Bone 2009;45:77-83.

Buie HR, Campbell GM, Klinck RJ, MacNeil JA, Boyd SK. Automatic segmentation of cortical and trabecular compartments based on a dual threshold technique for in vivo micro-CT bone analysis. Bone 2007;41:505-15.

Burghardt AJ, Kazakia GJ, Majumdar S. A local adaptive threshold strategy for high resolution peripheral quantitative computed tomography of trabecular bone. Annals of biomedical engineering 2007;35:1678-86.

Camacho NP, Rinnerthaler S, Paschalis EP, Mendelsohn R, Boskey AL, Fratzl P. Complementary information on bone ultrastructure from scanning small angle X-ray scattering and Fourier-transform infrared microspectroscopy. Bone 1999;25:287-93.

Carter Y, Thomas CD, Clement JG, Peele AG, Hannah K, Cooper DM. Variation in osteocyte lacunar morphology and density in the human femur--a synchrotron radiation micro-CT study. Bone 2013;52:126-32.

Chaffai S, Padilla F, Berger G, Laugier P. In vitro measurement of the frequency-dependent attenuation in cancellous bone between 0.2 and 2 MHz. J Acoust Soc Am 2000;108:1281-9.

Chappard C, Bensalah S, Olivier C, Gouttenoire PJ, Marchadier A, Benhamou C, Peyrin F. 3D characterization of pores in the cortical bone of human femur in the elderly at different locations as determined by synchrotron micro-computed tomography images. Osteoporosis international : a journal established as result of cooperation between the European Foundation for Osteoporosis and the National Osteoporosis Foundation of the USA 2012;

Chen H, Zhou X, Shoumura S, Emura S, Bunai Y. Age- and gender-dependent changes in three-dimensional microstructure of cortical and trabecular bone at the human femoral neck. Osteoporosis international : a journal established as result of cooperation between the European Foundation for Osteoporosis and the National Osteoporosis Foundation of the USA 2010;21:627-36.

Chen P, Miller PD, Recker R, Resch H, Rana A, Pavo I, Sipos AA. Increases in BMD correlate with improvements in bone microarchitecture with teriparatide treatment in postmenopausal women with osteoporosis. Journal of bone and mineral research : the official journal of the American Society for Bone and Mineral Research 2007;22:1173-80.

Cheng XG, Lowet G, Boonen S, Nicholson PH, Brys P, Nijs J, Dequeker J. Assessment of the strength of proximal femur in vitro: relationship to femoral bone mineral density and femoral geometry. Bone 1997;20:213-8.

Chih-Wei H, Chih-Jen L. A comparison of methods for multiclass support vector machines. IEEE Transactions on Neural Networks 2002;13:415-25.

Claes L, Recknagel S, Ignatius A. Fracture healing under healthy and inflammatory conditions. Nature reviews Rheumatology 2012;8:133-43.

Cohen GC. Higher-order numerical methods for transient wave equations. Berlin; New York: Springer, 2002.

Collino F, Tsogka C. Application of the perfectly matched absorbing layer model to the linear elastodynamic problem in anisotropic heterogeneous media. Geophysics 2001;66:

Cooper DM, Erickson B, Peele AG, Hannah K, Thomas CD, Clement JG. Visualization of 3D osteon morphology by synchrotron radiation micro-CT. Journal of anatomy 2011;219:481-9.

Cooper DM, Thomas CD, Clement JG, Turinsky AL, Sensen CW, Hallgrimsson B. Age-dependent change in the 3D structure of cortical porosity at the human femoral midshaft. Bone 2007;40:957-65.

Cortes C, Vapnik V. Support-vector networks. Machine Learning 1995;20:273-97.

Cover T, Hart P. Nearest neighbor pattern classification. IEEE Transactions on Information Theory 1967;13:21-7.

Cowin SC, Cardoso L. Fabric dependence of wave propagation in anisotropic porous media. Biomech Model Mechanobiol 2011;10:39-65.

Cunningham JL, Kenwright J, Kershaw CJ. Biomechanical measurement of fracture healing. J Med Eng Technol 1990;14:92-101.

Currey JD. The structure of bone tissue. In: ed. 2002. pp. 4

-26.

Currey JD. Bones: structure and mechanics. Princeton, N.J.; Oxford: Princeton University Press, 2006.

Delmas PD, Li Z, Cooper C. Relationship between changes in bone mineral density and fracture risk reduction with antiresorptive drugs: some issues with meta-analyses. Journal of bone and mineral research : the official journal of the American Society for Bone and Mineral Research 2004;19:330-7.

Dencks S, Barkmann R, Padilla F, Laugier P, Schmitz G, Gluer CC. Model-based estimation of quantitative ultrasound variables at the proximal femur. IEEE Trans Ultrason Ferroelectr Freq Control 2008;55:1304-15.

Dodd SP, Cunningham JL, Miles AW, Gheduzzi S, Humphrey VF. An in vitro study of ultrasound signal loss across simple fractures in cortical bone mimics and bovine cortical bone samples. Bone 2007;40:656-61.

Donath T, Pfeiffer F, Bunk O, Grunzweig C, Hempel E, Popescu S, Vock P, David C. Toward clinical X-ray phase-contrast CT: demonstration of enhanced soft-tissue contrast in human specimen. Investigative radiology 2010;45:445-52.

Dowdy S. Statistics for research. Hoboken N.J.: Wiley-Interscience, 2004.

Duda GN, Heller M, Albinger J, Schulz O, Schneider E, Claes L. Influence of muscle forces on femoral strain distribution. Journal of biomechanics 1998;31:841-6.

Duda GN, Schneider E, Chao EYS. Internal forces and moments in the femur during walking. Journal of biomechanics 1997;30:933-41.

Duda R. Pattern classification. New York: Wiley, 2001.

Duvall CL, Taylor WR, Weiss D, Guldberg RE. Quantitative microcomputed tomography analysis of collateral vessel development after ischemic injury. Am J Physiol Heart Circ Physiol 2004;287:H302-10.

El-Naqa I, Yongyi Y, Wernick MN, Galatsanos NP, Nishikawa RM. A support vector machine approach for detection of microcalcifications. IEEE Transactions on Medical Imaging 2002;21:1552-63.

Ericksen MF. Aging changes in thickness of the proximal femoral cortex. American journal of physical anthropology 1982;59:121-30.

Espinoza Orias AA, Deuerling JM, Landrigan MD, Renaud JE, Roeder RK. Anatomic variation in the elastic anisotropy of cortical bone tissue in the human femur. Journal of the mechanical behavior of biomedical materials 2009;2:255-63.

Evans GP, Behiri JC, Currey JD, Bonfield W. Microhardness and Young Modulus in Cortical Bone Exhibiting a Wide-Range of Mineral Volume Fractions, and in a Bone Analog. J Mater Sci-Mater M 1990;1:38-43.

Fawcett T. An introduction to ROC analysis. Pattern Recognition Letters 2006;27:861-74.

Fernandez Caballero JC, Martinez FJ, Hervas C, Gutierrez PA. Sensitivity versus accuracy in multiclass problems using memetic Pareto evolutionary neural networks. IEEE Trans Neural Netw 2010;21:750-70.

Fieldsend JE, Everson RM. Formulation and comparison of multi-class ROC surfaces. PROCEEDINGS OF THE ICML 2005 WORKSHOP ON ROC ANALYSIS IN MACHINE LEARNING 2005;41--8---8.

Firouzi K, Cox B, Treeby BE, Saffari N. A first-order k-space model for elastic wave propagation in heterogeneous media. The Journal of the Acoustical Society of America 2011;129:2611-.

Foiret J, Minonzio JG, Talmant M, Laugier P. Cortical bone quality assessment using quantitative ultrasound on long bones. Conference proceedings : Annual International Conference of the IEEE Engineering in Medicine and Biology Society IEEE Engineering in Medicine and Biology Society Conference 2012;2012:1121-4.

Foster FS, Pavlin CJ, Harasiewicz KA, Christopher DA, Turnbull DH. Advances in ultrasound biomicroscopy. Ultrasound In Medicine And Biology 2000;26:1-27.

Franzoso G, Zysset PK. Elastic anisotropy of human cortical bone secondary osteons measured by nanoindentation. Journal of biomechanical engineering 2009;131:021001.

Fratzl-Zelman N, Roschger P, Gourrier A, Weber M, Misof BM, Loveridge N, Reeve J, Klaushofer K, Fratzl P. Combination of nanoindentation and quantitative backscattered electron imaging revealed altered bone material properties associated with femoral neck fragility. Calcified tissue international 2009;85:335-43.

Fratzl P, Weinkamer R. Hierarchical Structure and Repair of Bone: Deformation, Remodelling, Healing. In: Zwaag S, ed. Self Healing Materials. Springer Netherlands, 2008. pp. 323-35.

Freeman TA, Patel P, Parvizi J, Antoci V, Jr., Shapiro IM. Micro-CT analysis with multiple thresholds allows detection of bone formation and resorption during ultrasound-treated fracture healing. Journal of orthopaedic research : official publication of the Orthopaedic Research Society 2009;27:673-9.

Gelalis ID, Politis AN, Arnaoutoglou CM, Korompilias AV, Pakos EE, Vekris MD, Karageorgos A, Xenakis TA. Diagnostic and treatment modalities in nonunions of the femoral shaft: a review. Injury 2012;43:980-8.

Gelse K, Olk A, Eichhorn S, Swoboda B, Schoene M, Raum K. Quantitative ultrasound biomicroscopy for the analysis of healthy and repair cartilage tissue. European cells & materials 2010;19:58-71.

Gerlanc M, Haddad D, Hyatt GW, Langloh JT, St Hilaire P. Ultrasonic study of normal and fractured bone. Clinical orthopaedics and related research 1975;175-80.

Gheduzzi S, Dodd SP, Miles AW, Humphrey VF, Cunningham JL. Numerical and experimental simulation of the effect of long bone fracture healing stages on ultrasound transmission across an idealized fracture. J Acoust Soc Am 2009;126:887-94.

Gill PJ, Kernohan G, Mawhinney IN, Mollan RA, McIlhagger R. Investigation of the mechanical properties of bone using ultrasound. Proceedings of the Institution of Mechanical Engineers Part H, Journal of engineering in medicine 1989;203:61-3.

Giraud-Guille MM. Twisted plywood architecture of collagen fibrils in human compact bone osteons. Calcified tissue international 1988;42:167-80.

Glüer CC. Quantitative ultrasound techniques for the assessment of osteoporosis: expert agreement on current status. The International Quantitative Ultrasound Consensus Group. Journal of Bone and Mineral Research: The Official Journal of the American Society for Bone and Mineral Research 1997;12:1280-8.

Granke M, Grimal Q, Saied A, Nauleau P, Peyrin F, Laugier P. Change in porosity is the major determinant of the variation of cortical bone elasticity at the millimeter scale in aged women. Bone 2011;49:1020-6.

Grassi L, Schileo E, Taddei F, Zani L, Juszczyk M, Cristofolini L, Viceconti M. Accuracy of finite element predictions in sideways load configurations for the proximal human femur. Journal of biomechanics 2012;45:394-9.

Graves RW. Simulating seismic wave propagation in 3D elastic media using staggered-grid finite differences. Bulletin of the Seismological Society of America 1996;86:1091-106.

Griffith JF, Genant HK. New advances in imaging osteoporosis and its complications. Endocrine 2012;42:39-51.

Grimal Q, Grondin J, Guerard S, Barkmann R, Engelke K, Gluer CC, Laugier P. Quantitative ultrasound of cortical bone in the femoral neck predicts femur strength: results of a pilot study. Journal of bone and mineral research : the official journal of the American Society for Bone and Mineral Research 2013a;28:302-12.

Grimal Q, Haupert S, Mitton D, Vastel L, Laugier P. Assessment of cortical bone elasticity and strength: mechanical testing and ultrasound provide complementary data. Medical engineering & physics 2009;31:1140-7.

Grimal Q, Raum K, Gerisch A, Laugier P. Derivation of the mesoscopic elasticity tensor of cortical bone from quantitative impedance images at the micron scale. ComputMethods BiomechBiomedEngin 2008;11:147-57.

Grimal Q, Rohrbach D, Grondin J, Barkmann R, Glüer C, Raum K, Laugier P. Modeling of femoral neck cortical bone for the numerical simulation of ultrasound propagation. Biomech Model Mechanobiol 2013b;submitted, under revision:

Grimal Q, Rus G, Parnell WJ, Laugier P. A two-parameter model of the effective elastic tensor for cortical bone. Journal of biomechanics 2011;44:1621-5.

Grondin J, Grimal Q, Engelke K, Laugier P. Potential of first arriving signal to assess cortical bone geometry at the Hip with QUS: a model based study. Ultrasound in medicine & biology 2010;36:656-66.

Grondin J, Grimal Q, Yamamoto K, Matsukawa M, Saied A, Laugier P. Relative contributions of porosity and mineralized matrix properties to the bulk axial ultrasonic wave velocity in human cortical bone. Ultrasonics 2012;52:467-71.

Guo XE, Liu XS, Wehrli FW. Advanced Structural Assessment of Bone Using CT and MRI. In: ed. Osteoporosis in Men. Elsevier, 2010. pp. 547-64.

Gupta HS, Schratter S, Tesch W, Roschger P, Berzlanovich A, Schoeberl T, Klaushofer K, Fratzl P. Two different correlations between nanoindentation modulus and mineral content in the bone-cartilage interface. Journal of structural biology 2005;149:138-48.

Haiat G, Padilla F, Cleveland RO, Laugier P. Effects of frequency-dependent attenuation and velocity dispersion on in vitro ultrasound velocity measurements in intact human femur specimens. IEEE T Ultrason Ferr 2006;53:39-51.

Haiat G, Padilla F, Peyrin F, Laugier P. Fast wave ultrasonic propagation in trabecular bone: numerical study of the influence of porosity and structural anisotropy. J Acoust Soc Am 2008;123:1694-705.

Hakulinen MA, Day JS, Toyras J, Weinans H, Jurvelin JS. Ultrasonic characterization of human trabecular bone microstructure. Physics in medicine and biology 2006;51:1633-48.

Hammer RR, Hammerby S, Lindholm B. Accuracy of radiologic assessment of tibial shaft fracture union in humans. Clinical orthopaedics and related research 1985;233-8.

Harwood PJ, Newman JB, Michael ALR. (ii) An update on fracture healing and non-union. Orthopaedics and Trauma 2010;24:9-23.

Heller MO, Bergmann G, Kassi JP, Claes L, Haas NP, Duda GN. Determination of muscle loading at the hip joint for use in pre-clinical testing. Journal of biomechanics 2005;38:1155-63.

Hellmich C, Barthelemy JF, Dormieux L. Mineral-collagen interactions in elasticity of bone ultrastructure - a continuum micromechanics approach. European Journal of Mechanics A-Solids 2004;23:783-810.

Hodgskinson R, Currey JD, Evans GP. Hardness, an indicator of the mechanical competence of cancellous bone. Journal of orthopaedic research : official publication of the Orthopaedic Research Society 1989;7:754-8.

Hofmann T, Heyroth F, Meinhard H, Franzel W, Raum K. Assessment of composition and anisotropic elastic properties of secondary osteon lamellae. J Biomech 2005;

Holzer G, von Skrbensky G, Holzer LA, Pichl W. Hip fractures and the contribution of cortical versus trabecular bone to femoral neck strength. Journal of bone and mineral research : the official journal of the American Society for Bone and Mineral Research 2009;24:468-74.

Hosokawa A. Numerical investigation of ultrasound refraction caused by oblique orientation of trabecular network in cancellous bone. IEEE Trans Ultrason Ferroelectr Freq Control 2011;58:1389-96.

Hu F, Jiang C, Shen J, Tang P, Wang Y. Preoperative predictors for mortality following hip fracture surgery: a systematic review and meta-analysis. Injury 2012;43:676-85.

Hua J. Optimal number of features as a function of sample size for various classification rules. Bioinformatics 2004;21:1509-15.

Hube R, Mayr H, Hein W, Raum K. Prediction of biomechanical stability after callus distraction by high resolution scanning acoustic microscopy. Ultrasound In Medicine And Biology 2006;32:1913-21.

Huiskes R, Ruimerman R, van Lenthe GH, Janssen JD. Effects of mechanical forces on maintenance and adaptation of form in trabecular bone. Nature 2000;405:704-6.

Hwang SN, Wehrli FW, Williams JL. Probability-based structural parameters from three-dimensional nuclear magnetic resonance images as predictors of trabecular bone strength. Medical physics 1997;24:1255-61.

Isaksson H, Malkiewicz M, Nowak R, Helminen HJ, Jurvelin JS. Rabbit cortical bone tissue increases its elastic stiffness but becomes less viscoelastic with age. Bone 2010a;47:1030-8.

Isaksson H, Nagao S, Malkiewicz M, Julkunen P, Nowak R, Jurvelin JS. Precision of nanoindentation protocols for measurement of viscoelasticity in cortical and trabecular bone. Journal of biomechanics 2010b;43:2410-7.

Isaksson H, Wilson W, van Donkelaar CC, Huiskes R, Ito K. Comparison of biophysical stimuli for mechano-regulation of tissue differentiation during fracture healing. Journal of biomechanics 2006;39:1507-16.

Jensen JA. A model for the propagation and scattering of ultrasound in tissue. J Acoust Soc Am 1991;89:182-90.

Jensen JA. Simulating Arbitrary-Geometry Ultrasound Transducers Using Triangles. 1996b.

Jensen JA. A new calculation procedure for spatial impulse responses in ultrasound. The Journal of the Acoustical Society of America 1999;105:3266-.

Jensen JA, Svendsen NB. Calculation of pressure fields from arbitrarily shaped, apodized, and excited ultrasound transducers. IEEE T Ultrason Ferr 1992;39:262-7.

Jorgensen CS, Kundu T. Measurement of material elastic constants of trabecular bone: a micromechanical analytic study using a 1 GHz acoustic microscope. JOrthopRes 2002;20:151-8.

Kanis JA, Oden A, Johnell O, Johansson H, De Laet C, Brown J, Burckhardt P, Cooper C, Christiansen C, Cummings S, Eisman JA, Fujiwara S, Gluer C, Goltzman D, Hans D, Krieg MA, La Croix A, McCloskey E, Mellstrom D, Melton LJ, 3rd, Pols H, Reeve J, Sanders K, Schott AM, Silman A, Torgerson D, van Staa T, Watts NB, Yoshimura N. The use of clinical risk factors enhances the performance of BMD in the prediction of hip and osteoporotic fractures in men and women. Osteoporosis international : a journal established as result of cooperation between the European Foundation for Osteoporosis and the National Osteoporosis Foundation of the USA 2007;18:1033-46.

Karjalainen J, Riekkinen O, Toyras J, Kroger H, Jurvelin J. Ultrasonic assessment of cortical bone thickness in vitro and in vivo. IEEE Trans Ultrason Ferroelectr Freq Control 2008;55:2191-7.

Karjalainen JP, Riekkinen O, Toyras J, Hakulinen M, Kroger H, Rikkonen T, Salovaara K, Jurvelin JS. Multi-site bone ultrasound measurements in elderly women with and without previous hip fractures. Osteoporosis international : a journal established as result of cooperation between the European Foundation for Osteoporosis and the National Osteoporosis Foundation of the USA 2012;23:1287-95.

Karunaratne A, Boyde A, Esapa CT, Hiller J, Terrill NJ, Brown SD, Cox RD, Thakker RV, Gupta HS. Symmetrically reduced stiffness and increased extensibility in compression and tension at the mineralized fibrillar level in rachitic bone. Bone 2013;52:689-98.

Kaufman JJ, Luo G, Siffert RS. Ultrasound simulation in bone. IEEE Trans Ultrason Ferroelectr Freq Control 2008;55:1205-18.

Kaufman JM, Reginster JY, Boonen S, Brandi ML, Cooper C, Dere W, Devogelaer JP, Diez-Perez A, Kanis JA, McCloskey E, Mitlak B, Orwoll E, Ringe JD, Weryha G, Rizzoli R. Treatment of osteoporosis in men. Bone 2013;53:134-44.

Kim TJ, Grill W. Determination of the velocity of ultrasound by short pulse switched sinusoidal excitation and phase-sensitive detection by a computer-controlled pulse-echo system. Ultrasonics 1998;36:233-8.

Kino GS. Acoustic waves: devices, imaging, and analog signal processing. Englewood Cliffs, N.J: Prentice-Hall, 1987.

Kooistra BW, Dijkman BG, Busse JW, Sprague S, Schemitsch EH, Bhandari M. The radiographic union scale in tibial fractures: reliability and validity. Journal of orthopaedic trauma 2010;24 Suppl 1:S81-6.

Kratzel C, Bergmann C, Duda G, Greiner S, Schmidmaier G, Wildemann B. Characterization of a rat osteotomy model with impaired healing. BMC musculoskeletal disorders 2008;9:135.

Krieg MA, Barkmann R, Gonnelli S, Stewart A, Bauer DC, Del Rio Barquero L, Kaufman JJ, Lorenc R, Miller PD, Olszynski WP, Poiana C, Schott AM, Lewiecki EM, Hans D. Quantitative ultrasound in the management of osteoporosis: the 2007 ISCD Official Positions. Journal of clinical densitometry : the official journal of the International Society for Clinical Densitometry 2008;11:163-87.

Krug R, Banerjee S, Han ET, Newitt DC, Link TM, Majumdar S. Feasibility of in vivo structural analysis of high-resolution magnetic resonance images of the proximal femur. Osteoporosis international : a journal established as result of cooperation between the European Foundation for Osteoporosis and the National Osteoporosis Foundation of the USA 2005;16:1307-14.

Krug R, Burghardt AJ, Majumdar S, Link TM. High-resolution imaging techniques for the assessment of osteoporosis. Radiologic clinics of North America 2010;48:601-21.

Krug R, Carballido-Gamio J, Burghardt AJ, Kazakia G, Hyun BH, Jobke B, Banerjee S, Huber M, Link TM, Majumdar S. Assessment of trabecular bone structure comparing magnetic

resonance imaging at 3 Tesla with high-resolution peripheral quantitative computed tomography ex vivo and in vivo. Osteoporosis international : a journal established as result of cooperation between the European Foundation for Osteoporosis and the National Osteoporosis Foundation of the USA 2008;19:653-61.

Krzanowski W. Principles of multivariate analysis : a user's perspective. Oxford [Oxfordshire] ;;New York: Oxford University Press, 2000.

Kubo T, Fujimori K, Cazier N, Saeki T, Matsukawa M. Properties of ultrasonic waves in bovine bone marrow. Ultrasound in medicine & biology 2011;37:1923-9.

Kular J, Tickner J, Chim SM, Xu J. An overview of the regulation of bone remodelling at the cellular level. Clinical biochemistry 2012;45:863-73.

Kundu T. Ultrasonic nondestructive evaluation: engineering and biological material characterization. Boca Raton, Fla: CRC Press, 2004.

Lakshmanan S, Bodi A, Raum K. Assessment of anisotropic tissue elasticity of cortical bone from high-resolution, angular acoustic measurements. IEEE T Ultrason Ferr 2007;54:1560-70.

Langer M, Liu Y, Tortelli F, Cloetens P, Cancedda R, Peyrin F. Regularized phase tomography enables study of mineralized and unmineralized tissue in porous bone scaffold. J Microsc 2010;238:230-9.

Langer M, Pacureanu A, Suhonen H, Grimal Q, Cloetens P, Peyrin F. X-Ray Phase Nanotomography Resolves the 3D Human Bone Ultrastructure. PLoS ONE 2012;7:e35691.

Langton CM, Palmer SB, Porter RW. The Measurement of Broadband Ultrasonic Attenuation in Cancellous Bone. Engineering in Medicine 1984;13:89-91.

Laugier P. Instrumentation for in vivo ultrasonic characterization of bone strength. IEEE transactions on ultrasonics, ferroelectrics, and frequency control 2008;55:1179-96.

Laugier P, Haïat G. Bone quantitative ultrasound. Dordrecht; New York: Springer Science+Business media B.V., 2011a.

Laugier P, Haïat G. Introduction to the Physics of Ultrasound. In: Laugier P, Haïat G, ed. Bone Quantitative Ultrasound. Springer Netherlands, 2011b. pp. 29-45.

Laurencin C, Khan Y, El-Amin SF. Bone graft substitutes. Expert review of medical devices 2006;3:49-57.

Le Floch V, Luo G, Kaufman JJ, Siffert RS. Ultrasonic assessment of the radius in vitro. Ultrasound in medicine & biology 2008;34:1972-9.

Leicht S, Raum K. Acoustic impedance changes in cartilage and subchondral bone due to primary arthrosis. Ultrasonics 2008;48:613-20.

Lemons RA, Quate CF. Acoustic microscope—scanning version. Applied Physics Letters 1974;24:

Lewiecki EM. Imaging Technologies for Assessment of Skeletal Health in Men. Current osteoporosis reports 2012;

Lienau J, Schmidt-Bleek K, Peters A, Haschke F, Duda GN, Perka C, Bail HJ, Schutze N, Jakob F, Schell H. Differential regulation of blood vessel formation between standard and delayed bone healing. JOrthopRes 2009;27:1133-40.

Lilliefors HW. On the Kolmogorov-Smirnov Test for Normality with Mean and Variance Unknown. Journal of the American Statistical Association 1967;62:399-402.

Linde F, Sorensen HC. The effect of different storage methods on the mechanical properties of trabecular bone. Journal of biomechanics 1993;26:1249-52.

Lotz JC, Cheal EJ, Hayes WC. Stress distributions within the proximal femur during gait and falls: implications for osteoporotic fracture. Osteoporosis international : a journal established as

result of cooperation between the European Foundation for Osteoporosis and the National Osteoporosis Foundation of the USA 1995;5:252-61.

Luo G, Kaufman JJ, Chiabrera A, Bianco B, Kinney JH, Haupt D, Ryaby JT, Siffert RS. Computational methods for ultrasonic bone assessment. Ultrasound In Medicine And Biology 1999;25:823-30.

Machado CB, Pereira WCD, Talmant M, Padilla F, Laugier P. Computational Evaluation of the Compositional Factors in Fracture Healing Affecting Ultrasound Axial Transmission Measurements. Ultrasound in Medicine and Biology 2010b;36:1314-26.

Majumdar S, Newitt D, Mathur A, Osman D, Gies A, Chiu E, Lotz J, Kinney J, Genant H. Magnetic resonance imaging of trabecular bone structure in the distal radius: relationship with X-ray tomographic microscopy and biomechanics. Osteoporosis international : a journal established as result of cooperation between the European Foundation for Osteoporosis and the National Osteoporosis Foundation of the USA 1996;6:376-85.

Malizos KN, Papachristos AA, Protopappas VC, Fotiadis DI. Transosseous application of low-intensity ultrasound for the enhancement and monitoring of fracture healing process in a sheep osteotomy model. Bone 2006;38:530-9.

Malo MKH, Rohrbach D, Isaksson H, Töyräs J, Jurvelin JS, Tamminen IS, Kröger H, Raum K. Longitudinal elastic properties and porosity of cortical bone tissue vary with age in human proximal femur. Bone 2013;53:451-8.

Manjubala I, Liu Y, Epari DR, Roschger P, Schell H, Fratzl P, Duda GN. Spatial and temporal variations of mechanical properties and mineral content of the external callus during bone healing. Bone 2009;45:185-92.

Mano I, Horii K, Takai S, Suzaki T, Nagaoka H, Otani T. Development of novel ultrasonic bone densitometry using acoustic parameters of cancellous bone for fast and slow waves. Jpn J Appl Phys 1 2006;45:4700-2.

Maylia E, Nokes LD. The use of ultrasonics in orthopaedics--a review. Technol Health Care 1999;7:1-28.

Mehta M, Checa S, Lienau J, Hutmacher D, Duda GN. In vivo tracking of segmental bone defect healing reveals that callus patterning is related to early mechanical stimuli. Eur Cell Mater 2012a;24:358-71.

Mehta M, Schmidt-Bleek K, Duda GN, Mooney DJ. Biomaterial delivery of morphogens to mimic the natural healing cascade in bone. Advanced drug delivery reviews 2012b;64:1257-76.

Mehta M, Strube P, Peters A, Perka C, Hutmacher D, Fratzl P, Duda GN. Influences of age and mechanical stability on volume, microstructure, and mineralization of the fracture callus during bone healing: is osteoclast activity the key to age-related impaired healing? Bone 2010;47:219-28.

Meyer D. The support vector machine under test. Neurocomputing 2003;55:169-86.

Minonzio JG, Talmant M, Laugier P. Guided wave phase velocity measurement using multi-emitter and multi-receiver arrays in the axial transmission configuration. J Acoust Soc Am 2010;127:2913-9.

Misof B, Roschger P, Fratzl P. 3.325 - Imaging Mineralized Tissues in Vertebrates. In: Editor-in-Chief: Paul D, ed. Comprehensive Biomaterials. Oxford: Elsevier, 2011. pp. 407-26.

Mitchell T. Machine learning. New York [etc.]: MacGraw-Hill, 1997.

Mitton D, Roux C, Laugier P. Bone Overview. In: Laugier P, Haïat G, ed. Bone Quantitative Ultrasound. Springer Netherlands, 2011. pp. 1-28.

Moilanen P, Talmant M, Bousson V, Nicholson PH, Cheng S, Timonen J, Laugier P. Ultrasonically determined thickness of long cortical bones: two-dimensional simulations of in vitro experiments. J Acoust Soc Am 2007a;122:1818.

Moilanen P, Talmant M, Nicholson PH, Cheng S, Timonen J, Laugier P. Ultrasonically determined thickness of long cortical bones: Three-dimensional simulations of in vitro experiments. J Acoust Soc Am 2007b;122:2439-45.

Momose A. Recent Advances in X-ray Phase Imaging. Jpn J Appl Phys 2005;44:6355-67.

Morgan EF, Mason ZD, Chien KB, Pfeiffer AJ, Barnes GL, Einhorn TA, Gerstenfeld LC. Micro-computed tomography assessment of fracture healing: relationships among callus structure, composition, and mechanical function. Bone 2009;44:335-44.

Mori T, Tanaka K. Average stress in matrix and average elastic energy of materials with misfitting inclusions. Acta Metallurgica 1973;21:571-4.

Mountziaris PM, Spicer PP, Kasper FK, Mikos AG. Harnessing and modulating inflammation in strategies for bone regeneration. Tissue engineering Part B, Reviews 2011;17:393-402.

Muller R, Ruegsegger P. Micro-tomographic imaging for the nondestructive evaluation of trabecular bone architecture. Stud Health Technol Inform 1997;40:61-79.

Muller R, Van Campenhout H, Van Damme B, Van Der Perre G, Dequeker J, Hildebrand T, Ruegsegger P. Morphometric analysis of human bone biopsies: a quantitative structural comparison of histological sections and micro-computed tomography. Bone 1998;23:59-66.

Nagatani Y, Mizuno K, Saeki T, Matsukawa M, Sakaguchi T, Hosoi H. Numerical and experimental study on the wave attenuation in bone--FDTD simulation of ultrasound propagation in cancellous bone. Ultrasonics 2008;48:607-12.

Nauleau P, Cochard E, Minonzio JG, Grimal Q, Laugier P, Prada C. Characterization of circumferential guided waves in a cylindrical cortical bone-mimicking phantom. J Acoust Soc Am 2012;131:EL289-94.

Nicholls PJ, Berg E, Bliven FE, Jr., Kling JM. X-ray diagnosis of healing fractures in rabbits. Clinical orthopaedics and related research 1979;234-6.

Nicholson PH, Lowet G, Cheng XG, Boonen S, van der Perre G, Dequeker J. Assessment of the strength of the proximal femur in vitro: relationship with ultrasonic measurements of the calcaneus. Bone 1997;20:219-24.

Nicholson PH, Lowet G, Langton CM, Dequeker J, Van der Perre G. A comparison of time-domain and frequency-domain approaches to ultrasonic velocity measurement in trabecular bone. Physics in medicine and biology 1996;41:2421-35.

Nicholson PH, Moilanen P, Karkkainen T, Timonen J, Cheng S. Guided ultrasonic waves in long bones: modelling, experiment and in vivo application. Physiological measurement 2002;23:755-68.

Nieminen HJ, Saarakkala S, Laasanen MS, Hirvonen J, Jurvelin JS, Toyras J. Ultrasound attenuation in normal and spontaneously degenerated articular cartilage. Ultrasound in medicine & biology 2004;30:493-500.

Nishiyama KK, Macdonald HM, Hanley DA, Boyd SK. Women with previous fragility fractures can be classified based on bone microarchitecture and finite element analysis measured with HR-pQCT. Osteoporosis international : a journal established as result of cooperation between the European Foundation for Osteoporosis and the National Osteoporosis Foundation of the USA 2012;

Njeh CF, Kearton JR, Hans D, Boivin CM. The use of quantitative ultrasound to monitor fracture healing: a feasibility study using phantoms. Medical engineering & physics 1998;20:781-6.

Nuzzo S, Lafage-Proust MH, Martin-Badosa E, Boivin G, Thomas T, Alexandre C, Peyrin F. Synchrotron radiation microtomography allows the analysis of three-dimensional microarchitecture and degree of mineralization of human iliac crest biopsy specimens: effects of etidronate treatment. Journal of bone and mineral research : the official journal of the American Society for Bone and Mineral Research 2002a;17:1372-82.

Nuzzo S, Peyrin F, Cloetens P, Baruchel J, Boivin G. Quantification of the degree of mineralization of bone in three dimensions using synchrotron radiation microtomography. MedPhys 2002b;29:2672-81.

Nyman JS, Reyes M, Wang X. Effect of ultrastructural changes on the toughness of bone. Micron 2005;36:566-82.

Oberender PO, Fritschi DA. Disease Management und Osteoporose: Versorgungsmängel bei einer relevanten Frauenkrankheit. Dtsch Arztebl International 2003;100:A-1728.

Oliver WC, Pharr GM. An Improved Technique for Determining Hardness and Elastic-Modulus Using Load and Displacement Sensing Indentation Experiments. J Mater Res 1992;7:1564-83.

Oliver WC, Pharr GM. Measurement of hardness and elastic modulus by instrumented indentation: Advances in understanding and refinements to methodology. J Mater Res 2004;19:3-20.

Pacureanu A, Langer M, Boller E, Tafforeau P, Peyrin F. Nanoscale imaging of the bone cell network with synchrotron X-ray tomography: optimization of acquisition setup. Medical physics 2012;39:2229-38.

Padilla F, Bossy E, Haiat G, Jenson F, Laugier P. Numerical simulation of wave propagation in cancellous bone. Ultrasonics 2006;

Panjabi MM, Lindsey RW, Walter SD, White AA, 3rd. The clinician's ability to evaluate the strength of healing fractures from plain radiographs. Journal of orthopaedic trauma 1989;3:29-32.

Panjabi MM, Walter SD, Karuda M, White AA, Lawson JP. Correlations of radiographic analysis of healing fractures with strength: a statistical analysis of experimental osteotomies. Journal of orthopaedic research : official publication of the Orthopaedic Research Society 1985;3:212-8.

Parfitt AM. Misconceptions (2): turnover is always higher in cancellous than in cortical bone. Bone 2002;30:807-9.

Parnell WJ, Abrahams ID. Dynamic homogenization in periodic fibre reinforced media. Quasi-static limit for SH waves. Wave Motion 2006;43:474-98.

Parnell WJ, Grimal Q. The influence of mesoscale porosity on cortical bone anisotropy. Investigations via asymptotic homogenization. JRSocInterface 2009;6:97-109.

Parnell WJ, Vu MB, Grimal Q, Naili S. Analytical methods to determine the effective mesoscopic and macroscopic elastic properties of cortical bone. Biomech Model Mechanobiol 2012;11:883-901.

Patrick E, Fischeriii F. A generalized -nearest neighbor rule. Information and Control 1970;16:128-52.

Pearce MS, Salotti JA, Little MP, McHugh K, Lee C, Kim KP, Howe NL, Ronckers CM, Rajaraman P, Craft AW, Parker L, de Gonzalez AB. Radiation exposure from CT scans in childhood and subsequent risk of leukaemia and brain tumours: a retrospective cohort study. Lancet 2012;

Peck SD, Briggs GA. A scanning acoustic microscope study of the small caries lesion in human enamel. Caries research 1986;20:356-60.

Peck SD, Rowe JM, Briggs GA. Studies on sound and carious enamel with the quantitative acoustic microscope. Journal of dental research 1989;68:107-12.

Pedrotti L, Bertani B, Mora R. Assessment of Fracture Healing. In: Mora R, ed. Nonunion of the Long Bones. Springer Milan, 2006. pp. 15-23.

Peters A, Schell H, Bail HJ, Hannemann M, Schumann T, Duda GN, Lienau J. Standard bone healing stages occur during delayed bone healing, albeit with a different temporal onset and spatial distribution of callus tissues. Histology and Histopathology 2010;25:1149-62.

Pfeiffer S, Crowder C, Harrington L, Brown M. Secondary osteon and Haversian canal dimensions as behavioral indicators. AmJPhysAnthropol 2006;

Pidaparti RM, Chandran A, Takano Y, Turner CH. Bone mineral lies mainly outside collagen fibrils: predictions of a composite model for osteonal bone. Journal of biomechanics 1996;29:909-16.

Pientka L, Friedrich C. [Osteoporosis: the epidemiologic and health economics perspective]. Zeitschrift fur arztliche Fortbildung und Qualitatssicherung 2000;94:439-44.

Pothuaud L, Benhamou CL, Porion P, Lespessailles E, Harba R, Levitz P. Fractal dimension of trabecular bone projection texture is related to three-dimensional microarchitecture. Journal of bone and mineral research : the official journal of the American Society for Bone and Mineral Research 2000;15:691-9.

Preininger B, Checa S, Molnar FL, Fratzl P, Duda GN, Raum K. Spatial-temporal mapping of bone structural and elastic properties in a sheep model following osteotomy. Ultrasound in medicine & biology 2011;37:474-83.

Preininger B, Gerigk H, Bruckner J, Perka C, Schell H, Ellinghaus A, Schmidt-Bleek K, Duda G. An experimental setup to evaluate innovative therapy options for the enhancement of bone healing using BMP as a benchmark - a pilot study. Eur Cell Mater 2012a;23:262-72.

Preininger B, Hesse B, Rohrbach D, Varga P, Gerigk H, Langer M, Peyrin F, Perka C, Raum K. Histogram feature-based classification improves differentiability of early bone healing stages from micro-computed tomographic data. Journal of computer assisted tomography 2012b;36:469-76.

Protopappas VC, Baga DA, Fotiadis DI, Likas AC, Papachristos AA, Malizos KN. An ultrasound wearable system for the monitoring and acceleration of fracture healing in long bones. IEEE Trans Biomed Eng 2005;52:1597-608.

Protopappas VC, Fotiadis DI, Malizos KN. Guided ultrasound wave propagation in intact and healing long bones. Ultrasound In Medicine And Biology 2006;32:693-708.

Protopappas VC, Kourtis IC, Kourtis LC, Malizos KN, Massalas CV, Fotiadis DI. Three-dimensional finite element modeling of guided ultrasound wave propagation in intact and healing long bones. J Acoust Soc Am 2007;121:3907-21.

Protopappas VC, Vavva MG, Fotiadis DI, Malizos KN. Ultrasonic monitoring of bone fracture healing. IEEE Trans Ultrason Ferroelectr Freq Control 2008;55:1243-55.

Qian JG, Song YW, Tang X, Zhang S. Examination of femoral-neck structure using finite element model and bone mineral density using dual-energy X-ray absorptiometry. Clin Biomech (Bristol, Avon) 2009;24:47-52.

Raudys SJ, Jain AK. Small sample size effects in statistical pattern recognition: recommendations for practitioners. IEEE Transactions on Pattern Analysis and Machine Intelligence 1991;13:252-64.

Raum K. Microelastic imaging of bone. IEEE Trans UltrasonFerroelectrFreqControl 2008;55:1417-31.

Raum K. Microscopic Elastic Properties, Bone Quantitative Ultrasound. In: Laugier P, Haïat G, ed. Springer Netherlands, 2011. pp. 409-39.

Raum K, Cleveland RO, Peyrin F, Laugier P. Derivation of elastic stiffness from site-matched mineral density and acoustic impedance maps. PhysMedBiol 2006a;51:747-58.

Raum K, Grimal Q, Laugier P, Gerisch A. Multiscale structure-functional modeling of lamellar bone. Proceedings of Meetings on Acoustics 2011;9:020005-15.

Raum K, Hofmann T, Leguerney I, Saied A, Peyrin F, Vico L, Laugier P. Variations of microstructure, mineral density and tissue elasticity in B6/C3H mice. Bone 2007a;41:1017-24.

Raum K, Jenderka KV, Klemenz A, Brandt J. Multilayer analysis: Quantitative scanning acoustic microscopy for tissue characterization at a microscopic scale. IEEE T Ultrason Ferr 2003;50:507-16.

Raum K, Kempf K, Hein HJ, Schubert J, Maurer P. Preservation of microelastic properties of dentin and tooth enamel in vitro--a scanning acoustic microscopy study. Dental materials : official publication of the Academy of Dental Materials 2007b;23:1221-8.

Raum K, Leguerney I, Chandelier F, Bossy E, Talmant M, Saied A, Peyrin F, Laugier P. Bone microstructure and elastic tissue properties are reflected in QUS axial transmission measurements. Ultrasound in medicine & biology 2005a;31:1225-35.

Raum K, Leguerney I, Chandelier F, Bossy E, Talmant M, Saied A, Peyrin F, Laugier P. Bone microstructure and elastic tissue properties are reflected in QUS axial transmission measurements. Ultrasound In Medicine And Biology 2005b;31:1225-35.

Raum K, Leguerney I, Chandelier F, Talmant M, Saied A, Peyrin F, Laugier P. Site-matched assessment of structural and tissue properties of cortical bone using scanning acoustic microscopy and synchrotron radiation muCT. PhysMedBiol 2006b;51:733-46.

Raum K, OBrien WD. Pulse-echo field distribution measurement technique for high-frequency ultrasound sources. IEEE T Ultrason Ferr 1997;44:810-5.

Raum K, Rohrbach D, Laugier P, Glüer CC, Barkmann R. Bone quality beyond bone mineral density – new diagnostic perspectives by quantitative ultrasound. Osteologie 2010;19:217-24.

Reisinger AG, Pahr DH, Zysset PK. Sensitivity analysis and parametric study of elastic properties of an unidirectional mineralized bone fibril-array using mean field methods. Biomech Model Mechanobiol 2010;9:499-510.

Reisinger AG, Pahr DH, Zysset PK. Elastic anisotropy of bone lamellae as a function of fibril orientation pattern. Biomech Model Mechanobiol 2011;10:67-77.

Rho JY, Kuhn-Spearing L, Zioupos P. Mechanical properties and the hierarchical structure of bone. Medical engineering & physics 1998;20:92-102.

Rohde K, Rohrbach D, Glüer C, Laugier P, Grimal Q, Raum K, Barkmann R. Influence of porosity, pore size and cortical thickness on the propagation of ultrasonic waves guided through the femoral neck cortex: a simulation study. Transactions on Ultrasonics, Ferroelectrics, and Frequency Control 2012;submitted paper:

Rohrbach D, Grondin J, Grimal Q, Laugier P, Barkmann R, Raum K. Evidence based numerical ultrasound simulations at the human femoral neck. Biomedizinische Technik, Rostock, conference proceeding 2010;

Rohrbach D, Hesse B, Preininger B, Perka C, Raum K. Assessment of soft and mineralized tissue formation in a rat bone healing model using quantitative ultrasound (QUS). The Journal of the Acoustical Society of America 2012a;131:3458.

Rohrbach D, Lakshmanan S, Peyrin F, Langer M, Gerisch A, Grimal Q, Laugier P, Raum K. Spatial distribution of tissue level properties in a human femoral cortical bone. Journal of biomechanics 2012b;45:2264-70.

Rohrbach D, Preininger B, Hesse B, Gerigk H, Perka C, Raum K. The early phases of bone healing can be differentiated in a rat osteotomy model by focused transverse-transmission ultrasound. Ultrasound in medicine & biology 2013;submitted and accepted:

Roschger P, Fratzl P, Eschberger J, Klaushofer K. Validation of quantitative backscattered electron imaging for the measurement of mineral density distribution in human bone biopsies. Bone 1998;23:319-26.

Roschger P, Gupta HS, Berzlanovich A, Ittner G, Dempster DW, Fratzl P, Cosman F, Parisien M, Lindsay R, Nieves JW, Klaushofer K. Constant mineralization density distribution in cancellous human bone. Bone 2003;32:316-23.

Roschger P, Paschalis EP, Fratzl P, Klaushofer K. Bone mineralization density distribution in health and disease. Bone 2008;42:456-66.

Roschger P, Plenk H, Jr., Klaushofer K, Eschberger J. A new scanning electron microscopy approach to the quantification of bone mineral distribution: backscattered electron image grey-levels correlated to calcium K alpha-line intensities. Scanning microscopy 1995;9:75-86; discussion -8.

Royall RM. The Effect of Sample Size on the Meaning of Significance Tests. The American Statistician 1986;40:313-5.

Royer D. Elastic waves in solids I. Berlin ; New York: Springer, 2000.

Rudy DJ, Deuerling JM, Espinoza Orias AA, Roeder RK. Anatomic variation in the elastic inhomogeneity and anisotropy of human femoral cortical bone tissue is consistent across multiple donors. Journal of biomechanics 2011;44:1817-20.

Ruimerman R, Hilbers P, van Rietbergen B, Huiskes R. A theoretical framework for strain-related trabecular bone maintenance and adaptation. Journal of biomechanics 2005;38:931-41.

Rupin F, Saïed A, Dalmas D, Peyrin F, Haupert S, Raum K, Barthel E, Boivin G, Laugier P. Assessment of Microelastic Properties of Bone Using Scanning Acoustic Microscopy: A Face-to-Face Comparison with Nanoindentation. Japanese Journal of Applied Physics 2009;48:

Saha S, Rao VV, Malakanok V, Albright JA. Quantitative Measurement of Fracture-Healing by Ultrasound. Biomaterials Medical Devices and Artificial Organs 1981;9:321-2.

Saied A, Raum K, Leguerney I, Laugier P. Spatial distribution of anisotropic acoustic impedance assessed by time-resolved 50-MHz scanning acoustic microscopy and its relation to porosity in human cortical bone. Bone 2008;43:187-94.

Salome M, Peyrin F, Cloetens P, Odet C, Laval-Jeantet AM, Baruchel J, Spanne P. A synchrotron radiation microtomography system for the analysis of trabecular bone samples. MedPhys 1999;26:2194-204.

Saulgozis J, Pontaga I, Lowet G, Van der Perre G. The effect of fracture and fracture fixation on ultrasonic velocity and attenuation. Physiological measurement 1996;17:201-11.

Schuit SCE, van der Klift M, Weel AEAM, de Laet CEDH, Burger H, Seeman E, Hofman A, Uitterlinden AG, van Leeuwen JPTM, Pols HAP. Fracture incidence and association with bone mineral density in elderly men and women: the Rotterdam Study. Bone 2004;34:195-202.

Schulte FA, Lambers FM, Kuhn G, Muller R. In vivo micro-computed tomography allows direct three-dimensional quantification of both bone formation and bone resorption parameters using time-lapsed imaging. Bone 2011;48:433-42.

Sedlin ED, Hirsch C. Factors affecting the determination of the physical properties of femoral cortical bone. Acta Orthop Scand 1966;37:29-48.

Segal SS, White TP, Faulkner JA. Architecture, composition, and contractile properties of rat soleus muscle grafts. The American journal of physiology 1986;250:C474-9.

Sornay-Rendu E, Munoz F, Garnero P, Duboeuf F, Delmas PD. Identification of osteopenic women at high risk of fracture: the OFELY study. Journal of bone and mineral research : the official journal of the American Society for Bone and Mineral Research 2005;20:1813-9.

Speirs AD, Heller MO, Duda GN, Taylor WR. Physiologically based boundary conditions in finite element modelling. Journal of biomechanics 2007;40:2318-23.

Sprague S, Bhandari M. An economic evaluation of early versus delayed operative treatment in patients with closed tibial shaft fractures. Archives of orthopaedic and trauma surgery 2002;122:315-23.

Stone KL, Seeley DG, Lui LY, Cauley JA, Ensrud K, Browner WS, Nevitt MC, Cummings SR. BMD at multiple sites and risk of fracture of multiple types: long-term results from the Study of Osteoporotic Fractures. Journal of bone and mineral research : the official journal of the American Society for Bone and Mineral Research 2003;18:1947-54.

Strube P, Mehta M, Putzier M, Matziolis G, Perka C, Duda GN. A new device to control mechanical environment in bone defect healing in rats. Journal of biomechanics 2008a;41:2696-702.

Strube P, Sentuerk U, Riha T, Kaspar K, Mueller M, Kasper G, Matziolis G, Duda GN, Perka C. Influence of age and mechanical stability on bone defect healing: age reverses mechanical effects. Bone 2008b;42:758-64.

Tabachnick B. Using multivariate statistics. Boston: Pearson/Allyn & Bacon, 2007.

Theodoridis S. Pattern recognition. Amsterdam ;;Boston: Elsevier/Academic Press, 2006.

Treeby BE, Cox BT. k-Wave: MATLAB toolbox for the simulation and reconstruction of photoacoustic wave fields. Journal of biomedical optics 2010a;15:021314.

Treeby BE, Cox BT. Modeling power law absorption and dispersion for acoustic propagation using the fractional Laplacian. J Acoust Soc Am 2010b;127:2741-48.

Treeby BE, Zhang EZ, Cox BT. Photoacoustic tomography in absorbing acoustic media using time reversal. Inverse Problems 2010;26:115003-.

Turner CH. Bone strength: current concepts. Annals of the New York Academy of Sciences 2006;1068:429-46.

Turner CH, Chandran A, Pidaparti RM. The anisotropy of osteonal bone and its ultrastructural implications. Bone 1995;17:85-9.

Turner CH, Rho J, Takano Y, Tsui TY, Pharr GM. The elastic properties of trabecular and cortical bone tissues are similar: results from two microscopic measurement techniques. Journal of biomechanics 1999;32:437-41.

van Haaren EH, van der Zwaard BC, van der Veen AJ, Heyligers IC, Wuisman PI, Smit TH. Effect of long-term preservation on the mechanical properties of cortical bone in goats. Acta Orthop 2008;79:708-16.

Van Rietbergen B, Huiskes R, Eckstein F, Ruegsegger P. Trabecular bone tissue strains in the healthy and osteoporotic human femur. Journal of bone and mineral research : the official journal of the American Society for Bone and Mineral Research 2003;18:1781-8.

Varga P, Dall'Ara E, Pahr DH, Pretterklieber M, Zysset PK. Validation of an HR-pQCT-based homogenized finite element approach using mechanical testing of ultra-distal radius sections. Biomech Model Mechanobiol 2011;10:431-44.

Varga P, Pahr DH, Baumbach S, Zysset PK. HR-pQCT based FE analysis of the most distal radius section provides an improved prediction of Colles' fracture load in vitro. Bone 2010;47:982-8.

Verhulp E, Van RB, Huiskes R. Load distribution in the healthy and osteoporotic human proximal femur during a fall to the side. Bone 2008;42:30-5.

Vetter A, Liu Y, Witt F, Manjubala I, Sander O, Epari DR, Fratzl P, Duda GN, Weinkamer R. The mechanical heterogeneity of the hard callus influences local tissue strains during bone healing: a finite element study based on sheep experiments. Journal of biomechanics 2011;44:517-23.

Virieux J. P-SV wave propagation in heterogeneous media: Velocity-stress finite-difference method. Geophysics 1986;51:

W.H.O. Assessment of fracture risk and its application to screening for postmenopausal osteoporosis. Geneva: World Health Organization, 1994.

Wachter NJ, Krischak GD, Mentzel M, Sarkar MR, Ebinger T, Kinzl L, Claes L, Augat P. Correlation of bone mineral density with strength and microstructural parameters of cortical bone in vitro. Bone 2002;31:90-5.

Wagermaier W, Fratzl P, Burghammer M, Roschger P. Spiral twisting of fiber orientation inside bone lamella. Biointerphases 2006;1:1-5.

Wall JC, Chatterji SK, Jeffery JW. Age-related changes in the density and tensile strength of human femoral cortical bone. Calcified tissue international 1979;27:105-8.

Wang X, Ni Q. Determination of cortical bone porosity and pore size distribution using a low field pulsed NMR approach. JOrthopRes 2003;21:312-9.

Wear KA. The effects of frequency-dependent attenuation and dispersion on sound speed measurements: applications in human trabecular bone. IEEE Trans Ultrason Ferroelectr Freq Control 2000;47:265-73.

Wear KA. Ultrasonic attenuation in human calcaneus from 0.2 to 1.7 MHz. IEEE Trans Ultrason Ferroelectr Freq Control 2001;48:602-8.

Weiner S, Arad T, Sabanay I, Traub W. Rotated plywood structure of primary lamellar bone in the rat: orientations of the collagen fibril arrays. Bone 1997;20:509-14.

Weiner W. THE MATERIAL BONE: Structure-Mechanical Function Relations. Annual Review of Materials Science 1998;28:271-98.

Weiss S, Zimmerman MC, Harten RD, Alberta FG, Meunier A. The acoustic and structural properties of the human femur. Journal of Biomechanical Engineering-Transactions of the Asme 1998;120:71-6.

Wolff J. Das Gesetz der Transformation der Knochen. Berlin: Verlag von August Hirschwald, 1892.

Yamamoto K, Nakatsuji T, Yaoi Y, Yamato Y, Yanagitani T, Matsukawa M, Yamazaki K, Matsuyama Y. Relationships between the anisotropy of longitudinal wave velocity and hydroxyapatite crystallite orientation in bovine cortical bone. Ultrasonics 2012;52:377-86.

Yeni YN, Norman TL. Fracture toughness of human femoral neck: effect of microstructure, composition, and age. Bone 2000;26:499-504.

Zebaze RM, Ghasem-Zadeh A, Bohte A, Iuliano-Burns S, Mirams M, Price RI, Mackie EJ, Seeman E. Intracortical remodelling and porosity in the distal radius and post-mortem femurs of women: a cross-sectional study. Lancet 2010;375:1729-36.

Zebaze RM, Jones AC, Pandy MG, Knackstedt MA, Seeman E. Differences in the degree of bone tissue mineralization account for little of the differences in tissue elastic properties. Bone 2011;48:1246-51.

Zhang Z, Zhang S, Zhang C-x, Chen Y-z. SVM for density estimation and application to medical image segmentation. Journal of Zhejiang University Science B 2006;7:365-72.

Zhou SA, Brahme A. Development of phase-contrast X-ray imaging techniques and potential medical applications. Phys Med 2008;24:129-48.

Zimmerman MC, Prabhakar A, Chokshi BV, Budhwani N, Berndt H. The acoustic properties of normal and imbedded bovine bone as measured by acoustic microscopy. Journal of biomedical materials research 1994;28:931-8.

Zioupos P. Ageing human bone: factors affecting its biomechanical properties and the role of collagen. J Biomater Appl 2001;15:187-229.

Zou W, Hunter N, Swain MV. Application of polychromatic microCT for mineral density determination. Journal of dental research 2011;90:18-30.

Zupan J, Komadina R, Marc J. The relationship between osteoclastogenic and anti-osteoclastogenic pro-inflammatory cytokines differs in human osteoporotic and osteoarthritic bone tissues. Journal of biomedical science 2012;19:28.

Zysset PK. Indentation of bone tissue: a short review. Osteoporosis international : a journal established as result of cooperation between the European Foundation for Osteoporosis and the National Osteoporosis Foundation of the USA 2009;20:1049-55.